

**QUALITATIVE AIR FLOW MODELLING AND
ANALYSIS OF DATA CENTRE AIR CONDITIONING
AS MULTIPLE JET ARRAY**

*Thesis submitted to
Cochin University of Science and Technology
in fulfilment of the requirements for
the award of the degree of
Doctor of Philosophy*

by

PREMNATH R.

(Reg. No. 3532)

Under the supervision of

Prof. (Dr). G. MADHU

**DIVISION OF SAFETY AND FIRE ENGINEERING
SCHOOL OF ENGINEERING
COCHIN UNIVERSITY OF SCIENCE AND TECHNOLOGY
KOCHI – 682022, KERALA, INDIA.**

November 2011

Dedicated to
The Ever Loving Memmories of
My Grand Parents
Chelat Raman Menon and Janaki Amma
My Beloved Father
Prof. K. Ramankutty Menon
and
My Loving Brother
Prof. Gopinath. R

DIVISION OF SAFETY AND FIRE ENGINEERING
SCHOOL OF ENGINEERING
COCHIN UNIVERSITY OF SCIENCE AND TECHNOLOGY
KOCHI – 682022, KERALA, INDIA.

Dr. G.MADHU
Professor and Head

Ph: 0484-2862180
Fax: 91-484-2550952
e-mail: profmadhu@cusat.ac.in

Certificate

This is to certify that the thesis entitled “**QUALITATIVE AIR FLOW MODELLING AND ANALYSIS OF DATA CENTRE AIR CONDITIONING AS MULTIPLE JET ARRAY**” submitted by **PREMNATH.R** to the Cochin University of Science and Technology, Kochi for the award of the degree of **Doctor of Philosophy** is a bonafide record of research work carried out by him under my supervision. The contents of this thesis, in full or in parts, have not been submitted to any other Institute or University for the award of any degree or diploma.

Dr. G. Madhu
Research Guide

Place: Kochi-22
Date:

Declaration

I here by declare that the thesis entitled 'QUALITATIVE AIR FLOW MODELLING AND ANALYSIS OF DATA CENTRE AIR CONDITIONING AS MULTIPLE JET ARRAY' is based on the original work done by me under the supervision of Prof.(Dr).G.MADHU, Head, Division of Safety and Fire Engineering, School of Engineering, Cochin University of Science and Technology, Kochi. No part of this thesis has been presented for any other degree from any other University or Institution.

Premnath R

Kochi-22

Date:

Acknowledgement

I wish to express my deep sense of gratitude to my guide **Prof. G. Madhu** for his invaluable guidance. Throughout the course of this research work, he has provided the inspiration and kept the interest burning in me. I thank him for his keen interest at every stage of my Ph D programme. He is one of the kindest human being I have seen among the teaching community. In every sense he has been a true teacher, and a great philosopher to me. I express my sincere gratitude to **Dr.V.N. Narayanan Namboothiri**, Member, Doctoral Committee, for his valuable and timely help.

I am extremely thankful to **Mr. Varun Ramakrishnan** one of my favourite old students who guided me in developing the modelling methodology and the fundamentals of the software without which this work would not have been successful. I am greatly indebted to **Dr. Suresh.P.R** my colleague who introduced me into the fascinating world of jet theory. It was the discussions with him which led me to the idea of combining the theory of jets and data centre air flow by which I could explain the data centre air flow qualitatively.

I express my heartfelt gratitude to **Mr. Manu Kumar. V** my classmate, who is a legend in the field of data centre for introducing me into the field of data centre. He taught me the technologies of data centre cooling and worked together in the design and thermal assessment of many live data centre. From that experience only I could derive the present problem and solve it.

I wish to thank my mother **P.Indira Menon**, my wife **Usha**, children **Ramu** and **Govind**, niece **Janu**, for the affectionate support and encouragement they have rendered during the course of my research work,

I thank **God** almighty for giving me the opportunity to do this work,

Premnath.R |

Abstract

Data centre is a centralized repository, either physical or virtual, for the storage, management and dissemination of data and information organized around a particular body of knowledge or pertaining to a particular business. Data centre is the back bone and nerve centre of the present IT revolution. Data centre are expected to serve uninterruptedly round the year enabling them to perform their functions, it consumes enormous energy in the present scenario. Tremendous growth in the demand from IT industry made it customary to develop newer technologies for the better operation of data centre. Energy conservation activities in this field took its pace only recently and lot of activities are going on at the industry level but not much at the academic level. Energy conservation activities in data centre mainly concentrate on the air conditioning system since it is the major mechanical sub-system which consumes considerable share of the total power consumption of the data centre.

The data centre energy matrix is best represented by power utilization efficiency (PUE), which is defined as the ratio of the total facility power to the IT equipment power. Its value will be greater than one and a larger value of PUE indicates that the sub-systems draw more power from the facility and the performance of the data centre will be poor from the stand point of energy conservation. PUE values of 1.4 to 1.6 are achievable by proper design and management techniques. Optimizing the air conditioning system brings enormous opportunity in bringing down the PUE value. The air conditioning system can be optimized by two approaches namely, thermal management and air flow management. Thermal management systems are now introduced by some companies but they are highly sophisticated and costly and do not catch much attention in the field. The present thermal management technique involves industry best practices and thumb rules.

Data centre air conditioning system can be effectively optimized by the air flow management technique which is introduced through this thesis. By this method, handling of excess volume of air is avoided and both quantity and quality of the air flow are controlled to get best results. For this purpose, a systematic design procedure and coding system for the perforated vent tile is introduced for the first time in this work. The first task in this work was to identify a suitable scientific method to explain the air flow pattern within the data centre. Theory of jet which is a well developed concept is adopted to explain the qualitative nature of the air flow in the data centre. In the present study, air flow through the perforated vent tiles are considered and modelled as multiple jet arrays using Fluent software. The flow through these multiple jet arrays are computationally studied to explain the physics of air flow mechanism which ultimately gives the necessary cooling to data centre.

Preliminary studies on axisymmetric jets revealed the influence of the orifice diameter and tile thickness on the jet development characteristics. Based on this study, the optimum values of the dimensions of the orifice and the tile thickness are selected. The merging characteristics of plane multiple jets are studied for varying pitches. Based on the results, the necessary theories for merging of multiple jets are proposed. These theories are then applied to the merging of the three dimensional multiple jets and jet modules.

The perforated vent tiles which are used at present in the data centre do not have any scientific design or designation status. They are categorized simply based on the open area ratio and no information is available with respect to the tile orifice configuration. This work identifies that the tile orifice configuration has got remarkable influence on the flow characteristics and this must be considered while designing the tiles and must be designated according to the orifice configuration. The tile designation method proposed in the thesis is simple and self explanatory. Based on this design procedure, two different categories of tiles can be developed, standard tiles and combination tiles. The standard tiles give the flow characteristics

of a single tile, while the combination tiles can be converted into three different configurations and can give three different flow characteristics for the same pressure difference across the tile.

This work identifies the importance of plenum pressure on the performance of the data centre. The present methodology followed in the industry considers the pressure drop across the tile as a dependant variable, but it is shown in this work that this is the only one independent variable that is responsible for the entire flow dynamics in the data centre, and any design or assessment procedure must consider the pressure difference across the tile as the primary independent variable. This concept is further explained by the studies on the effect of dampers on the flow characteristics. The dampers have found to introduce an additional pressure drop there by reducing the effective pressure drop across the tile. The effect of damper is to change the flow both in quantitative and qualitative aspects. But the effect of damper on the flow in the quantitative aspect is only considered while using the damper as an aid for capacity control. Results from the present study suggest that the use of dampers must be avoided in data centre and well designed tiles which give required flow rates must be used in the appropriate locations.

In the present study the effect of hot air recirculation is studied with suitable assumptions. It identifies that, the pressure drop across the tile is a dominant parameter which governs the recirculation. The rack suction pressure of the hardware along with the pressure drop across the tile determines the point of recirculation in the cold aisle. The positioning of hardware in the racks play an important role in controlling the recirculation point. The present study is thus helpful in the design of data centre air flow, based on the theory of jets. The air flow can be modelled both quantitatively and qualitatively based on the results.

KEYWORDS: Data centre, air conditioning, air flow dynamics, computational fluid dynamics, energy conservation, perforated vent tiles, multiple jets.

CONTENTS

Acknowledgement	ix
Abstract	xi
List of tables	xix
List of figures	xxi
Nomenclature	xxix

Chapter 1

INTRODUCTION..... 01 - 14

1.1 Preamble -----	01
1.2 Introduction-----	02
1.3 Data Centre and Energy Perspective-----	03
1.4 Data Centre Airconditioning-----	05
1.5 Raised Floor air Conditioning Systems-----	06
1.6 Problem Formulation -----	11
1.7 Objectives and Scope-----	13
1.8 Organisation of the Thesis -----	13

Chapter 2

THEORY OF JETS 15 - 27

2.1 Introduction-----	15
2.2 Over View of Jet Flows -----	15
2.3 Structure and Development of a Free Jet-----	16
2.4 Factors Influencing Jet Spread-----	19
2.4.1 Inlet Velocity Profile -----	19
2.4.2 Nozzle Geometry-----	20
2.4.3 Jet Reynolds Number-----	20
2.4.4 Half Width and Virtual Origin of the Jet -----	21
2.4.5 Jet Instabilities-----	22
2.4.6 Coherent Structures-----	22
2.4.7 Isothermal and Non- isothermal Jet Spreading-----	23
2.4.8 Self Similarity -----	23
2.4.9 Role of Side Walls in Jet Flow-----	24
2.4.10 Turbulent Length Scales -----	25
2.4.11 Aspect Ratio -----	25
2.4.12 Intermittency-----	26
2.5 Conclusion -----	26

Chapter 3

LITERATURE REVIEW 29 - 49

3.1 Introduction-----	29
3.2 Experimental Investigations on Single Jet -----	30
3.3 Theoretical Modelling and Predictions for Single Jet-----	32
3.4 Twin And Multiple Jet Interactions -----	39
3.5 Data Centre air Conditioning -----	43
3.6 Conclusion -----	48

Chapter 4

NUMERICAL METHODOLOGY AND VALIDATION 51 - 63

4.1 Introduction-----	51
4.2 Governing Equations -----	52
4.3 Boundary Conditions -----	57
4.4 Pre-Processor & Solver-----	59
4.5 Grid Generation Details -----	60
4.6 Convergence Criteria -----	61
4.7 Validation Problem -----	61
4.8 Computer Systems Used -----	62
4.9 Conclusion -----	63

Chapter 5

AXISYMMETRIC JETS 65 - 73

5.1 Introduction-----	65
5.2 Modelling Methodology-----	65
5.3 Grid Independency Study -----	66
5.4 Results and Discussion -----	67
5.5 Conclusion -----	73

Chapter 6

PLANE JETS 75 - 99

6.1 Introduction-----	75
6.2 Single Jet-----	75
6.3 Twin Jet -----	78
6.4 Triple Jet -----	78

6.5	Differential Triple Jet-----	79
6.6	Results and Discussion -----	79
6.6.1	Single Jet-----	80
6.6.2	Twin Jet-----	84
6.6.3	Triple Jet-----	89
6.6.4	Differential Triple Jet-----	94
6.7	Conclusion-----	99

Chapter 7

THREE DIMENSIONAL JETS..... 101 - 145

7.1	Introduction-----	101
7.2	Single Jet-----	101
7.3	Twin Jet-----	105
7.4	Triple Jet-----	106
7.5	Differential Triple Jet-----	107
7.6	Four Jet Module-----	109
7.7	Five Jet Module-----	110
7.8	Results and Discussion-----	111
7.8.1	Single Jet-----	112
7.8.2	Twin Jet-----	116
7.8.3	Triple Jet-----	121
7.8.4	Differential Triple Jet-----	128
7.8.5	Four Jet Module-----	131
7.8.6	Five Jet Module-----	138
7.9	Conclusion-----	144

Chapter 8

DESIGN AND ANALYSIS OF PERFORATED VENT TILES..... 147 - 205

8.1	Introduction-----	147
8.2	Tile Design And Solution Domain-----	147
8.3	Tile Calculations-----	150
8.3.1	Tile C10T10P4A30-----	150
8.3.2	Tile C10T10P6A20-----	152
8.3.3	Tile C12T10P4A30-----	153
8.3.4	Tile C12T10P6A25-----	154
8.3.5	Tile C14T10P4A40-----	155
8.3.6	Tile C14T10P6A30-----	156
8.3.7	Tile C14C8T10P6A40-----	157
8.4	Results and Discussion-----	158

8.4.1 Tile C10T10P4A30 -----	159
8.4.2 Tile C10T10P6A20 -----	169
8.4.3 Tile C12T10P4A30 -----	172
8.4.4 Tile C12T10P6A25 -----	176
8.4.5 Tile C14T10P4A40 -----	180
8.4.6 Tile C14T10P6A30 -----	184
8.4.7 Tile C14C8T10P6A40 -----	188
8.5 Conclusion -----	203

Chapter 9

EFFECT OF DAMPER AND RECIRCULATION 207 - 241

9.1 Introduction -----	207
9.2 Effect of Damper -----	208
9.3 Effect of Recirculation -----	208
9.4 Results and Discussion -----	210
9.4.1 Effect of Damper -----	210
9.4.2 Effect of Recirculation -----	213
9.5 Conclusion -----	241

Chapter 10

CONCLUSIONS AND SUGGESTIONS

FOR FUTURE WORK..... 243 - 250

10.1 Major Conclusions from the Present Study -----	243
10.2 Scope for Future Work -----	247
10.3 SWOT Analysis -----	248
10.3.1 Strength -----	249
10.3.2 Weakness -----	249
10.3.3 Opportunity -----	249
10.3.4 Threats -----	250

REFERENCES..... 251 - 256

LIST OF PUBLICATIONS BASED ON RESEARCH WORK..... 257

CURRICULUM VITA..... 259

List of Tables

Table 5.1	Comparison of physical data of axisymmetric jets -----	72
Table 6.1	Comparison of velocities of single plane jets -----	83
Table 6.2	Comparison of twin jet velocities -----	84
Table 6.3	Comparison of triple jet velocities -----	93
Table 6.4	Comparison of differential triple jet Velocities -----	94
Table 7.1	Mass and velocity correction factors for different grid pattern -----	105
Table 7.2	Comparison of mass flow rates and velocities of 3D Single jets -----	113
Table 7.3	Comparison of mass flow rates and velocities of 3D Twin jets -----	119
Table 7.4	Comparison of mass flow rates and velocities of 3D triple jets -----	126
Table 7.5	Comparison of mass flow rates and velocities of 3D differential triple jets -----	130
Table 7.6	Comparison of mass flow rates and velocities of 3D four jet modules-----	135
Table 7.7	Comparison of mass flow rates and velocities of 3D five jet modules -----	142
Table 8.1	Mass flow rate of tile C10T10P4A30140-----	159
Table 8.2	Mass flow rate of tile C10T10P6A20150-----	169
Table 8.3	Mass flow rate of tile C12T10P4A30153-----	173
Table 8.4	Mass flow rate of tile C12T10P6A25156-----	176
Table 8.5	Mass flow rate of tile C14T10P4A40160-----	180
Table 8.6	Mass flow rate of tile C14T10P6A30163-----	184
Table 8.7	Mass flow rate of tile C14C8T10P6A40167 -----	188
Table 8.8	Percentage overall velocity reduction of various tile models ¹⁷⁷ -----	199
Table 9.1	Flow rates in the cold aisle with varying rack suction pressure ¹⁹⁰ -----	214

List of Figures

Figure 1.1	Data centre air flow pattern -----	07
Figure 1.2	Perforated tile with 56% open area ratio Top view. -----	08
Figure 1.3	Perforated tile with 25% open area ratio Top view. -----	08
Figure 1.4	Top view of a floor grating used in a conventional data centre-----	09
Figure 1.5	Bottom view of a tile showing the damper -----	09
Figure 1.6	CFD plot showing hot air recirculation. -----	10
Figure 2.1	Flow structure of a free jet-----	17
Figure 2.2	Development of a plane jet with side walls -----	18
Figure 2.3	Virtual origin and half width-----	21
Figure 2.4	Shear layer instabilities in a jet -----	22
Figure 2.5	Development of boundary layers on side walls -----	25
Figure 2.6	Aspect ratio of a rectangular jet nozzle-----	26
Figure 3.1	Figure showing cold/hot aisle segregation -----	44
Figure 4.1	Validation of present work with experimental results. -----	62
Figure 5.1	Solution domain and boundary types of axisymmetric jet-----	66
Figure 5.2	Development of near field velocity for different grid structures -----	67
Figure 5.3	Centre line velocity decay for different grid structures -----	67
Figure 5.4	Jet velocity profile at 20d for different grid structures -----	67
Figure 5.5	Jet velocity profile at 40d for different grid structures -----	67
Figure 5.6	Half width variation for different jet models at t = 6mm -----	68
Figure 5.7	Half width variation for different jet models at t = 8mm -----	68
Figure 5.8	Half width variation for different jet models at t = 10mm-----	68
Figure 5.9	Half width variation for different jet models at t = 12mm-----	68
Figure 5.10	Half width variation for different jet models at t = 14mm-----	68
Figure 5.11	Centre line velocity decay for different jet models at t =10mm -----	70
Figure 5.12	Near field velocity for different jet models at t =10mm -----	70
Figure 5.13	y velocity at Xs for different jet models at t = 10mm -----	70
Figure 5.14	Self similarity of 10by10 jet at various x/d locations -----	71
Figure 5.15	Self similarity of 12by10 jet at various x/d locations -----	71
Figure 5.16	Self similarity of 14by 10 jet at various x/d locations-----	71
Figure 6.1	Solution domain and boundary types of plane jet-----	76
Figure 6.2	Centreline velocity decay for various grid structures -----	77
Figure 6.3	Near field velocity development for various grid structures -----	77
Figure 6.4	Velocity profile at 30d for various grid structures -----	77
Figure 6.5	Velocity profile at 50d for various grid structures -----	77
Figure 6.6	Velocity profile at 70d for various grid structures -----	77
Figure 6.7	Solution domain and boundary types of twin jet-----	78

Figure 6.8	Solution domain and boundary types of triple jet-----	79
Figure 6.9	Comparison of half width variation of different jet models-----	80
Figure 6.10	Comparison of velocity decay of different jet models-----	80
Figure 6.11	Comparison of near field velocity of different jet models-----	80
Figure 6.12	Velocity profiles of 10by10 jet of different jet models-----	80
Figure 6.13	Velocity profiles of 12by10 jet of different jet models-----	80
Figure 6.14	Velocity profiles of 14by10 jet at different locations-----	81
Figure 6.15	Comparison of velocity profiles of different jet models at 20d-----	81
Figure 6.16	Comparison of velocity profiles of different jet models at 40d-----	81
Figure 6.17	Comparison of velocity profiles of different jet models at 60d-----	81
Figure 6.18	Comparison of velocity profiles of different jet models at 80d-----	81
Figure 6.19	Comparison of velocity profiles of different jet models at 100d-----	81
Figure 6.20	Self similarity velocity profiles of 10by10PJ at different locations-----	82
Figure 6.21	Self similarity velocity profiles of 12by10PJ at different locations-----	82
Figure 6.22	Self similarity velocity profiles of 14by10PJ at different locations-----	82
Figure 6.23	Comparison of velocity beyond merging point for different twin jet models-----	85
Figure 6.24	Comparison of y velocity at merging point for different twin jet models-----	86
Figure 6.25	Comparison of velocity profile at $(x/d) = 40$ for different twin jet models-----	86
Figure 6.26	Comparison of half width of various twin jet models for pressure difference 37.376 Pa.-----	87
Figure 6.27	Comparison of half width of twin jet models for varying pressure difference-----	87
Figure 6.28	Self similarity of 10by10P4TJ (1) at different locations-----	88
Figure 6.29	Self similarity of 10by10P6TJ (1) at different locations-----	88
Figure 6.30	Self similarity of 12by10P4TJ (1) at different locations-----	88
Figure 6.31	Self similarity of 12by10P6TJ (1) at different locations-----	88
Figure 6.32	Self similarity of 14by10P4TJ (1) at different locations-----	89
Figure 6.33	Self similarity of 14by10P4TJ (1) at different locations-----	89
Figure 6.34	Self similarity of 10by10P4TJ (2) at different locations-----	89
Figure 6.35	Self similarity of 10by10P6TJ (2) at different locations-----	89
Figure 6.36	Comparison of velocity profiles of various triple jet models at merging point.-----	91
Figure 6.37	Position of complete merging point for a triple jet model-----	91
Figure 6.38	Comparison of half width of triple jets with twin jets-----	92
Figure 6.39	Self similarity of 10by10P4TrJ at various locations-----	92
Figure 6.40	Self similarity of 10by10P6TrJ at various locations-----	92
Figure 6.41	Comparison of velocity beyond merging point for various triple jet models-----	94

Figure 6.42	Position of complete merging point of a differential triple jet model-----	97
Figure 6.43	Comparison of half width of a differential triple jet and triple jet models-----	97
Figure 6.44	Self similarity of 2by10by10+12by10P4DTrJ at different locations -----	98
Figure 6.45	Self similarity of 2by10by10+12by10P6DTrJ at different locations -----	98
Figure 6.46	Comparison of velocity profiles of differential triple jet models at merging point.-----	98
Figure 6.47	Comparison of velocity beyond merging point of differential triple jet models -----	99
Figure 7.1	Two grid points per edge -----	102
Figure 7.2	Three grid points per edge-----	102
Figure 7.3	Four grid points per edge -----	103
Figure 7.4	Six grid points per edge-----	103
Figure 7.5	Solution domain and boundary types for 3D Single jet-----	104
Figure 7.6	Solution domain and boundary types for 3D Twin jet -----	106
Figure 7.7	Solution domain and boundary types for 3D Triple jet -----	107
Figure 7.8	Solution domain and boundary types for 3DDifferential triple jet -----	108
Figure 7.9	Solution domain and boundary types for 3D Four Jet module. -----	109
Figure 7.10	Solution domain and boundary types for 3D Five Jet module. -----	111
Figure 7.11	Comparison of Velocity decay of different 3D single jet models -----	112
Figure 7.12	Comparison of Near field velocity of different 3D single jet models -----	112
Figure 7.13	Velocity plot of 3d8by10 at 10d-----	114
Figure 7.14	Velocity plot of 3d8by10 at 20d-----	114
Figure 7.15	Velocity plot of 3d8by10 at 30d-----	114
Figure 7.16	Velocity plot of 3d8by10 at 40d-----	114
Figure 7.17	Velocity plot of 3d10by10 at 10d-----	114
Figure 7.18	Velocity plot of 3d10by10 at 20d-----	114
Figure 7.19	Velocity plot of 3d10by10 at 30d-----	114
Figure 7.20	Velocity plot of 3d10by10 at 40d-----	114
Figure 7.21	Velocity plot of 3d12by10 at 10d-----	115
Figure 7.22	Velocity plot of 3d12by10 at 20d-----	115
Figure 7.23	Velocity plot of 3d12by10 at 30d-----	115
Figure 7.24	Velocity plot of 3d12by10 at 40d-----	115
Figure 7.25	Velocity plot of 3d14by10 at 10d-----	115
Figure 7.26	Velocity plot of 3d14by10 at 20d-----	115
Figure 7.27	Velocity plot of 3d14by10 at 30d-----	115
Figure 7.28	Velocity plot of 3d14by10 at 40d-----	115
Figure 7.29	Comparison of velocity profile at point of maximum velocity on merging axis for different 3d twin jet-----	116
Figure 7.30	Velocity plane of 3d10by10P4TJ at point of maximum velocity -----	117

Figure 7.31	Comparison of velocity profiles of 3d twin jets at plane of merging -----	118
Figure 7.32	Velocity plane of 3d10by10P4TJ at merging point-----	118
Figure 7.33	Velocity profiles of 3d10by10P4TJ at x and y direction at merging point-----	119
Figure 7.34	Comparison of velocity distribution of 3d twin jet models-----	121
Figure 7.35	Comparison of velocity profile at first merging point 3D triple jet models -----	122
Figure 7.36	Velocity plane of 3D10by10P4TrJ at first merging point -----	122
Figure 7.37	Velocity plane of 3D10by10P6TrJ at first merging point -----	122
Figure 7.38	Comparison of velocity profile at second merging point of 3D triple jet models -----	123
Figure 7.39	Velocity plane of 3D10by10P4TrJ at second merging point-----	123
Figure 7.40	Velocity plane of 3D10by10P6TrJ at second merging point-----	123
Figure 7.41	Comparison of velocity profile at third merging point of 3D triple jet models -----	124
Figure 7.42	Velocity plane of 3D10by10P4TrJ at third merging point -----	124
Figure 7.43	Velocity plane of 3D10by10P6TrJ at third merging point -----	124
Figure 7.44	Velocity profiles of 3d10by10P4TJ at x and y axis at third merging point-----	125
Figure 7.45	Velocity plane of 3D10by10P4TrJ at final merging point -----	125
Figure 7.46	Velocity plane of 3D10by10P6TrJ at final merging point -----	125
Figure 7.47	Velocity profiles of 3d10by10P4TJ at x and y axis at final merging point-----	126
Figure 7.48	Comparison of velocity distribution of 3d triple jet models-----	127
Figure 7.49	Velocity profiles at x and y of 3d10by10+12by10P4DTrJ at third merging point -----	128
Figure 7.50	Velocity profiles at x and y of 3d12by10+8by10P4DTrJ at third merging point -----	128
Figure 7.51	Velocity plane of 3d10by10+12by10P4DTrJ at third merging point-----	129
Figure 7.52	Velocity plane of 3d10by10+8by10P4DTrJ at third merging point -----	129
Figure 7.53	Velocity profiles at x and y of 3d10by10+12by10P4DTrJ at final merging point -----	129
Figure 7.54	Velocity profiles at x and y of 3d 12by10+8by10P4DTrJ at final merging point -----	129
Figure 7.55	Velocity plane of 3d10by10+12by10P4DTrJ at final merging point -----	130
Figure 7.56	Velocity plane of 3d10by10+8by10P4DTrJ at final merging point-----	130
Figure 7.57	x and y velocity profiles at first merging point of 3d4J10by10P4 -----	132
Figure 7.58	Velocity plot at first merging point of 3d4J10by10P4 -----	132
Figure 7.59	x and y velocity profiles at second merging point of 3d4J10by10P4-----	132
Figure 7.60	Velocity plot at second merging point of 3d4J10by10P4-----	132
Figure 7.61	x and y velocity profiles at third merging point of 3d4J10by10P4-----	133

Figure 7.62	Velocity plot at third merging point of 3d4J10by10P4-----	133
Figure 7.63	x and y velocity profiles at third merging point of 3d4J10by10P6-----	134
Figure 7.64	Velocity plot at third merging point of 3d4J10by10P6-----	134
Figure 7.65	x and y velocity profiles at third merging point of 3d4J12by10P4-----	134
Figure 7.66	Velocity plot at third merging point of 3d4J12by10P4-----	134
Figure 7.67	x and y velocity profiles at third merging point of 3d4J12by10P6-----	134
Figure 7.68	Velocity plot at third merging point of 3d4J12by10P6-----	134
Figure 7.69	x and y velocity profiles at third merging point of 3d4J14by10P4-----	135
Figure 7.70	Velocity plot at third merging point of 3d4J14by10P4-----	135
Figure 7.71	x and y velocity profiles at third merging point of 3d4J14by10P6-----	135
Figure 7.72	Velocity plot at third merging point of 3d4J14by10P6-----	135
Figure 7.73	Comparison of velocity distribution of 3d4J modules-----	137
Figure 7.74	x and y velocity profiles at first merging point of 3d4J12by10+8by10P6-----	139
Figure 7.75	Velocity plot at first merging point of 3d4J12by10+8by10P6-----	139
Figure 7.76	xy velocity profile at first merging point of 3d4J12by10+8by10P6-----	139
Figure 7.77	x and y velocity profiles at final merging point of 3d4J12by10 +8by10P6-----	140
Figure 7.78	Velocity plot at final merging point of 3d4J12by10+8by10P6-----	140
Figure 7.79	xy velocity profile at final merging point of 3d4J12by10+8by10P6-----	140
Figure 7.80	x and y velocity profiles at final merging point of 3d4J14by10 +8by10P6-----	141
Figure 7.81	Velocity plot at final merging point of 3d4J14by10+8by10P6-----	141
Figure 7.82	xy velocity profile at final merging point of 3d4J14by10+8by10P6-----	141
Figure 7.83	x and y velocity profile at final merging point of 3d4J14by10 +10by10P6-----	141
Figure 7.84	Velocity plot at final merging point of 3d4J14by10+10by10P6-----	141
Figure 7.85	xy velocity profile at final merging point of 3d4J14by10 +10by10P6-----	142
Figure 7.86	Comparison of velocity distribution of 5 jet module with 4 jet modules-----	143
Figure 8.1	Basic tile dimensions and quarter tile boundary conditions-----	149
Figure 8.2	Details of standard tile C10T10P4A30-----	151
Figure 8.3	Details of standard tile C10T10P6A20-----	152
Figure 8.4	Details of standard tile C12T10P4A30-----	153
Figure 8.5	Details of standard tile C12T10P6A25-----	154
Figure 8.6	Details of standard tile C14T10P4A40-----	155
Figure 8.7	Details of standard tile C14T10P6A30-----	156
Figure 8.8	Details of combination tile C14C8T10P6A40-----	158
Figure 8.9	Mass flow rate calibration curve for tile C10T10P4A30 (a)-----	160
Figure 8.10	Mass flow rate calibration curve for tile C10T10P4A30 (b)-----	161
Figure 8.11	Variation of centre line velocity of tile C10T10P4A30 for various pressure differences-----	161

Figure 8.12	Velocity in x direction for various z positions for different pressure differences -----	162
Figure 8.13	Velocity plots at different z locations for pressure difference $\Delta P = 37.376$ Pa-----	163
Figure 8.14	Velocity plots at different z locations for pressure difference $\Delta P = 31.147$ Pa -----	164
Figure 8.15	Velocity plots at different z locations for pressure difference $\Delta P = 24.917$ Pa-----	165
Figure 8.16	Velocity plots at different z locations for pressure difference $\Delta P = 18.688$ Pa-----	166
Figure 8.17	Velocity plots at different z locations for pressure difference $\Delta P = 12.459$ Pa-----	167
Figure 8.18	Velocity plots at different z locations for pressure difference $\Delta P = 6.229$ Pa-----	168
Figure 8.19	Mass flow rate calibration curve for tile C10T10P6A20 (a)-----	170
Figure 8.20	Mass flow rate calibration curve for tile C10T10P6A20 (b)-----	170
Figure 8.21	Variation of centre line velocity of tile C10T10P6A20 for various pressure differences-----	171
Figure 8.22	Velocity in x direction for various z positions for different pressure differences -----	171
Figure 8.23	Mass flow rate calibration curve for tile C12T10P4A30 (a)-----	173
Figure 8.24	Mass flow rate calibration curve for tile C12T10P4A30 (b)-----	174
Figure 8.25	Variation of centre line velocity of tile C12T10P6A30 for various pressure differences-----	174
Figure 8.26	Velocity in x direction for various z positions for different pressure differences -----	175
Figure 8.27	Mass flow rate calibration curve for tile C12T10P6A25 (a)-----	177
Figure 8.28	Mass flow rate calibration curve for tile C12T10P6A25 (b)-----	177
Figure 8.29	Variation of centre line velocity of tile C12T10P6A25 for various pressure differences-----	178
Figure 8.30	Velocity in x direction for various z positions for different pressure differences -----	179
Figure 8.31	Mass flow rate calibration curve for tile C14T10P4A40 (a)-----	181
Figure 8.32	Mass flow rate calibration curve for tile C14T10P4A40 (b)-----	181
Figure 8.33	Variation of centre line velocity of tile C14T10P4A40 for various pressure differences-----	182
Figure 8.34	Velocity in x direction for various z positions for different pressure differences -----	183
Figure 8.35	Mass flow rate calibration curve for tile C14T10P6A30 (a)-----	185
Figure 8.36	Mass flow rate calibration curve for tile C14T10P6A30 (b)-----	185
Figure 8.37	Variation of centre line velocity of tile C14T10P6A30 for various pressure differences-----	186

Figure 8.38	Velocity in x direction for various z positions for different pressure differences -----	187
Figure 8.39	Mass flow rate calibration curve for tile C14C8T10P6A40 (a)-----	189
Figure 8.40	Mass flow rate calibration curve for tile C14C8T10P6A40 (b) -----	189
Figure 8.41	Variation of centre line velocity of tile C14C8T10P6A40 for various pressure differences-----	190
Figure 8.42	Velocity in x direction for various z positions for different pressure differences -----	191
Figure 8.43	Velocity plots at different z locations for pressure difference $\Delta P = 37.376$ Pa -----	192
Figure 8.44	Velocity plots at different z locations for pressure difference $\Delta P = 31.147$ Pa -----	193
Figure 8.45	Velocity plots at different z locations for pressure difference $\Delta P = 24.917$ Pa -----	194
Figure 8.46	Velocity plots at different z locations for pressure difference $\Delta P = 18.688$ Pa-----	195
Figure 8.47	Velocity plots at different z locations for pressure difference $\Delta P = 12.459$ Pa -----	196
Figure 8.48	Velocity plots at different z locations for pressure difference $\Delta P = 6.229$ Pa -----	197
Figure 8.49	Comparison of average centre line velocity of tiles of various tile models-----	198
Figure 8.50	Percentage velocity reduction of various tile models -----	199
Figure 8.51	Comparison of z velocity along x direction for $\Delta P = 37.376$ Pa at $x = 0.5$ m for various tile models-----	201
Figure 8.52	Comparison of z velocity along x direction for $\Delta P = 37.376$ Pa at $x = 1.0$ m for various tile models-----	202
Figure 8.53	Comparison of z velocity along x direction for $\Delta P = 37.376$ Pa at $x = 1.5$ m for various tile models-----	202
Figure 8.54	Comparison of z velocity along x direction for $\Delta P = 37.376$ Pa at $x = 2.1336$ m for various tile models -----	203
Figure 9.1	Basic tile dimensions and quarter tile boundary conditions-----	209
Figure 9.2	Variation of z velocity along x direction at different z positions-----	211
Figure 9.3	Variation of Tile, Rack & Recirculation flow with rack suction pressure for various pressure differences across the tile. -----	215
Figure 9.4	The centre line velocity decay for different pressure difference across the tile with various rack suction pressures-----	218
Figure 9.5	Comparison of centre line velocity for different Rack suction pressure for various pressure difference across the tile -----	222
Figure 9.6	z velocity along x direction for pressure difference of 37.376 Pa at various z locations -----	223
Figure 9.7	z velocity along x direction for pressure difference of 31.147 Pa t various z locations -----	224

Figure 9.8	z velocity along x direction for pressure difference of 24.917 Pa t various z locations -----	225
Figure 9.9	z velocity along x direction for pressure difference of 18.688 Pa t various z locations -----	226
Figure 9.10	z velocity along x direction for pressure difference of 12.459 Pa t various z locations -----	227
Figure 9.11	z velocity along x direction for pressure difference of 6.229 Pa t various z locations -----	228
Figure 9.12	Velocity plots at the centre of the tile and the aisle side at a pressure difference of 37.376 Pa across the tile for various rack suction pressure -----	229
Figure 9.13	Velocity plots at the centre of the tile and the aisle side at a pressure difference Figure of 31.147 Pa across the tile for various rack suction pressure -----	230
Figure 9.14	Velocity plots at the centre of the tile and the aisle side at a pressure difference of 24.917 Pa across the tile for various rack suction pressure -----	231
Figure 9.15	Velocity plots at the centre of the tile and the aisle side at a pressure difference of 18.688 Pa across the tile for various rack suction pressure -----	232
Figure 9.16	Velocity plots at the centre of the tile and the aisle side at a pressure difference of 12.459 Pa across the tile for various rack suction pressure -----	233
Figure 9.17	Velocity plots at the centre of the tile and the aisle side at a pressure difference of 6.229 Pa across the tile for various rack suction pressure -----	234
Figure 9.18	Velocity plots in x and y directions for 37.376 Pa at different z locations for various rack suction pressure -----	235
Figure 9.19	Velocity plots in x and y directions for 31.147 Pa at different z locations for various rack suction pressure -----	236
Figure 9.20	Velocity plots in x and y directions for 24.917 Pa at different z locations for various rack suction pressure -----	237
Figure 9.21	Velocity plots in x and y directions for 18.688 Pa at different z locations for various rack suction pressure -----	238
Figure 9.22	Velocity plots in x and y directions for 12.459 Pa at different z locations for various rack suction pressure -----	239
Figure 9.23	Velocity plots in x and y directions for 6.229 Pa at different z locations for various rack suction pressure -----	240

Nomenclature

English Symbols

b_u	Jet half-width (of velocity), mm
C_{2u}	Virtual origin for half-width decay
C_μ, C_1, C_2	Constants in k- ϵ model
d	Diameter of jet, mm
g	Acceleration due to gravity, m/sec ²
H	Shape factor
k	Turbulent kinetic energy or Thermal conductivity
K_{2u}	Slope of half-width decay
P	Pressure, Pitch of orifices
R	Gas constant, J/kg K
Re	Reynolds Number
Re_λ	Taylor Reynolds Number
T	Absolute temperature, K
t	Thickness of orifice or tile, mm
U	Mean velocity at any station, m/sec
u, v	Velocities in x and y directions
U_c	Mean velocity at centreline, m/sec
U_∞	Free stream velocity, m/sec
x	Axial direction (for plane and axisymmetric jets)
y	Transverse direction (for plane and axisymmetric jets)
z	Axial direction for Three dimensional jets and Tiles

Greek Symbols

δ	Displacement thickness, mm
ϵ	Turbulent kinetic energy dissipation rate, m ² /sec ³
θ	Momentum thickness, mm
μ	Effective viscosity
μ_t	Turbulent viscosity
ν	Kinematic Viscosity, m ² /sec
ρ	Density, kg/m ³
τ	Viscous shear stress

Abbreviations

ANSI	American National Standards Institute
ASHRAE	American Society of Heating Ventilating and Air conditioning Engineers
CFD	Computational Fluid Dynamics
CPE	Compute Power Efficiency
CRAC	Computer Room Air Conditioner
DCiE	Data Centre Infrastructure Efficiency
DNS	Direct Numerical Solution
DTrJ	Plane Jet (Differential Triple Jet)
EIA	Electronics Industries Alliance
IT	Information Technology
PDU	Power Distribution Units
PJ	Plane Jet (Single Jet)
PUE	Power Utilization Efficiency or Power Usage Effectiveness
RS	Rack Suction pressure in Pascal
SST	Shear Stress Transport
TI	Turbulent Intensity
TIA	Telecommunications Industry Association
TJ	Plane Jet (Twin Jet)
TrJ	Plane Jet (Triple Jet)

<i>Contents</i>	1.1 Preamble
	1.2 Introduction
	1.3 Data Centre and Energy Perspective
	1.4 Data Centre air Conditioning
	1.5 Raised Floor air Conditioning Systems
	1.6 Problem Formulation
	1.7 Objectives and Scope
	1.8 Organization of the Thesis

1.1 Preamble

Data centre is a facility used to house mission critical computer systems and associated components. It generally includes environmental controls (air conditioning, fire suppression etc), redundant / backup power supplies, redundant internet connections and high security. Data centre have become the back bone of the present information technology revolution and it is growing at a rapid pace to support the unlimited demand of the modern world.

As the data centre grows in its size and capacities, the power consumption of the system also shoots up. Increased power demand for running a modern high power density data centre has put a brake on the fast growth of this technology. It is now mandatory that the data centre must be operated economically since the prices of information and communication technology services are being slashed down day by day. Most of the energy conservation activities in a data centre are concerned with the auxiliary systems, since the computer hardware are electronic equipments working with very high efficiencies and conservation of energy is not significant in

them. The mechanical sub-system of the data centre which consumes major portion of the additional energy is the air conditioning system. Hence energy conservation activities on air conditioning system are gaining importance and industries are trying to develop methods to improve the efficiency of air conditioning system.

Energy efficiency in air conditioning system can be achieved either by thermal management or by air flow management. Thermal management deals with the capacity control of the air conditioning system by controlling the temperature of the cold air supplied to the data centre to remove heat from the equipments. The energy conservation activities presently considered by industries are in this direction. Energy conservation by air flow management is seldom discussed and has not gained popularity. The role of thermal management and air flow management in improving the energy efficiency of air conditioning in data centre has not so far been taken up for academic research, even though there are many unexplored areas. This research work focuses on the aspect of energy conservation in data centre air conditioning through air flow management.

1.2 Introduction

In this chapter, an attempt is made to bring out the general concepts of data centre and its energy perspective and cooling issues. A brief introduction to data centre energy matrix is made for better understanding of the energy aspects related to data centre. The need and evolution of data centre cooling is explained in the succeeding section and the criticality of data centre cooling and energy conservation aspects are discussed. The raised floor air conditioning technology which is commonly used for large scale data centres is explained. The core concept of data centre air flow dynamics and its relevance to the present research topic is introduced. The role of perforated tiles in air flow dynamics and the effect of dampers on conventional perforated tiles are discussed. The importance of computational fluid dynamics (CFD) in data centre design and assessment is

highlighted. The effect of hot air recirculation as observed in computational fluid flow analysis of data centre is addressed with proper importance.

1.3 Data Centre and Energy Perspective

Data centres are the ‘nerve centres’ of new economy or special environments that house the latest advancements in computer processing and business innovations [Data centre resource guide-2007]. Data centre centralize and consolidate information technology resources, enabling organizations to conduct business around the clock and around the year. Modern data centre must be capable of continuously supporting the industry on a 7 days/week, 24 hours/day, and 365 days/year basis with current power densities ranging from 500 to 1080 W/m². The industry trend of faster processing speed requirements and high power consuming servers may result in power densities up to 1950 W/m² in the foreseeable future [Christopher Kurkjian, 2006].

The power density as referred in data centre in W/m² is defined as the ratio of the total electronic power capacity available to the computing equipments in Watts to the total raised floor area in m² of the data centre’s computer room. The computer room floor of the data centre would incorporate all the computing equipments, required access for that equipment, egress paths, air conditioning equipments and power distribution units (PDU’s).

Most of the modern data centre use standard IT cabinet of 2.2 m height. IT cabinets are sub divided into 42 U’s of available computing equipment installation, with the U being the incremental unit height of computing equipment. Each U is approximately 44.5 mm. A modern 1U rack server uses 550 Watts of power and dissipate equal amount of heat to the surroundings. A fully loaded 42U rack will consume over 10 kW of power and generate over 10 kW of heat [Christopher Kurkjian, 2006]. The performance of electronic equipments is directly related to the working environments. They are not expected to perform above a

predetermined temperature condition. Hence for the safe and continued operation of electronic equipments, the heat generated during their operation must be removed from the site as and when it is generated; otherwise this heat will increase the temperature of the equipments. This makes the electronic equipment cooling highly sensitive and most critical in the industry.

Data centre are considered as mission critical facilities which require to function year round without any interruption. For achieving this, electronic equipments must be kept in the controlled environment for long time. This suggests that, the air conditioning system should also be capable of supporting the data centre uninterruptedly. A 42U rack consuming 10 kW of power will require another 5 kW of power for running the cooling system. In the present era of power crisis and spiralling cost concerns of energy, it is imperative to identify the various energy sinks using power and their efficiency. Added to this, are the concern over greenhouse gas emissions related to the generation of power. The understanding of the utilization pattern of energy between various points of power consumption can be explained by data centre energy matrix such as power utilization efficiency or power usage effectiveness (PUE), compute power efficiency (CPE) and data centre infrastructure efficiency (DCiE) [The green grid, 2007]. Power utilization efficiency is defined as the ratio of total facility power to the IT equipment power. PUE can range from 1 to infinity. A PUE value approaching 1 would indicate 100% efficiency (all power is used by the IT equipments only). Currently there are no comprehensive data sets which show the true spread of the PUE of data centre. By adopting proper design a PUE value below 1.6 can be achievable.

A PUE value of 2 indicates that for 1 kW of IT load the total facility power is 2 kW of which 1 kW of power is utilized for the data centre supporting utilities including the air conditioning. Any energy conservation activity must concentrate on this 1 kW and measures are to be adopted for bringing this value down. Among all supporting utilities concerned with data centre, except the air conditioning

system all are electrical or electronic systems which are operating at their maximum efficiency level. The only mechanical system used as a critical system in data centre is the air conditioning system which has got its own inherent inefficiencies. Hence any energy conservation activity in data centre must concentrate on the effective utilization of the air conditioning system to consume less power for the removal of heat generated from the IT equipments and bring down the PUE to below 1.6.

1.4 Data Centre Air Conditioning

The evolution of data centre air conditioning started with simple server rooms cooled by conventional central air conditioning system which is used for comfort air conditioning purposes or with individual split coolers. In both cases the entire server room is cooled down to a predetermined low temperature around 14-20⁰C. Such systems are still in use but are limited to very small capacities. In the beginning stages, for low power density racks the overall thermal load on the data centre was low and the total power required to run the data centre was not significantly higher. But due to the increased demand of the industry and evolution of high power density servers, the total thermal load of the data centre has gone up from Mega Watts to Giga Watts or more. It is worth to note that conventional centralized or split server room cooling is highly inefficient since it handles large volumes of air in their air flow circuits. It has to handle both the IT load and the room load which is significantly large. Large air volumes to be cooled down to large temperature differences will increase the cooling load of the refrigeration system thereby increasing the power requirement. Large air volumes will also increase the power input to the blower of the air conditioning system there by increasing the total power.

The central core of data centre cooling now focuses on two questions ‘Where to cool?’ and ‘How much to cool?’. It is not necessary that the entire server room must be cooled down to the low temperature; instead, only the rack needs to be

cooled. Hence the answer to the question ‘Where to cool?’ is the racks only. The answer to the question ‘How much’ requires more explanation. The racks will have different power densities and may be operating at different power factors. The rack load is hence dynamic in nature and one cannot design an air conditioning system for such a dynamic condition. The rack power is calculated by adding the rated powers of all the individual servers or other equipments placed in the racks. The amount of cooling required for each rack can be calculated and the amount of air required to cool the rack can be arrived with the help of industry best practices. In this approach the air at all other parts of the room does not participate in cooling and will exist at higher temperatures. This will reduce the volume of air being handled by the blower and the refrigeration system. In this case the volume of air processed will be approximately equal to the volume required to take the IT thermal load.

1.5 Raised Floor air Conditioning Systems

The answer to the fundamental questions ‘Where to cool?’ and ‘How much to cool?’ related to data centre cooling can be obtained by introducing raised floor air conditioning system. In this type of systems, the data centre consists of three separate sections namely the under floor plenum (conventionally called cold plenum), the computer room where the equipment racks and other accessories are kept and the over head plenum (hot plenum). The under floor plenum and the room are separated by mild steel frame fabrication since the floor has to take heavy loads due to the racks and equipments. The room and the over head plenum are separated by a false ceiling since it does not have to support any load except light fittings and fire alarm devices. The third section, the over head plenum is mandatory and the data centre without separate over head plenum is designated as room return system. The concept of raised floor air conditioning system is explained in the Fig 1.1 [Bash *et al.*, 2006].

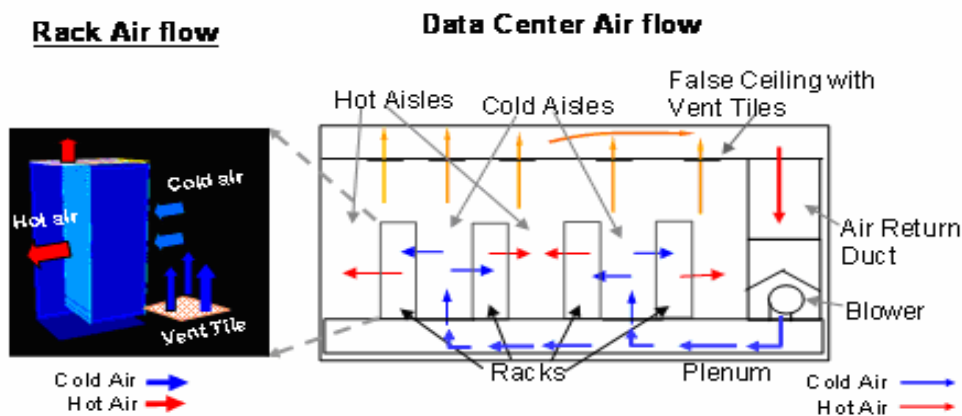


Fig. 1.1 Data centre air flow pattern

The data centre cooling load is generally taken as the total rated installed IT load on the racks plus other minor heat generating electronic equipment on the floor. Cooling of the racks and equipments are achieved by the circulation of air which is cooled to a predetermined value by the CRAC (Computer Room Air Conditioner). The cold air from the CRAC is delivered to the under floor plenum with zero static pressure. The air will decelerate as it flows and fill the entire cold plenum there by creating a pressure difference across the cold plenum and the room. The air from the cold plenum will be discharged to the room through the perforated tiles placed on the mild steel fabricated floor. The air discharging from the tiles will flow upward and enter into the rack due to the suction created by the system fans provided with the servers and absorbs the heat generated in the electronic components. The hot air is exhausted out at the rear of the racks and will move upward due to thermal stratification. The hot air will be collected through hot tiles placed in the false ceiling in the hot plenum from where it is sucked back to the CRAC units. The cooling effectiveness of the data centre depends on the air flow pattern from the perforated tiles. The total air flow dynamics within the data centre is a strong function of the perforated tile design and the pressure difference across it [Karki *et al.*, 2003].

The currently existing data centre are employing 2 feet by 2 feet (0.6096m by 0.6096 m) or 1 foot by 1 foot (0.3048 m by 0.3048m) tiles made of metal structures

of different thickness having different orifice configurations. They are designated by their respective open area ratio. A plot of ΔP (pressure difference) against Q (volume flow rate) is used for finding the flow rates at different values of pressure differences. Open area ratio means the percentage area open in a square tile with reference to the total area of the tile. The open area ratio of common tiles varies from 25% to 56%. Few conventional tiles used currently in data centre are shown in Fig 1.2 to 1.4.

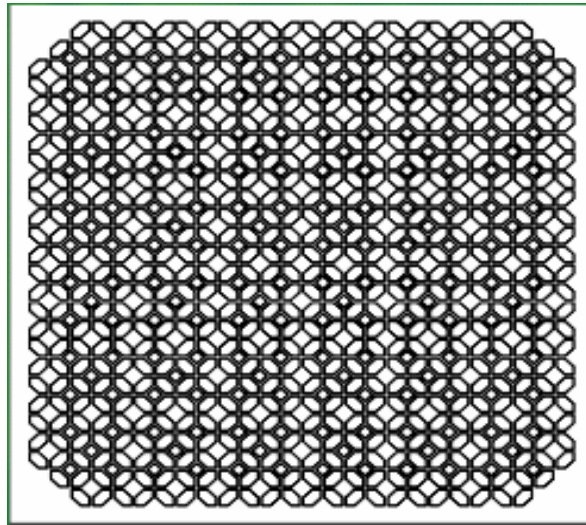


Fig 1.2 Perforated tile with 56% open area ratio. Top view.

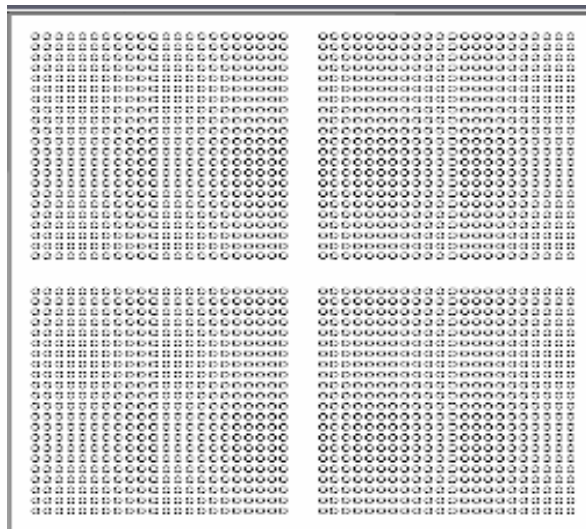


Fig 1.3: Perforated tile with 25% open area ratio. Top view.

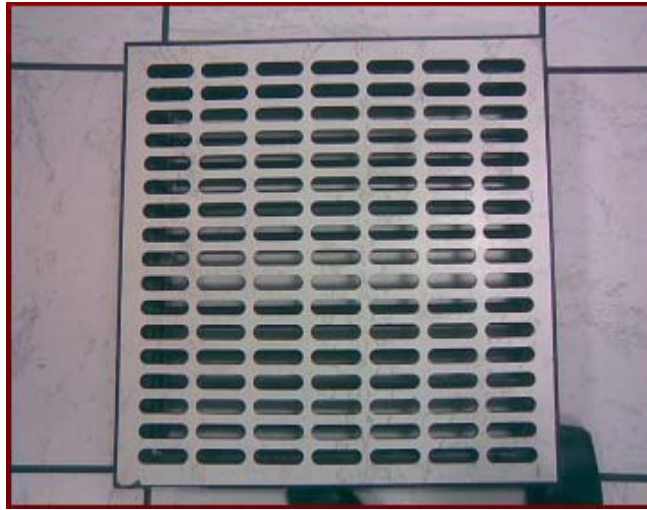


Fig 1.4: Top view of a floor grating used in a conventional data centre

The ΔP vs Q plot of the tiles will quantitatively support the performance of the tiles but it will not give any idea about the flow pattern of air beyond the tiles. Most of the perforated tiles are provided with dampers at the bottom of the tiles for capacity control. The flow rates through the tiles can be varied by changing the damper position. Fig 1.5 shows a tile with damper used in industry.



Fig 1.5: Bottom view of a tile showing the damper

The cooling design in a high power density data centre is quite complex. The conventional method of energy balance in sizing the air conditioner and intuitive distribution of air does not suffice. Computational Fluid Dynamics (CFD)

modelling is necessary to design the air flow distribution [Karki *et al.*, 2003]. Data centre industry relies on CFD results for their design and assessment. Since data centre are mission critical facilities with very high level of security with restricted entry, a real time analysis or experimentation is not possible as it may affect the availability of servers for regular service. Hence the only possible method for research in this field is computational methods. CFD analysis of data centre reported that, at certain discrete points in the data centre, recirculation of hot air occurs. Recirculation occurs when the hot air exhausted from the rack mount computing device is fed back into its own intake. This is more common in room air return systems without separate hot plenum. This recirculation will lead to elevated temperatures of the servers situated in these locations and they will become hot spots. Fig 1.6 shows the recirculation effect in data centre air flow [Goren, 2008].

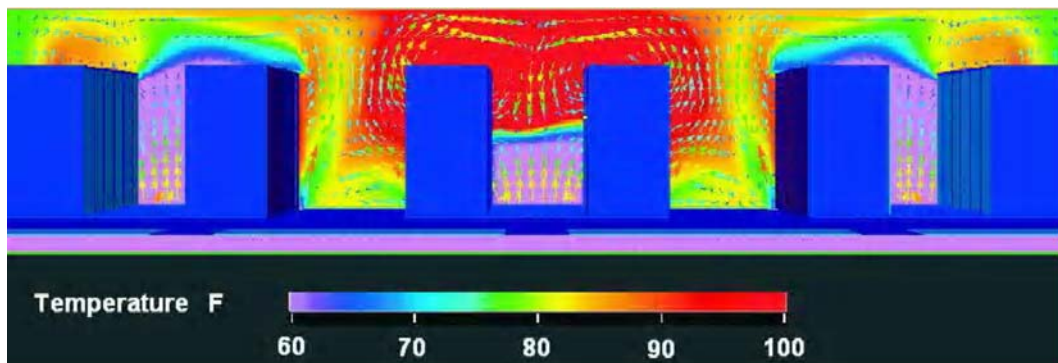


Fig 1.6: CFD plot showing hot air recirculation.

The region that appears in RED in the figure shows the recirculation effect of hot air. Overheating the servers above a particular value of temperature will damage the system and as a safety measure the systems will automatically shut down if the environment temperature exceeds a predetermined value ranging from 40 to 45⁰C. These servers will not be available until the situation is attended and rectified. Hence hot spots due to recirculation will increase the down time of the

data centre and must be addressed properly. In modern data centre, routine CFD assessment is carried out for predicting the performance of the data centre.

1.6 Problem Formulation

The currently used perforated tiles in data centre mentioned in the previous section are quantitatively designed. It is observed that as the pressure difference across the tile increases, the flow rate increases. The pressure difference across the tiles depends on the under floor plenum pressure as the room pressure is atmospheric. The plenum pressure cannot be increased beyond certain values due to the following reasons. As the plenum pressure increases, the back pressure on the blower of the CRAC unit will increase which will increase the power consumption of the blower since it has to develop more torque. As the plenum pressure increases, cracks and other minor openings on the floor, wall and any partitions in the under floor plenum will become active and precious cold air will leak through these positions to outside which causes loss of energy. In a data centre, cold air is supposed to flow only through the perforated tiles. As the plenum pressure increases the air will leak through the small gaps between the perforated tiles as they are loosely placed on the floor for easy removal and this air will have very little momentum and they cannot move up and will spread and settle at the bottom of the room. This cold air will not be available for cooling purpose and is wasted.

It is found that, in a well designed data centre the pressure difference across the tiles will be around 0.15 inches of water column (37.376 Pa). The plenum pressure is a strong function of the total open area on the entire floor; this in turn depends on number of tiles and nature of tiles placed on the floor. Hence it can be stated that the total air flow dynamics of a data centre is fully dependant on the tile design and its deployment. Air issuing from the tiles definitely has a quality with respect to its velocity apart from its mass flow rates. As the plenum pressure increases, the velocity of air issuing from the tiles also increases. The velocity of

cold air in front of the racks in a data centre is a major factor in achieving proper and effective cooling. It is found that, there exists an optimum range of velocities at which the racks can suck sufficient air from the bulk air moving up in front of them. If the velocities are higher, even if cold air is available in front of racks, the rack system fan may not be able to suck air into the system from the high velocity bulk stream. If the velocities are less the vertical distance travelled by the bulk air will be less, more air will flow through the bottom and middle section of the racks and the systems at the top region of the rack may not get sufficient cold air. The system fan cannot suck air with large pressure differences as this will increase the velocity of air through the systems thereby reduce the contact time for effective heat transfer.

Since perforated tile design plays a key role in data centre air flow dynamics, it is essential to have a qualitative analysis of the air flow in data centre by proper design of the perforated tiles. In the present research work, tiles are considered as multiple arrays of circular orifices through which air is discharged into the confined space between two racks. In order to model this tile flow, concepts of jet theories are introduced into data centre air flow. In the present analysis, temperature effects are not considered since the temperature of the jet discharging from the tile and the confined volume are the same. In this research work, the jets are treated as isothermal jets. The present research work attempts to use the fundamentals of isothermal air jets discharged into confined large volume for modelling the data centre tile flow. The aim of the present research work is to designate the perforated tiles quantitatively and qualitatively. The present work also focuses on the effect of dampers on air flow dynamics and on the recirculation effects. Computational Fluid Dynamics analysis is proposed for all these studies.

Finally the research topic is arrived as QUALITATIVE AIR FLOW MODELLING AND ANALYSIS OF DATA CENTRE AIR CONDITIONING AS MULTIPLE JET ARRAY. Data centre perforated tiles are modelled as multiple jet array system in a CFD tool to arrive at a qualitative standard for data centre air flow.

1.7 Objectives and Scope

The objectives of the present work are to:

- Introduce the concept of qualitative treatment of air flow in data centre air conditioning.
- Introduce a tile coding system to designate the perforated vent tiles used in the raised floor of data centre.
- Introduce the concept of custom made tiles for specific application in order to get optimized air flow pattern within the cold aisle.
- Introduce a new tile design practice giving flexibility in managing the air flow within the data centre effectively.
- Explain the effect of dampers in the qualitative air flow distribution within the data centre.
- Explain the phenomenon of hot air recirculation in detail and give scientific and systematic explanation for the physical mechanism of this phenomenon and the effect of plenum pressure and the rack suction pressure on recirculation.

1.8 Organization of the Thesis

Various chapters of the thesis are organized according to the following sequence. Chapter 1 gives an introduction to the research scenario and the problem of research. In Chapter 2 necessary theory of jets are included. A review of earlier investigations on the related topics is presented in Chapter 3. Chapter 4 provides the numerical methodology and validation of the software used for the present work. A detailed study on axisymmetric jets is made in Chapter 5. Flow and merging characteristics of plane jets are detailed in Chapter 6. Chapter 7 explains the modelling and flow characteristics of three dimensional jets of single jet to five jet modules. Chapter 8 deals with the detailed coding, design, modelling and

analysis of perforated vent tiles. Chapter 9 addresses two important issues such as effect of damper and recirculation effect in data centre air flow. Each chapter is structured to give an introduction to the topic under that chapter and a conclusion to the discussions. Chapter 10 details the major conclusions of the present work and the contribution to the energy conservation in air conditioning system. A proposal for future research work is also given in this chapter.

.....❧.....

Contents	2.1 Introduction
	2.2 Overview of Jet Flows
	2.3 Structure and Development of a Free Jet
	2.4 Factors Influencing Jet Spread
	2.5 Conclusion

2.1 Introduction

In this chapter, the basic jet theory is explained in detail. An overview on jet flow is given to understand the basic jet classifications like free jet, confined jet and isothermal and non-isothermal jets. The structure and development of a free jet is explained to bring out the different zones in jet flow. Later, the factors affecting the jet spread are discussed in detail to illustrate the physics of jet flow.

2.2 Overview of Jet Flows

Over the past six decades, jets have been the subject of extensive experimental and analytical research. Circular and plane jets are used in a variety of applications. Some of the common applications of jets occur in drying processes, air curtains for room conditioning, heating and ventilating applications. In these, parameters like the jet spread rate and potential core decay play a strong role in deciding the efficiency of mixing for the process. Shear layer is the region in which most of the interactions and mixing between the ambient and jet fluids take place. Therefore, understanding the fluid dynamic phenomena in the shear layer during the downstream evolution of a jet is important.

In spite of the voluminous research literature available on turbulent jets issuing from circular and non circular nozzles, there are still some important aspects which require greater attention. For instance, in plane jets of large aspect ratio, primarily planar spreading occurs in the near field. But at larger distances, the

differential rates of shear layer growth in two lateral directions results in 3-D features such as the axis switching phenomena. The jet shear layers also actively participate in the entrainment of ambient fluid and in the growth of turbulent flow fluctuations [Sato.H, 1964]. Far away from the nozzle exit, the jet loses any memory of the nozzle cross sectional shape and the flow asymptotically attains the self- similar profile of a round jet. The turbulent flow fluctuations also evolve as the jet spreads with increase in axial distance; the rates of evolution of the mean flow field and turbulent fluctuations however, are quite different.

Free jets can be defined as a pressure driven unrestricted flow of a fluid into a quiescent ambience, the wall ceiling or obstruction does not influence the jet. Since a fluid boundary cannot sustain a pressure difference across it, the subsonic jet boundary is a free shear layer in which the static pressure is constant throughout. The boundary layer at the exit of the device develops as a free shear layer, mixing with the ambient fluid thereby entraining the ambient fluid in the jet stream. Thus, the mass flow at any cross section of the jet progressively increases thereby the jet spreads along the downstream direction. In order to conserve momentum, the jet centreline velocity decreases with downstream distance.

If the air jet performance is influenced by reverse flows, created by the same jet entraining ambient air, this is called a confined jet. Particularly if the air jet is attached to a surface, it is an attached air jet. When considering the temperature difference between the supply air and room ambient air, the air jets can be divided into isothermal jets and non-isothermal jets. The buoyancy forces will have a role in deciding the trajectory of jets, the location where the jet attaches and separates from the ceiling or floor and the spread of jet. In the present study the air jet is considered as confined isothermal jet discharging into a large volume.

2.3 Structure and Development of a Free Jet

A free jet is a fluid mass that discharges into an infinitely large environment of ambient fluid. The flow structure in a free jet has been studied by many researchers

and four distinct zones have been identified from these studies. In ASHRAE literature the development of a jet is divided into four zones, related to centreline velocity decay. The structure of a free jet is shown in Fig 2.1 [Yue.Z, 1999]

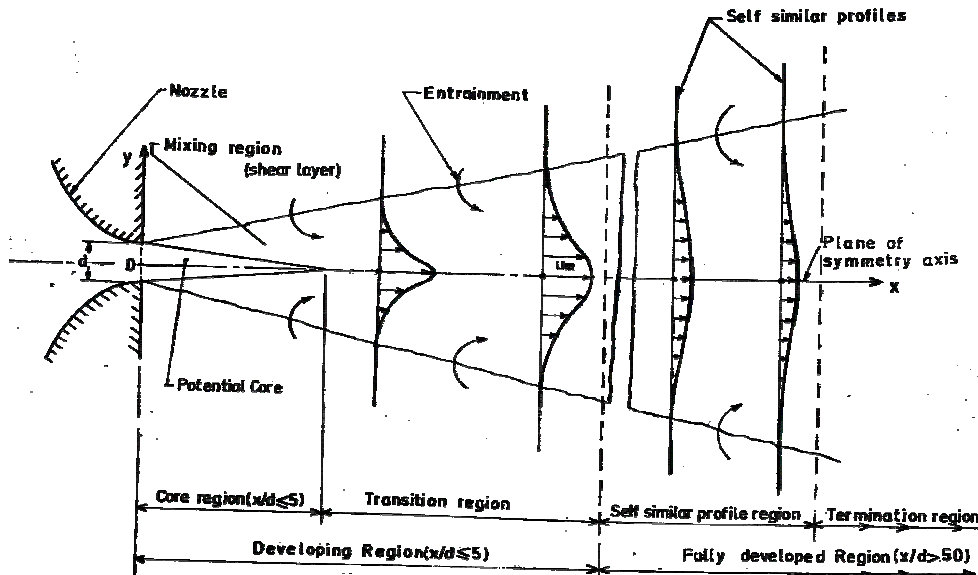


Fig 2.1 Flow structure of a free jet [Yue.Z, 1999]

Zone 1: The convergent zone: This region is called the potential core of the jet where the centreline velocity is equal to the nozzle outlet velocity. This region normally extends up to $4d$ to $6d$, where d is the diameter of the nozzle exit.

Zone 2: This transition zone: It is the region in which the centreline velocity starts to decay. The velocity decay can be approximated as proportional to $x^{-0.5}$, where x is the axial distance. This usually corresponds to a region from $6d$ to $20d$, and it is known as the interaction region where shear layers from both sides merge.

Zone 3: The self similar zone: In this region transverse velocity profiles are similar at different values of x and the centreline velocity decay is approximately proportional to x^{-1} .

Zone 4: The termination zone: In this region the centreline velocity decays rapidly. Although this zone has been studied by several researchers, the actual mechanisms in this zone are not understood properly.

For an axial jet, the first two zones are strongly influenced by the diffuser, the third zone is the developed jet, and the fourth zone is the zone of jet termination. In the first three zones, room air is entrained into the jet and mixed with supply air. In the fourth zone, the jet collapses inward from the boundaries and the supply air is distributed to the room air as the jet disintegrates [Rajaratnam.N, 1976].

It is sufficient to have knowledge of the first three zones in most engineering applications. Because of the large velocity difference at the surface of discontinuity between the jet fluid and ambient, large eddies are formed, which cause intense lateral mixing. As a result of this mixing, fluid within the jet is decelerated and the fluid surrounding the jet is accelerated and in fact it is entrained into the jet flow. As a consequence of entrainment, the width of the jet increases.

Fig. 2.2 illustrates the schematic view of plane jet emanating from rectangular nozzle of large aspect ratio with axial distance.

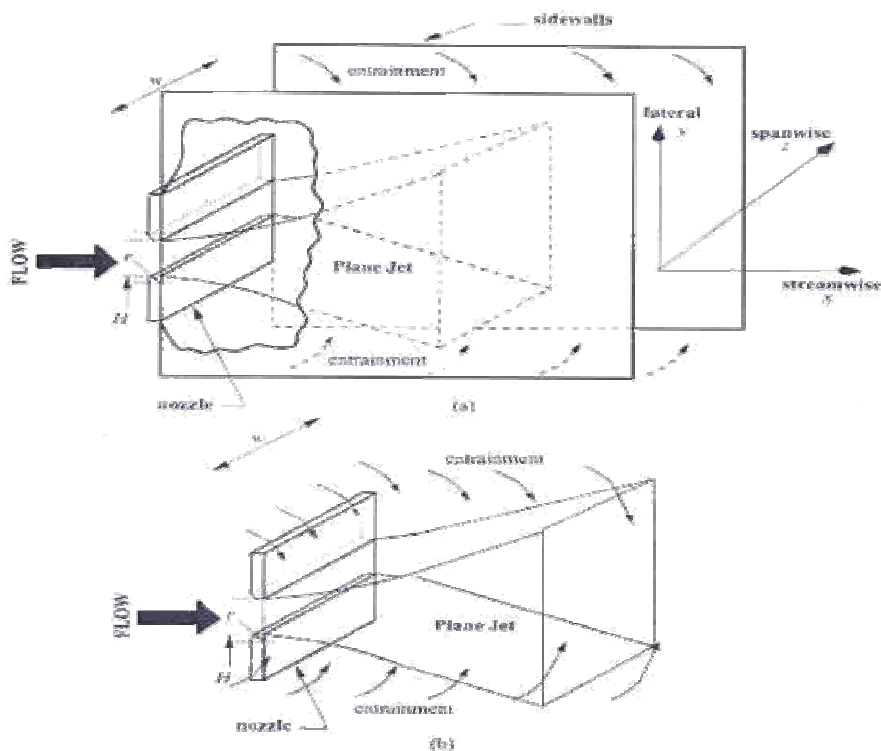


Fig 2.2 Development of a plane jet with side walls

The jet is confined within two parallel sidewalls attached to the short sides of the nozzle and oriented in the x-y plane. Such a configuration excludes the spread of the jet in the z-direction.

2.4 Factors Influencing Jet Spread

Several factors such as the jet inlet velocity profile, nozzle geometry, jet Reynolds number and fluid temperature at the inlet, affect the jet spread. Here, a brief account of the factors and phenomena which influence jet growth is presented.

2.4.1 Inlet Velocity Profile

The initial condition of the jet influences the downstream development of flow. The flow profile at jet inlet can be generally categorized into one of the four types: laminar, nominally laminar, highly disturbed and fully turbulent. The laminar and fully turbulent conditions are asymptotic limiting states, and the second or third case is typically achieved. The mean velocity profile in the shear layer at jet inlet is identical to the Blasius profile in the laminar case. The shear layer instability induced fluctuations will occur with peak values near the jet boundaries. The spectrum for the laminar shear layer flow has typically a few peaks, but without considerable broadband components. The parameters that are usually obtained to assess the nozzle exit (i.e. jet inlet) conditions are;

$$\text{Displacement thickness } \delta = \int_{-\infty}^{\infty} \left(1 - \frac{U}{U_{\infty}}\right) dy \text{ -----(2.1)}$$

$$\text{Momentum thickness } \theta = \int_{-\infty}^{\infty} \frac{U}{U_{\infty}} \left(1 - \frac{U}{U_{\infty}}\right) dy \text{ -----(2.2)}$$

$$\text{Shape factor } H = \frac{\delta}{\theta} \text{ -----(2.3)}$$

The value of shape factor is 2.5 for a laminar boundary layer condition at the nozzle exit and 1.4 for fully developed turbulent boundary layer condition. A value falling in between this range of shape factor means that the boundary layers are transitional in nature.

2.4.2 Nozzle Geometry

The feature of the jet flow is significantly affected by the nozzle geometry. The far field mean centreline velocity function of a round jet and plane jet are different. The former is a function of x^{-1} while the later $x^{0.5}$. The transition characteristics of the jets also depend on the nozzle cross sectional shape. Non-circular jets, especially rectangular jets with large aspect ratios undergo the phenomenon of axis switching. During this phenomenon, the major and minor axes switch with axial distance. This is due to the different spread rates for the jet in the two lateral directions. This phenomenon is absent in round jets. Nozzle geometries has got important role to play in defining the initial velocity profile of the jet. Sharp edged orifice geometry may produce a saddle-backed initial velocity profile [Elbanna *et al.*, 1983] while a top hat profile is obtained with a smooth contraction nozzle. Depending on the Reynolds number, fully developed laminar or turbulent profiles at the exit are obtained for jets discharging from long two dimensional channels.

2.4.3 Jet Reynolds Number

Reynolds number of a plane jet is defined in terms of the height of the nozzle, bulk mean velocity U_0 and kinematic viscosity ν of the jet fluid as

$$\text{Re} = \frac{U_0 d}{\nu} \text{-----} \quad (2.4)$$

If the jet discharges through a contoured plane nozzle, the velocity variation at jet inlet will be a top hat profile and bulk mean velocity is close to the nozzle exit

centreline velocity. An alternative definition of the Reynolds number can be based on the local jet half width and the local centreline velocity, in the form

$$Re_{b_u} = \frac{U_c b_u}{\nu} \text{-----(2.5)}$$

2.4.4 Half Width and Virtual Origin of the Jet

Jet half width at any axial location is defined as the distance between the centreline and a transverse plane where the mean velocity becomes half of the corresponding centreline velocity. Half width generally increases linearly with x except in regions of axis switching. Slope of the half width line in the axial direction is called as spread rate. Usually, the spread rate of a high Reynolds number turbulent jet is 0.11 while that of a laminar jet is around 0.4. Virtual origin is the point from which the jet appears to be originating as shown in fig. 2.3.

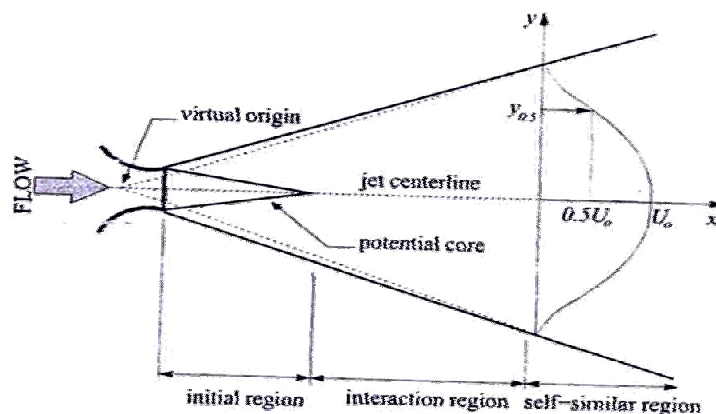


Fig 2.3 Virtual origin and half width

It may be different from the geometric origin and may be located inside or outside the nozzle, depending upon the nozzle exit boundary layer profiles. Virtual origin is related to the half width through the expression

$$\frac{b_u}{d} = K_{2u} \left(\frac{x}{d} \pm C_{2u} \right) \text{-----(2.6)}$$

Where C_{2u} is the virtual origin and K_{2u} is the spread rate. Also, b_u is the jet half width.

2.4.5 Jet Instabilities

Depending on the initial velocity profile, beyond certain axial distance, the jet fluid discharging from the nozzle develops flow oscillations in the shear layer. These oscillations will roll up to form vortices which increase in size and strength with the axial distance. The vortices will influence the entrainment of the ambient fluid and the mixing of the ambient fluid and the jet fluid. The vortex interactions will result in the transition of the flow to turbulent regime. Flow visualization studies reveal stark differences in the development of circular and non- circular jets [Batchelor *et al.*, 2000]. The development of vortices in the shear layer and the ultimate transition of an initially laminar jet to turbulent flow, are shown in Fig 2.4

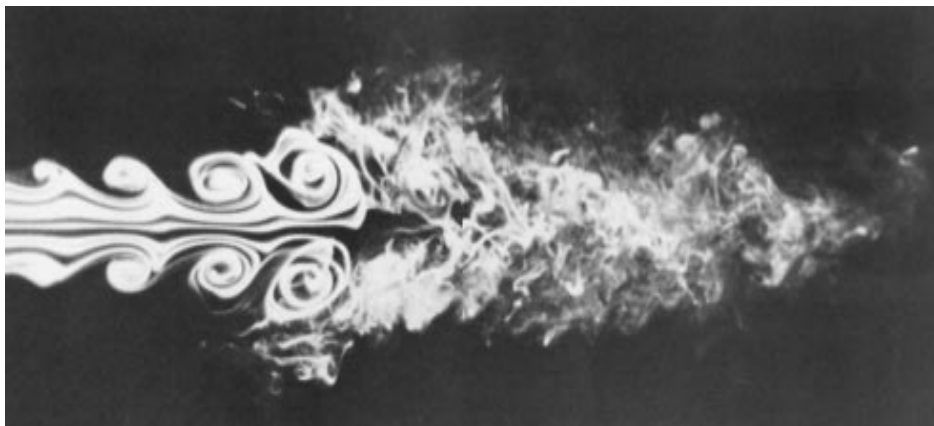


Fig 2.4 Shear layer instabilities in a jet

2.4.6 Coherent Structures

Coherent structures are defined as a connected, large scale turbulent fluid mass with a phase correlated vorticity over its spatial extent i.e. underlying the three dimensional random vorticity fluctuations characterizing turbulence, there is an organized component of the vorticity which is phase correlated (coherent) over the whole structure [Hussain, 1983]. Development of coherent structures in a jet is dependent on initial conditions and hence amenable to control. It is possible to find out the frequency of formation of such structures and can be controlled by using

acoustic excitation. The enhanced fundamental mode modifies the flow in such a way so as to destroy the fine grained turbulence production mechanisms. Because of viscous dissipation, the fine scale turbulence then decays downstream, allowing the coherent structures to amplify and spread the mean motion. Structures start developing in the highly unstable shear layer near the nozzle lips [Thomas F.O, 1986]. These will then grow by engulfing the ambient fluid till a distance of 20 times nozzle height. Further downstream, some of the coherent structures merge and form larger structures. Thus, even in the far field, presence of coherent structures can be identified.

2.4.7 Isothermal and Non- isothermal Jet Spreading

An isothermal jet is one in which the jet fluid temperature and the surrounding fluid temperature are the same. On the other hand, in the case of a non-isothermal jet, the jet fluid temperature is different from that of the medium into which it is discharged. Non- isothermal jets may be buoyant or non- buoyant. When the Richardson number is very small, the fluid temperature has the role of a passive scalar and buoyancy effects are insignificant in such a case [Kotsovinos. N.E, 1977]. The dynamics of instabilities and turbulence development are considerably different in non-isothermal jets.

2.4.8 Self Similarity

Self preservation or self-similarity is said to occur when the profiles of velocity (or any other quantity) can be brought to congruence by simple scale factors which depend on only one transformed coordinate. A consequence of self preservation is that the governing equations of jet flow can be reduced to ordinary differential equation form. Alternatively, a flow is said to be self preserving if there exist solutions to its dynamical equations and boundary conditions for which, throughout its evolution, all terms have the same relative value at the same relative location. Thus, self preservation implies that the flow has reached a kind of

equilibrium where all of its dynamical influences evolve together, and no further relative dynamical readjustment is necessary. Self preservation is therefore an asymptotic state [Carazzo *et al.*, 2006] in which a particular flow attains after its internal adjustments are completed. Several kinds of self preservation states are possible, for instance: 1) Flows can be fully self preserving at all orders of the turbulence moments and at all scales of motion. 2) Flows can be partially self preserving in that they are self preserving at the level of the mean momentum equations only, or up to only certain orders of the turbulence moments or at certain scales. For example, a general mathematical expression for jet flow that has attained self- similarity for mean velocity is given by

$$\frac{U}{U_c} = f\left(\frac{y}{\delta}\right) \text{-----}(2.7)$$

Where U and U_c are the local and centreline velocities in a transverse plane and δ is a measure of the local jet width.

2.4.9 Role of Side Walls in Jet Flow

The walls placed parallel to the x-y plane will force two dimensional spreading behaviours of a jet by preventing entrainment from sides. This is illustrated in fig 2.2. Though two-dimensionality is enforced in the near region, boundary layers start growing from the sidewalls [Deo.R.C, *et al.*, November 2007]. Therefore, downstream development of flow will be different for a plane jet discharging through a rectangular nozzle with and without side walls. Though the presence of a side wall can extend the region of two- dimensionality, it is also important to note that the boundary layers growing from the sidewalls influence the jet development in the far field as shown in Fig 2.5.

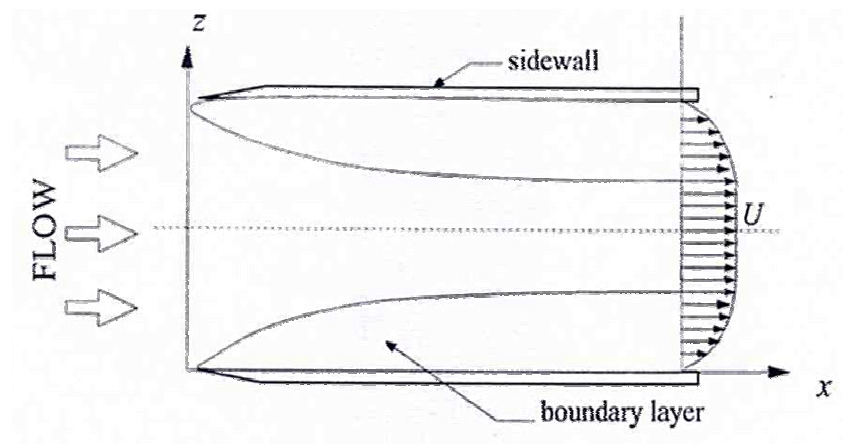


Fig 2.5 Development of boundary layers on side walls

2.4.10 Turbulent Length Scales

The turbulent flow consists of eddies of different sizes. Kinetic energy from the main flow is transferred to the turbulent eddy cascade (through production mechanism), at the largest scales of motion. This energy is then handed down to smaller and smaller scales through an inviscid process called vortex stretching [Pope, 2000]. At the smallest scales, the eddy kinetic energy is dissipated by viscous action. The large scale motion is often non-isotropic with strongly preferred directions. However, for many turbulent flows, the fine scale motion is locally isotropic. The average size of large eddies is called as integral length scale. The size of the smallest eddy at which dissipation is taking place is called as the Kolmogorov scale. Taylor micro- scale is the size of an intermediate eddy in the energy cascade process.

2.4.11 Aspect Ratio

The jet aspect ratio, (at nozzle exit) is an important factor for non circular jets that influences phenomena such as axis- switching and the jet evolution with axial distance. The growth of the shear layers along the major and minor axis directions is likely to be different. For rectangular nozzles in particular, the corner vortices at the sharp corners exert some influence on jet spreading in the near field [Deo.R.C,

August 2007]. The ratio of the major axis (z) to minor axis (y) dimensions is defined as the aspect ratio (AR) of a rectangular jet. In the present case, $AR = w/d$. A high aspect ratio will ensure that, when measured in the centre plane ($z=0$) of the plane jet, the flow is statistically two dimensional and free from the effects of side walls, for a major part of the jet flow. The pictorial view of a rectangular jet nozzle of large aspect ratio is shown in Fig 2.6. [Krothapalli *et al.*, 1981]

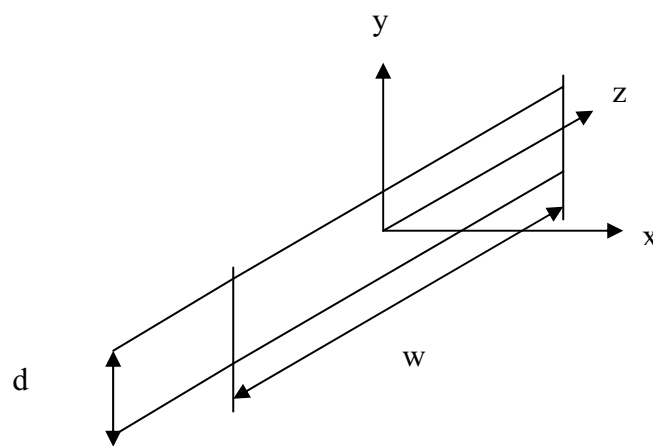


Fig 2.6 Aspect ratio of a rectangular jet nozzle

2.4.12 Intermittency

Flow visualization studies reveal that there is a highly contorted moving surface called viscous super layer that separates regions of turbulent and non-turbulent flow [List.E.J, 1982]. Regions of turbulent flow are characterized by large vorticity whereas non-turbulent flow is often irrotational. At a fixed location towards the edge of the flow, the fluid motion is some times turbulent and sometimes non turbulent. This type of flow is said to be intermittent.

2.5 Conclusion

The basic flow characteristics and the terminologies involved in the jet flow are explained in detail. The present study focuses on confined isothermal jet for its

further analysis. The half width of the jet and the centerline velocity decay are taken as major criteria for the selection of jet in the proposed study. The present study is not intended to go in depth with the theory of development of jets. The basic flow characteristics of a jet flow are used to select different orifice configurations for getting better air flow pattern in the data centre environment.

.....END.....

Contents	3.1 Introduction
	3.2 Experimental Investigations on Single Jet
	3.3 Theoretical Modelling and Predictions for Single Jet
	3.4 Twin and Multiple Jet Interactions
	3.5 Data Centre Air Conditioning
	3.6 Conclusion

3.1 Introduction

In this chapter, a brief review of literatures on jets and data centre is presented. The objective of the present work is to apply the concepts of jet flow to explain the data centre airflow. A detailed investigation of the multi complex phenomenon of jet flow is not made in this chapter. Some of the basic literatures on the fundamental jet flow are referred here for explaining the flow characteristics. Literature from jets is discussed in two sections dealing with experimental investigation and theoretical modelling and prediction for single jet and multiple jets. Data centre is presently an industrial concern and is not an area of academic research. Being a highly confidential and critical facility, research papers are not available in this field. Data centre air conditioning is a field which is still in its infancy and energy conservation concepts are just being introduced. Bureau of Energy Efficiency, Government of India and Confederation of Indian Industry jointly started preliminary works in framing data centre building codes and practices in India. The literature available regarding data centre and its thermal environment control are in the form of technical notes of companies and white papers published in this field. Some of these literatures are reviewed in this chapter.

3.2 Experimental Investigations on Single Jet

Comings and Miller (1957) conducted measurements of mean velocity, turbulent and static pressure in the mixing region of a jet of air discharging from a slot nozzle into still air. They observed that the two dimensional flow that they were investigating was essentially incompressible. They observed that the deviations that exist from isobaric conditions are appreciable and local turbulent stress has close relation to these deviations. Negative static pressure were observed everywhere in the mixing region. However, this was absent in the potential wedge region very near to the nozzle.

Bradbury (1965) investigated a plane jet exhausting into a slow moving parallel air stream. Self preservation is attained at a distance about thirty times the jet width down stream. The turbulent measurements and structures were compared with that of a self preserving wake and found that they were similar.

Bradshaw (1966) conducted experiments to study the effect of initial conditions on the development of a free shear layer in a round jet. It was reported that the virtual origin moves downstream when the initial boundary layer is laminar. The position of virtual origin depends on both boundary layer thickness and Mach number. It is observed that, transition takes place upstream of the nozzle exit at high Reynolds number. The virtual origin is influenced by the laminar boundary layer developed upstream of the trip. It is difficult to attain self preservation in the case of an initially turbulent boundary layer.

Sforza *et al.* (1966) conducted numerical and experimental studies in jets with varying shapes for the jet orifice. They studied turbulent, three-dimensional, incompressible jets discharging into ambient air. From the study, it was found that such jets exhibit basic flow field characteristics such as the potential core, characteristic decay region and the axisymmetric type decay region. Another important finding of this work is that, low speed jets that originate from non-circular orifices evolve into circular jets far downstream of the orifice.

Becker and Massaro (1968) studied an axisymmetric jet with a velocity distribution radially uniform at the nozzle mouth except for a laminar boundary layer at the wall for the varicose instability. They investigated different instability phenomenon which includes the rolling up of the cylindrical vortex layer into ring vortices, the coalescence of ring vortex pairs, and the eventual disintegration into turbulent eddies as a function of Reynolds number. They employed smoke photography, stroboscopic observation and the light scatter technique for this study.

Wynanski and Fiedler (1969) investigated the axisymmetric, incompressible, isothermal turbulent jet using linearized constant temperature hot wire anemometer for a circular jet at high Reynolds number. They covered an axial distance of 100 nozzle diameter. They reported the experimental values of Reynolds stresses, autocorrelation, longitudinal and lateral correlation, integral length scales and dissipation terms. They observed that longitudinal fluctuations become self similar at around 40 nozzle diameter and the radial and tangential turbulent intensities attain self similarity around 70 nozzle diameters.

Chervay and Tutu (1978) investigated a round jet for its temperature and vorticity fields. They adopted both conventional and conditional measurements. They found that, large scale turbulent motions were responsible for the bulk of heat and momentum transport. By filtered correlation measurement they showed that, small scales were more efficient in transporting heat than in transporting momentum. In this study they presented an exact equation for intermittency.

Krothapalli *et al.* (1980) conducted studies to measure the velocity components and the turbulent shear stresses in the central planes of a rectangular incompressible jet issuing into a quiet surrounding at ambient pressure. Three distinct regions were observed as a potential core region, a two-dimensional-type region and an axisymmetric-type region. He observed that for the smallest dimension of the nozzle, similarity both in mean velocity and shear stress profiles was observed beyond 30 widths downstream of the nozzle exit on the central plane.

But along the central plane containing the long dimension of the nozzle, the mean velocity, shear stress and rms velocity profiles did not exhibit self- similarity.

Namer and Otugen (1988) conducted experimental studies to find the effects of jet Reynolds number on the development of a plane jet. The results showed that there is no growth in turbulence level inside the potential core. They observed a decrease in the core length with increase in Reynolds number, and the turbulent energy is distributed among a broader range of eddy sizes. The power spectrum is not at all affected by variation in axial location at constant Reynolds number. This indicates that that eddies of the same size contain the same amount of relative energy at various axial locations.

Panchapakesan and Lumley (1993) conducted experiments on a round jet of air discharging into quiescent atmosphere, using hot-wire anemometer. They used hot wire probes mounted on a moving shuttle. This eliminated the rectification errors due to the flow reversals in the intermittent region of the jet. They measured moments of velocity fluctuations up to the fourth order to characterise turbulent transport in the jet. With this they evaluated the current models for triple moments that occur in Reynolds equation. They showed that non-dimensional rms velocity fluctuations along the jet centre-line approach asymptotic limits.

3.3 Theoretical Modelling and Predictions for Single Jet

It is believed that, the solution of the complete set of Navier-Stokes equation which is time dependent can be used to study the turbulent flows that are encountered frequently in practice. Due to the availability of fast computers, it is possible to use direct numerical solutions (DNS) for solving simple geometries and low Reynolds number flow problems. Since this method is not practicable as it is very expensive and time consuming, solutions based on the time-averaged equations are used for engineering calculations. This is no shortcoming because an engineer is usually concerned only with the time-averaged effects of turbulence,

even when the mass flow is unsteady [Bradshaw, 1971]. However, averaging eliminates some of the information contained in the Navier-Stokes equation.

The numerical procedures which are used to solve the turbulence models can be divided into integral and differential types. The differential methods involve direct assumptions for Reynolds stresses at a point and seek the solution of the governing equations in their partial differential form. Whereas, the integral methods include the integral parameters of the shear layer momentum thickness, shape factor, skin friction coefficient etc. The important difference between the above two calculation methods is the type of turbulence model rather than the numerical procedure. The advantage of differential procedure is that the restrictions and inaccuracy that arise from the need to parameterise the velocity profiles are avoided. Differential methods introduce substantially more detailed information about turbulence.

Love (1958) conducted numerical investigations on an axisymmetric jet. He approximated the boundary of a supersonic axisymmetric jet, for moderate static pressure ratios. He used one-dimensional relations and Prandtl-Meyer turning for arriving at the results. The approximate boundary layer was observed to fall below the exact boundary layer (calculated by the method of characteristics) for all Mach numbers,.

Eastman and Radtke (1963) conducted studies for calculating the location of normal shock wave in the exhaust plume of a jet. They used a method-of-characteristics program for this study. They proposed that the location of normal shock wave coincides with the point of minimum pressure. They compared the predicted results with experimental data and found both agree each other. This implies that the normal shock is not induced by viscous effects and it is also not affected by the downstream flow.

Albini (1965) conducted studies on under expanded jets. He performed an approximate analysis to investigate the structure of the jet. He assumed the flow as

inviscid and the diffusion effects and atmospheric density gradients were neglected. The approximate thickness of shock layer was estimated using a homogenous shock layer model. However, the model was seen to be more accurate only far away from the exit.

Bradshaw *et al.* (1966) by defining three empirical functions relating the turbulent intensity, diffusion and dissipation of the shear stress profile, they converted the turbulent energy equation into differential equation for the turbulent shear stress. This equation, the mean momentum equation and the mean continuity equation form a hyperbolic system. For a wide range of pressure gradients they performed numerical investigation by the method of characteristics with preliminary conventional calculation method. Nearly all the empirical information required has been derived solely from the boundary layer in zero pressure gradients.

Launder and Hanjalic (1972) approximated the transport equation for Reynolds stress tensor and the turbulent energy dissipation rate of a turbulence model, thereby providing effective solution for closure problem. This resulted in the solution of seven transport equations and only six constants to be determined experimentally. The proposed approximation thus lead to satisfactory predictions of the component stress levels in the plane homogeneous turbulence. This includes the non-equality of the lateral and transverse normal stress components. Hence they proposed a simple model for the boundary layer flows where the transport equations are solved only for shear stress, turbulence energy and dissipation rate.

Launder and Spalding (1974) while reviewing the problem of making numerical prediction of turbulent models, the observed the following. When the transport equation of the mean flow behaviour is solved simultaneously for the magnitude of the turbulent kinetic energy and its dissipation rate, the computational economy, the range of applicability and the physical reality are best served by the present turbulence models.

Launder *et al.* (1975) presented a numerical solution for two dimensional inhomogeneous shear flows like jet, the wake, the mixing layer and the plane channel flow. Such flows are grouped into strained homogeneous flows. They considered Reynolds stresses along with turbulence energy dissipation rate for the solution of the transport equation to develop a turbulence model. They observed that, for flow over curved surfaces the secondary strain term has got a strong influence on closure.

Rodi (1975) studied the relative merits and demerits of different turbulence models for analyzing the jet flow. He observed that, whenever turbulence transport and history effects are important, the use of mixing length model, which was widely used for simple shear layer calculations, are not suitable. It is found to be difficult to specify the mixing length distribution in flows which are more complex than simple shear layer flows. In order to prescribe the length scale distribution realistically, one equation model is found to be superior to the mixing length model. One equation models employ a transport equation for kinetic energy of turbulence, which accounts for the turbulent transport and history effects. The k- ϵ model is superior to predict many different flows with accuracy sufficient for practical purpose than the one equation model. The use of an isotropic eddy viscosity in the k- ϵ model does not describe certain important flow phenomenon. Stress equation models are capable of simulating the turbulent process more realistically. They are capable of describing many features that are not possible to model with the isotropic eddy viscosity model. But they are very complex and computationally expensive so they are not very suitable for practical applications.

Kostovinos (1978) conducted studies in the conservation of momentum in axial direction of a turbulent jet. The free jets exhibit a basic feature by which they induce flow towards themselves. For a plane jet which is discharging out of a wall, for the induced flow, there exists a component in the direction opposite to the direction of the jet flow. The tendency of this reverse flow is to reduce the

momentum flux from the initial value. The positive pressure field which builds up throughout the potential region also tends to reduce the momentum flux. This study revealed that the reduction in momentum flux is not negligible. They compared the reduction in momentum flux obtained from their approximate model with existing experimental results. They found that they are in fair agreement.

Kostovinos (1978) considered different types of jets such as plane jet in space, plane jet out of a wall and round jet out of a wall for studying the conservation of volume flux in free turbulence. He concluded that the analysis can be extended to any free turbulent shear layer like mixing layers and plumes.

Pope (1978) gives an explanation for the anomaly existed for the prediction of spread rates of round jets and plane jets. The values of the constants which are used in the boundary layer flows predicted the velocity fields in two dimensional plane jets quite accurately. But when applied to axisymmetric jets, large errors occurred. The spreading rate of a round jet is overestimated by about 40% by this approach. But experimental data suggests that the spread rate of round jet is about 15% less than that of a plane jet. Since no vortex stretching can take place in a two dimensional flow as the mean vorticity vector is normal to the plane of the flow. But for an axisymmetric jet as the jet spreads, rings or vortices are stretched. This causes the effective viscosity to be lower and the spread rate is also lower in a round jet than in a plane jet. Based on his study, he modified the constants of $k-\epsilon$ model and conducted the analysis. He found that the spread rate and the velocity profiles were in excellent agreement with the measured counterparts.

Mcguirk and Rodi (1979) introduced a finite-difference model for the three dimensional heated surface jets discharging into stagnant water. The $k-\epsilon$ model solved the basic governing equations and determined the turbulent shear stresses and heat fluxes. When compared with the measured values, the predicted values of jet half width, centreline excess temperature and velocity decay were found to agree. But the lateral velocity and temperature profiles were not in good agreement

with the measured values. This was attributed due to the fact that, the model was not capable of accommodating the recirculation flow of the heated water.

Looney and Walsh (1984) studied three different categories of jet flows which includes, laminar free jet, developing turbulent free jet and turbulent impinging jets of different configurations. They presented the numerical solution of the governing equations for all the three flow models. They compared the solutions of the Navier-Stokes equations for the laminar flow case with their analytical boundary layer solution and established the accuracy of the numerical procedure. The two equation turbulence model along with the Reynolds averaging achieved the solution of the closure problem with three alternative algebraic expressions for the turbulent stress. They reported that, the approach was capable of maintaining consistency in predictions and agreement with the measurable quantities.

Paullay *et al.* (1985) conducted studies on the effect of eddy viscosity in the standard k- ϵ turbulence model in governing the self similarity of incompressible plane and radial jets. They found that when the eddy viscosity was defined by the model, the equations governing self similarity have a solution that is not analytical at the jet edge. They observed that a co-ordinate transformation accounts for the lateral distribution of the eddy viscosity by stretching of the similarity variable. By this approach they arrived at a simplified set of governing equations suitable for efficient computational solution. They obtained highly resolved solutions for the velocity, turbulent kinetic energy and dissipation rate profiles. Entrainment, velocity decay rate and growth rate were also possible to obtain with the method.

Rodi and Scheuerer (1986) conducted studies on the relative merits of the one equation and the k- ϵ turbulence model under adverse pressure gradient boundary layers. They found that the one equation model is superior to k- ϵ model in predicting the situation. They found that, this was due to the over prediction of the skin friction coefficient by the k- ϵ model. This led to the tendency of the predicted flow to remain attached where experiments indicate separation in the respective

region. They modified the k - ϵ equation emphasising the generation rate due to deceleration. This resulted in improved predictions for both moderately and strongly decelerated flow.

Martynenko and Korovkin (1993) conducted numerical studies on self similar equations for the velocity and temperature fields of a plane jet. They provided the solutions for different Prandtl numbers. They were successful in providing the solutions for velocity, temperature, kinetic energy of turbulence and rate of its dissipation. Their numerical scheme employing non similar partial differential equation showed good agreement with experimental data except for the heat flux distribution in the transverse direction.

Peterson and Hotton (1995) conducted numerical analysis on axisymmetric jet for turbulent cross stress and pressure in the developing region. The developing region they referred corresponds to a region immediately after the potential core and prior to the fully developed flow. They observed that up to 100 nozzle diameters downstream the flow is not fully similar while the flow is turbulent. This was due to the presence of the higher order statistical quantities. They observed that the uncertainties with the measurement of Reynolds stress will give high degree in experimental measurements. They tried for a combination model of most easily measured experimental quantities with the numerical model to give better Reynolds stress estimate.

Seffal and Michaelides (1996) conducted studies on axisymmetric jets by developing a similarity method to transform the partial differential equations onto ordinary differential equations. They changed the k - ϵ turbulence model equation and optimised the solution. The results thus obtained agreed well with available experimental data of the velocity and the shear stress profiles.

Liu and Bellhouse (2005) analysed a supersonic nozzle and a diffuser incorporating a low Reynolds number k - ϵ turbulence model. They used a modified

implicit flux vector splitting (MIFVS) solver for the Navier-Stokes equations for this study. The results obtained showed good agreement with experimental data.

3.4 Twin and Multiple Jet Interactions

Tanaka (1970 & 1974) conducted experiments with the help of a constant temperature hot-wire anemometer on a dual jet which is discharged from two parallel slot nozzles. He observed the existence of a recirculation flow region between the two jets, owing to the entrainment of the ambient fluid. Due to this, the two jets attract each other, with the axis of each jet forming an arc of a circle. There are stable symmetric contra-rotary vortices with flow recirculation in the region surrounded by the jets. This is the reason for the negative velocity between the two jets. He made measurements on axial velocity, turbulence and static pressure in combined flow at different axial locations for three different inter nozzle spacing. These values were compared with the values of a single jet. He observed similarity between the velocity profiles of the combined flow and the theoretical profile of a single jet. The turbulence intensity distributions were different from those of a single jet and the combined jet. This is attributed to the difference in the entrainment and mixing characteristics. They made the following conclusions from the work. Static pressure in the combined jet is negative and shows minimum value at the centre of profile. For the combined jet and a single jet, similarity in the width of jet spread exists and both spread linearly downstream. In the combined jet, the total fluxes in the downstream direction are not conserved and the decay of maximum velocity is stronger than that of a single jet. This is expected due to the presence of the recirculation zone between the two jets.

Murai *et al.* (1976) conducted experimental studies on two plane interacting jets. For this study he considered two plane incompressible turbulent jets discharging at an angle from the nozzle exit plane. This was to study jet confluence phenomena. They recorded the velocity and pressure distributions in the recirculation region and in the combined jet region. They found that, due to the

confluence, the axial momentum flux and the energy flux decreases. They further concluded that this decrease is independent of the separation distance between the nozzles and the angle at which the jets are emanating.

Krothapalli *et al.* (1980 & 81) conducted experimental studies on incompressible free and partially-confined jets discharging from a rectangular array of equally spaced nozzles. He adopted hot-wire measurements for this study. The mean velocity profiles of the individual jets were found to be independent of each other if the inter nozzle spacing is larger. It was found that, similar profiles upstream of the merging region for single jet and multiple jets are identical. The growth rate in multiple jet configurations is greater than that of a single jet further downstream of the merging point. The entire flow field appeared as if it emerges from a single two-dimensional slot. Thus, it is concluded that, the multiple jet array will exhibit single jet behaviour beyond the merging point.

Raghunathan and Reid (1981) reported the interaction of multiple jets with more than five jets in a plane. They studied a radial configuration of five and nine jets with a central jet. They observed that the jets merge to form a single jet at a downstream distance of about few nozzle diameters. They noted that the peak velocity shifted towards the central axis from the outer jets. They concluded that, as the number of jet increases the decay of axial velocity increases and the jet spread and momentum are slightly less than that of a single jet. They conducted noise spectral studies to achieve noise suppression using multiple jet configurations. They observed that multiple jet configurations are advantageous in noise reduction without significant loss in momentum.

Elbanna *et al.* (1983) conducted studies on the interaction of twin jet configuration for turbulent measurement. They measured mean velocities, turbulent intensities and Reynolds shear stresses. They also observed that, the velocity profile and decay rates of the merged jet as similar to those of a single jet beyond the merging point. They observed the maximum velocity fluctuations to occur at

the nozzle edges and the minimum values at the axis of each jet. The axial velocity fluctuations exhibit a saddle-back shape profile in the region beyond the merging point and are not self similar. The variation of Reynolds stress is similar to that exhibited by a single jet.

Okamoto *et al.* (1985) studied the interaction of twin turbulent circular jets. They varied the inter nozzle spacing and studied the velocity and static pressure distributions for twin jets. They compared these results with the values of a jet parallel to plane wall. They concluded that, twin jets interact and combine in the form of an elliptical jet, which evolves to become circular far downstream. The position of maximum velocity shifts from the axis of the nozzle to the mid-point between the jets.

Seiner *et al.* (1988) conducted studies on the scaled models of F-15 and B-1B aircrafts. They investigated the problem of supersonic plume resonance in the inter-nozzle region. Spectrum of pressure fluctuations in the inter nozzle spacing indicates dynamic loading. They concluded that, by simple geometric modification of one nozzle these dynamic loads can be effectively suppressed.

Elbanna and Sabbagh (1989) conducted studies on flow field characteristics of twin impinging plane jets. They conducted flow visualization studies which revealed the influence of both geometric parameters and relative strength of the two jets on the position of counter-rotating vortices as well as the deflection of up-wash. They took hot-wire measurements to study the jet decay rates and concluded that, the rate of jet decay in two-impinging jet flow is greater than that for a single free jet. If the impinging jets are dissimilar, the weaker jet spreads and decays at a rate much greater than that of the strong jet.

Wlezien (1989) conducted investigations on identical twin convergent/divergent nozzles as a function of inter nozzle spacing. He observed that the nozzle spacing strongly influences the modal amplitudes for two coupled jets. They studied the coupling of the two jets as a function of Mach number and nozzle spacing. If the

nozzle spacing is reduced, coupling occurs at low Mach numbers but it is suppressed at high Mach numbers. They observed the reverse for large nozzle spacing and amplitude of coupled jets is independent of the design Mach number.

Lin and Sheu (1991) conducted experiments on twin plane subsonic jets discharging into still surrounding. They also concluded the jet attract each other, merge and eventually combine to resemble a single jet. They observed that this was due to entrainment of surrounding air. They studied the presence of a connecting end wall between the jets and observed that this will increase the decay of maximum velocity as well as jet spread rates in the converging region, while it has no effect on the combined region.

Moustafa (1994) conducted experimental studies on high speed twin jets emanating from two axisymmetric convergent nozzles. The study revealed that the main features of high speed twin jets are quite similar to those of low-speed incompressible jets. He observed that as the nozzle spacing increases, the jet half width will increase and it is greater than that for a single jet in the near field. The jet width attains a maximum value in the subsonic flow regime and decreases near sonic pressure ratio.

Moustafa (1995) conducted studies on the over-expanded twin axisymmetric jets to analyse the effects of Mach number, pressure ratio and nozzle spacing. He concluded that with respect to the behaviour of total pressure profiles, decay and spreading rates of over-expanded jets have some similarities with under-expanded jets. Mach number affects the shock cell strength and position, while nozzle spacing affects the bending of jet axes.

Niimi *et al.* (1996) with the help of laser-induced fluorescence, they conducted flow visualization studies on two, three and four parallel supersonic jets. They found that the nozzle arrangement has got a role in the formation of second cell. The second cell is formed in the interacting region with intense expansions in

radial direction for linear nozzle arrangement. The second cell becomes dominant in downstream with intense expansion between adjacent cells for triangular or square arrangements.

3.5 Data Centre air Conditioning

Patel *et al.* (2001) discusses on the energy conservation aspects of data centre with respect to the capacity control of the cooling system. They introduced the concept of smart cooling and this can be implemented with the help of a powerful CFD tool. They explain both under floor and overhead cooling systems used in data centre industry. The data centre cooling can be improved by taking two key parameters, the mass flow and the temperature. They explained the data centre design and put forward steps for energy saving with the help of CFD analysis of a data centre in detail. The paper emphasizes the use of CFD analysis in data centre design and its validity in the data centre industry. They used the concept of smart tiles that regulates the velocity and volume flow rate of air by changing the tile opening (with the help of dampers).

Sullivan (2002) is the inventor of hot/cold aisle concept in 1992. The solution for avoiding down time of a data centre is to have a strategic plan for how the server farm will be implemented. A best practice is to use rows of equipment racks in an alternating arrangement of cold aisles and hot aisles. A cold aisle is defined as having perforated floor tiles that allow cooling air to come up from the plenum under the raised floor, and a hot aisle has no perforated tiles. In the cold aisle, the equipment racks are arranged face to face so the cooling air discharged up through the perforated floor tiles is sucked into the face of the computer hardware and exhausted out of the back of the equipment racks onto the adjacent hot aisles. Hot aisles are literally hot because the objective of the alternating cold and hot aisle design is to separate the source of cooling air from hot air discharge which returns to the computer-room cooling unit. Therefore, no perforated tiles should be placed in the hot aisles, as this would mix hot and cold air and thereby lower the

temperature of the air returning to the cooling units, which reduces their useable capacity. Hot aisles should be hot! Cold aisles should be cold! This alternating arrangement of cold aisles and hot aisles is as shown in Fig 3.1.

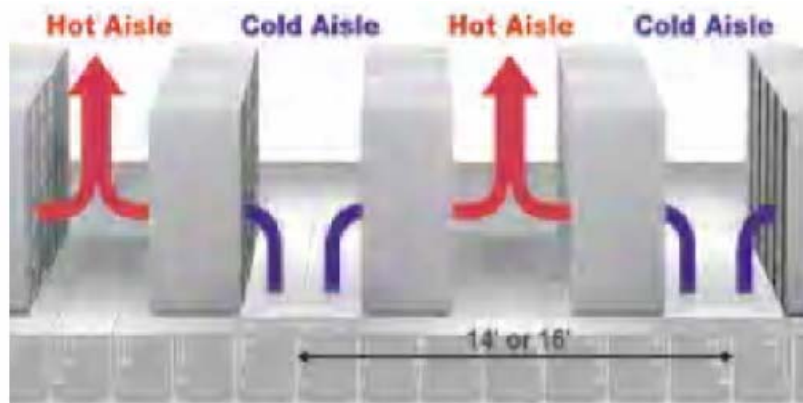


Fig 3.1 Figure showing cold/hot aisle segregation

This system is not perfect because some equipment manufacturers bring cooling air in from the bottom of their equipment and exhaust out through the top and/or sides. And some equipment is designed to bring air in from the sides and exhaust out the top, or bring air in from the top and exhaust out the bottom. Works are being under way in different agencies to develop an industry standard for this.

Karki *et al.* (2003) introduces a computational fluid dynamics model for calculating the air flow rates through perforated tiles in raised floor data centre. This study further applied to a real time data centre measures the actual flow rates through the tiles and is found that the actual and numerical results are in good agreement. This paper clearly reveals the acceptance of CFD tools in data centre modelling and analysis.

Kurkjian (2006) in his white paper presents a detailed study of the power growth in data centre industry for the past few decades Detailed comparisons of the IT equipment power consumption of different types of rack servers are discussed. He also explains the significance of hot/cold aisle segregation in detail. In this

white paper he underlines the use of CFD in predicting the air flow through the air flow devices in the data centre. He highlights the usage of CFD in data centre design and identification of hot spots in data centre. He suggests few positions for CRAC and rack layouts. He also discussed about the ceiling mound cooling system which is commonly used along with raised floor design to support high density racks.

Data centre resource guide-Anixter (2007) gives the essential factors regarding data centre infrastructure facilities. As recommended by the American Society of Heating, Refrigerating and Air-conditioning Engineers (ASHRAE) and the ANSI/TIA/EIA-942 data centre standard, the first step to gaining control of excess heat is to reconfigure the cabinet layout into a hot aisle/cold aisle arrangement. According to the recent ANSI/TIA/EIA-942 data centre standard, when a raised floor is used to provide equipment cooling for the data centre, the minimum aisle width should be at least 3 feet. Typically, cold aisles are 4 feet wide to allow two full size perforated floor tiles in front of cabinets with active components. Hot aisles should be wide enough to allow unrestricted access to data and power cabling. Additionally, these standards state that the data and power cabling should be located under the hot aisle.

In conjunction with the new layout, it is essential to install blanking panels in every open bay, in all cabinets in high density area. These inexpensive but effective panels have been shown to greatly reduce the undesirable mixing of hot discharge air with cold inlet air. In an attempt to direct hot discharge air into the hot aisle, it is also recommended that solid stops and solid side panels be installed between all cabinets in a row. Additionally, the installation of air dams in front of the cabinet is recommended to block hot air from slipping around the sides of the mounded components and mixing with the cold intake air. Finally, it recommends that precision sized Computer Room Air Conditioner (CRAC) be placed at either end of the hot aisles.

In the white paper published by The green grid (2007), two data centre matrix power usage efficiency (PUE) and data centre infrastructure efficiency (DCiE) are explained.

$$\text{PUE} = \text{Total facility power} / \text{IT equipment power}$$

And its reciprocal, the DCiE is defined as

$$\text{DCiE} = 1/\text{PUE} = (\text{IT equipment power} / \text{Total facility power}) \times 100.$$

Here, the total facility power is defined as the power measured at the utility meter (power dedicated solely to the data centre). The IT equipment power is defined as the power that is used to manage process or rout data within the data centre. The components of these loads in the matrix are described below.

IT equipment power- This includes the load associated with all of the IT equipment, such as compute, storage, and network equipment, along with supplemental equipment such as KVM switches, monitors, and workstations/laptops used to monitor or otherwise control the data centre.

Total Facility Power- This includes everything that supports the IT equipment load such as: power delivery components such as UPS, switch gear, generators, PDU, batteries, and distribution losses external to the IT equipment. Cooling system components such as chillers, computer room air conditioning units (CRAC), and direct expansion air handler (DX) units, pumps, and cooling towers. Compute, network, and storage nodes. Other miscellaneous component loads such as data centre lighting.

The PUE and DCiE provide a way to determine opportunities to improve a data centre's operational efficiency. How a data centre compares with competitive data centre, if the data centre operators are improving the designs and processes over time and opportunities to repurpose energy for additional IT equipment.

Goren (2008) discussed the design issues connected with the legacy data centre. In practice, the airflow in the legacy data centre is very much unpredictable, and has numerous inefficiencies, which are proliferated as power densities increase. Bypass air, recirculation and air stratification are the dominant airflow characteristics throughout the data centre. Bypass airflow is defined as conditioned air that does not reach computer equipment. The most common form of bypass air is when air supplied from the precision air conditioning units is delivered directly back to the air conditioners intake. Examples of this include leakage areas such as air penetrating through cable cut-outs, holes under enclosures, or misplaced perforated tiles that blow air directly back to the air conditioners intake. Other examples of bypass airflow include air that escapes through holes in the computer room perimeter walls and nonsealed doors. Recirculation occurs when the hot air exhausted from the rack mounted computing device is fed back into its own intake. This principally occurs in servers located at the highest points of a high density enclosure. Recirculation can result in potential overheating and damage to computing equipment and as a result may cause disruption to mission critical services in the data centre.

Air stratification in the data centre is defined as the layering effect of temperature gradients from the bottom to the top of the enclosure. In general, in a raised floor environment, air is delivered at approximately 13°C from under the floor through perforated tiles. The temperature, as the air first penetrates the perforated tile, remains the same as the supply temperature, but as the air moves vertically up the enclosure, air temperatures gradually increases. In high density enclosures, it is not uncommon for temperatures to exceed 32°C at the server intakes mounted at the highest point of the enclosure. However the recommended temperature range for server intakes as stated by ASHRAE Technical Committee 9.9, Mission Critical Facilities is between 20°C and 25°C. Thus, in a legacy data centre design we are essentially over cooling the computer room by sending extremely cold air under the raised floor because there is a lack of temperature control as the air moves upward through the front of the enclosure.

Seaton (2008) addresses the phenomenon of hot air recirculation. He introduces the concept of air isolation to cool high density data centres effectively. The hot air isolation includes, the cabinets with ducted exhausts directing heated air into a suspended ceiling plenum, cabinets direct- ducted back to the cooling unit, enclosed hot aisles with exhaust air ducted out of the data centre space.

Seaton (2008) conducted studies on how to decrease the data centre cooling costs. In his case study of a 600 kW data centre, having cold aisle hot aisle segregation, there were several hot spots in the cabinets with higher power densities. He used CFD modelling for this purpose. The initial scenario required 14 CRAC units with a cooling capacity of 385 TR and still experienced hot spots. The containment scenario required only 7 CRAC units of 220 TR and resulted in no hot spots. The ducted exhaust cabinets and improved tile locations in the containment scenario reduced 7 CRAC units from the plan, totalling 165 TR of excess capacity (40 % of the original capacity).

3.6 Conclusion

Based on the above review the following conclusions are made. In the field of jet, a lot of research publications are available with respect to different aspects of jet flow. The present study is not making any attempt to go into detailed investigations of the jet flow; rather it uses the basic concepts to explain the tile flow. In the field of data centre air conditioning, detailed research papers are not available. The literatures available in this field are in the form of white papers and technical reports for internal circulation in the industries concerned. From these literatures it is evident that an analysis of air flow patterns in a data centre environment by any method is not yet made. Attempts are being made with the help of CFD analysis to improve the cooling efficiency but none of these address the qualitative air flow analysis within the data centre. Hence the present investigation of qualitative air flow analysis and subsequent tile geometry generation is expected to have high impact in the industry. It also proposed to

address the phenomenon of hot air recirculation and give a qualitative explanation for this. The present work thus attempts to consolidate the practical issues in the data centre air flow dynamics with the help of computational fluid dynamics for conservation of energy.

.....❧.....

Contents	4.1 Introduction
	4.2 Governing Equations
	4.3 Boundary Conditions
	4.4 Pre-Processor & Solver
	4.5 Grid Generation Details
	4.6 Convergence Criteria
	4.7 Validation Problem
	4.8 Computer Systems Used
	4.9 Conclusion

4.1 Introduction

Turbulent flows, which are of great practical importance, are three dimensional and time dependant. Computer methods of solving the differential fluid dynamics are well advanced even for three dimensional time dependant flows. To meet the practical need for computation of turbulent flow, turbulence models are developed. These consist of a set of differential equations, and associated algebraic equations and constants, the solution of which, in conjunction with those of Navier-Stokes equation, closely simulate the behaviour of real turbulent fluids.

This chapter describes the numerical methodology for single, multiple and matrix array of jets. The governing equations, boundary conditions and grid employed for the simulation along with details of numerical procedure are described. The result of the validation problem is also presented.

4.2 Governing Equations

The governing equations for a compressible Newtonian fluid, the Navier-Stokes equation in the absence of source term in co-ordinate invariant form can be written as [Blazek.J, 2001]

$$\frac{\partial p}{\partial t} + \frac{\partial}{\partial x_i}(\rho v_i) = 0 \quad \text{-----(4.1)}$$

$$\frac{\partial}{\partial t}(\rho v_i) + \frac{\partial}{\partial x_j}(\rho v_j v_i) = -\frac{\partial p}{\partial x_i} + \frac{\partial \tau_{ij}}{\partial x_j} \quad \text{-----(4.2)}$$

$$\frac{\partial}{\partial t}(\rho E) + \frac{\partial}{\partial x_j}(\rho v_j H) = \frac{\partial}{\partial x_j}(v_i \tau_{ij}) + \frac{\partial}{\partial x_j} \left(k \frac{\partial T}{\partial x_j} \right) \quad \text{-----(4.3)}$$

and the equation of state $P = \rho RT$ -----(4.4)

In the above equation v_i denotes the velocity component and x_i stands for a co-ordinate direction respectively. The components of the viscous shear stress tensor τ_{ij} are defined as;

$$\tau_{ij} = 2\mu S_{ij} + \lambda \frac{\partial v_k}{\partial x_k} \delta_{ij} = 2\mu S_{ij} - \left(\frac{2\mu}{3} \right) \frac{\partial v_k}{\partial x_k} \delta_{ij} \quad \text{-----(4.5)}$$

The components of strain rate tensor are given by;

$$S_{ij} = \frac{1}{2} \left(\frac{\partial v_i}{\partial x_j} + \frac{\partial v_j}{\partial x_i} \right) \quad \text{-----(4.6)}$$

The total energy and total enthalpy are obtained from;

$$E = e + \frac{1}{2} v_i v_i \quad \text{and} \quad H = h + \frac{1}{2} v_i v_i \quad \text{-----(4.7)}$$

Turbulence models

The outstanding feature of a turbulent flow is that the molecules move in a chaotic fashion along complex irregular paths. Because of the increased momentum and energy exchange between the molecules and solid walls, turbulent flows lead at the same conditions to higher skin friction and heat transfer as compared to laminar flows. These fluctuations increase the mixing of transported quantities such as momentum, energy, and species concentration, and cause the transported quantities to fluctuate as well. Since these fluctuations can be of small scale and high frequency, they are computationally too expensive to simulate directly in practical engineering calculations. The instantaneous (exact) governing equations can be time-averaged or manipulated to remove the small scales, resulting in a modified set of equations that are computationally less expensive to solve.

The direct simulation of turbulence by time dependant Navier-Stokes equation known as direct numerical solution (DNS) is applicable only to relatively simple flow problems at low Reynolds numbers. A more wide spread utilization of the DNS is prevented by the fact that the number of grid points needed for sufficient spatial resolution scales as $Re^{9/4}$ and CPU time as Re^3 [Blazek.J, 2001]. In order to account for the effects of turbulence in an approximate manner, a large variety of turbulence models are developed. There are five principal classes of turbulence models: algebraic, one-equation, multiple equation, second-order closures (Reynolds stress models) and large-eddy simulation (LES). The equations for mean flow contain nine components of the viscous shear stress tensor (of which only six are independent) as unknowns in addition to ρ , T, P and v_i . Hence, the system contains more unknowns than the number of governing equations. This illustrates the closure problem of turbulence.

A turbulence model is a computational procedure to close the system of mean flow equations. Turbulence models allow the calculation of the mean flow without first calculating the full time-dependent flow field. Turbulence models to close the

Reynolds- Averaged Navier- Stokes equations (RANS) can be divided into two broad categories, according to whether or not the Reynolds stress tensor is simulated using a combination of physical relations and assumptions (First-order models) or it is directly resolved into its six components (Second-order models). The first three models mentioned above belong to the first order closure models. They are based mostly on the eddy viscosity hypothesis of Boussinesq, but for certain applications on non linear eddy viscosity formulations. Boussinesq assumption states that, in analogy to laminar viscous diffusion terms, the turbulent stresses are related to mean strain rate through an apparent scalar turbulent viscosity according to the relation,

$$\tau'_{ij} = -\rho v_i v_j = \mu_t \left(\frac{\partial v_i}{\partial x_j} + \frac{\partial v_j}{\partial x_i} \right) - \frac{2}{3} \left(\rho k + \mu_t \frac{\partial v_i}{\partial x_i} \right) \delta_{ij} \text{ -----(4.8)}$$

In turbulence models that employ Boussinesq assumption, the central issue is how the eddy viscosity is computed. First-order models include zero-equation (Mixing Length model), one-equation (Spalart-Allmaras model) and two-equation turbulence models.

(a) Spalart-Allmaras model

The Spalart-Allmaras one equation turbulence model [Spalart.S.R, 1992] employs transport equation for an eddy viscosity variable $\tilde{\nu}$. This model solves the transport equation for a quantity that is a modified form of the turbulent kinematic viscosity. This is identical to the turbulent kinematic viscosity except in the near-wall (viscous-affected) region. The transport equation for $\tilde{\nu}$ is:

$$\frac{\partial}{\partial t} (\bar{\rho} \tilde{\nu}) + \frac{\partial}{\partial x_i} (\bar{\rho} \tilde{\nu} u_i) = G_\nu + \frac{1}{\sigma_\nu} \left[\frac{\partial}{\partial x_j} \left\{ (\mu + \bar{\rho} \tilde{\nu}) \frac{\partial \tilde{\nu}}{\partial x_j} \right\} + C_{b2} \bar{\rho} \left(\frac{\partial \tilde{\nu}}{\partial x_j} \right)^2 \right] - Y_\nu + S_\nu \text{ -----(4.9)}$$

G_ν is the production of turbulent viscosity and Y_ν is the destruction of turbulent viscosity that occurs in the near-wall region due to wall blocking and viscous damping. C_{b2} and σ_ν are model constants and ν is the molecular kinematic viscosity.

(b) k-ε model

The widely acclaimed two-equation turbulence model is the k-ε model. In this model, μ_t is obtained by assuming that it is proportional to the product of turbulent velocity scale (\mathcal{G}) and length scale (ℓ). These scales are obtained from two parameters, k (turbulent kinetic energy) and ε (dissipation rate of kinetic energy). The velocity and length scales are taken as $k^{1/2}$ and $\frac{k^{3/2}}{\varepsilon}$ respectively.

Hence μ_t can be expressed as:

$$\frac{\mu_t}{\rho} = \nu_t \propto \mathcal{G} \ell \propto k^{1/2} \frac{k^{3/2}}{\varepsilon} = \frac{k^2}{\varepsilon} \text{-----(4.10)}$$

$$\mu_t = C_\mu \rho \frac{k^2}{\varepsilon} \text{-----(4.11)}$$

The two differential equations that govern the transport of turbulent kinetic energy and its dissipation rate are given by:

$$\frac{\partial}{\partial x_j} (\bar{\rho} \bar{u}_j k) = \frac{\partial}{\partial x_j} \left[\left(\mu_t + \frac{\mu_t}{\sigma_k} \right) \frac{\partial k}{\partial x_j} \right] - \overline{\rho u'_i u'_j} \frac{\partial \bar{u}_i}{\partial x_j} - \bar{\rho} \varepsilon - Y_M \text{-----(4.12)}$$

$$\frac{\partial}{\partial x_j} (\bar{\rho} \bar{u}_j \varepsilon) = \frac{\partial}{\partial x_j} \left[\left(\mu_t + \frac{\mu_t}{\sigma_\varepsilon} \right) \frac{\partial \varepsilon}{\partial x_j} \right] - C_1 \frac{\varepsilon}{k} \left(\overline{\rho u'_i u'_j} \frac{\partial \bar{u}_i}{\partial x_j} + C_3 G_b \right) - C_2 \bar{\rho} \frac{\varepsilon^2}{k} \text{---(4.13)}$$

C_1 and C_2 are constants in this model with values $C_1 = 1.44$ and $C_2 = 1.92$. The turbulent Prandtl numbers for k and ε are given by $\sigma_k = 1.0$ and $\sigma_\varepsilon = 1.3$ respectively for the standard k-ε model. G_b is the generation of turbulence kinetic energy due to buoyancy, while Y_M represents the contribution of the fluctuating dilatation in compressible turbulence to the overall dissipation rate. The value of C_μ is constant and is equal to 0.09 for standard k-ε model.

The k- ϵ (realizable) model was developed to satisfy certain mathematical constraints on the normal stresses, consistent with the physics of turbulent flows. For large values of strain rate, the normal stress, $\overline{u^2}$, which by definition is a positive quantity, becomes negative (eq. 4.8). Also, the Schwarz inequality for shear stresses ($\overline{u_\alpha u_\beta}^2 \leq \overline{u_\alpha^2} \overline{u_\beta^2}$) can be violated when the mean strain rate is large. To ensure the realizability C_μ is expressed as function of mean flow (mean deformation) and turbulence (k and ϵ). The round-jet anomaly is considered to be mainly due to the modelled dissipation equation. For instance, the spreading rate in planar jets is predicted reasonably well, but prediction of the spreading rate for axisymmetric jets is unexpectedly poor. Hence, a new model equation for dissipation based on the dynamic equation of the mean-square vorticity fluctuation is adopted for the k- ϵ (realizable) model.

(c) k- ω model

The standard k- ω model is an empirical model based on model transport equations for the turbulence kinetic energy (k) and the specific dissipation rate (ω), which can also be thought of as the ratio of ϵ to k. The two versions of k- ω model are the standard k- ω model and the sst k- ω model. The sst model differs from the standard model in two ways: (i) gradual change from the standard k- ω model in the inner region of the boundary layer to a high-Reynolds-number version of the k- ω model in the outer part of the boundary layer, (ii) modified turbulent viscosity formulation to account for the transport effects of the principal turbulent shear stress. The transport equations for k- ω (sst) model are:

$$\frac{\partial}{\partial x_i} (\overline{\rho k u_i}) = \frac{\partial}{\partial x_j} \left(\Gamma_k \frac{\partial k}{\partial x_j} \right) + \tilde{G}_k - Y_k \quad \text{-----(4.14)}$$

$$\frac{\partial}{\partial x_i} (\overline{\rho \omega u_i}) = \frac{\partial}{\partial x_j} \left(\Gamma_\omega \frac{\partial \omega}{\partial x_j} \right) + G_\omega - Y_\omega + D_\omega \quad \text{-----(4.15)}$$

In these equations, \tilde{G}_k represents the generation of turbulence kinetic energy due to mean velocity gradients, G_ω represents the generation of ω . Γ_k and Γ_ω represent the effective diffusivity of k and ω , respectively. Y_k and Y_ω represent the dissipation of k and ω due to turbulence. D_ω represents the cross diffusion term.

The Boussinesq hypothesis is used in the Spalart-Allmaras model, the k - ε models, and the k - ω models. The advantage of this approach is the relatively low computational cost associated with the computation of the turbulent viscosity. In the case of the Spalart-Allmaras model, only one additional transport equation (representing turbulent viscosity) is solved. In the case of k - ε and k - ω models, two additional transport equations (for the turbulence kinetic energy, k and either the turbulence dissipation rate, ε or the specific dissipation rate, ω) are solved. The disadvantage of the Boussinesq hypothesis is that it assumes μ_t is an isotropic scalar quantity, which is strictly not true. The second-order models do not make use of Boussinesq approximation and solves the individual stress components directly, rather than using algebraic relations for stresses. For this reason, second-order models are more general than the first-order models for flows with sudden change in the main strain rate.

4.3 Boundary Conditions

An important part of numerical simulation is the definition of appropriate boundary conditions. While all the fluid flow problems are governed by the Navier-Stokes equations, what distinguishes one problem from the other are the boundary conditions. Thus, specification of required boundary conditions completes the mathematical problem formulation. The boundary conditions specified usually belong to one of the categories described here [Klaus. A.H, 1993]:

- 1) *Dirichlet* type wherein the value of flow variable is specified at the boundary.
- 2) *Neumann* type wherein the normal gradient or flux of the variable is specified.
- 3) *Mixed* type wherein a linear combination of the variable and its derivative is specified.

The boundary conditions employed for single and multiple supersonic 2D and 3D free jets are as follows [Fluent Inc, 2005]:

Pressure inlet : The boundary condition for this study is pressure inlet as the pressure difference between the static pressures of plenum and the room which is the driving potential of the jet.

Pressure outlet: Pressure outlet boundary conditions require the specification of a static (gauge) pressure at the outlet boundary. The value of the specified static pressure is used only when the flow is subsonic. Pressure will be extrapolated from the flow in the interior. All other flow quantities are extrapolated from the interior. A set of "backflow" conditions is also specified, whether the flow reverses its direction at the pressure outlet boundary during the solution process.

Symmetry : Symmetry boundary conditions are used when the physical geometry of interest, and the expected pattern of the flow/thermal solution, has mirror symmetry as in the case of twin 2D and 3D jets. A zero normal gradient is applied for the flow variables U, P and T at the symmetry boundary. Also, the velocity component across the symmetry plane is set as zero.

$$\frac{\partial U}{\partial y} = \frac{\partial P}{\partial y} = \frac{\partial T}{\partial y} = 0 ; \frac{\partial W}{\partial y} = 0, V = 0$$

- Axis : The axis boundary type must be used as the centreline of an axisymmetric single jet.
- Wall : Wall boundary conditions are used to bound fluid and solid regions. No slip for velocity is imposed for an adiabatic wall,
$$U = V = W = 0 ; \frac{\partial T}{\partial n} = 0$$
- Turbulence: Hydraulic diameter and turbulence intensity is prescribed for inlet and outlet boundary conditions.

4.4 Pre-Processor & Solver

The pre-processor used for creating geometry and for generating the corresponding computational grid in the present work is GAMBIT (version-2.3.16). Most models can be built directly within GAMBIT's solid geometry modeller, or imported from any major CAD/CAE system. A comprehensive set of highly automated and size function driven meshing tools ensure that the best mesh can be generated, whether structured, unstructured, or hybrid. The governing equations and the boundary conditions described above have been solved using the commercial viscous flow solver called FLUENT (version-6.3.26).

The conservation equations of mass, momentum and energy are incorporated in this solver using a control volume based finite volume method. In addition, the perfect gas equation is also included. The partial differential equations (with the boundary conditions) of the problem are converted into a set of non-linear algebraic equations by integrating them over each of the control volumes. The solution for the resulting algebraic equation set is obtained using suitable iterative solvers. Due to computational time and memory constraints, first-order turbulence models are used in the present work. Pressure based implicit solver is selected which solves the governing equations of continuity and momentum simultaneously. Governing equations for additional scalars (k and ε/ω) are solved sequentially. The coupled

set of governing equations is discretized in time for both steady and unsteady calculations. In the steady case, it is assumed that time marching proceeds until a steady-state solution is reached. Once the continuous phase equations are solved, the discrete phase injections are created and the coupled flow is solved.

4.5 Grid Generation Details

For any fluid flow simulation using numerical discretization techniques, the discretized volumes must be small enough to resolve the flow physics in detail and proper location of node points in the domain is needed. For this, the space where the flow is to be captured – the physical space – is divided into a large number of geometric elements called grid cells. This process is termed as grid generation. The grids normally consist in two dimensions of triangles or quadrilaterals, and in three dimensions of tetrahedral, hexahedral, prisms or pyramids [Blazek. J, 2001].

The generalised coordinate transformation produces a system of equations which can be applied to any regular and non-singular geometry or grid system. The advantage of this form is; since uniform unit spacing is used, the computational domain has a one to one correspondence with the positive integers and therefore regular unweighted difference formulas can be used in the numerical scheme. This produces a computer code which can be applied to a wide variety of problems without modification of the equations and numerical scheme. Physical boundary surfaces can be mapped on to coordinate surfaces, which makes application of boundary conditions easier [Pulliam.T.H, 1994].

There are wide varieties of methods for generating grid systems. Algebraic methods such as conformal mapping, quadratic functions or the control function approach has been widely employed. Numerical approach of using elliptic solvers is also widely used. The most important requirements placed on a grid generation tool are that, there must not be any holes between the grid cells but also the grid cells do not overlap. The grid cells should be smooth; there should be no abrupt

changes in the volume of the grid cells or in the stretching ratio and the elements should be as regular as possible.

4.6 Convergence Criteria

The convergence criterion for the iterative solution procedure of the present study is that the normalized overall residue value is less than or equal to 10^{-6} for x or z velocity, 10^{-5} for continuity and scalars in the turbulence equations. The second important norm considered for the convergence of the solution is that the mass imbalance should be less than or equal to 0.5% between the inlet and outlet boundaries. The first norm controls local convergence at cell level, while the second norm considers convergence of the overall solution in an integrated sense.

4.7 Validation Problem

Any software used for the analysis must be validated for its accuracy and reliability with the experimental results. The software used for this analysis is FLUENT (version 6.3.26). The experimental model for this validation study is selected from the most cited and reputed journal paper by N.R. Panchapakeshan and J.L. Lumley, 'Turbulence measurements in axisymmetric jets of air and helium. Part 1. Air Jet. Published in International Journal of Fluid Mechanics (1993), Vol, 246, pp. 197-223.

In this paper an axisymmetric jet of 6.1 mm diameter is studied for varying conditions. An axisymmetric jet of the same diameter is modelled in the software and the boundary conditions are applied to the best possible ways. In experimental investigations provisions were made to compensate for the entrainment effect on the jets, but in CFD modelling this provision was not available. The numerical simulation is carried out using $k-\epsilon$ (realizable) turbulence model. The jet is subjected to an initial velocity of 27 m/sec and the turbulent intensity at the orifice exit was of the order of 0.01% as given in the experimental studies.

The result of the numerical modelling is compared with the experimental results for axial mean velocity profile across the jet at $x/d = 60$ and is shown in figure 4.1.

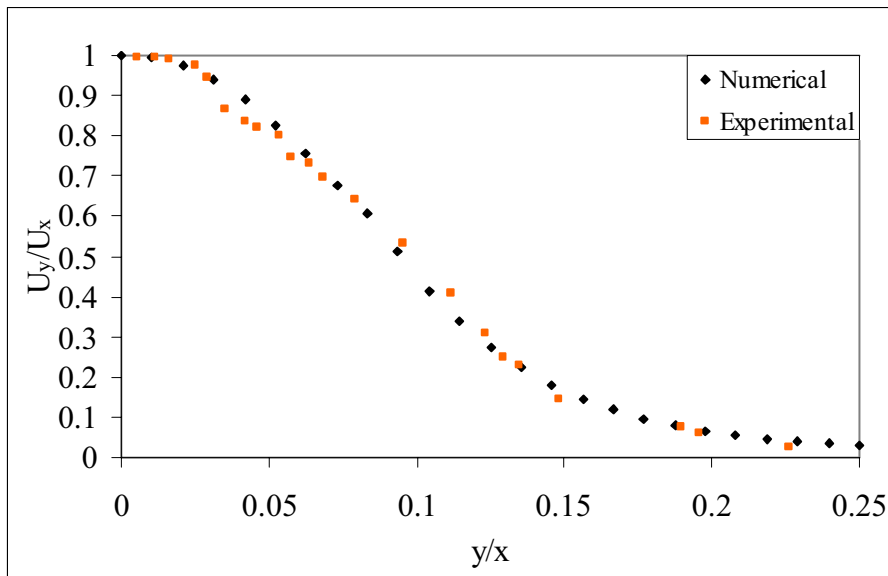


Fig 4.1 Validation of present work with experimental results.

From the above figure it is clear that the CFD modelling closely matches with the experimental results and the adopted modelling methodology and the turbulence model are valid and reliable for continuing the work.

4.8 Computer Systems Used

The numerical modelling of the present work involves modelling of axisymmetric jets to multiple plane jets and three dimensional jet array systems. In all these cases structured mapping mesh structure is employed. The mesh number varies from 35000 to 3500000. The models having mesh numbers less than 1500000 are solved in Fujitsu Siemens system having Intel Pentium dual core processor with 2 GB ram, 32 bit operating system. Models having higher meshes are solved in an HP Proliant Server ML 350 having Intel Zeon 5050 processor with 4GB FBD ram, 64 bit operating system.

4.9 Conclusion

The numerical simulation methodology employed in the present study has been discussed in detail. The essential theories of the numerical modelling are discussed briefly. The pre-processor and solver used in the present study are also explained. A detailed validation study of the software and the turbulence model is done. From the validation it is concluded that the results obtained in this study by using the selected turbulence model is only marginally different from the experimental data used for validation. CFD results are always being considered as preliminary approximation to a real problem and even this accuracy level is highly important and approved by the data centre industry.

.....✍.....

Contents	5.1	Introduction
	5.2	Modelling Methodology
	5.3	Grid Independency Study
	5.4	Results and Discussion
	5.5	Conclusion

5.1 Introduction

In this chapter axisymmetric jets of different configurations are modelled and analyzed with respect to their important flow characteristics such as half-width, centre line velocity decay etc. A detailed modelling methodology followed in the analysis such as the modelling domain, boundary conditions and the boundary values are discussed. A grid independency study is conducted for finding the best grid pattern that is to be followed in the present analysis. The result of the grid independency study is presented in this chapter. Different jet configurations based on different diameter and tile thickness combinations are analyzed with the best grid structure and the results are discussed. Based on the results the jet configuration for further study is selected.

5.2 Modelling Methodology

In the present study axisymmetric jets are designated by 'd by t', where d is the diameter of the jet and t the thickness of the tile. A 12 by 10 jet means the jet diameter is 12mm and the tile thickness is 10mm. The jet diameter and tile thickness are varied from 6mm to 14mm giving 25 models for investigation. The analysis domain consists of 100d in x direction (jet axial direction) and 15 d in y direction (jet spread). The domain for analysis is shown in Fig 5.1 along with the necessary boundary types used. The operating parameter for the flow is the

pressure difference across the tile and this value is assigned to the inlet boundary. The wall boundary condition as shown in Fig 5.1 is used to simulate the floor where no flow takes place across it. Outlet boundary condition is selected as pressure outlet with atmospheric pressure. The axis boundary condition is the unique characteristic of axisymmetric problems. The model selected for the analysis is the standard k- ϵ realizable turbulence model.

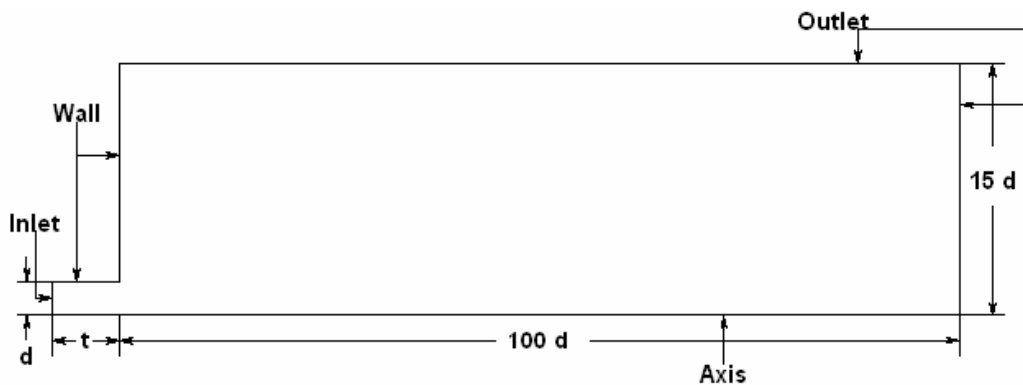


Fig 5.1 Solution domain and boundary types of axisymmetric jet

5.3 Grid Independency Study

To proceed with any CFD analysis the model should be studied for its independency with respect to the grids. This is called the grid independency study in CFD. In grid independency study the model is assigned with different meshing levels from coarse to fine and the results are studied for consistency. If the solutions show consistency with the assigned meshing patterns, it is concluded that the solution is independent of grid structure. Then the lowest gridding patterns can be selected for future analysis.

For grid independency study, Model 6 by 6 (orifice diameter = 6mm, tile thickness = 6mm.) is used and is modelled for different grid numbers of 64000, 46000, 35000, 25000 and 18000 (64K, 46K, 35K, 25K and 18K). The pressure difference across the tile is assigned a value of 37.376 Pa (0.15 inches of water column). The results of grid independency study is given in the figures 5.2 to 5.5

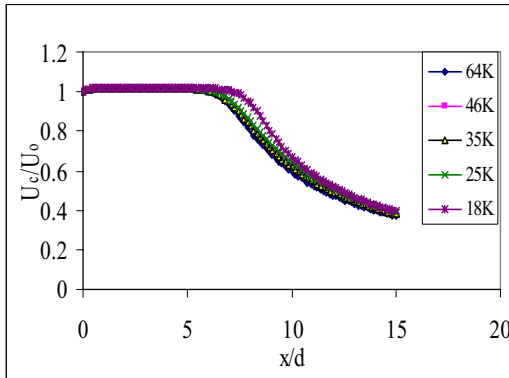


Fig 5.2 Development of near field velocity for different grid structures

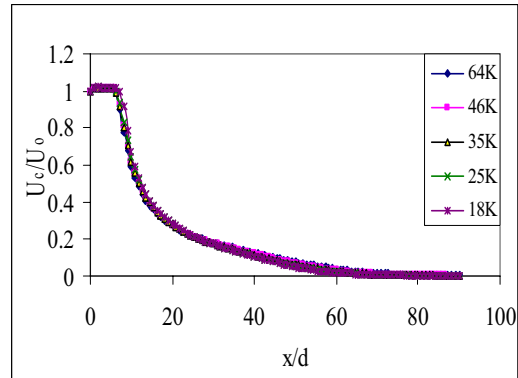


Fig 5.3 Centre line velocity decay for different grid structures

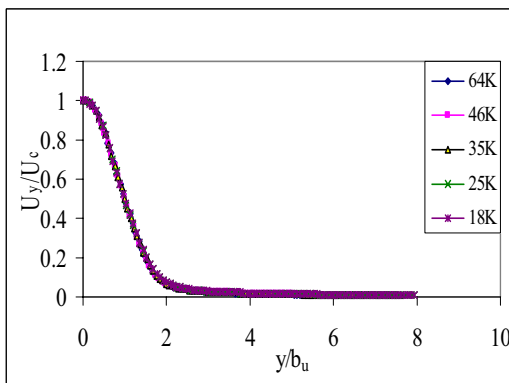


Fig 5.4 Jet velocity profile at 20d for different grid structures

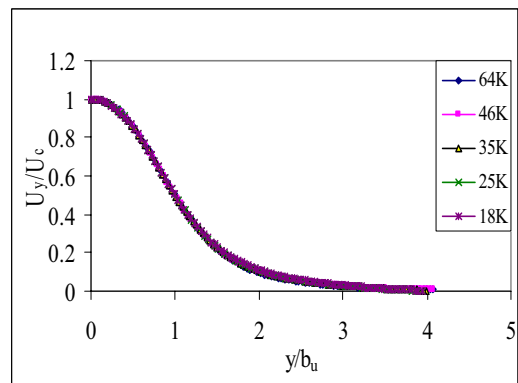


Fig 5.5 Jet velocity profile at 40d for different grid structures

From the above plots it is clear that the respective parameters coincide for all grid patterns except for the coarse mesh of 18K. The first four grid patterns show consistency and in this range of grid, the solution is grid independent. The grid pattern can be selected according to 25K, but in order to capture micro flows the grid structure is selected as 35K for further study.

5.4 Results and Discussion

Different jet geometries are modelled and analyzed. The models are classified into two groups and analyzed:

- 1) Jets with same diameter and varying tile thickness
- 2) Jets with same tile thickness and varying diameters

The parameters selected for analysis are, half width variation, development of near field velocity, centre line velocity decay and axial velocity variation at X_s .

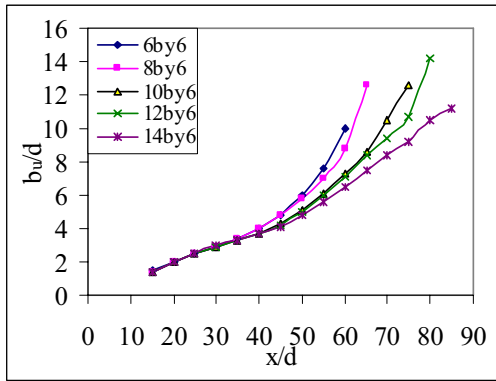


Fig 5.6 Half width variation for different jet models at $t = 6\text{mm}$

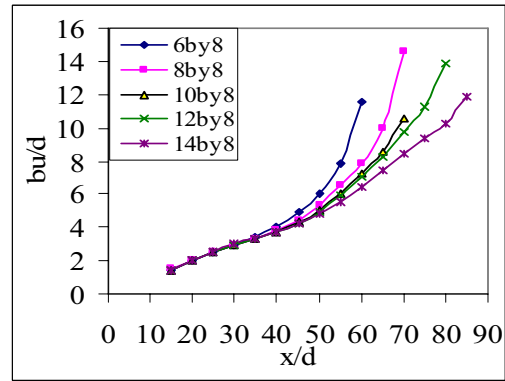


Fig 5.7 Half width variation for different jet models at $t = 8\text{mm}$

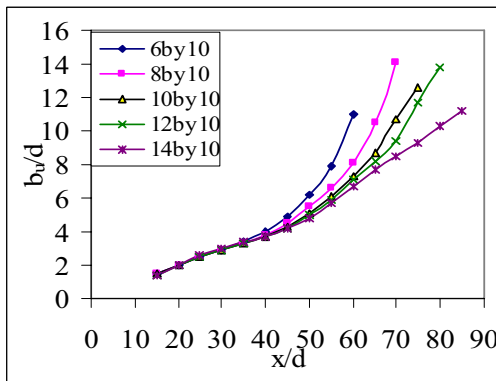


Fig 5.8 Half width variation for different jet models at $t = 10\text{mm}$

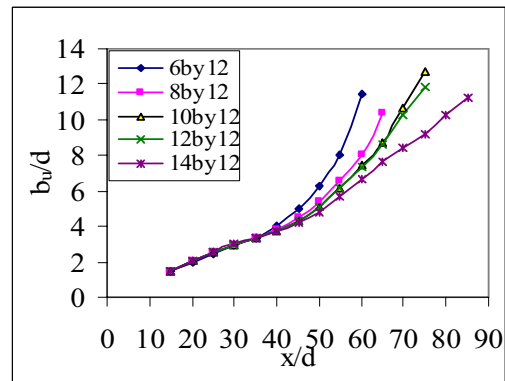


Fig 5.9 Half width variation for different jet models at $t = 12\text{mm}$

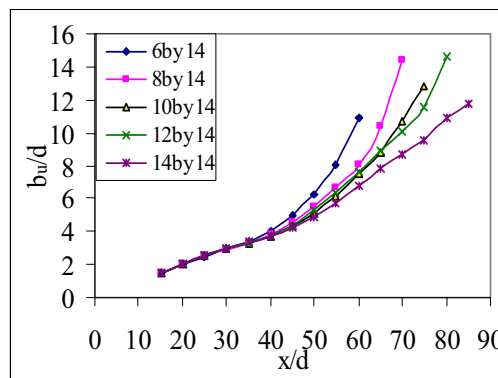


Fig 5.10 Half width variation for different jet models at $t = 14\text{mm}$

The important variable used for the selection of jet combination is taken as the half width variation, since it defines the spreading characteristics of the jet. The results plotted for jets with same tile thickness and varying diameters are given in figures 5.6 to 5.10 for half width variation.

From the above plots, it is clear that thicknesses of 6 mm and 8mm and orifice diameters of 6mm and 8mm are not suitable for use in data centre tiles since, smaller diameters will result in higher spread rates in the lateral (y) direction and their forward momentum may be less. The aim of this work is to establish a velocity distribution in the cold aisle from the tile to the top of the rack. Diameters 10mm and 12 mm exhibit similar characteristics; they have low spread and decay. An orifice with diameter 14mm performs better among all but it can be considered only for special case since its packing density is low (number of orifices/unit area). Tile thickness of 6mm and 8mm are not feasible from practical point of view as the tiles are load bearing and they should have sufficient thickness to bear the load even after perforating them with holes. Tile thickness 10mm and 12 mm are found to be suitable from the strength and flow characteristics point of view. Thickness 14mm does not provide any advantage but it will introduce more friction and hence lower velocities of the jet. Diameters 6mm and 8mm can be used in combination with other diameter jets to obtain different area ratio tiles. The figures 5.11 to 5.13 illustrate the various variables selected for analysis for tile thickness of 10mm.

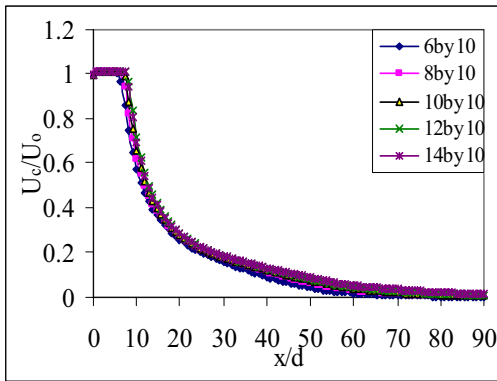


Fig 5.11 Centre line velocity decay for different jet models

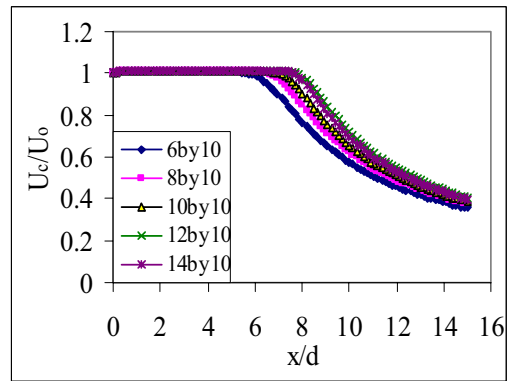


Fig 5.12 Near field velocity for different jet models

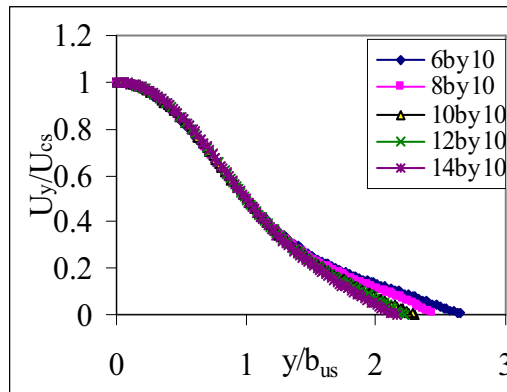


Fig 5.13 Y velocity at X_s for different jet models

The self similarity velocity profiles of jets with diameters 10mm, 12mm and 14mm are shown in the figures 5.14 to 5.16.

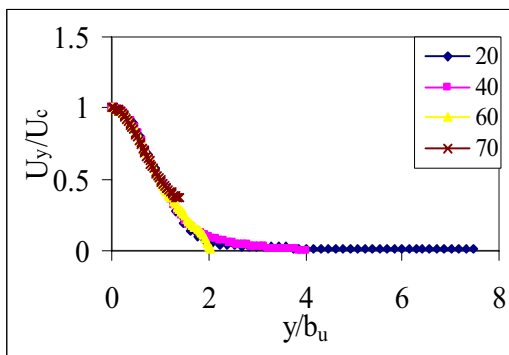


Fig 5.14 Self similarity of 10 by 10 jet at various x/d locations

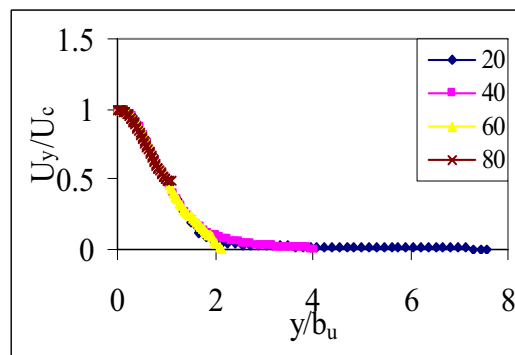


Fig 5.15 Self similarity of 12 by 10 jet at various x/d locations

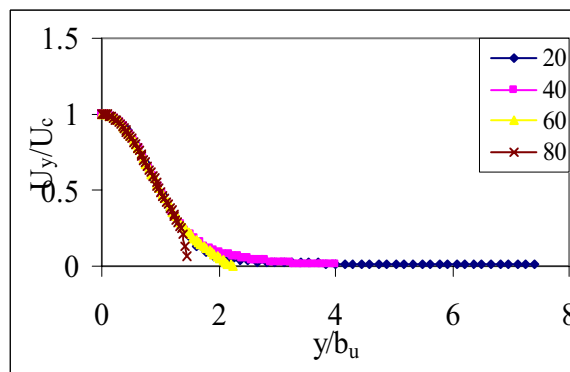


Fig 5.16 Self similarity of 14 by 10 jet at various x/d locations

The comparison of different physical parameters for different jet models is given in Table 5.1.

Table 5.1 Comparison of physical data of different axisymmetric jet models

COMPARISON OF PHYSICAL DATA OF MODELS							
MODEL	U_o	U_{max}	X_{max}/d	X_s/d	U_{cs}	b_{us}	$m \times 10^4$
6by6	7.67208	7.80448	1.25	49.47	0.38361	0.03504	2.487
6by8	7.69845	7.80228	1.212	48.69	0.38492	0.03451	2.447
6by10	7.69953	7.80274	1.33	48.112	0.38498	0.0339	2.4
6by12	7.71549	7.8025	1.25	47.67	0.38577	0.03356	2.364
6by14	7.7204	7.80145	1.417	47.45	0.38603	0.03345	2.324
8by6	7.70027	7.80395	1.313	51.29	0.38502	0.04879	4.527
8by8	7.67986	7.80229	1.375	53.86	0.384	0.04978	4.431
8by10	7.69182	7.80177	1.438	53.173	0.3846	0.04932	4.373
8by12	7.70258	7.80127	1.563	53.225	0.38512	0.04889	4.318
8by14	7.71223	7.80094	1.75	52.7	0.38562	0.04874	4.266
10by6	7.68134	7.80325	1.1	57.29	0.38406	0.06607	7.11
10by8	7.675	7.80136	1.4	57.322	0.38376	0.06596	7.007
10by10	7.68588	7.80097	1.5	56.88	0.38428	0.06514	6.934
10by12	7.69623	7.80067	1.6	56.361	0.38481	0.06472	6.864
10by14	7.70578	7.80047	2.25	55.96	0.38529	0.06417	6.798
12by6	7.69796	7.80592	1.042	58.67	0.3849	0.08191	10.346
12by8	7.70159	7.80541	1.042	58.56	0.38508	0.08068	10.246
12by10	7.70773	7.80484	1	58.56	0.38539	0.0809	10.15
12by12	7.69853	7.80057	1.792	56.72	0.38493	0.07907	10.017
12by14	7.70736	7.8004	1.875	55.73	0.38537	0.07879	9.937
14by6	7.70104	7.80527	1	62.697	0.38505	0.09918	14.153
14by8	7.67748	7.80032	1.57	62.997	0.38387	0.09873	13.95
14by10	7.68534	7.80024	1.57	61.34	0.38427	0.09743	13.847
14by12	7.69381	7.80004	1.61	61.65	0.38469	0.09727	13.747
14by14	7.70241	7.80001	1.75	60.35	0.38512	0.09589	13.653

X_s is the position where the jet axial velocity reduces to 5% of the jet exit velocity. The physical parameters of jets are designated as

U_o – Jet exit velocity in m/sec

U_{max} – Jet maximum velocity in m/sec

X_{max}/d – nondimensional position of maximum velocity

X_s/d – nondimensional position where the jets exit velocity reduces to 5%.

U_{cs} – Axial velocity at X_s in m/sec

b_{us} – Half width at X_s in m. (distance from the axis where the axial velocity is half)

m – mass flow rate in Kg/sec.

5.5 Conclusion

A preliminary study on axisymmetric jets is made and sufficient information is collected regarding the behaviour of different configuration of jets. A detailed grid independency study is conducted and the modelling methodology and information about the solution domain is also made. Based on the results, the jet configurations for the present research are identified. The tile thickness is fixed as 10 mm due to practical reasons and the diameters are selected as 10mm, 12mm and 14mm for primary tiles and 6mm and 8mm diameters for combination tiles along with the first set of diameters. From the self similarity velocity profiles of these jets, it can be seen that the jets are self similar beyond x/d values of 20. But in the far region (beyond $x/d = 80$) the lateral profiles deviate, the reason being the low velocity jets lose their momentum in the far region.

.....END.....

Contents	6.1 Introduction
	6.2 Single Jet
	6.3 Twin Jet
	6.4 Triple Jet
	6.5 Differential Triple Jet
	6.6 Results and Discussion
	6.7 Conclusion

6.1 Introduction

This chapter explains the modelling and analysis of plane jets like single jet, twin jets, triple jets and differential triple jets. The necessary designation methodology followed for assigning the jet combinations are explained in this chapter. Each type of jet is dealt separately regarding its modelling and solution domain details. A grid independency study is done for single plane jet and the best grid pattern is selected which is followed in other jets also. Multiple jet combinations are analyzed for its merging details. A detailed discussion of the results is presented in this chapter.

6.2 Single Jet

In this section three configurations of plane jets are studied to get better understanding about the jet characteristics. The plane jets are designated by 'd by t PJ'. The selected configurations are 10 by 10 PJ, 12 by 10 PJ and 14 by 10 PJ. A grid independency study is carried out to find the best grid structure for the analysis using the 10 by 10 PJ model. The model is given 7 different grid structures, 75000, 65000, 60000, 53000, 48000, 44000 and 37000

(75K,65K,60K,53K,48K,44K and 37K). The solution domain for analysis is shown in Fig 6.1 along with the necessary boundary types used. The pressure difference across the tile is assigned a value of 37.376 Pa (0.15 inches of water column).

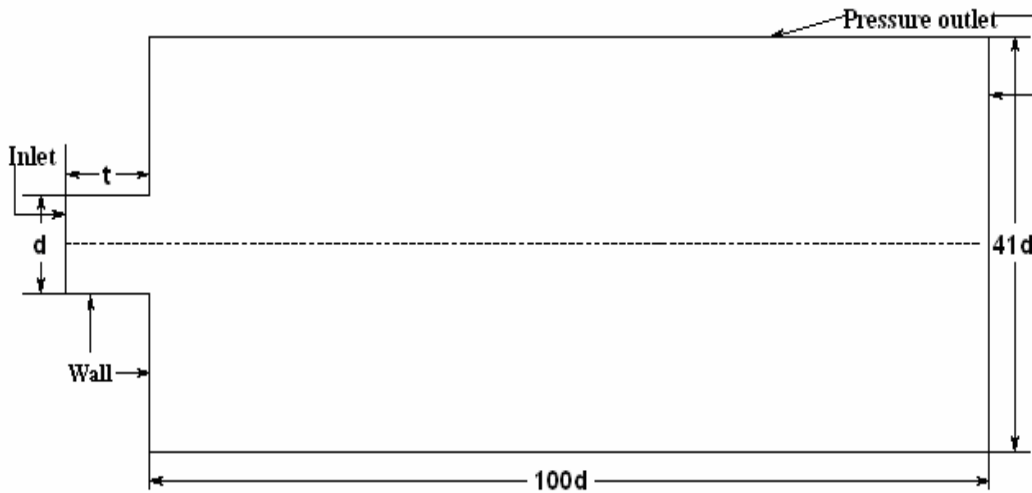


Fig 6.1 Solution domain and boundary types of plane jet

The results of the grid independency study are given in the figures 6.2 to 6.6.

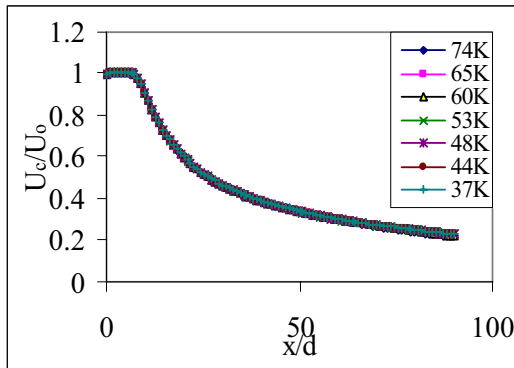


Fig 6.2 Centreline Velocity decay for various grid structures.

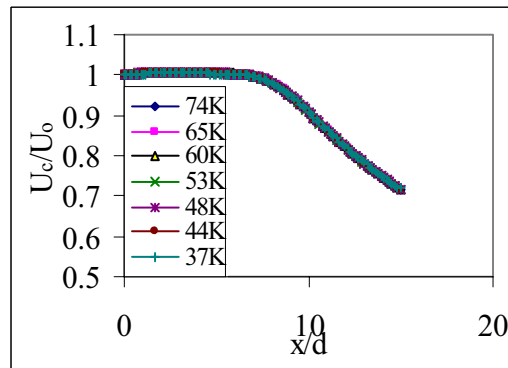


Fig 6.3 Near field velocity development for various grid structures.

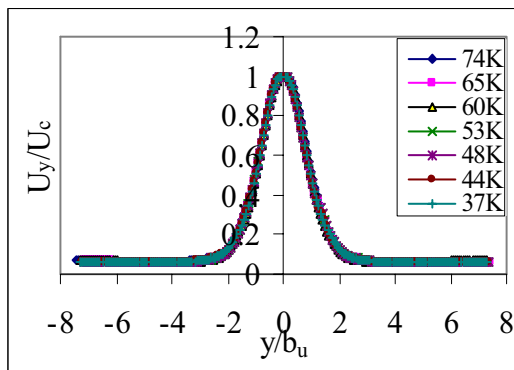


Fig 6.4 Velocity profile at 30d for various grid structures.

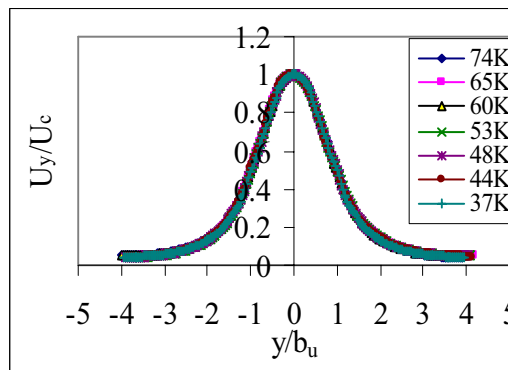


Fig 6.5 Velocity profile at 50d for various grid structures.

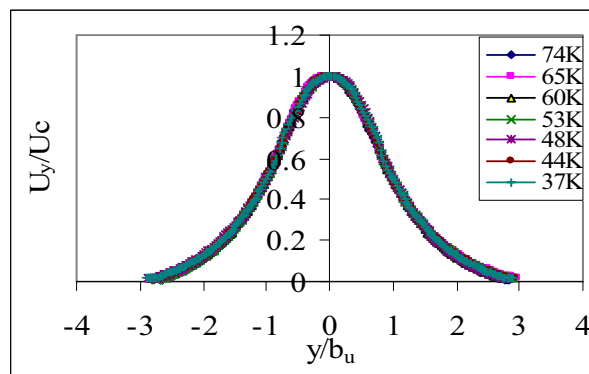


Fig 6.6 Velocity profile at 70d for various grid structures.

The grid independency study reveals that the solution is independent of grid pattern; hence the grid pattern corresponding to 37K model is selected for further analysis.

6.3 Twin Jet

Twin jets are developed using the basic single jet configurations analyzed in the previous section. The distance between the two single jets is designated as pitch (P). The pitch values selected for analysis are 4mm and 6mm. All the twin jet combinations are analyzed for two sets of pressure differences. The selected pressure differences are 37.376 Pa and 18.688 Pa. The twin jets are designated by the following method, 'd by t PxTJ(y)'. Where d- the diameter of jet, t- the thickness of tile, P- pitch, x- pitch value, TJ-twin jet and y- pressure difference across the tile (1 or 2). 1 refers to 37.376 Pa and 2 refer to 18.688 Pa. In this method 12 twin jet models are developed and analyzed. The solution domain and the boundary types are presented in Fig 6.7.

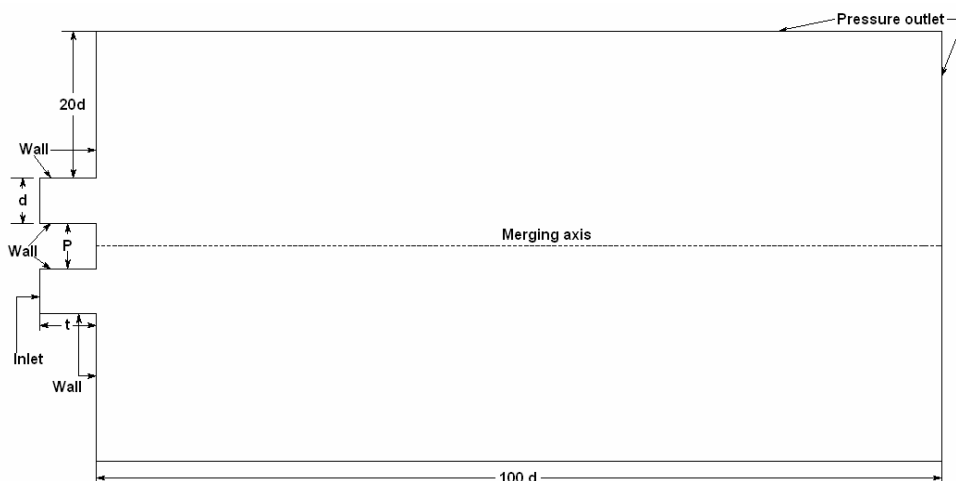


Fig 6.7 Solution domain and boundary types of twin jet

6.4 Triple Jet

Triple jets are developed by using the basis of single jet configuration; the jets are designated by 'd by t PxTrJ'. Triple jets are analyzed for only one pressure difference (37.376 Pa). The pitch values are taken as 4mm and 6mm. This will give six triple jet configurations for analysis. The solution domain and the boundary types are presented in Fig 6.8.

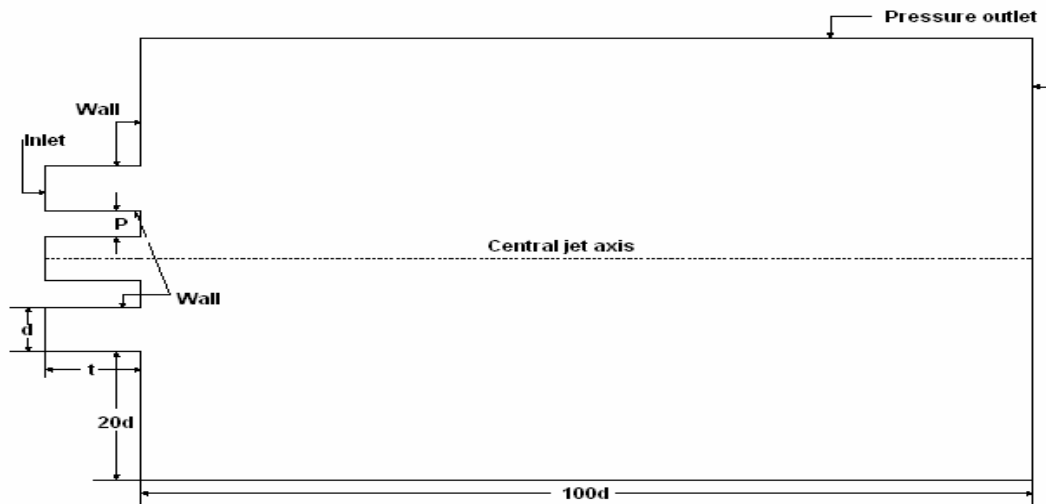


Fig 6.8 Solution domain and boundary types of triple jet

6.5 Differential Triple Jet

Differential triple jets are developed to study the interaction of jets of different diameters when they are placed in the same plane. This study will give an insight to the relative influence of a jet on other jets of different diameters. In differential triple jets, two jets will have the same diameter to form the top and bottom jet and another jet of a different diameter will form the central jet. The differential triple jets are represented as '2 by d_1 by $t+d_2$ by t PxDTTrJ'. In this combination, the jet having diameter d_2 forms the central jet and the other two jets of diameter d_1 form the top and bottom jets. All the three jets have same thickness of 10mm and all are placed at a pitch of 4mm or 6mm. The differential triple jets are analyzed for a single pressure difference of 37.376 Pa. The solution domain of the triple jet configuration is based on the bigger jet diameter. The other details of the solution domain and boundary types are the same as that of triple jet configuration as given in Fig 6.8

6.6 Results And Discussion

The results of all the above jet models are summarized in the following sections and a detailed discussion is also made.

6.6.1 Single Jet

Three plane jets under consideration are modelled and analyzed using the 37K grid pattern. The half width variation, centreline velocity decay, development of near field velocity, the velocity profile comparisons and the self similarity plots are given in figures 6.9 to 6.22.

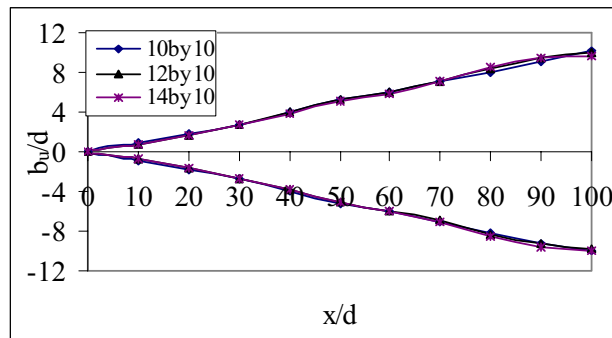


Fig 6.9 Comparison of half width variation of different jet models

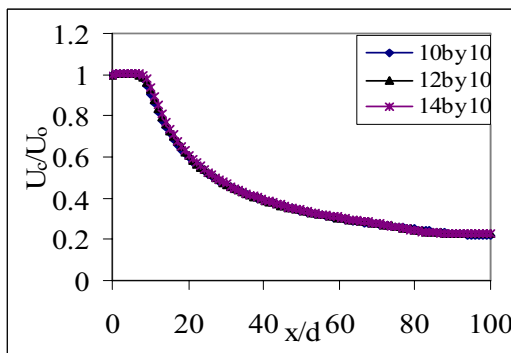


Fig 6.10 Comparison of velocity decay of different jet models.

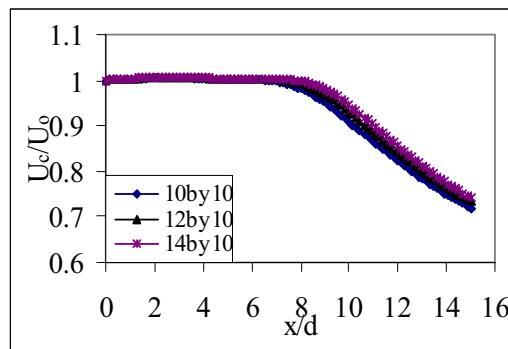


Fig 6.11 Comparison of near field velocity of different jet models.

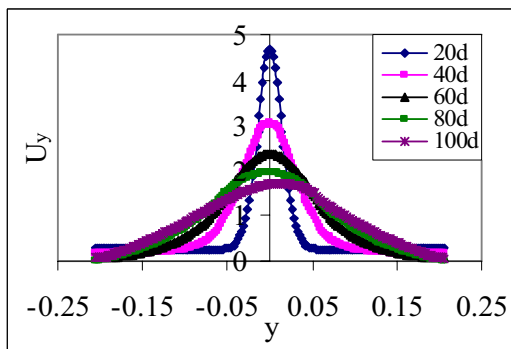


Fig 6.12 Velocity profiles of 10 by 10 jet at different locations.

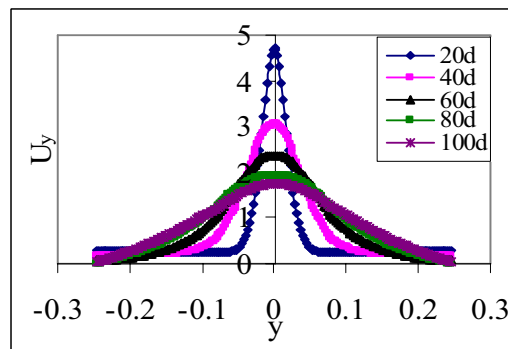


Fig 6.13 Velocity profiles of 12 by 10 jet at different locations.

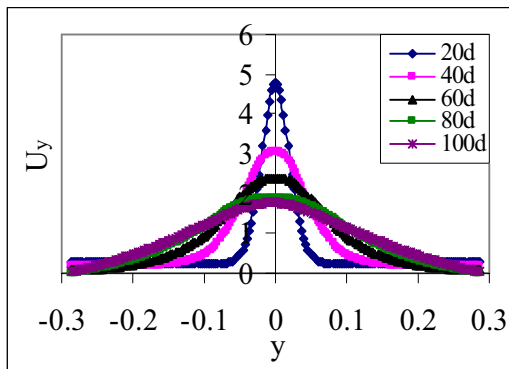


Fig 6.14 Velocity profiles of 14 by 10 jet at different locations.

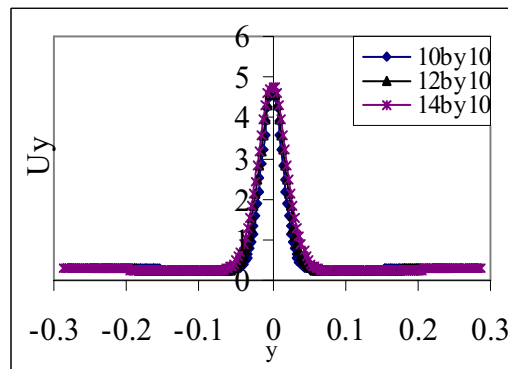


Fig 6.15 Comparison of velocity profiles of different jet models at 20d.

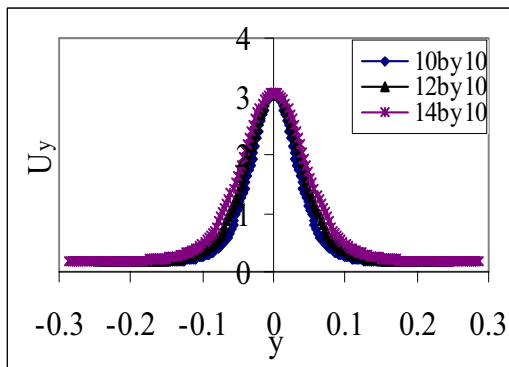


Fig 6.16 Comparison of velocity profiles of different jet models at 40d.

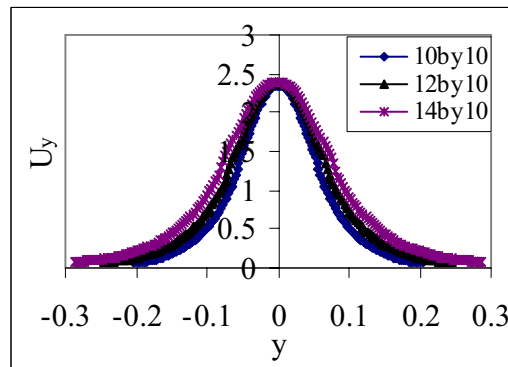


Fig 6.17 Comparison of velocity profiles of different jet models at 60d.

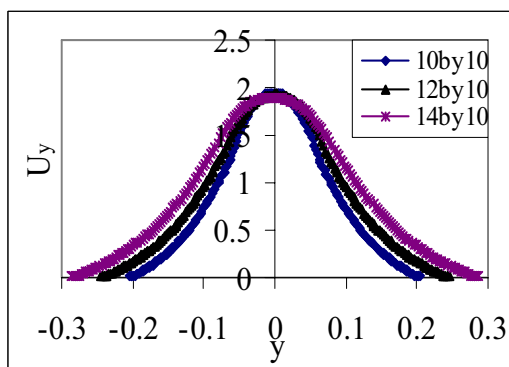


Fig 6.18 Comparison of velocity profiles of different jet models at 80d.

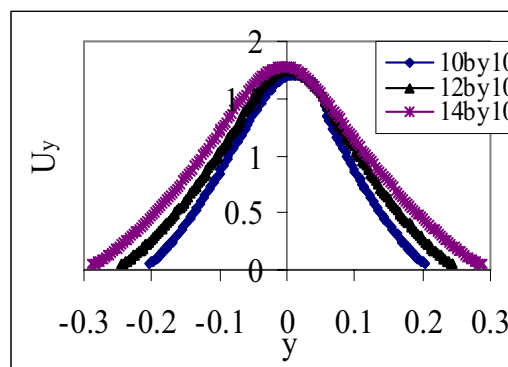


Fig 6.19 Comparison of velocity profiles of different jet models at 100d.

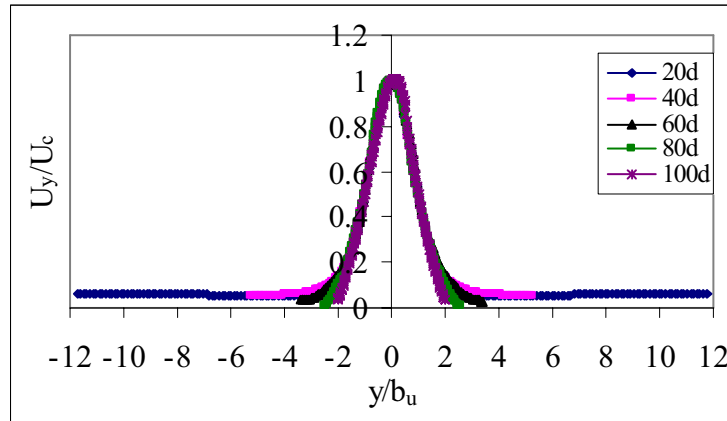


Fig 6.20 Self similarity velocity profiles of 10 by 10PJ at different locations.

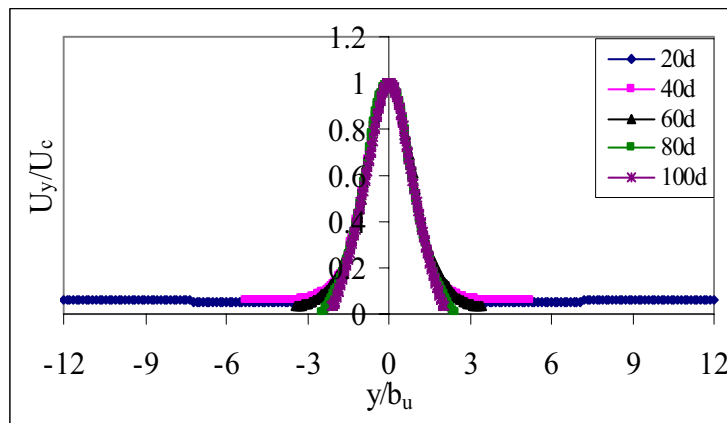


Fig 6.21 Self similarity velocity profiles of 12 by 10PJ at different locations.

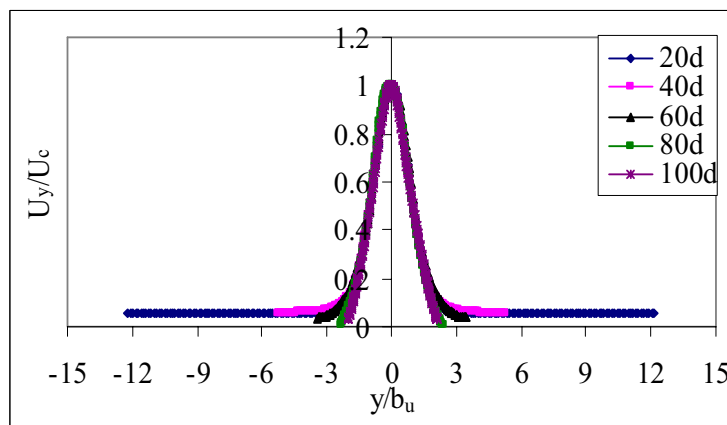


Fig 6.22 Self similarity velocity profiles of 14 by 10PJ at different locations.

The different velocity values of plane jets are summarized in Table 6.1

Table 6.1 Comparison of velocities of single plane jets

Model	U_0	U_{\max}	x	x/d	U_0 -Jet exit velocity m/sec
10 by10 PJ	7.7659	7.802	0.024	2.4	U_{\max} -Jet maximum velocity m/s
12 by10 PJ	7.7662	7.8033	0.026	2.17	
14 by10 PJ	7.7663	7.8035	0.03	2.14	x- position of maximum velocity m

From the half width variation plot of the jets, it can be seen that the three jets exhibit similar characteristics with respect to spread rates. The velocity decay and the near field velocity development are also similar for the three jets. The velocity profiles at different x/d positions show that as the diameter of the jet increases the spread increases in the y direction for x/d values beyond 40. This may be due to the increased mass flow and momentum occurring at higher jet diameters. The increase in mass flow and momentum will lead to higher entrainment of the surrounding air. This behaviour results in an extended velocity profile in y direction. From Table 6.1 it can be seen that the three jets have equal exit and maximum velocities for the same pressure difference. The location of maximum velocity increases slightly as the diameter increases. As the jet diameter increases, the strength of the jet is more and the decay is less. But this effect is not much significant to make a notable change in the velocity profile. From the self similarity figures of the jet it can be seen that the jets are self similar beyond x/d values of 20.

6.6.2 Twin Jet

The merging characteristics of different twin jet configurations are summarized in the Table 6.2.

Table 6.2 Comparison of twin jet velocities.

Jet Model	U_o	U_m	U_{av}	$(x/d)_m$	where
10by10P4TJ(1)	8.06051	6.78904	4.097584	17.9179	U_o - Exit velocity of jet m/s
10by10P4TJ(2)	5.69736	4.78064	2.790963	17.2172	
10by10P6TJ(1)	8.1343	6.58692	4.048058	18.6186	U_m - Merging velocity of jet m/s
10by10P6TJ(2)	5.74997	4.63317	2.752152	17.9179	
					U_{av} - Average velocity of jet after merging m/s
12by10P4TJ(1)	8.03217	6.87227	4.112664	18.5185	$(x/d)_m$ - merging position
12by10P4TJ(2)	5.67718	4.84105	2.80458	18.1181	
12by10P6TJ(1)	8.11322	6.69454	4.078335	19.1191	(1) ΔP = 37.376 Pa
12by10P6TJ(2)	5.73484	4.71182	2.776728	18.5185	
					(2) ΔP = 18.688 Pa
14by10P4TJ(1)	8.00783	6.93515	4.113829	19.019	
14by10P4TJ(2)	5.66003	4.88669	2.813632	18.7187	
14by10P6TJ(1)	8.09216	6.77494	4.089483	19.5195	
14by10P6TJ(2)	5.71971	4.7709	2.796598	19.019	

It can be seen that all the twin jet combinations show an increase in the jet exit velocity with respect to the corresponding plane jet values. This increase in velocity is due to the creation of an additional pressure drop resulting from the mutual entrainment of the jet. The rate of increase in velocity in all the configurations is the same. As the pitch increases the exit velocity shows an increase. This is due to the fact that as pitch increases, the merging point shifts to the downstream. This is clear from the $(x/d)_m$ values, which will provide an increase in the entrainment area below the merging point in between the jets. Since

the two jets are identical, their merging axis will be at the mid way as shown in Fig 6.7. The merging point is located as the maximum velocity point on the merging axis. The merging velocity shows a decrease as the pitch increases. This is natural as they merge at a point further downstream in x direction where the individual velocities are lower. The average velocities beyond the merging point also shows a decreasing trend as pitch increases. This is also due to the reason that the merging velocities decrease as the pitch increases. The downstream velocities are still lower and the average velocity is also low. This shows that the pitch cannot be increased beyond 6mm with respect to the steady average velocity after merging as this average velocity plays an important role in data centre air flow through perforated tiles.

As the pressure difference across the tiles decreases (in the analysis it is reduced to half) all the parameters under consideration tend to decrease. The trend is identical and it is concluded that as the pressure difference across the tiles decreases the jet characteristics decline steadily. The figures 6.23 and 6.24 illustrate the comparison of jet velocities beyond the merging point and the velocity profiles at merging point of different twin jet combinations respectively.

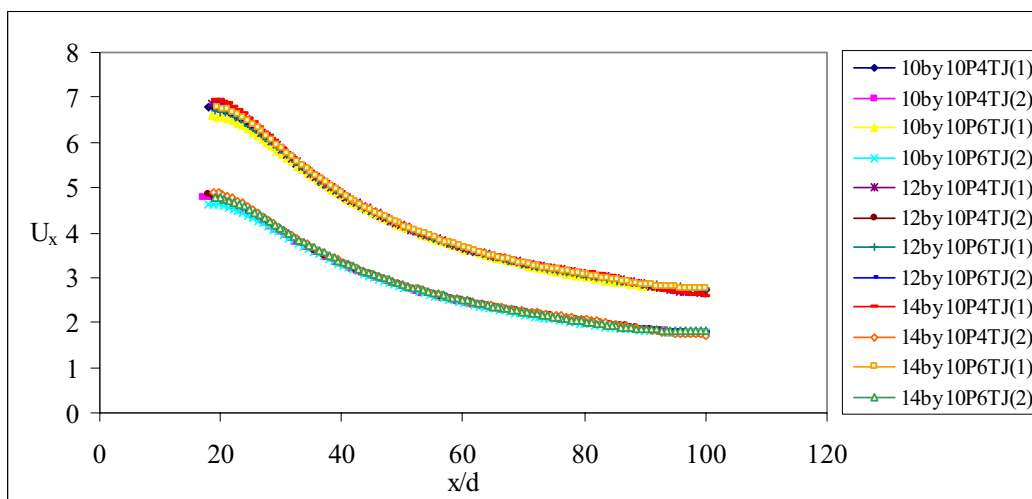


Fig 6.23 Comparison of velocity beyond merging point for different twin jet models.

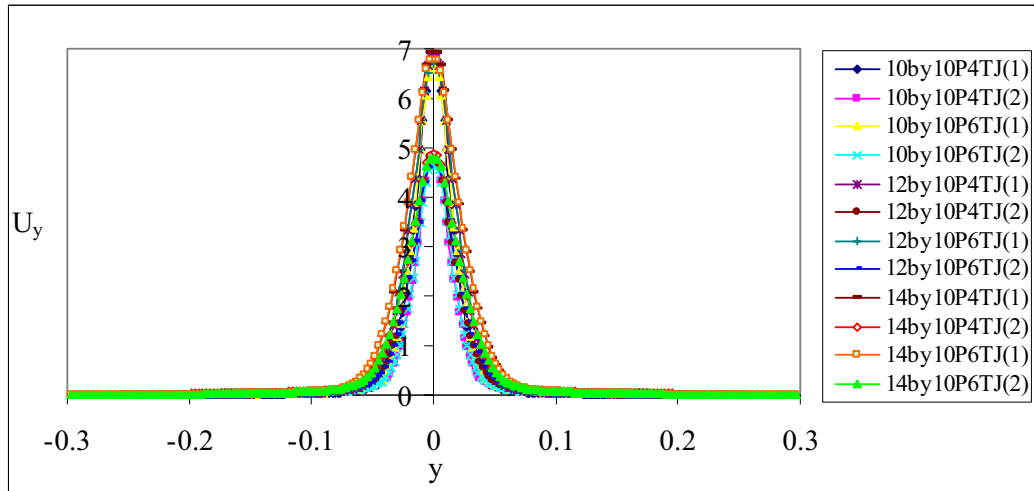


Fig 6.24 Comparison of y velocity at merging point for different twin jet models.

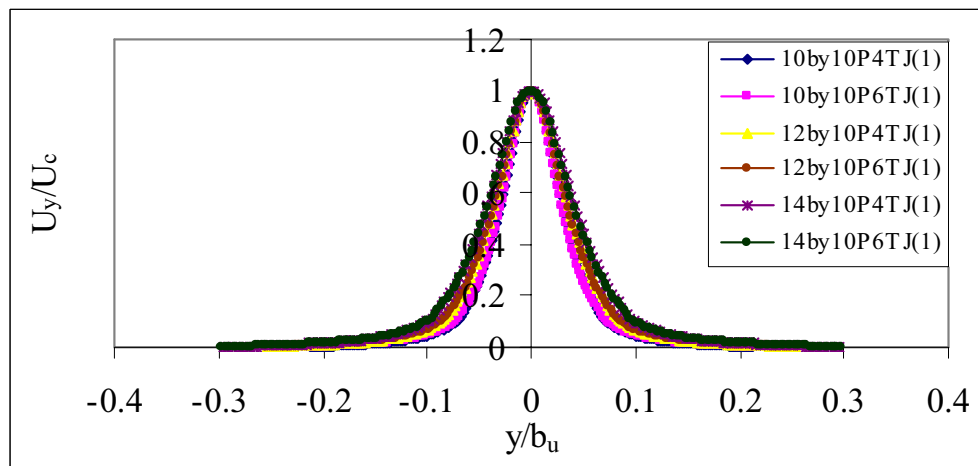


Fig 6.25 Comparison of velocity profile at $(x/d) = 40$ for different twin jet models.

The Figure 6.25 shows a comparison of velocity profile at $(x/d) = 40$, which shows that the velocity profiles differ as the jet diameter changes; but the velocity profiles are similar for a jet with same diameter but different pitches. This shows that after merging, the velocity profile is independent of the pitch.

The figure 6.26 illustrates the half width variation of different twin jet configurations for pressure difference of 37.376 Pa.

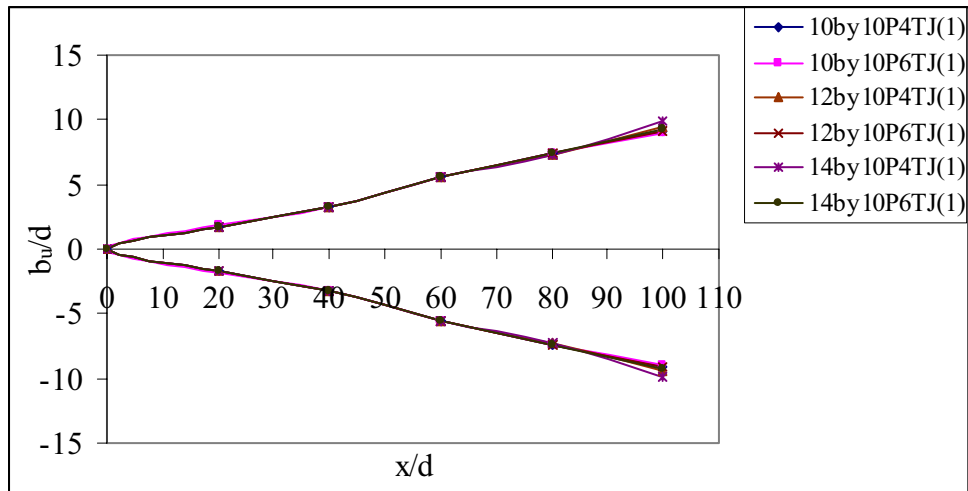


Fig 6.26 Comparison of half width of various twin jet models for pressure difference 37.376 Pa.

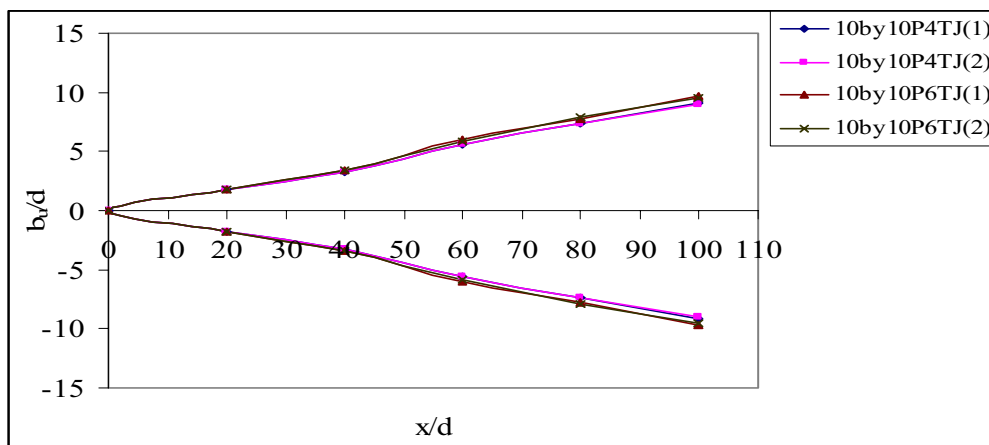


Fig 6.27 Comparison of half width of twin jet models for varying pressure difference

From the figure 6.27, it can be observed that the half width variation of the twin jet combinations for a particular pressure difference is similar after the merging point. All twin jet models merge before $(x/d) = 20$, from (x/d) values 20 to 40 the jet spread shows a linear variation and beyond $(x/d) = 40$ it shows a non-linear variation. Up to $(x/d) = 40$ the merged jet stabilizes and after that the jet spreads in the y direction as a single jet. When the pressure difference across the tile reduces the half width variation follows the same trend but the half width variation slightly changes as the pitch changes for same diameter jets. These results

are highly encouraging as the velocity profile after merging is independent of jet diameter and the pitch. This information enables the tile designer to design different area ratio tiles without affecting the air flow pattern within the data centre.

The figures 6.28 to 6.35 illustrate the self similarity of the merged twin jets for different (x/d) locations.

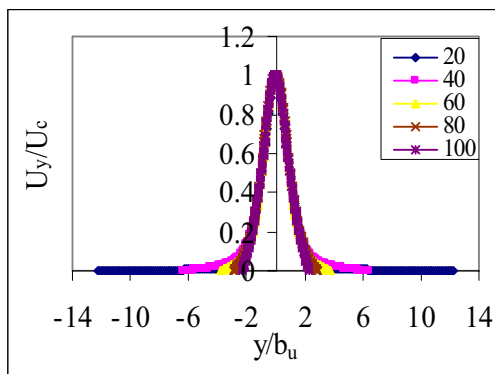


Fig 6.28 Self similarity of 10 by 10 P4TJ(1) at different locations

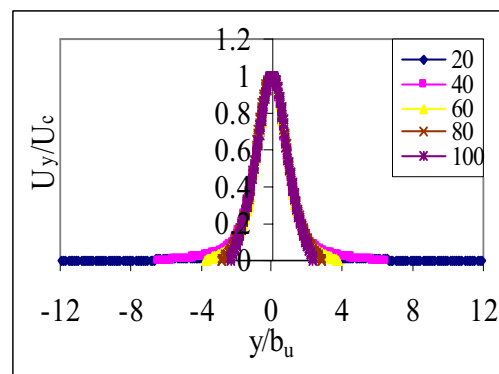


Fig 6.29 Self similarity of 10 by 10 P6TJ(1) at different locations

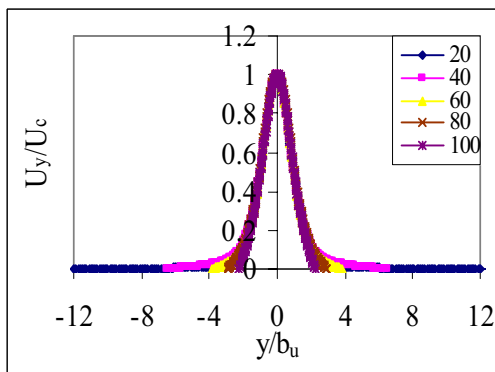


Fig 6.30 Self similarity of 12 by 10 P4TJ (1) at different locations.

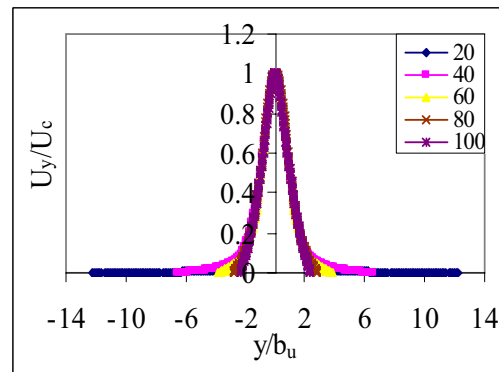


Fig 6.31 Self similarity of 12 by 10 P6TJ (1) at different locations.

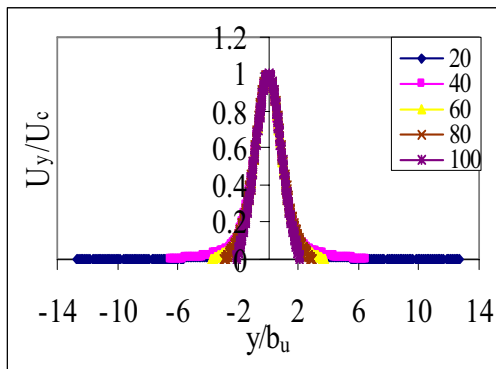


Fig 6.32 Self similarity of 14 by 10 P4TJ (1) at different locations.

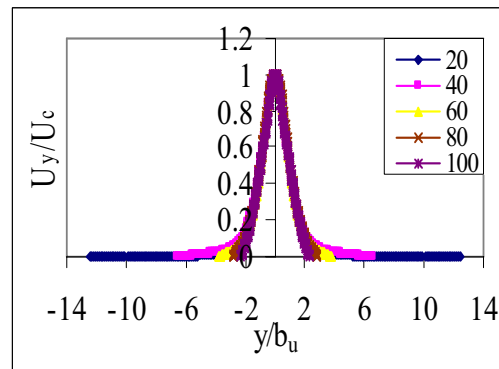


Fig 6.33 Self similarity of 14 by 10 P6TJ (1) at different locations.

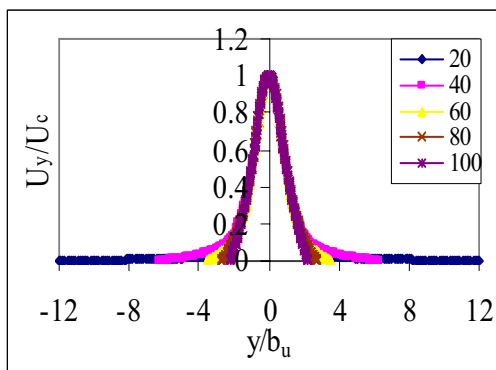


Fig 6.34 Self similarity of 10 by 10 P4TJ (2) at different locations.

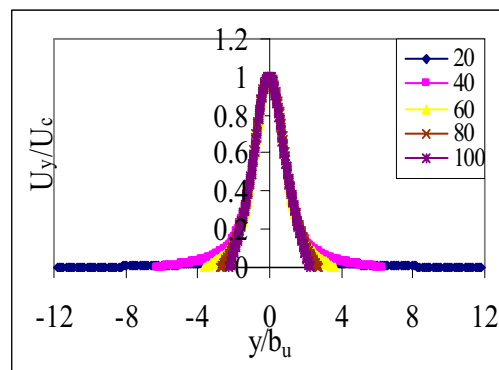


Fig 6.35 Self similarity of 10 by 10 P6TJ (2) at different locations.

From the above figures it is clear that the twin jets exhibit self similarity after they merge and shows the characteristics of a single jet thereafter. This is found to be true for all values of operating pressure differences across the jet.

6.6.3 Triple Jet

The merging characteristic of triple jet is totally different from that of twin jet. The twin jet exhibits a definite point of merging which can be located by the maximum velocity in the merging axis. In triple jet models there exist three axes of merging. The first axis is the merging axis of the top jet and the central jet and is drawn through the centre of the top jet and the central jet. The second axis is the merging axis of the bottom jet and the central jet and the third axis is the central jet axis itself. The merging process of the three jets is highly

complex as all the three jets will mutually entrain each other and merge. The top jet and the central jet will merge with each other, at the same time, the central jet and the bottom jet will merge at a symmetrical position. In the present analysis, it is assumed that the triple jet model is symmetric about the central jet axis so that the bottom merging axis need not be considered as it is similar to the top merging axis. The top merging axis velocity increases to a maximum value and then decreases. The maximum velocity point on the top merging axis is considered as the primary merging point of the top jet and the central jet. Corresponding to this it is possible to get a similar point on the bottom merging axis also. At this point of the triple jet model the velocity profile is expected to have a profile similar to that of a twin jet, as the top jet and central jet merges and bottom jet and central jet merges and both proceeds as independent jets downstream giving a twin jet profile. But the actual profile at the primary merging point is not distinctly as that of twin jet. This is because the lateral portion of the central jet merges with the respective jets over and below it, the core of the central jet is still moving with much higher velocities than the primary merging velocity.

In order to find the exact location where the three jets merge, the primary merging point velocity is located in the central jet velocity axis and this position along the central jet axis is considered as the complete merging point of the three jets. At this point the velocity profile shows similar characteristics as that of a single jet. The figure 6.36 shows the velocity profiles of all triple jet configurations at their respective complete merging point.

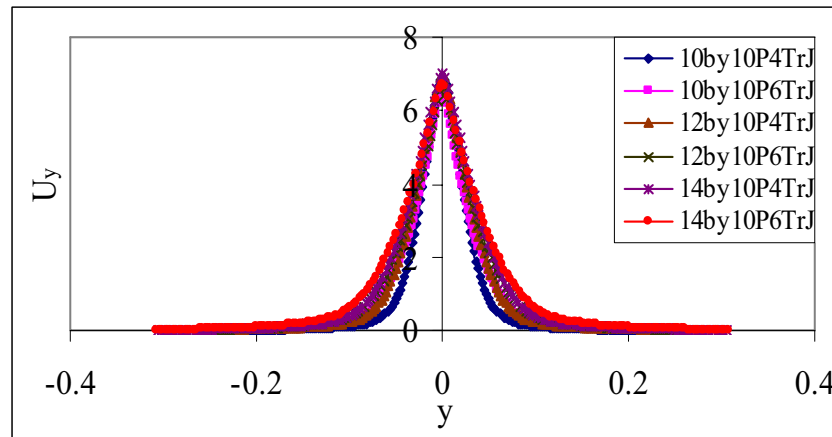


Fig 6.36 Comparison of velocity profiles of various triple jet models at merging point.

At the point of complete merging, it is observed that for all models of triple jets the central jet velocity decay shows an abrupt change in its slope. For a considerable distance upstream of this point, the velocity decay curve is flatter and immediately after this point the curve becomes steeper showing faster velocity decay. This behaviour of triple jet models is similar to that of a single jet whose velocity decay becomes faster beyond the potential core region. Hence the selection of the complete merging point can be justified since the velocity decay beyond this point is similar to that of single jet velocity decay. The figure 6.37 shows the complete merging point on the central jet axis where the slope changes.

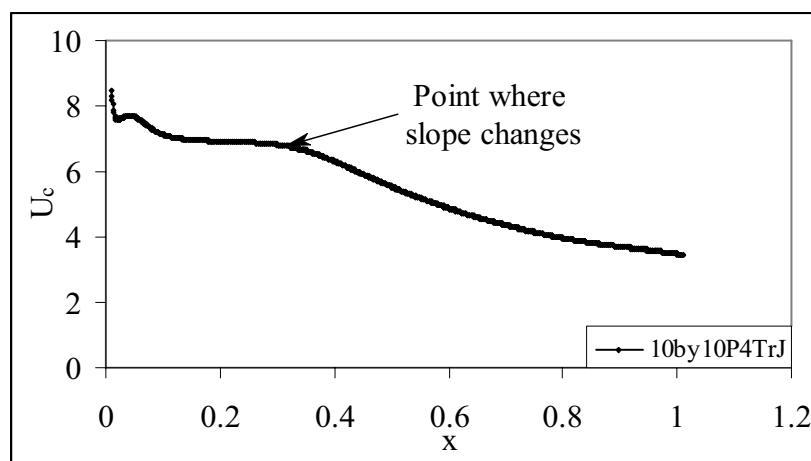


Fig 6.37 Position of complete merging point for a triple jet model.

The figure 6.38 shows the half width variation of triple jet and the comparison with twin jet.

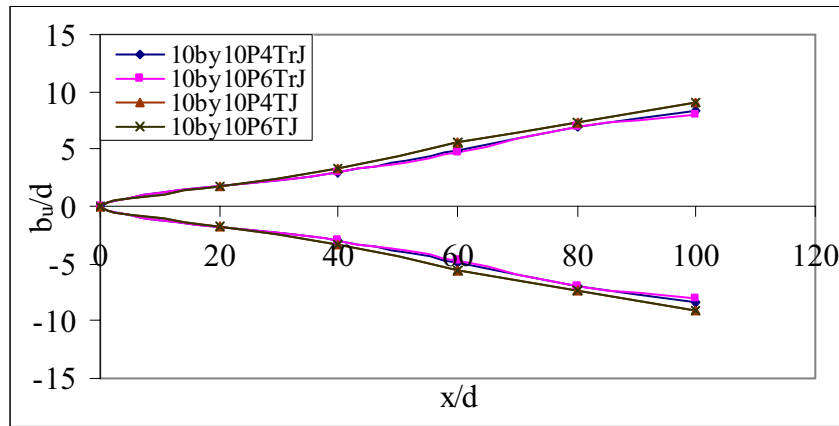


Fig 6.38 Comparison of half width of triple jets with twin jets.

From the figure, it is clear that the triple jet is having similar characteristics as that of a single jet beyond (x/d) values of 40. The half width variation of a triple jet is less than that of a twin jet of similar configuration. It can be inferred that the triple jets are stronger than twin jets. The self similarity plots of triple jet are shown in figures 6.39 and 6.40.

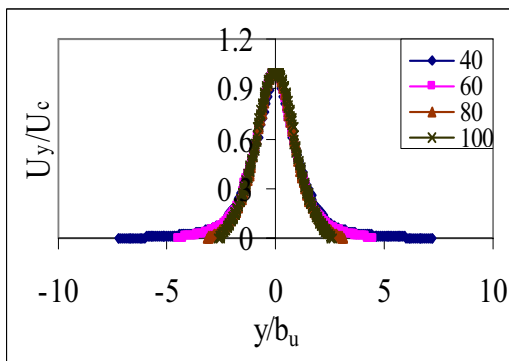


Fig 6.39 Self similarity of 10 by 10P4 TrJ at various locations.

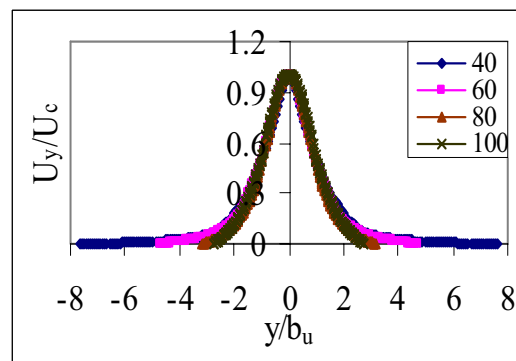


Fig 6.40 Self similarity of 10 by 10 P6TrJ at various locations.

The velocities of triple jet models are summarized in Table 6.3.

Table 6.3 Comparison of triple jet velocities.

Model	U_{oc}	U_{ot}	U_{mt}	x_{mt}/d	x_m/d	U_{av}
10by10P4TrJ	8.46908	8.10183	6.84578	14.2142	27.5775	4.86916
10by10P6TrJ	8.75502	8.20736	6.52901	18.018	39.8615	4.63883
12by10P4TrJ	8.38394	8.06397	6.94368	15.6156	31.3269	4.81689
12by10P6TrJ	8.68384	8.18478	6.64548	18.8188	39.6918	4.68078
14by10P4TrJ	8.31579	8.03317	7.00715	16.5165	33.3	4.78594
14by10P6TrJ	8.61663	8.16035	6.73097	19.3193	39.5344	4.70055

U_{oc} - Central jet exit velocity m/s

U_{ot} - Top jet exit velocity m/s

U_{mt} - Top merging axis velocity m/s

x_{mt}/d - Top merging point location

x_m/d - Complete merging position on central jet

U_{av} - Average velocity beyond complete merging point m/s

The twin jet geometries exhibit slightly decreasing trend for jet exit velocity as the jet diameter increases. As the pitch increases the jet exit velocity increases and decreases as jet diameter increases. The triple jets also follow the same trend in jet exit velocities as that of twin jets. The corresponding velocities in triple jet configurations are greater than that in twin jet configurations. The central jet shows much higher velocities when compared to the other jets. This is due to the fact that the neighbouring jets entrain the central jet from two sides thereby enabling the central jet to accelerate more. The central jet will also entrain the neighbouring jets but the side jets will be entrained by the central jet only on one side. From the other side stagnant air entrains in to the side jets there by their acceleration and hence the velocities will be less than that of the central jet.

The merging point velocities in triple jets are higher than that of twin jet models for pitch values of 4mm. But for 6mm pitch the merging point velocities for triple jet is less than the corresponding values of twin jet. This is due to the increased influence of the recirculation zone present between the triple jets compared to twin jets. As pitch

increases this zone builds up more and will influence the velocity decay thereby reducing the merging point velocity. But this effect is not much significant to create a large velocity decrease. The average velocities beyond complete merging are higher in the case of triple jets. The velocity decay of triple jets after complete merging is shown in the figure 6.41.

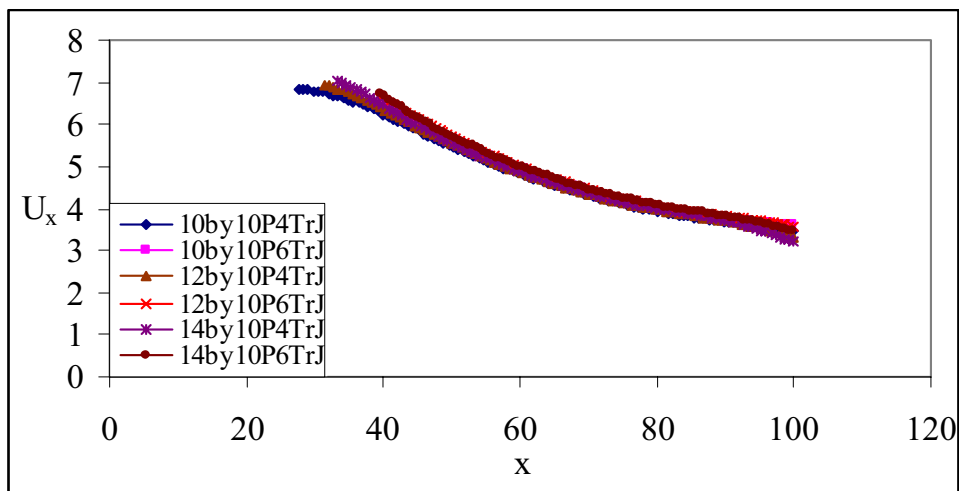


Fig 6.41 Comparison of velocity beyond merging point for various triple jet models..

6.6.4 Differential Triple Jet

The merging characteristics of differential triple jets are quiet similar to that of triple jet. The top merging velocity and the complete merging point are located in similar method for differential jets also. The different velocity values are given in Table 6.4.

Table 6.4 Comparison of differential triple jet Velocities.

Model	U_{oc}	U_{ot}	U_{mt}	x_{mt}	x_m	U_{av}
2by10by10+12by10P4DTrj	8.3769	8.0946	6.8621	0.15775	0.35961	4.5316
2by10by10+14by10P4DTrJ	8.3062	8.0898	6.8601	0.15515	0.40484	4.9056
2by12by10+8by10P4DTrJ	8.6567	8.1018	6.8121	0.23222	0.36817	4.4961
2by12by10+10by10P4DTrJ	8.4756	8.0698	6.9156	0.19258	0.26826	4.8919
2by10by10+12by10P6DTrJ	8.6613	8.2013	6.5361	0.19258	0.45395	4.4247
2by10by10+14by10P6DTrj	8.5781	8.1959	6.5308	0.19018	0.48623	4.8093
2by12by10+8by10P6DTrJ	8.8845	8.1988	6.6332	0.23222	0.36779	4.5042
2by12by10+10by10P6DTrJ	8.7789	8.1913	6.6441	0.23583	0.43921	4.5849

The differential triple jet model 2 by 10 by 10+12 by 10 P4DTrJ is developed by replacing the central jet of 10 by 10 P4TrJ by a 12 by 10 plane jet. The results from table 6.4 says that, the central jet exit velocity and top jet exit velocity of the differential triple jet is less than the corresponding value of the triple jet even though the third jet is a larger diameter jet. When the number of jets increases, the individual jet velocity will be higher than the corresponding plane single jet exit velocity. This is due to the additional momentum developed by mutual entrainment of the jets. When the central jet of a triple jet is replaced by a plane jet of higher diameter, a reduction in the individual jet velocity occurs and the additional momentum developed due to mutual merging is less than that in a similar triple jet. The bigger central jet, as it develops, will try to deflect the neighbouring jet outwards there by loose its momentum at the beginning and shows a reduced exit velocity. At the same time smaller jets experience a resistance towards their growth as the central jet deflects them outward and their exit velocities are also less. This trend will continue till the first merging location is reached. The top merging velocity of differential triple jet is higher than that in the triple jet. This is due to the fact that the differential triple jet merges little early where the velocities are higher. The average velocity after merging is still higher for triple jet configuration even though the top merging velocity is low. This is evident from the position of the complete merging point of differential triple jet. The complete merging of the differential triple jet takes place at a point further downstream compared with the triple jet.

When the central jet of a 12 by 10 P4TrJ is replaced by a 14 by 10 plane jet to develop 2 by 12 by 10+14 by 10 P4DTrJ, the results follow the same trend as before. Hence it can be generalized that when the central jet of a triple jet is replaced by a higher diameter jet, except the top merging velocity, all other important velocities decrease. The reduction in average velocity after merging is of big concern. Even though the merging takes place at a farther downstream location with respect to triple jet, the merging velocity is higher due to the dominance of the

higher momentum of the larger diameter jet. The reduction in the average velocity is due to the higher decay rates.

When the central jet of a 12 by 10 P4TrJ is replaced by a 8 by 10 plane jet to develop 2 by 12 by 10+8 by 10 P4DTrJ, the central jet exit velocity and the top jet exit velocity increases while the top merging velocity decreases. This behaviour is exactly opposite to that seen in the previous cases. The increase in the exit velocities of the jet can be explained as follows. Since the central jet is smaller, it cannot deflect the bigger outer jets; rather, the bigger jets entrain the smaller jet completely thereby increasing the potential for higher velocities. The differential triple jet and the triple jet merge at a similar position. The reduction in merging velocity indicates that the decay rates are larger for differential triple jets. The average velocity after complete merging shows a decreasing trend which needs further explanation. The central jet of 12 by 10 P4TrJ is replaced by a 10 by 10 plane jet to make another combination to investigate this interaction. All velocities except the average velocity follow the same trend after complete merging. The average velocity shows an increasing trend. In order to confirm the trend of average velocity another combination is tried by replacing the central jet of a 10 by 10 P4TrJ by an 8 by 10 plane jet. All the velocities are found to follow the same trend, but the average velocity shows a different trend. Hence it can be concluded that when the central jet of a triple jet is replaced by a smaller diameter jet, all velocities including the merging velocity increases, which is a desirable result for data centre tile flow. But the average velocity after complete merging is dependant on the relative diameters of the central and the main jets.

When the pitch of the models is increased the trends are exactly the same as that of the previous cases. A comparison of the differential triple jets with respect to different pitch values was made. Even though the individual jet velocities increase due to the presence of increased reversed flow region between the jets, the merging velocity and the average velocities decrease considerably. From the results, it is clear that whether it is a triple jet combination or differential triple jet

combination, the performance of the model is better with respect to merging characteristics when the pitch is lower. This trend is evident from the Table 6.4. The complete merging point located in the triple jet models indicated a sudden change in slope in the central jet velocity decay curve as shown in figure 6.37. In differential triple jets also, it is possible to have the same trend, which is shown in the figure 6.42.

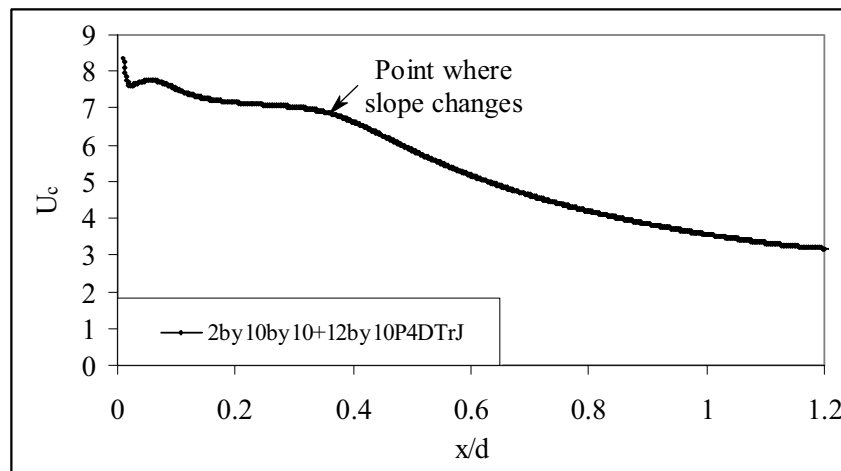


Fig 6.42 Position of complete merging point of a differential triple jet model.

The figure 6.43 shows the half width variation of a differential triple jet and the comparison with a triple jet. It can be seen that the differential triple jets are having lesser spread rate than that of a triple jet combination

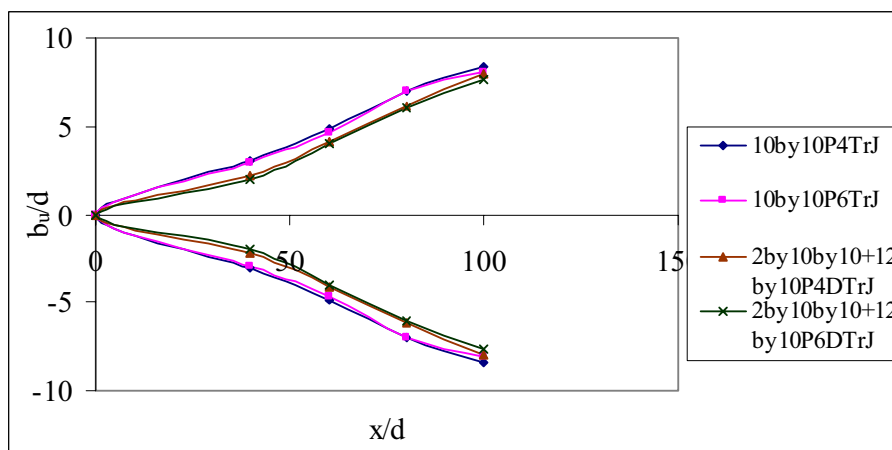


Fig 6.43 Comparison of half width of a differential triple jet and triple jet models.

The self similarity plots of the differential triple jet are shown in figures 6.44 and 6.45.

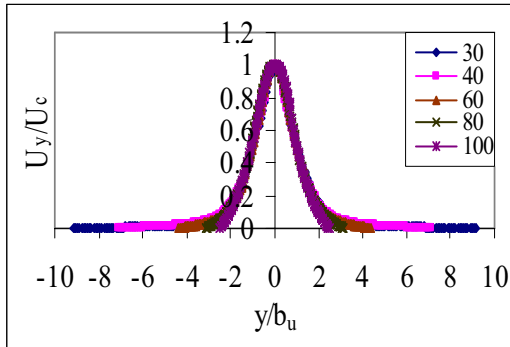


Fig 6.44 Self similarity of 2by10by10+12by 10P4DTrJ at different locations.

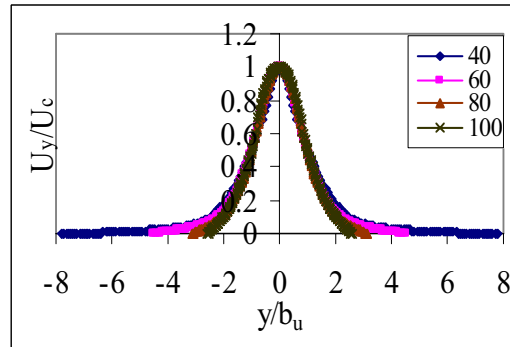


Fig 6.45 Self similarity of 2by10by10+12by 10P6DTrJ at different locations.

The figure 6.46 shows the velocity profiles of all differential triple jet configurations at their respective complete merging point.

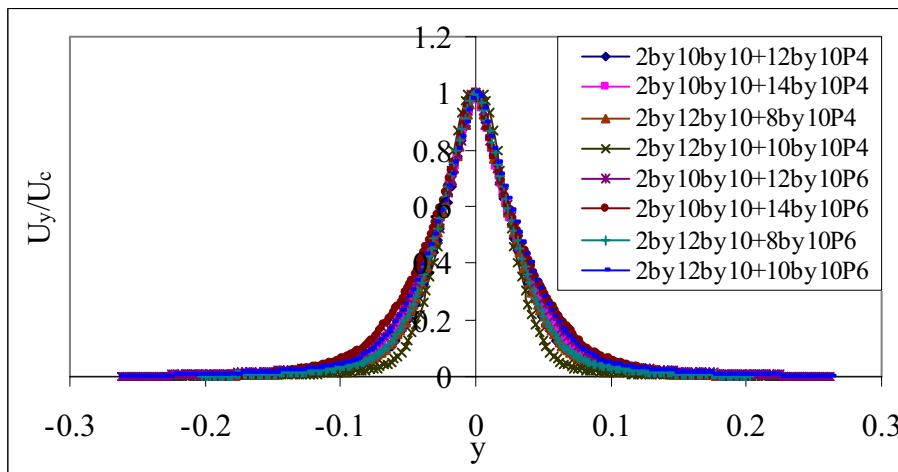


Fig 6.46 Comparison of velocity profiles of differential triple jet models at merging point.

The velocity decay of triple jets after complete merging is shown in the figure 6.47

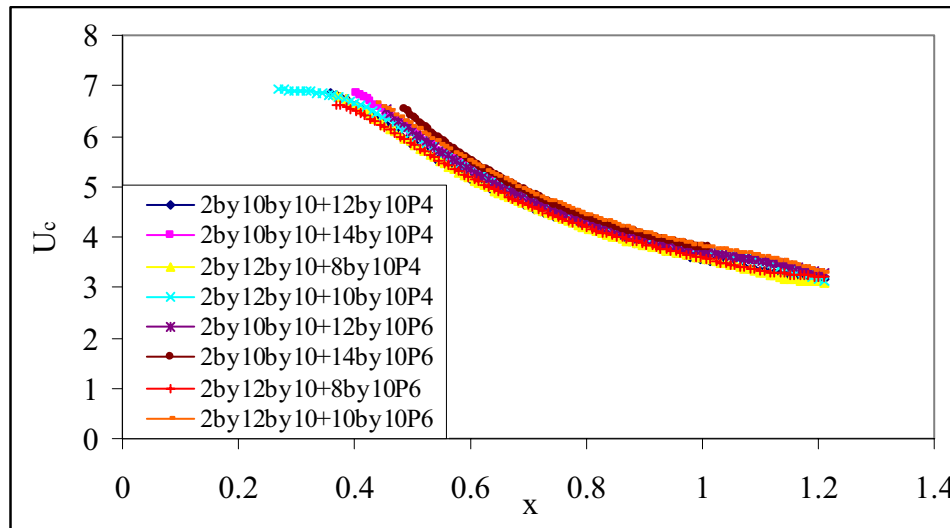


Fig 6.47 Comparison of velocity beyond merging point of differential triple jet models.

6.7 Conclusion

In this chapter a detailed study of different plane jet and multiple jet configurations are carried out. The grid independency study conducted on plane jet confirmed that the solution is independent of grid structure. The self similarity condition of plane jet and different multiple jet models are studied. The multiple jet models are found to be self similar beyond the complete merging point. The relative advantage and disadvantages of triple jets and differential triple jets are analyzed in detail. The mass flow rates of plane jets are used only for a qualitative analysis. The plane jets, which are 2D in nature, will assume unit thickness in the third dimension and hence the flow rates will be higher. The velocities also follow these higher values. Therefore, for the purpose of comparison with 3D data, the trend of the results of the 2D jets is used. The results obtained for plane jets are found to be highly significant for further study and design of multiple array of similar jets and combination of dissimilar jets.

.....✍.....

Contents	7.1 Introduction
	7.2 Single Jet
	7.3 Twin Jet
	7.4 Triple Jet
	7.5 Differential Triple Jet
	7.6 Four Jet Module
	7.7 Five Jet Module
	7.8 Results and Discussion
	7.9 Conclusion

7.1 Introduction

In this chapter, the detailed study of the three dimensional jets are made for getting the real behaviour of the jets for different jet configurations. Single jets of 4 basic configurations are modelled and analyzed for their velocity and mass flow characteristics. Suitable mass flow correction factors are introduced for use in further analysis. Twin jets, triple jets and differential triple jets of different configurations are modelled and analyzed to get their merging characteristics. 4 jet modules which form the basis of ordinary design tiles and 5 jet modules for combination tiles are modelled and analyzed. The results of all these analysis are explained in detailed in the respective sections.

7.2 Single Jet

Three dimensional single jets are designated by 3d d by t, where d and t stand for the diameter and the thickness respectively. Four basic single jet models are modelled for analysis as 3d 8 by 10, 3d 10 by 10, 3d 12 by 10 and 3d 14 by

10. While developing the 3d models of circular jets, it is observed that the mass flow rate through the orifice as predicted by the analysis changes, as the meshing pattern changes within the circular orifice. It is not a problem connected with grid independency as other variables do not change their values. The changes in the mass flow rates as predicted by the analysis for different mesh structures within the circular geometry are found to be due to the difficulty in tracing a circular path with a structured mesh pattern. If 2 grid points are used on each edge, the circle will be traced as a polygon having eight sides (octagon), the mass flow calculated will be the flow through an area equivalent to the area of the octagon inscribed in the circle. But the actual mass flow through the circular orifice will be larger than this flow rate. In order to approximate the actual flow rate through a circular orifice, models with mesh pattern corresponding to 3, 4 and 6 grid points are developed and analyzed, each will trace the circle as polygons having sides 12, 16 and 24 inscribed in the same circle. The grid pattern of these models are shown in Fig 7.1 to Fig 7.4

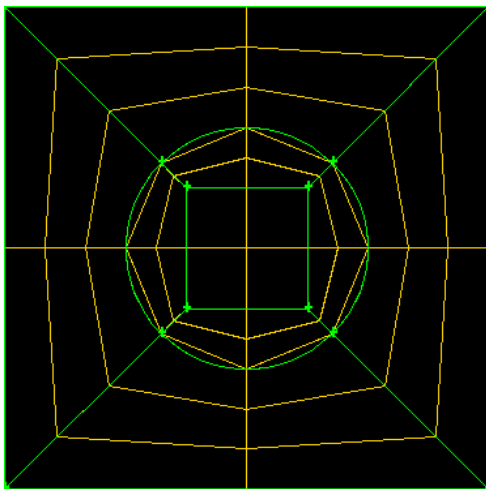


Fig 7.1 Two grid points per edge

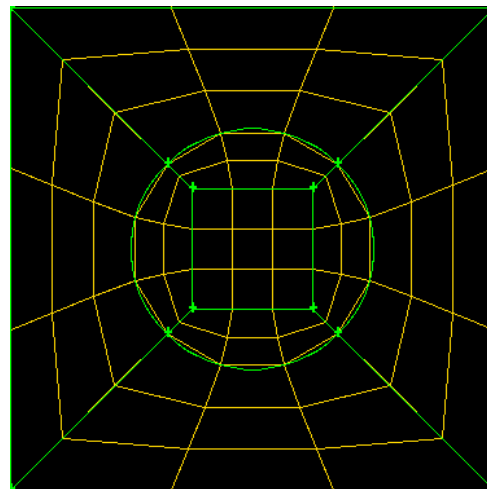


Fig 7.2 Three grid points per edge

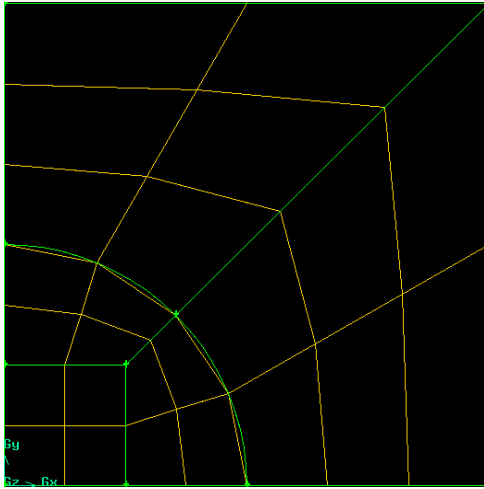


Fig 7.3 Four grid points per edge

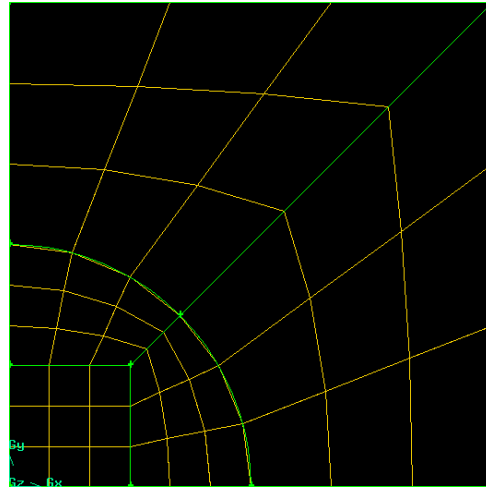


Fig 7.4 Six grid points per edge

It can be seen that the six grid points on each edge, traces the circle completely but still some discrepancies are existing in the mass flow rates. Trying to increase the grid points over six will result in a highly unstable analysis and the solution will not converge. As the grid points are increased the grid size within the circle reduces and below certain values, the grid will begin to capture micro flows and the solution will tend to diverge from stable solution. The approximation ends up with six grid condition and the required correction factors for mass flow for two grid point and six grid point are obtained. The velocity of the jet is not much affected by this phenomenon as the velocity depends only on the pressure difference across the tile. The velocity correction factors are calculated for all single jet geometries but are found to be very close to one.

The solution domain and the necessary boundary conditions used in single jet analysis are shown in figure 7.5. The jet is modelled as quarter of its shape and the complete geometry is established by using the symmetry boundary condition.

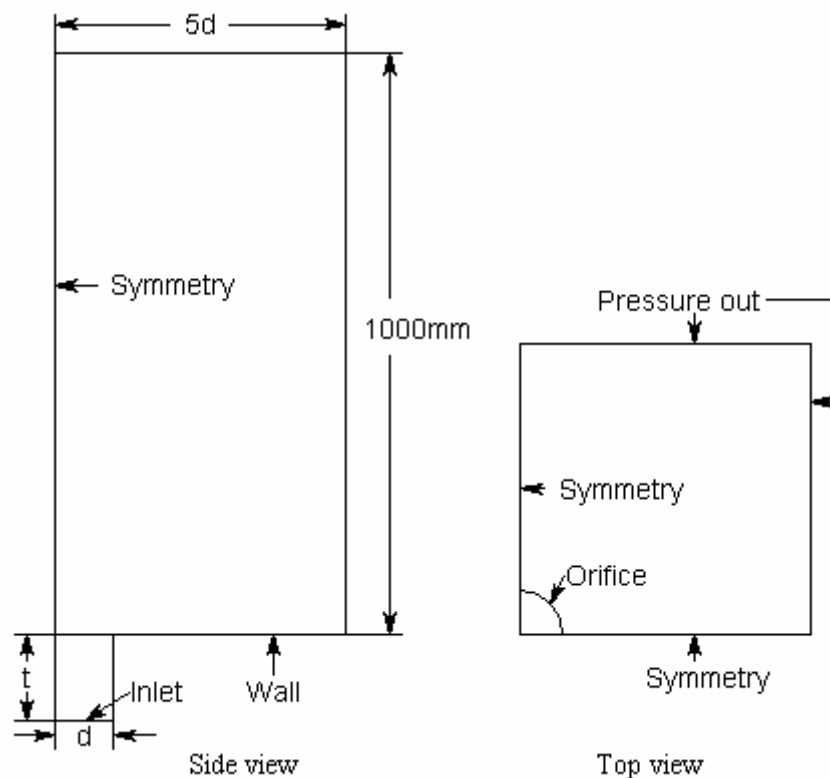


Fig 7.5 Solution domain and boundary types for 3D Single jet

In the forthcoming analysis of full tile the meshing pattern selected for the circular orifice is two grid points on each edge. If the grid points are increased, the total mesh number will be too large which will make the solution difficult. Hence the mass flow correction and velocity correction factors based on two grid pattern are established for full tile solution. But in the analysis of single jet, the meshing pattern selected is the one based on six grid points on each edge. The mass correction factors used here are calculated accordingly and the velocity correction factor is taken as unity. The mass flow correction factor and velocity correction factors are given in Table 7.1. The single jet configurations are solved for a pressure difference of 37.376 Pa across the tile. All three dimensional single jets are solved with gravity consideration to get the real time values.

Table 7.1 Mass and velocity correction factors for different grid pattern.

Model	C_{m2}	C_{m6}	C_v
3d8by10	1.1446	1.0478	0.9988
3d10by10	1.1296	1.0312	0.9986
3d12by10	1.1255	1.0262	0.9992
3d14by10	1.1209	1.0186	0.9981
C_{m2} - mass correction factor for 2 grid points			
C_{m6} - mass correction factor for 6 grid points			
C_v - Velocity correction factor for 6 grid points			

7.3 Twin Jet

Three dimensional twin jets are designated as 3d d by t PxTJ, with usual notations. The pitch selected for modelling is 4mm and 6mm which give six twin jet configurations for analysis. The configuration is similar to that of plane twin jet. The developed models are 3d 10 by 10 P4TJ, 3d 10 by 10 P6TJ, 3d 12 by 10 P4TJ, 3d 12 by 10 P6TJ, 3d 14 by 10 P4TJ and 3d 14 by 10 P6TJ. The jet orifice is meshed using 6 grid points on each edge to trace the circular orifice. The twin jet is modelled as half single jet as shown in the Fig 7.6 and the complete twin jet geometry is established by using the two symmetry boundary conditions. The solution domain and the necessary boundary types are shown in the Fig 7.6. The twin jet configurations are solved for a pressure difference of 37.376 Pa across the tile. All the three dimensional twin jets are solved with gravity consideration to get the real time values.

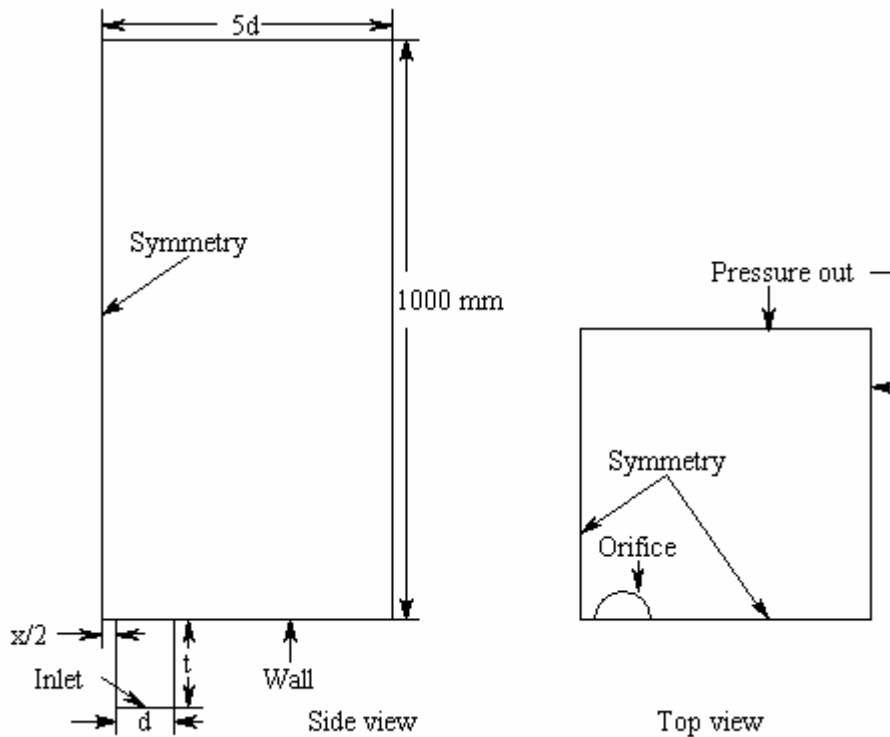


Fig 7.6 Solution domain and boundary types for 3D Twin jet

7.4 Triple Jet

Three dimensional triple jets are designated by $3d \times d \times t$ PxTrJ. Here also, six basic models are developed according to the pitch values of 4mm and 6mm. The basic models developed are, $3d \times 10 \times 10$ P4TrJ, $3d \times 10 \times 10$ P6TrJ, 12×10 P4TrJ, 12×10 P6TrJ, 14×10 P4TrJ and 14×10 P6TrJ. The jet orifice is meshed using 6 grid points on each edge to trace the circular orifice. The central jet is modelled as a quarter jet and the side jets are modelled as half jets as shown in the Fig 7.7. The complete triple jet geometry is established by using the two symmetry boundary conditions. The solution domain and the necessary boundary types are shown in the Fig 7.7. The triple jet configurations are solved for a pressure difference of 37.376 Pa across the tile. All the three dimensional triple jets are solved with gravity consideration to get the real time values.

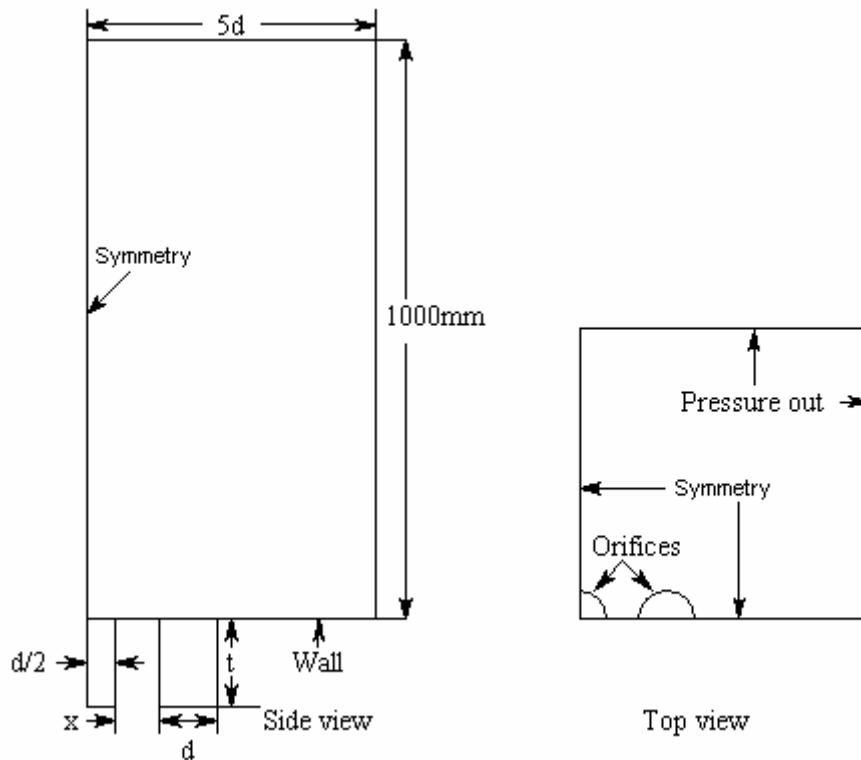


Fig 7.7 Solution domain and boundary types for 3D Triple jet

7.5 Differential Triple Jet

Three dimensional differential triple jets are designated as $3d_2$ by d_1 by $t+d_2$ by t PxDTrJ, similar to that of plane jets. Here the modelling strategy is concentrating on specific influence of dissimilar jets placed in the same plane. Here the modelling is done in two groups as follows. The first group consists of models comprising of two bigger jets of 12 by 10 and 14 by 10 placed in between a smaller twin jet combination of 10 by 10. With two different pitch values the four models obtained are:

$3d_2$ by 10 by 10+12 by 10 P4DTrJ, $3d_2$ by 10 by 10+12 by 10 P6DTrJ

$3d_2$ by 10 by 10+14 by 10 P4DTrJ, $3d_2$ by 10 by 10+14 by 10 P6DTrJ.

The next group consists of models comprising of two smaller jets of 8 by 10 and 10 by 10 placed in between a bigger twin jet combination of 12 by 10. With two different pitch values the four models obtained are:

3d 2 by 12 by 10+8 by 10 P4DTrJ, 3d 2 by 12 by 10+8 by 10 P6DTrJ

3d 2 by 12 by 10+10 by 10 P4DTrJ, 3d 2 by 12 by 10+10 by 10 P6DTrJ.

The central jet is modelled as a quarter jet and the side jets are modelled as half jets as shown in the Fig 7.8. The complete triple jet geometry is established by using the two symmetry boundary conditions. The solution domain and the necessary boundary types are shown in the Fig 7.8, which is same as that used for triple jets except for the central jet diameter. The triple jet configurations are solved for a pressure difference of 37.376 Pa across the tile. All the three dimensional differential triple jets are solved with gravity consideration to get the real time values.

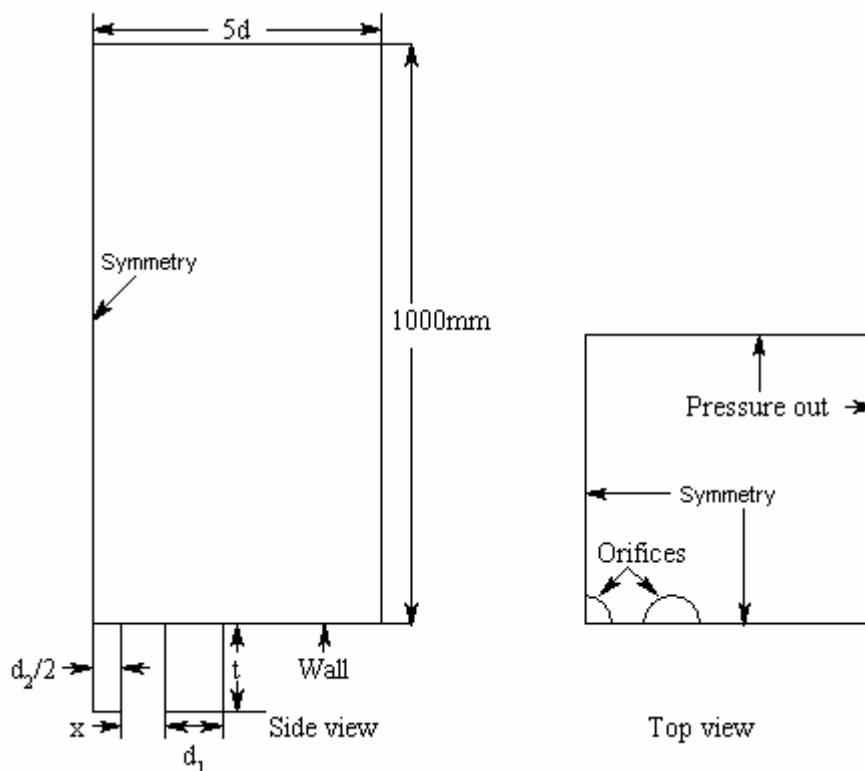


Fig 7.8 Solution domain and boundary types for 3D Differential triple jet

7.6 Four Jet Module

Three dimensional four jet models are developed as the fundamental clustering of multiple jets leading to a 2 feet by 2feet (0.6096m by 0.6096m) full perforated standard tile, as a full tile is comprised of a number of such four jet modules. Four jet modules are designated by $3d\ 4J\ d\ by\ t\ Px$ with usual notations. Six configurations are developed for the two pitch values and are designated as $3d\ 4J\ 10\ by\ 10\ P4$, $3d\ 4J\ 10\ by\ 10\ P6$, $3d\ 4J\ 12\ by\ 10\ P4$, $3d4J12by10P6$, $3d4J14by10P4$ and $3d4J14by10P6$. Four jet module is modelled as quarter of the full solution domain with a full orifice of the required diameter positioned at the required location to get the half the pitch clearance as shown in Fig 7.9. The symmetry boundary conditions will give the full solution domain with four jet positioned at the required pitch. Four jet modules are also solved for a pressure difference of 37.376 Pa across the tile. The solution domain and the boundary type are shown in the figure 7.9. All the three dimensional four jet models are solved with gravity consideration to get the real time values.

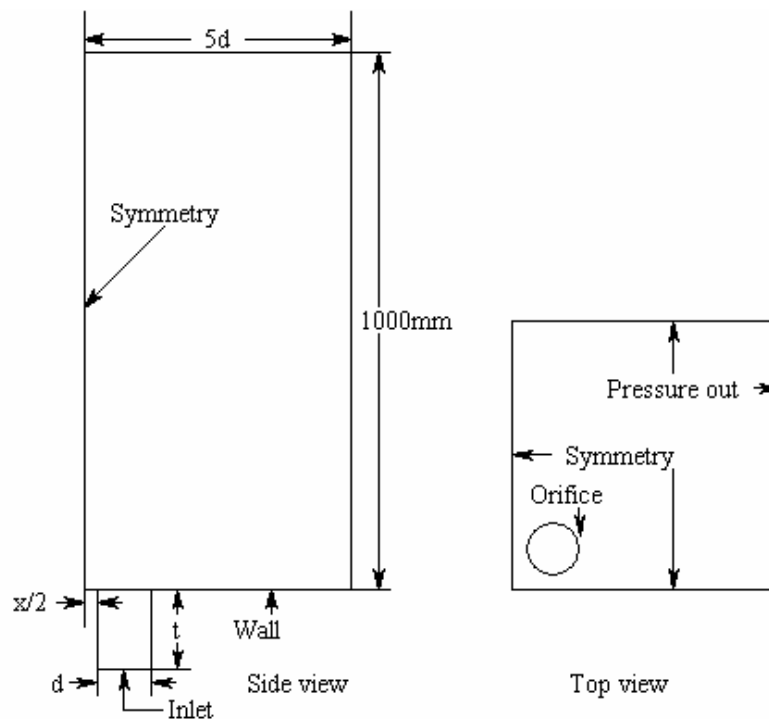


Fig 7.9 Solution domain and boundary types for 3D Four Jet module.

7.7 Five Jet Module

Three dimensional five jet models are developed as the fundamental clustering of combination tiles which contain jets of dissimilar diameters. The modelling and solution domain of five jet module is similar to that of four jet module; the fifth jet of different diameter is placed at the centre of the four jets. Five jet modules are designated by 3d 4J d_1 by $t+d_2$ by t Px. Theoretically it is possible to develop a number of five jet combinations with the selected single jet geometries. But while designing the combination, the practical feasibility must also be considered as this has to form the basic part of a full tile operating in a practical situation. Developing a five jet combination with a smaller or bigger jet placed in between four similar jets with P4 structure will lead to practically non feasible situation. The minimum clear distance left between any two jets is of high concern as far as the structural strength of the tile is concerned. In certain combinations with P4 structure, the four similar jets will have 4mm clearance between them, but the fifth jet placed in between will not maintain this clearance. The clearance between the central jet and the main jets will always be lower than the pitch and in some combination; they may overlap and change the jet configuration. Hence the five jet module is practically feasible only with P6 configuration. Even in P6 configuration, it is not practically feasible to place a bigger diameter jet at the centre as it will reduce the clearance distance considerably. A clear distance less than 2.5 mm is not acceptable with respect to its strength point of view. In this analysis three models are developed in this category as 3d 4J 12 by 10+8 by 10 P6, 3d 4J 14 by 10+8 by 10 P6 and 3d 4J 14 by 10+10 by 10 P6

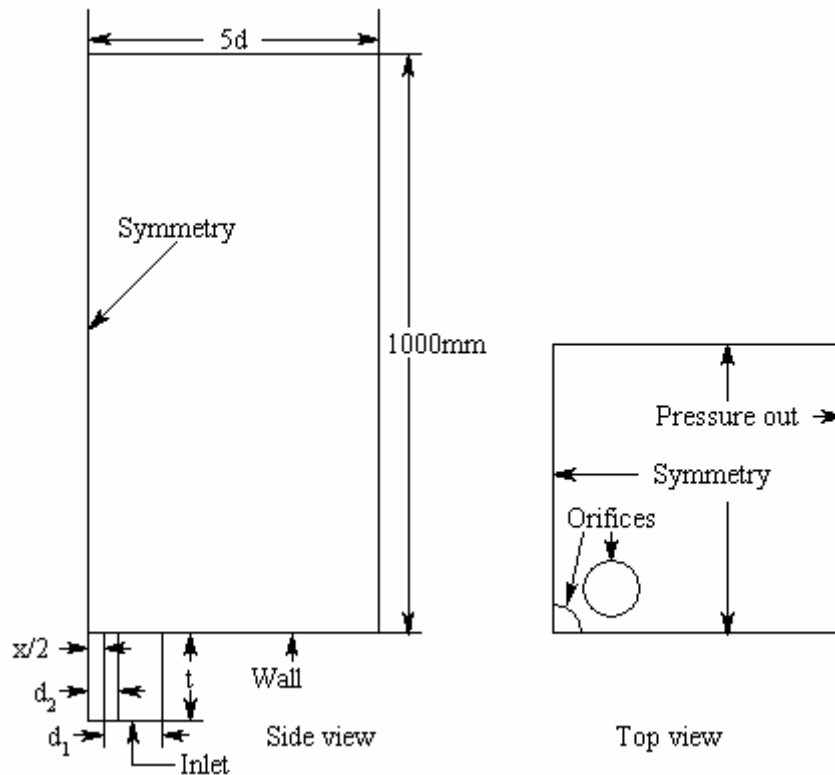


Fig 7.10 Solution domain and boundary types for 3D Five Jet module.

Five jet module is modelled as quarter of the full solution domain with a full orifice of the required main jet diameter and a quarter orifice of the central jet positioned at the required location to get half the pitch clearance as shown in the Fig 7.10. The symmetry boundary conditions will give the full solution domain with four jet positioned at the required pitch and the fifth jet at the centre. Five jet modules are also solved for a pressure difference of 37.376 Pa across the tile. The solution domain and the boundary type are shown in Fig 7.10. All the three dimensional five jet models are solved with gravity consideration to get the real time values.

7.8 Results and Discussion

The results of all the above jet models are summarized in the following sections and a detailed discussion is also made.

7.8.1 Single Jet

The four three dimensional single jets under consideration are modelled and solved for a pressure difference of 37.376 Pa across the tile. The results from various plots are taken up for analysis. The half width variations of 3D jets are not plotted since the jet profile and spread in three dimension can be taken at any position along the jet. In this analysis, the usual non dimensional parameters like x/d and U_y/U_c are not used for plotting the centre line velocity decay and near field velocity development. Here the velocities along the axial distance in the downstream are considered. This is because in 3D jet analysis, more importance is given to the real time values in order to have qualitative treatment of the data rather than to have a scaled value to compare them in a common platform. These comparisons are already made in the previous chapters. The centre line velocity decay and development of near field velocity of different jets are given in Figures 7.11 and 7.12.

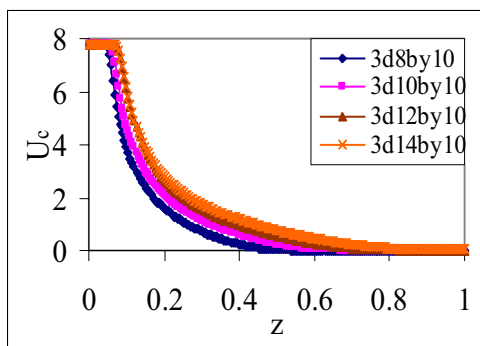


Fig 7.11 Comparison of velocity decay of different 3D single jet models.

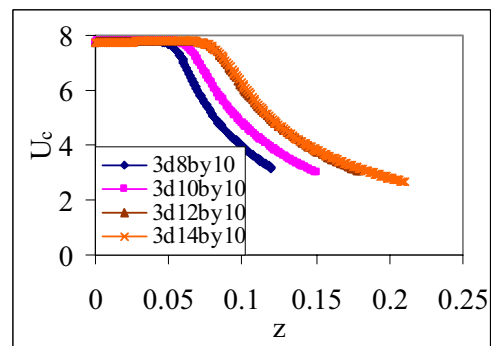


Fig 7.12 Comparison of near field velocity of different 3D single jet models

From the above plots, it can be seen that the 12 mm and 14 mm jets have better velocity characteristics than the other two. They maintain sufficiently higher velocities at the downstream than others, at the same time having longer potential core region. This suggests that these jets are much stronger than the other two since they possess higher momentum.

The comparison of mass flow rates and velocities at different x/d locations are given in the Table 7.2.

Table 7.2 Comparison of mass flow rates and velocities of 3D Single jets

Model	$m_c \times 10^3$	C_{m6}	$m_a \times 10^3$	U_0	U_{10}	U_{20}	U_{30}
3d8by10	0.45596	1.0478	0.47775	7.75927	5.08729	2.18183	1.19055
3d10by10	0.72419	1.0312	0.74678	7.76207	4.80495	2.09995	1.1559
3d12by10	1.04762	1.0262	1.07507	7.76008	4.91755	2.12172	1.17354
3d14by10	1.43505	1.0186	1.46174	7.75719	4.12785	1.9263	1.09426
m_c - calculated mass flow rate kg/sec m_a - actual (corrected) mass flow rate kg/sec U_0 - Centre line velocity at jet exit m/sec U_{10} - Centre line velocity at 10d m/sec U_{20} - Centre line velocity at 20d m/sec U_{30} - Centre line velocity at 30d m/sec							

The mass flow rates of the jets steadily increases as the jet diameter increases. The velocities at different x/d locations show different value from that shown in the velocity decay curve. This is because the x location of 8 mm jet and 14 mm at same x/d location are different. An x/d value of 40 refers to 0.32 m in the downstream of 8 mm jet and 0.56 m for 14 mm jet. This is the reason for the lower velocity for higher diameter jets.

The Figures 7.13 to 7.28 will explain the velocity profile and spread of all jets at different x/d locations.

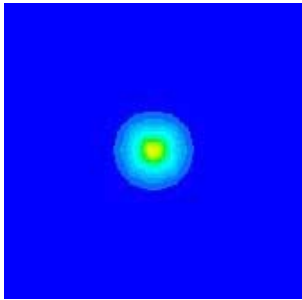


Fig 7.13 Velocity plot of 3d 8 by 10 at 10d.

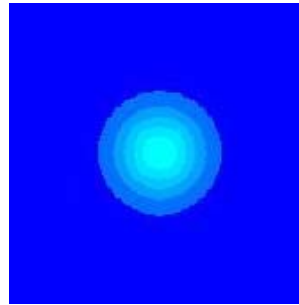


Fig 7.14 Velocity plot of 3d 8 by 10 at 20d.

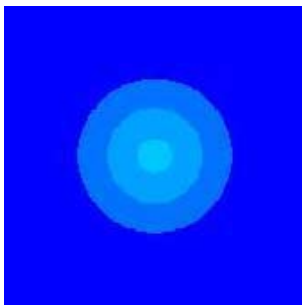


Fig 7.15 Velocity plot of 3d 8 by 10 at 30d.

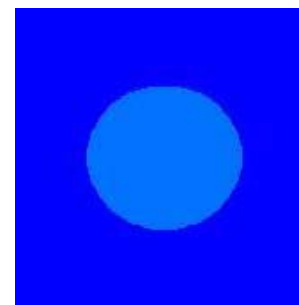


Fig 7.16 Velocity plot of 3d 8 by 10 at 40d.

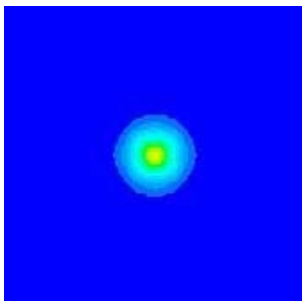
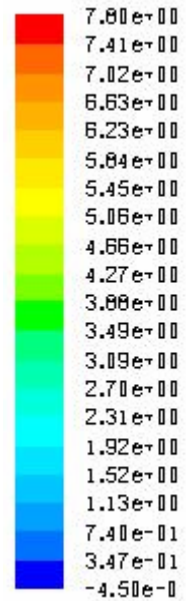


Fig 7.17 Velocity plot of 3d 10 by 10 at 10d.

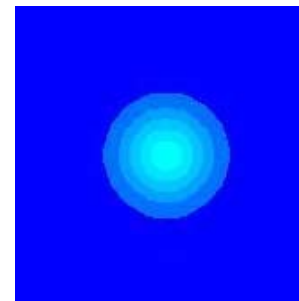


Fig 7.18 Velocity plot of 3d 10 by 10 at 20d.

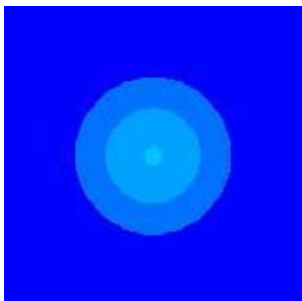


Fig 7.19 Velocity plot of 3d 10 by 10 at 30d.

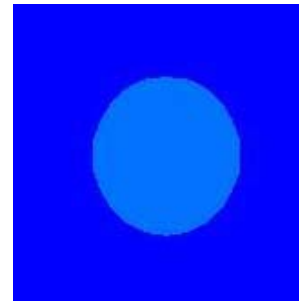
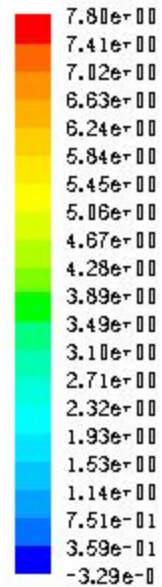


Fig 7.20 Velocity plot of 3d 10 by 10 at 40d.



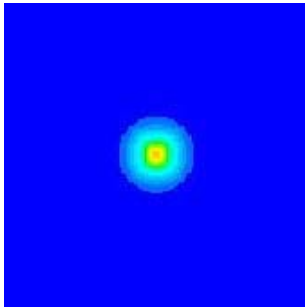


Fig 7.21 Velocity plot of 3d 12 by 10 at 10d.

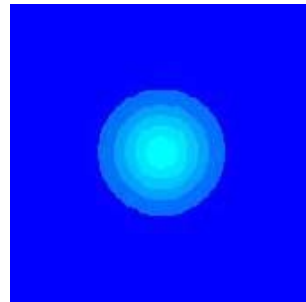


Fig 7.22 Velocity plot of 3d 12 by 10 at 20d.



Fig 7.23 Velocity plot of 3d 12 by 10 at 30d.

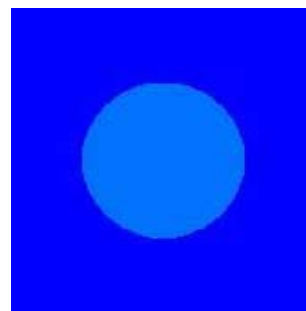


Fig 7.24 Velocity plot of 3d 12 by 10 at 40d.

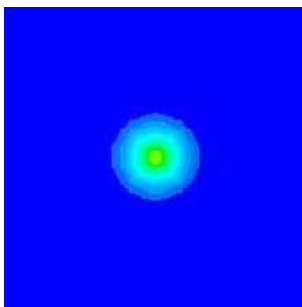


Fig 7.25 Velocity plot of 3d 14 by 10 at 10d.

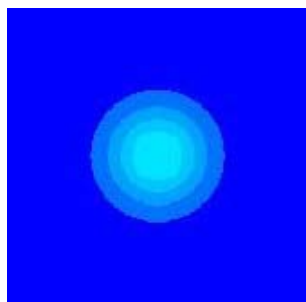


Fig 7.26 Velocity plot of 3d 14 by 10 at 20d.



Fig 7.27 Velocity plot of 3d 14 by 10 at 30d.

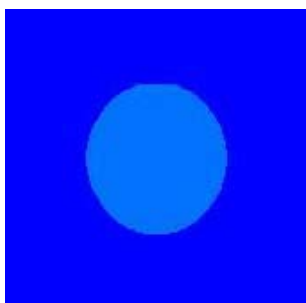
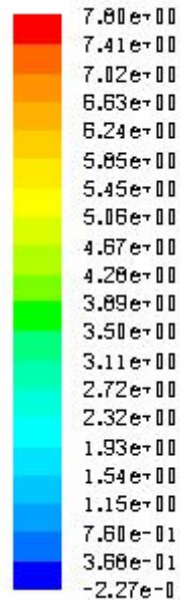


Fig 7.28 Velocity plot of 3d 14 by 10 at 40d.



From the velocity profile plots it is observed that the influence of the jet beyond x/d value of 40 is negligible and the jet terminates at these values of downstream conditions.

7.8.2 Twin Jet

The merging of three dimensional twin jet is entirely different from the merging of plane jets with respect to the jet interaction. The approach followed for locating the merging point of plane twin jets at the maximum velocity point on the merging axis cannot be applied in the case of three dimensional twin jets. At the point of maximum velocity in the merging axis of a three dimensional twin jet, the velocity profile in x and y direction shows two peaks as in the case of a twin jet. This shows that the jets are not merged completely at this point. This is further verified by analysing the velocity plot at that location which shows the profiles of two active jet cores.

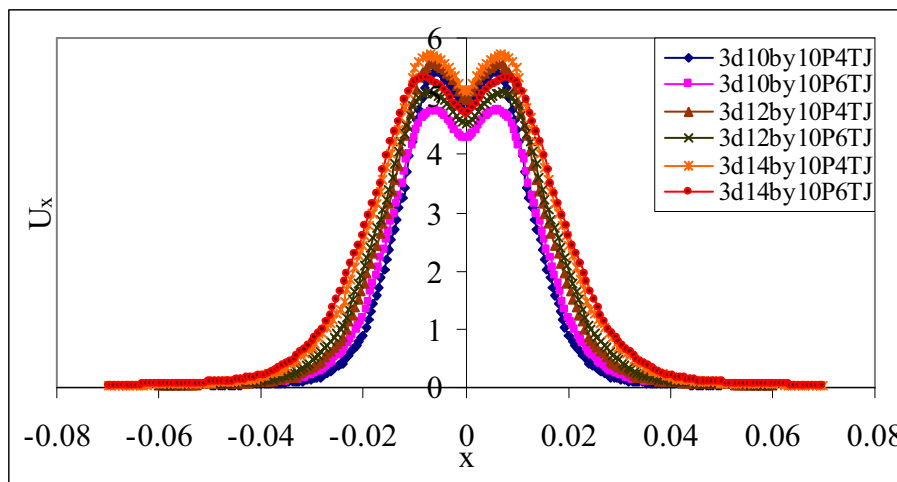


Fig 7.29 Comparison of velocity profile at point of maximum velocity on merging axis for different 3d twin jets.

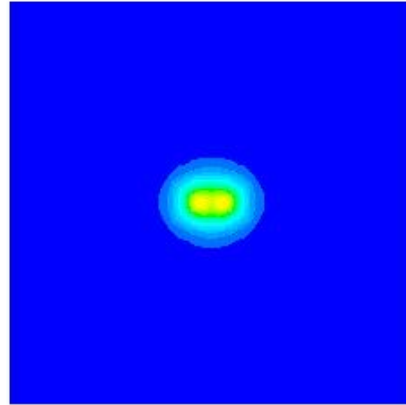


Fig 7.30 Velocity plane of 3d 10 by 10 P4TJ at point of maximum velocity

The velocity profiles of all twin jets studied at the above point is shown in Fig7.29. The velocity plane for 3d 10 by 10 P4TJ at this point is shown in Fig 7.30 which shows two active jet cores at this location suggesting that the merging has not taken place. Further, from the velocity plane it is clear that the velocity plot is not circular but it is elliptical in profile. The velocity plots of all jet combinations studied follow the same trend. This indicates that during merging interaction, the jets spread more in x direction and converge in the y direction. This is the reason for getting two peaks at the point of maximum velocity point on the merging axis. The velocity profiles at this point in x and y direction do not confirm each other when plotted on a single plot. At complete merging point the following conditions must be satisfied. The velocity profiles in x and y directions should have only one peak and the velocity plane should be circular. The velocity profiles in x and y direction must confirm themselves when plotted on a single plot, to have the single jet characteristics. This appeared to be an iterative procedure to locate the complete merging point of three dimensional twin jets.

As a first approximation the merging characteristics of the similar plane twin jet was transferred to three dimensional twin jet. The different velocity plots and profiles are made by transferring the merging locations of similar plane twin jets to

corresponding three dimensional twin jets. The velocity profiles in the x direction at these points are shown in the figure 7.31.

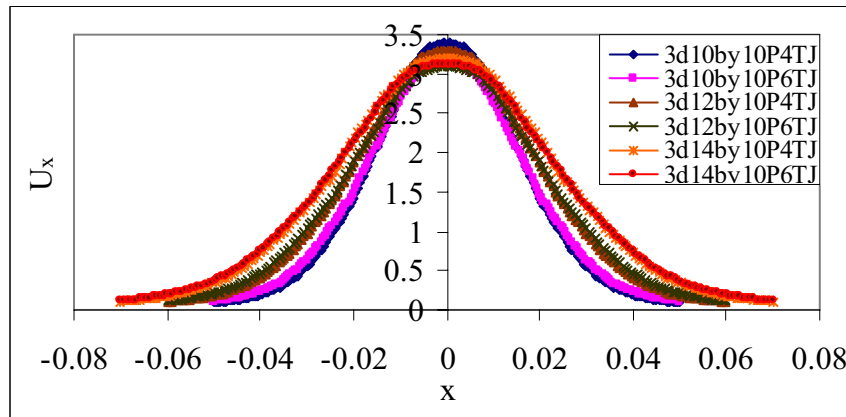


Fig 7.31 Comparison of velocity profiles of 3d twin jets at plane of merging

The velocity profiles are similar to that of a single jet since it has got only one peak. The velocity plot drawn at the merging point of 3d 10 by 10 P4TJ corresponds to that of a single jet as shown in the figure 7.32.

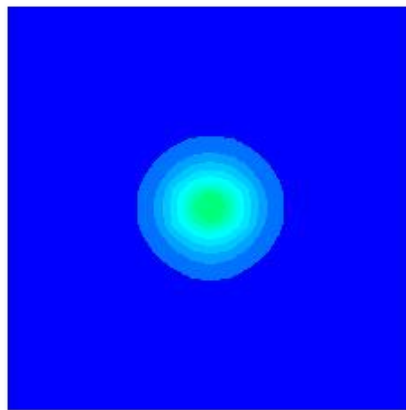


Fig 7.32 Velocity plane of 3d 10 by 10 P4TJ at merging point.

Similar velocity profiles and velocity planes were considered at little upstream positions of this point to verify the complete merging conditions. But the profiles do not confirm to that of a single jet characteristics until this point is reached. The x and y velocity comparison of 3d 10 by 10 P4TJ at this point is given in the figure 7.33.

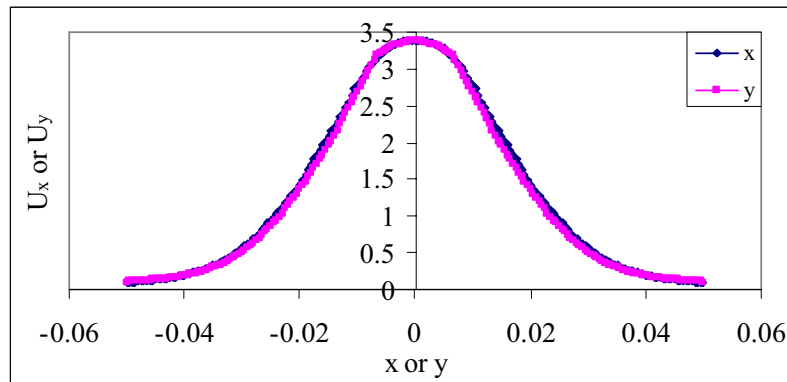


Fig 7.33 Velocity profiles of 3d10by10P4TJ at x and y direction at merging point. The figure shows that the two profiles confirm each other suggesting the complete merging of twin jets.

Similar studies conducted on all the six three dimensional twin jet geometries revealed the same trend. Hence the complete merging point of a three dimensional twin jet can be deemed to be same as that of a similar plane twin jet geometry. This shows the importance of the studies made with plane twin jets before studying the three dimensional twin jets. It was quite difficult to arrive at the merging characteristics of three dimensional twin jets without the results of plane twin jets. The merging characteristic velocities and the mass flow rates are summarized in the table shown in Table 7.3.

Table 7.3 Comparison of mass flow rates and velocities of 3D Twin jets

Model	$m_a \times 10^3$	U_0	x_m	U_m	U_{av}
3d10by10P4TJ	1.5	7.7707	0.17918	3.3855	1.6524
3d10by10P6TJ	1.4998	7.7677	0.18619	3.1508	1.5732
3d12by10P4TJ	2.1611	7.7752	0.22222	3.2909	1.6256
3d12by10P6TJ	2.1608	7.7725	0.22943	3.1024	1.5601
3d14by10P4TJ	2.9273	7.7775	0.26627	3.1851	1.5962
3d14by10P6TJ	2.9273	7.7761	0.27327	3.1289	1.5816

m_a - Mass flow rate kg/sec
 U_0 - Jet exit velocity m/sec
 x_m - Jet merging location along jet axis m
 U_m - Velocity at merging point m/sec
 U_{av} - Average velocity of jet beyond merging point m/sec

The mass flow rates of twin jets show an increase when compared with the values predicted by the single jet values multiplied by two. This increase is due to the additional pressure difference created by the mutual entrainment of the individual jets. This corresponds to an increase in jet exit velocity when compared to that of a corresponding single jet. The merging location as obtained from the three dimensional twin jet studies shows an increase as the jet diameter increases. This is due to the inherent higher momentum of the jets as the diameter increases. The merging velocities decrease steadily as the jet diameter increases. The reason for this result is due to the fact that the merging takes place after the potential core of the individual jets where the velocity decay is predominant and as it moves downstream the velocities are less.

As the pitch changes, the mass flow reduces but will be still higher than the single jet predictions. The jet exit velocities are also found to decrease due to the increased entrainment of surrounding stagnant air present between jets as pitch increases. The average velocities beyond merging decreases as the jet diameter increases. All jets terminate at about $47.5d$ in the downstream location. The average velocity is calculated from the merging point to $47.5d$ of each jet. The $47.5d$ position is different for different jet diameters and as jet diameter increases, this position moves further downstream where the velocities are lower. This is the reason for reduced average velocity as jet diameter increases. The jet velocity plots of three dimensional twin jets are shown in the figure 7.34.

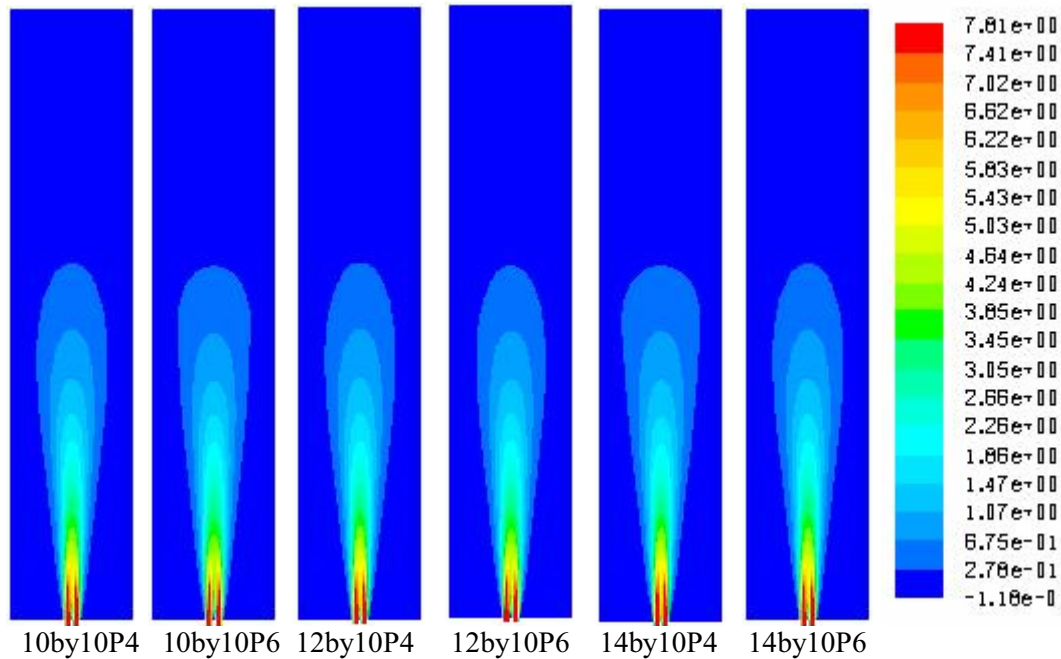


Fig 7.34 Comparison of velocity distribution of 3d twin jet models

The portions appearing in red colour represent the potential core of the jets where the velocities are higher. The complete merging point corresponds to the region shown in orange colour. The complete merging takes place where the orange colour terminates and it is clear from Fig 7.32 and Fig 7.34.

7.8.3 Triple Jet

Three dimensional triple jets are analyzed for their merging characteristics by applying the merging conditions of the corresponding plane triple jets as in the case of three dimensional twin jets. In triple jets the side jets will merge with the centre jet with respect to an axis passing through the mid point of the jets and the jets will finally merge along the central jet axis. The centre line velocity decay of the individual jets in three dimensional triple jets is different from that in the case of plane triple jets. In three dimensional triple jets, the individual jets show centre line velocity decay similar to that of a three dimensional single jet. The maximum velocity position on the merging axis between side jet and central jet (first merging point) is located and the velocity profiles in x direction and the three dimensional

velocity plot are drawn for all jets at this point. The velocity plots are shown in Figures 7.35 to 7.37.

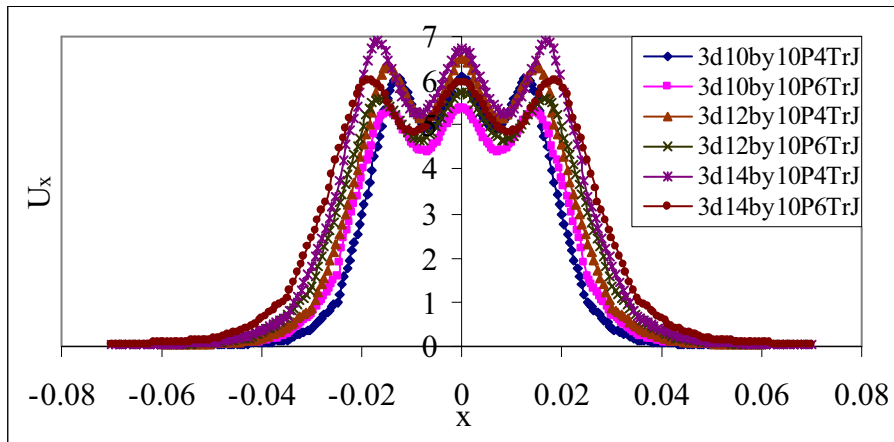


Fig 7.35 Comparison of velocity profile at first merging point of 3D triple jet models.

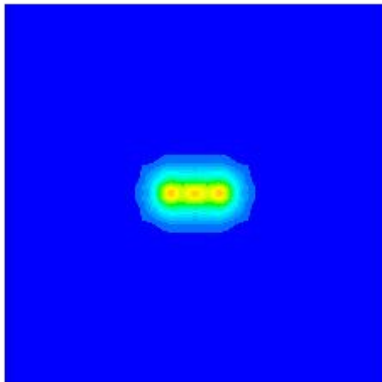


Fig 7.36 Velocity plane of 3D 10 by 10 P4TrJ at first merging point.

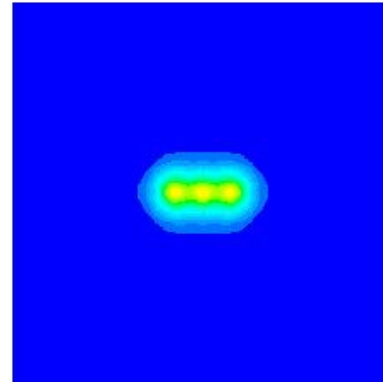


Fig 7.37 Velocity plane of 3D 10 by 10 P6TrJ at first merging point.

From the above figures, it is evident that the jets are still having the triple jet characteristics and they are at the early phase of merging.

The maximum velocity on the first merging point is transferred to the central jet to locate the probable merging point on the central jet (second merging point) and the similar velocity profiles and planes are drawn for all the triple jet

configurations. The velocity profiles along x direction and the velocity plot at second merging point are shown in figures 7.38 to 7.40.

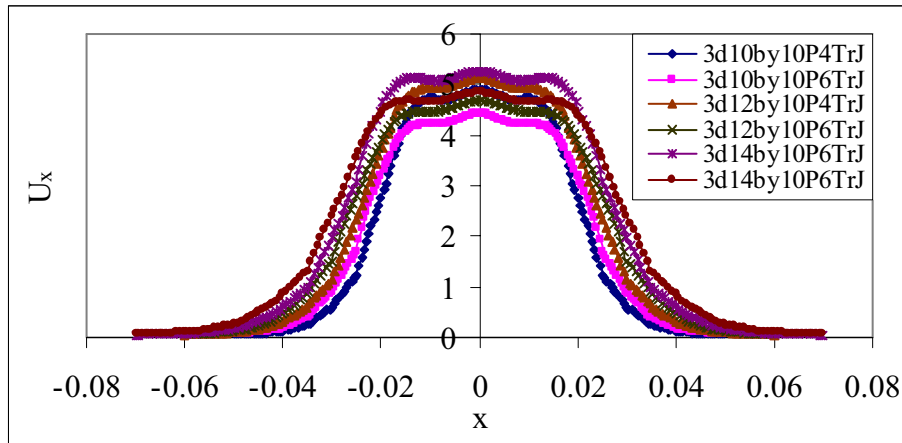


Fig 7.38 Comparison of velocity profile at second merging point of 3D triple jet models.

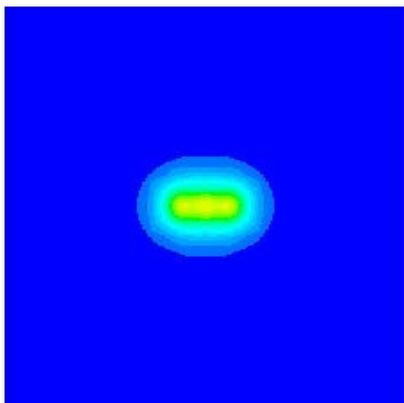


Fig 7.39 Velocity plane of 3D 10 by 10 P4TrJ at second merging point.

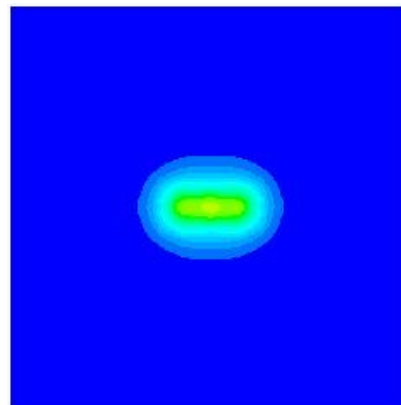


Fig 7.40 Velocity plane of 3D 10 by 10 P6TrJ at second merging

The above figures suggest that the merging of the three jets is still at an early phase and the three jet cores are clearly visible. As pitch increases, the axial velocity decreases and the spread increases.

Now the merging point corresponding to the maximum velocity on the merging axis of plane triple jet is transferred to the central jet axis of three

dimensional triple jet to get the third merging point of three dimensional triple jet. The velocity profiles and plots for all jets and are shown in figures 7.41 to 7.43.

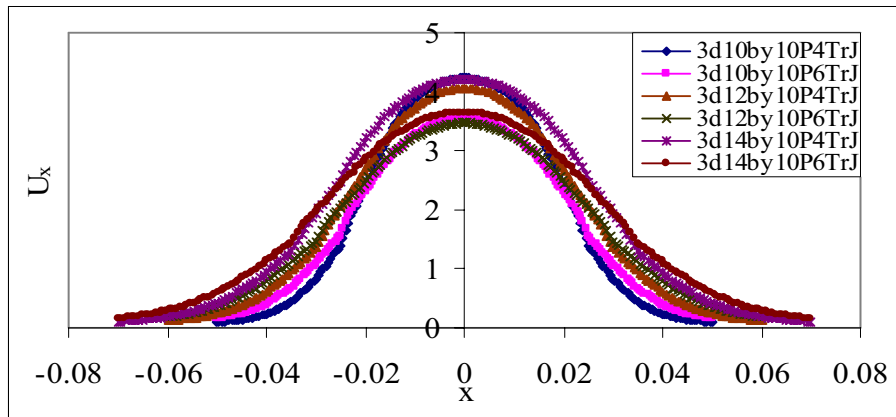


Fig 7.41 Comparison of velocity profile at third merging point of 3D triple jet models.

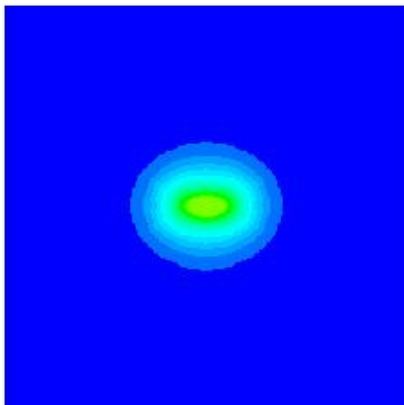


Fig 7.42 Velocity plane of 3D 10 by 10 P4TrJ at third merging point

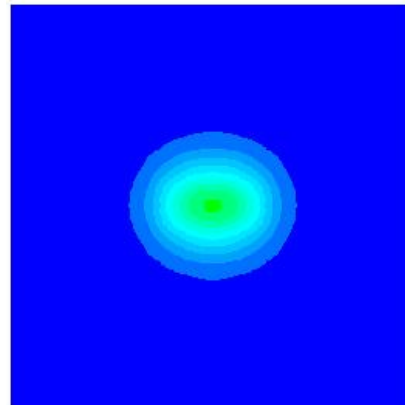


Fig 7.43 Velocity plane of 3D 10 by 10 P6TrJ at third merging point.

The velocity plots in the x direction shows single jet profile but the velocity plane is still elliptical showing that the merging is not complete. This is further confirmed by the comparison of x and y velocity profiles of a triple jet configuration on a single plot. The x and y velocity comparison of 10 by 10P4 jet is shown in Figure 7.44.

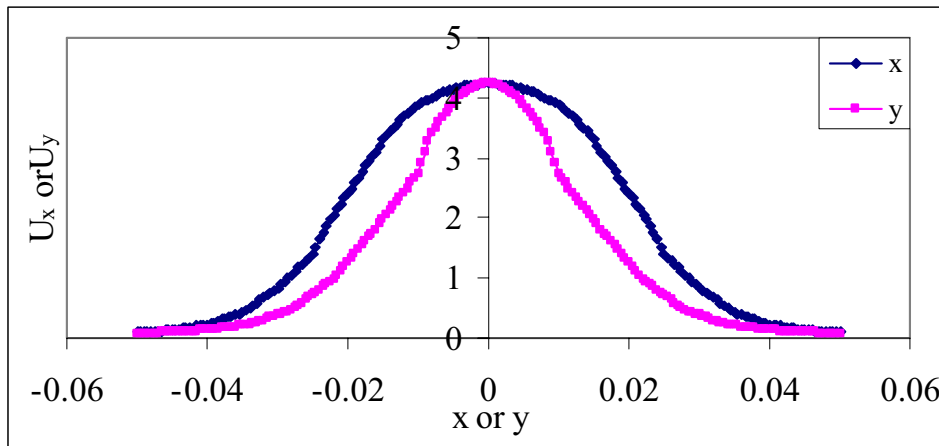


Fig 7.44 Velocity profiles of 3d 10 by 10 P4TJ on x and y axis at third merging point.

The two velocity profiles do not confirm themselves indicating that the merging is not complete and the contraction in y direction is still significant. These plots are similar for all geometries under consideration.

The final merging location on the central jet axis of plane triple jet configuration is transferred to the central jet axis of the three dimensional triple jet to get the complete merging point. The velocity plane obtained at this position is shown in figures 7.45 and 7.46.

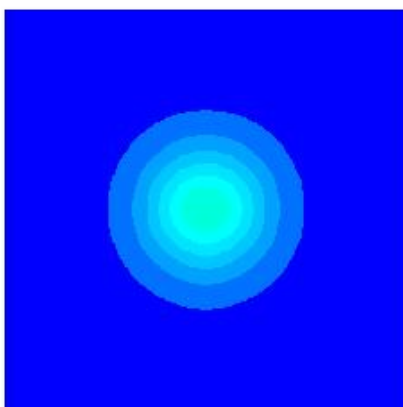


Fig 7.45 Velocity plane of 3D 10 by 10 P4TrJ at final merging point.

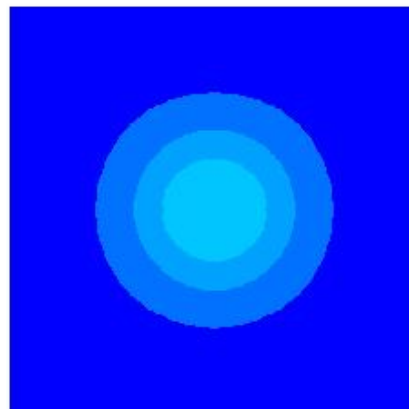


Fig 7.46 Velocity plane of 3D 10 by 10 P6TrJ at final merging point.

The velocity plot shows complete merging of the three jets since the plot is circular. This is further verified by comparing the x and y velocity plots at the complete merging point of the jet configurations under analysis. The x and y comparison of 10 by10 P4TrJ is shown in figure 7.47.

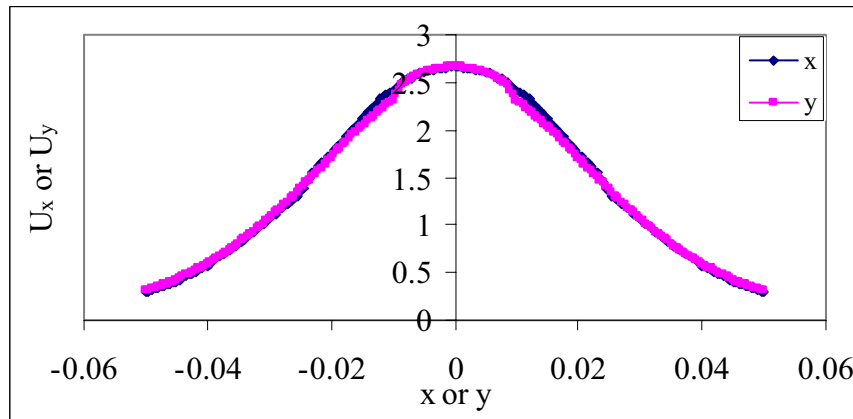


Fig 7.47 Velocity profiles of 3d 10 by 10 P4TrJ on x and y axis at final merging point.

The x and y velocity profiles confirm themselves showing that the jets merge completely at this point. Similar studies are conducted with all the triple jet models and it is confirmed that all the three dimensional triple jet configurations follow the same trend.

The merging characteristics velocities and the mass flow rates are summarized in the Table 7.4.

Table 7.4: Comparison of mass flow rates and velocities of 3D triple jets.

Model	$m_a \times 10^3$	U_{0c}	U_{0t}	x_m	U_m	U_{av}
3d10by10P4TrJ	2.2514	7.7715	7.7762	0.27578	2.6588	1.5328
3d10by10P6TrJ	2.2506	7.7681	7.7723	0.39862	1.5021	1.076
3d12by10P4TrJ	3.2441	7.7745	7.7801	0.38592	2.1581	1.3443
3d12by10P6TrJ	3.2432	7.772	7.7774	0.4863	1.4315	1.0432
3d14by10P4TrJ	4.387	7.7799	7.7833	0.4762	2.1118	1.3698
3d14by10P6TrJ	4.385	7.7755	7.7799	0.56348	1.5336	1.1218
U_{0c} - Central jet exit velocity m/sec						
U_{0t} - Top jet exit velocity m/sec						

The mass flow rates of triple jets show an increase when compared with the values predicted by the single jet multiplied by three. This increase is due to the additional pressure difference created by the mutual entrainment of the individual jets. This corresponds to an increase in jet exit velocity when compared to that of a corresponding single jet and twin jet models. The merging location gets extended as the jet diameter increases as in the case of twin jets. The merging velocities are also having the same decreasing trend as that of twin jets. As the pitch changes, the mass flow reduces but will be still higher than the single jet predictions. The jet exit velocities are also found to decrease due to the increased entrainment of surrounding stagnant air present between jets. The average velocities beyond merging decreases as the jet diameter increases. All jets terminate at about $52.5d$ in the downstream location. The average velocity is calculated from the merging point to $52.5d$ of each jet. The $52.5d$ position is different for different jet diameters. As jet diameter increases this position moves further downstream where the velocities are lower. This is the reason for reduction in average velocity as jet diameter increases. The jet velocity plots of three dimensional twin jets are shown in figure 7.48.

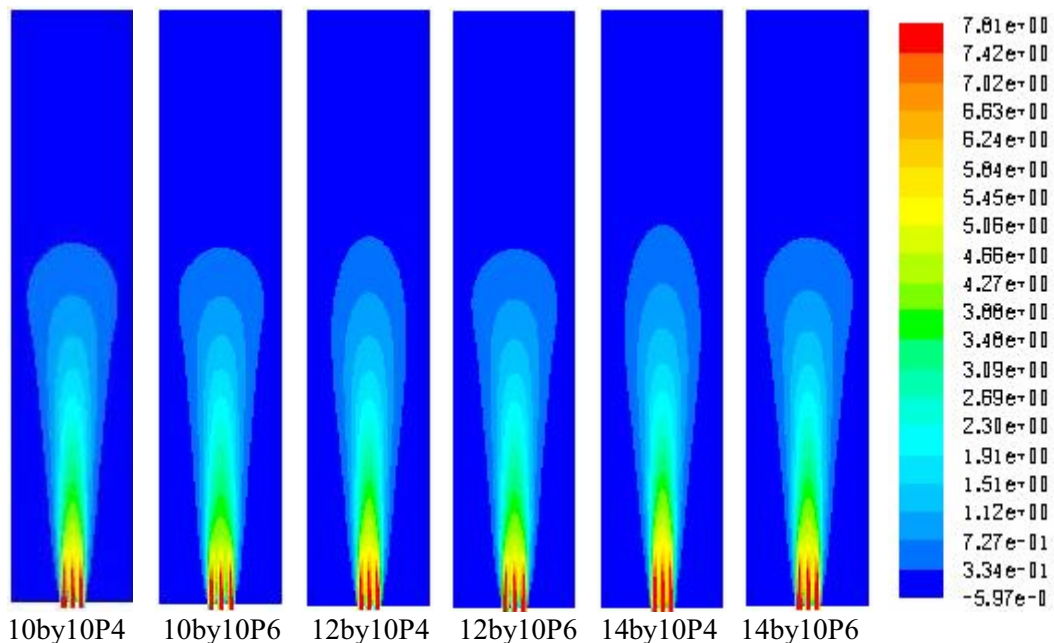


Fig 7.48 Comparison of velocity distribution of 3d triple jet models

The portions that appear in red colour represent the potential core of the jets where the velocities are higher. The complete merging region is shown in orange colour and the complete merging takes place at the region where the orange colour terminates. At the point of complete merging, the central jet velocity decay does not show an abrupt change in its slope in the case of 3D triple jets. This trend was observed in the case of plane triple jets. In three dimensional triple jets the central jet velocity decay is similar to that of a single jet that gradually decreases until the jet terminates.

7.8.4 Differential Triple Jet

The merging analysis of three dimensional differential triple jets follows the same procedure as that followed for triple jets. The merging points of the corresponding plane differential triple jets are transferred to the three dimensional triple jets to obtain the merging characteristics. The velocity profiles on x and y axis and the velocity plot at the third merging point of 3d 10 by 10+12 by 10 P4DTrJ and 3d 12 by 10+8 by 10 P4DTrJ are given in figures 7.49 and 7.50.

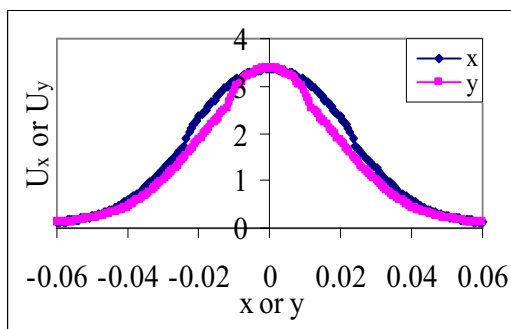


Fig 7.49 Velocity profiles on x and y axis of 3d 10 by 10+12 by 10 P4DTrJ at third merging point.

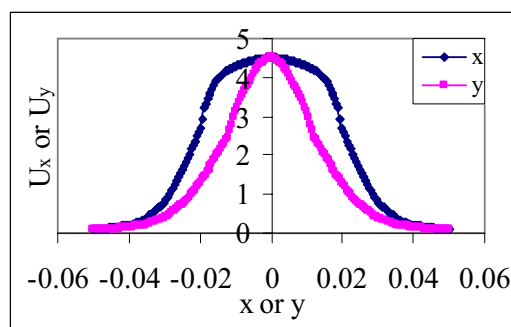


Fig 7.50 Velocity profiles on x and y axis of 3d 12 by 10+8 by 10 P4DTrJ at third merging point.

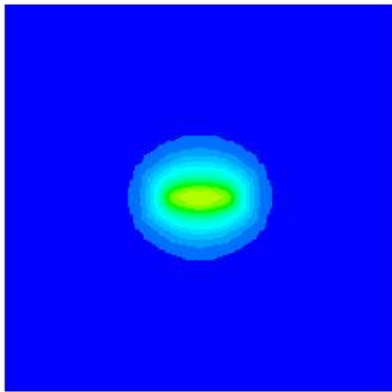


Fig 7.51 Velocity plane of 3d 10 by 10+12 by 10 P4DTrJ at third merging point.

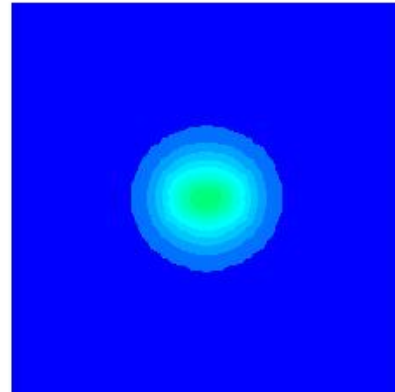


Fig 7.52 Velocity plane of 3d 10 by 10+8 by 10 P4DTrJ at third merging point.

The figures 7.51 and 7.52 show that the merging is not complete at the point of consideration. The profiles and plots corresponding to the final merging point of the same jet combinations are shown in figures 7.53 to 7.56.

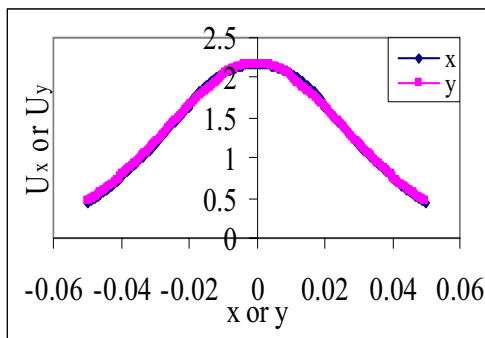


Fig 7.53 Velocity profiles on x and y axis of 3d 10 by 10+12 by 10 P4DTrJ at final merging point.

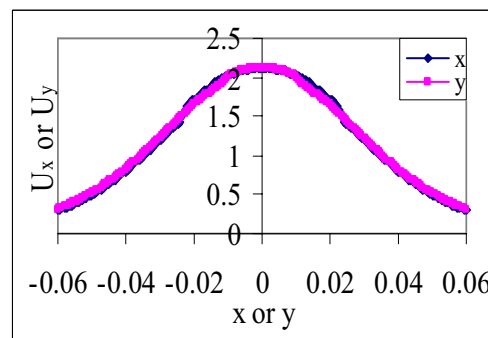


Fig 7.54 Velocity profiles on x and y axis of 3d 12 by 10+8 by 10 P4DTrJ at final merging point.

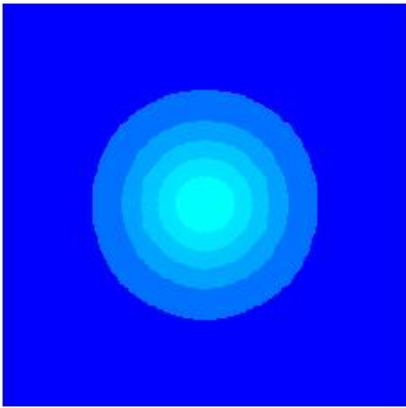


Fig 7.55 Velocity plane of 3d 10 by 10+12 by 10 P4DTrJ at final merging point.

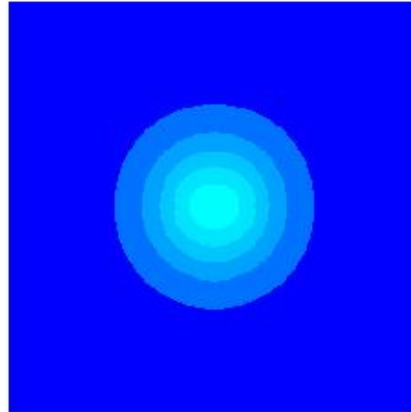


Fig 7.56 Velocity plane of 3d 10 by 10+8 by 10 P4DTrJ at final merging point.

The x and y velocity profiles confirm themselves showing that the jets merge completely at this point. Similar studies are conducted with all the differential triple jet models and it is confirmed that all the three dimensional differential triple jet configurations follow the same trend.

The merging characteristic velocities and the mass flow rates of three dimensional triple jets are summarized in Table 7.5.

Table 7.5 Comparison of mass flow rates and velocities of 3D differential triple jets.

Model	$m_a \times 10^3$	U_{0c}	U_{0t}	x_m	U_m	U_{av}
3d2by10by10+12by10P4DTrJ	2.5764	7.7726	7.79	0.359614	2.1719	1.4767
3d2by10by10+12by10P6DTrJ	2.5823	7.7684	7.7787	0.453954	1.2116	0.9911
3d2by10by10+14by10P4DTrJ	2.9596	7.7743	7.7909	0.404841	1.8309	1.3851
3d2by10by10+14by10P6DTrJ	2.9585	7.7716	7.7871	0.486226	1.2375	1.1195
3d2by12by10+8by10P4DTrJ	2.6309	7.7827	7.7701	0.368167	2.1218	1.2717
3d2by12by10+8by10P6DTrJ	2.6335	7.7784	7.7699	0.367787	2.1348	1.253
3d2by12by10+10by10P4DTrJ	2.9041	7.7788	7.7781	0.268258	3.2496	1.7435
3d2by12by10+10by10P6DTrJ	2.9007	7.7703	7.7702	0.439208	1.7331	1.1479

The mass flow rates of differential triple jets show comparable results with the values of triple jets. The mass flow rate of a differential triple jet model with a smaller diameter jet at the centre of two bigger jets give same mass flow rate as that of a triple jet of bigger diameter jets. The jet exit velocity shows an increase when compared with corresponding triple jets. The merging location gets extended for geometries having bigger jet at centre and contracts for models with smaller jets at centre. This feature is highly useful for tile design as the jets merge early with small diameter jets at centre. The velocity profile will be more stable and uniform for the remaining part of the flow. The merging velocities are lower for models with bigger jets at centre and higher for models with smaller jets at centre. This also encourages the use of this combination for combination tiles. As the pitch changes the mass flow reduces but will be still comparable with that of triple jets of same pitch. The jet exit velocities are also reduced due to the increased entrainment of surrounding stagnant air present between the jets as pitch increases. The average velocities beyond merging decreases as the pitch increases. All jets terminate at about 52.5d in the downstream location. The average velocity is calculated from the merging point to 52.5d of each jet. Since the 52.5d position is different for different jet diameters, as jet diameter increases this position moves further downstream where the velocities are lower. This is the reason for reduced average velocity as jet diameter increases.

7.8.5 Four Jet Module

The analysis of three dimensional four jet modules follows the same procedure as that followed for other jet configuration studies. In 3d 4J module two primary merging axes are defined as Z_x and Z_y , the line on x and y axis in z direction that passes through the mid point of the two jets. The location of maximum velocity point on this axis is called the x and y merging points. Due to symmetry, these locations and the velocity at this point are same for the jet module. The second probable merging point is selected as the maximum velocity point on the central merging axis. The third merging point is located by transferring the x or

y merging velocity onto the central merging axis. The velocity profiles along x and y directions and the velocity plot at all the three points for the six 3d 4J modules are drawn. The velocity profiles and velocity plot for 3d 4J 10 by 10P4 module corresponding to first merging point are shown in figures 7.57 and 7.58.

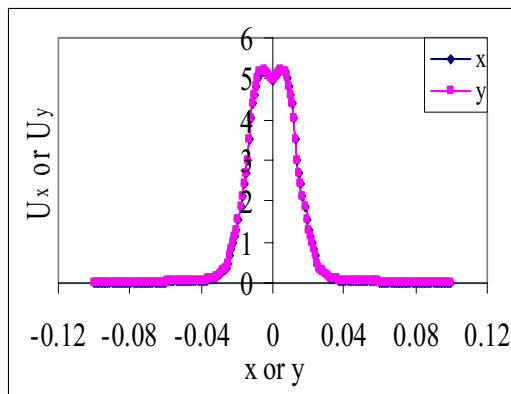


Fig 7.57 x and y velocity profiles at first merging point of 3d 4J 10 by10 P4

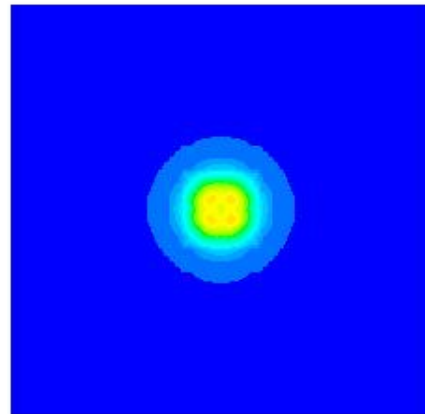


Fig 7.58 Velocity plot at first merging point of 3d 4J 10 by10 P4

The velocity profiles confirm themselves at this point since the axes are axes of symmetry, but both profiles show two peaks and the plots show four active jet cores indicating that the merging has not taken place at this point. Similar velocity profiles and velocity plot are obtained at the second merging point for the same jet module and are shown in figures 7.59 and 7.60.

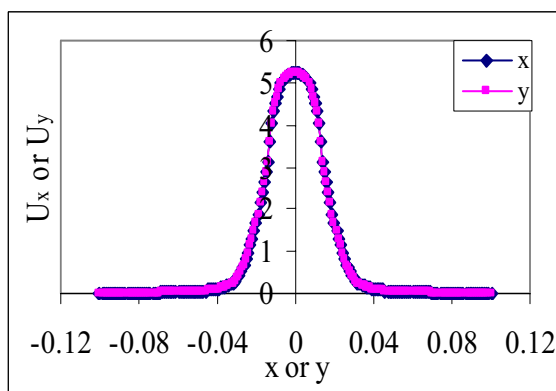


Fig 7.59 x and y velocity profiles at second merging point of 3d 4J 10 by 10 P4

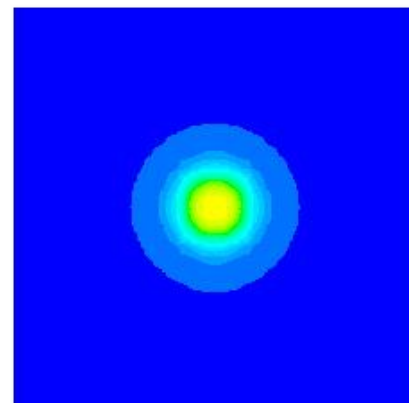


Fig 7.60 Velocity plot at second merging point of 3d 4J 10 by10 P4

The x and y velocity profiles confirm themselves and it shows only one peak similar to that of a single jet but in the velocity plot, the central core is still exhibiting the presence of four cores hence it is not circular, but away from the central merge axis the profile is circular. This means that some more adjustments are required for the central core to have complete merging of the four jets. The velocity profiles and velocity plot at the third merging point for the same jet are shown in figures 7.61 and 7.62.

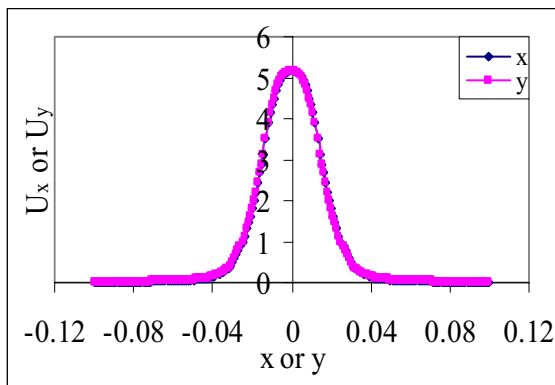


Fig 7.61 x and y velocity profiles at third merging point of 3d 4J 10 by 10 P4

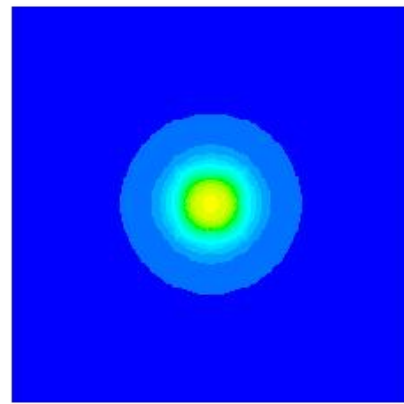


Fig 7.62 Velocity plot at third merging point of 3d 4J 10 by 10 P4

The x and y velocity profiles confirm themselves and the profile is smoother at the peak showing more single jet characteristics. In the velocity plot the centre core shows more stability as the four core pattern disappear and the core has become circular indicating that the merging is complete. Hence the third merging point considered above can be treated as the complete merging point of a four jet module. All the six models studied shows the same trend and the merging conditions explained above are applicable for all three dimensional four jet modules. The velocity profiles and velocity plot of all other jet models at the complete merging point are compared in figures 7.63 to 7.72.

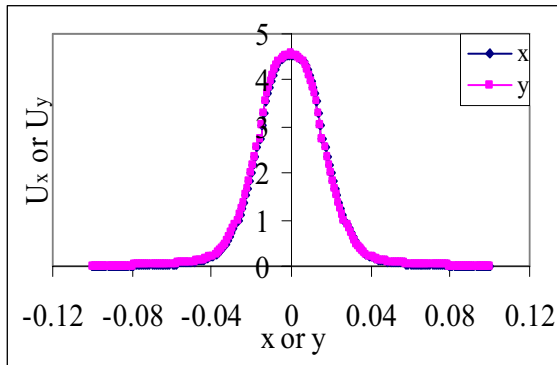


Fig 7.63 x and y velocity profiles at third merging point of 3d 4J 10 by 10 P6

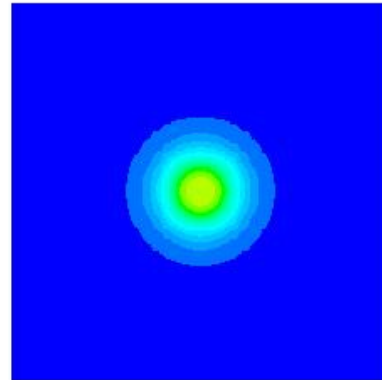


Fig 7.64 Velocity plot at third merging point of 3d 4J 10 by 10 P6

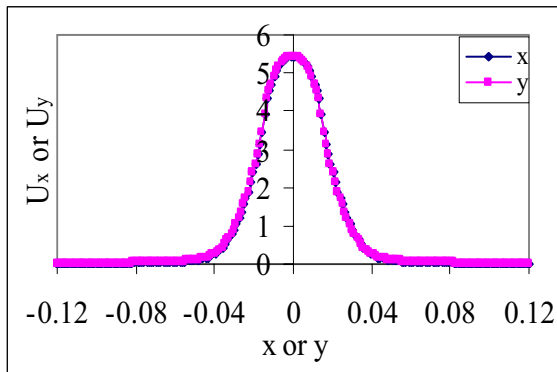


Fig 7.65 x and y velocity profiles at third merging point of 3d 4J 12 by 10 P4

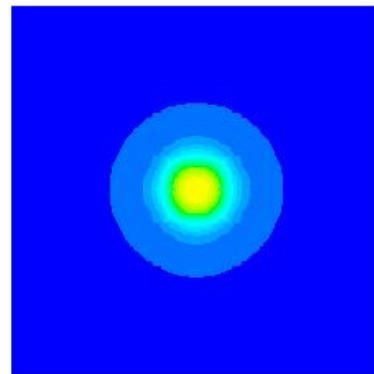


Fig 7.66 Velocity plot at third merging point of 3d 4J 12 by 10 P4

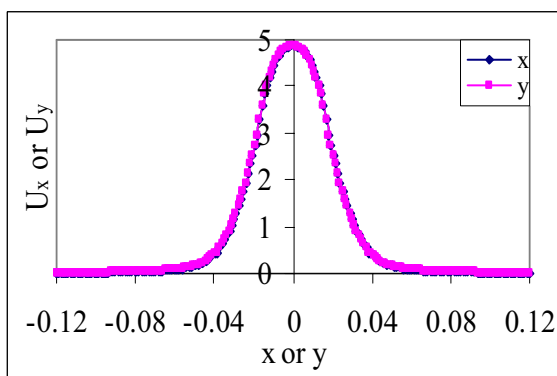


Fig 7.67 x and y velocity profiles at third merging point of 3d 4J 12 by 10 P6

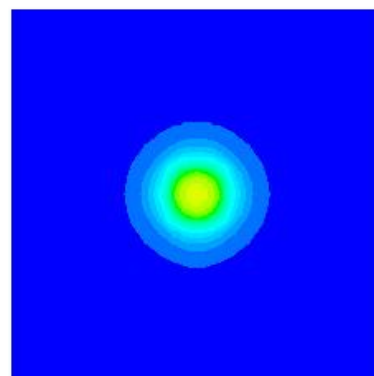


Fig 7.68 Velocity plot at third merging point of 3d 4J 12 by 10 P6

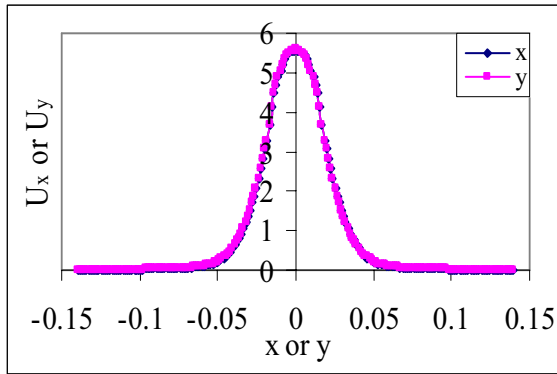


Fig 7.69 x and y velocity profiles at third merging point of 3d 4J 14 by 10 P4

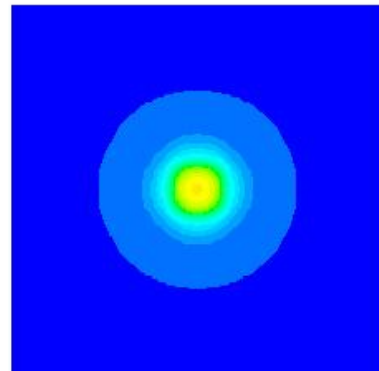


Fig 7.70 Velocity plot at third merging point of 3d 4J 14 by 10 P4

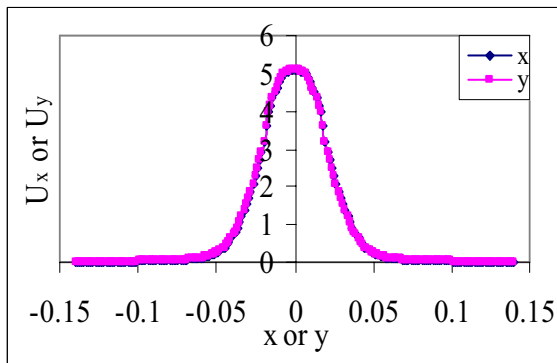


Fig 7.71 x and y velocity profiles at third merging point of 3d 4J 14 by 10 P6

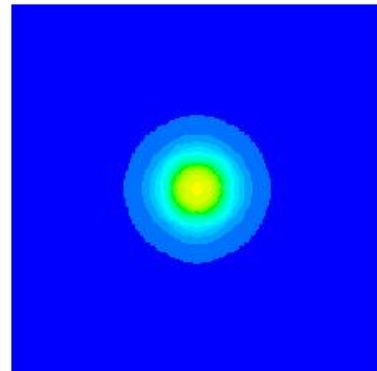


Fig 7.72 Velocity plot at third merging point of 3d 4J 14 by 10 P6

The mass flow rates, merging positions and the velocities of three dimensional four jet modules are given in the Table 7.6.

Table 7.6 Comparison of mass flow rates and velocities of 3D four jet modules

Model	$m_a * 10^3$	U_0	x_m	U_m	U_{av}
3d4J10by10P4	3.0259	7.8785	0.16263	5.1634	1.8059
3d4J10by10P6	3.0107	7.8423	0.16369	4.5591	1.4404
3d4J12by10P4	4.3713	7.8877	0.21109	5.4491	2.1672
3d4J12by10P6	4.3487	7.8521	0.19204	4.8673	1.5814
3d4J14by10P4	5.9039	7.8973	0.32065	5.5717	2.7215
3d4J14by10P6	5.9031	7.8631	0.22795	4.1179	1.7569

U_0 – Main jet exit velocity m/sec

The mass flow rates of four jet modules are greater than the flow rates of four single jets of similar diameter irrespective of the pitch of the four jet module. The mass flow rate decreases as the pitch changes from 4mm to 6mm in all models but this difference narrows down as the jet diameter increases and for 14mm jet the difference in mass flow rate is negligible. This information is important for the design of tiles especially for the design of combination tiles which are possible only with 6mm pitch value.

The jet velocities with four jet modules are higher than any other three dimensional jet configurations. This is due to the symmetry of the configuration and the jets are interacting in three dimensional profiles providing higher mutual entrainments for the jets and results in higher velocities. The merging location of the four jet modules show a significant change from all other multiple jet studies in plane and three dimensional jets. In all other jet models the merging distance increases considerably as the pitch increases which is already discussed in the previous sections. While considering the merging characteristics of 3d 4J 10 by 10 model the first merging point distance increases as pitch increases but the increase is very small when compared with the respective values obtained for twin jet or triple jet models. The second merging point distance is the same for both the pitch values. The third merging point distance shows a marginal increase. When the diameter and pitch increases all the three merging point locations contract and this contraction is substantial for 14 mm jets. This behaviour of the jet is just opposite to that of any other cases. This shows that as the jet diameter increases, higher pitch values will reduce the merging distance along downstream and the jets will merge at lower location. This can be further confirmed by analyzing the velocity plot of all the jets in the z direction as shown in figure 7.73.

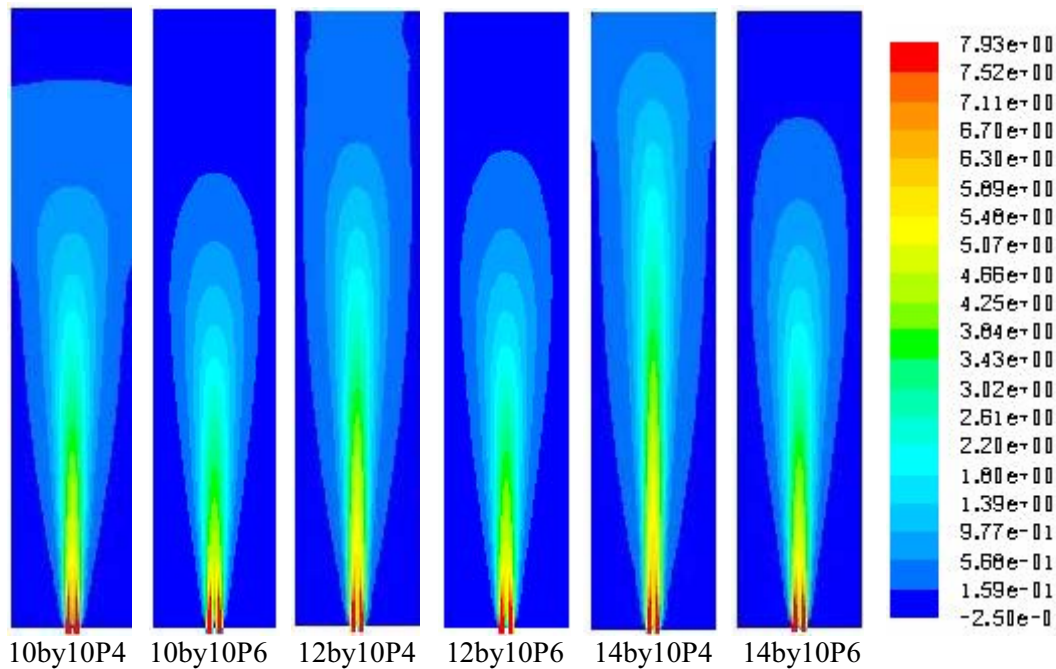


Fig 7.73 Comparison of velocity distribution of different 3d4J modules.

From fig 7.73, it can be seen that as the jet diameter increases for P4 configuration the jet spread increases progressively and the jets diffuses to the surrounding air faster and is not capable of holding its profile for a longer distance. For P6 configuration all the three jets show similar spread characteristics, the spread is less and it retains the profile until it terminates. The termination point extends further downstream as the jet diameter increases. The two configurations (P4 and P6) behave differently with respect to the jet characteristics. This shows that the pitch is having significant effect on multiple jet configurations.

The x and y merging point distances are higher for 10 by 10 P6 model but the velocity at this point is lesser than the velocity at the corresponding P4 model. Even though the second merging point distances are the same for both models, the corresponding velocity is lower for P6 model and the third merging point velocity is also lower for P6 model. Even though this follows the normal trend, it is obvious that the trend is going to take a turn. This is observed in 12 by 10 and 14 by 10 models. Here the merging point distance reduces but the velocities also reduce. The

main reason for this is the increased recirculation zone below the merging points of P6 models. Due to the presence of large recirculation zone in P6 models near the jet exit, the jet loses its energy and momentum at the early phase of its development. They merge early but with a lower velocity at the jet outer profile while the jet core is sufficiently strong. Hence the jet loses more energy during the early part of the irreversible merging while overcoming the recirculation zone. Finally when it reaches the complete merging point they merge early but with lower velocities. This lower velocity will reduce the entrainment at the shear layer; the jet holds its profile and terminates as a single jet around 85d downstream.

In P4 jets, the recirculation zone at the beginning of the jet is not considerable and hence the jet spread is very small at the beginning. They have to travel more to meet with each other even though the pitch is less. When they meet, the peripheral velocities with which they merge is higher and the P4 models maintain higher merging velocities. Since the velocities are higher after merging, they can entrain more air in the shear layer thereby increasing the spread and it loses the velocity profile of a single jet. The jet spreads to a longer distance and instead of getting terminated the jet will disintegrate at distances more than 100d downstream. The average velocity after merging for P6 models is higher since the average velocity is calculated from the final merging point to 100d distance. Since P6 jets terminate before 85d, its average velocities beyond the complete merging point are less.

7.8.6 Five Jet Module

The final merging point of the five jet module is determined first by defining the x and y merging points on x and y axes and transferring the velocity at x or y merging point onto the central jet axis. In five jet module the central jet maximum velocity is obtained at the central jet exit itself. Hence in five jet module, only two merging points need to be considered. The velocity profile and velocity plot of 3d 4J 12 by 10+8 by 10 P6 at the x and y merging point is given in figures 7.74 and 7.75.

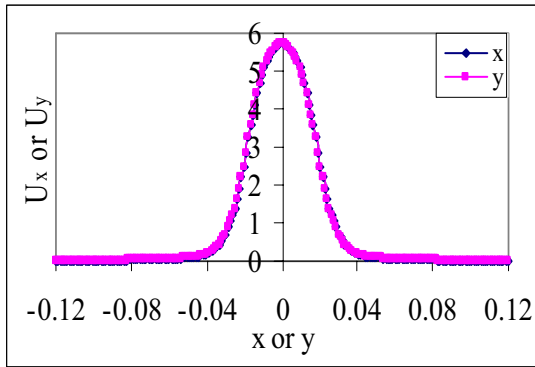


Fig 7.74 x and y velocity profiles at first merging point of 3d 4J 12 by 10+8 by 10 P6

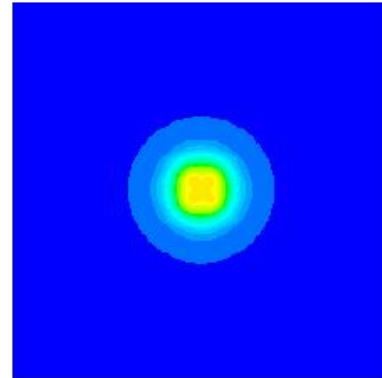


Fig 7.75 Velocity plot at first merging point of 3d 4J 12 by 10+8 by 10 P6

The velocity profiles confirm themselves at this point since they are symmetry profiles, but the profile is not similar to that of single jet characteristics even though it does not show multiple peaks at this point. This is because the profile is obtained along the x and y axis where the core of the main jets do not interact but the axis passes through the core of the central jet and it shows profiles very close to that of a single jet. From the velocity plot at this point, four active cores of the main jets are clearly visible indicating that the merging process is not complete. This is more evident from the velocity profile shown in figure 7.76 which is obtained along an axis in xy direction which passes through both central and main jets. The profile shows three peaks indicating that the three diagonal jets are not merged at this point.

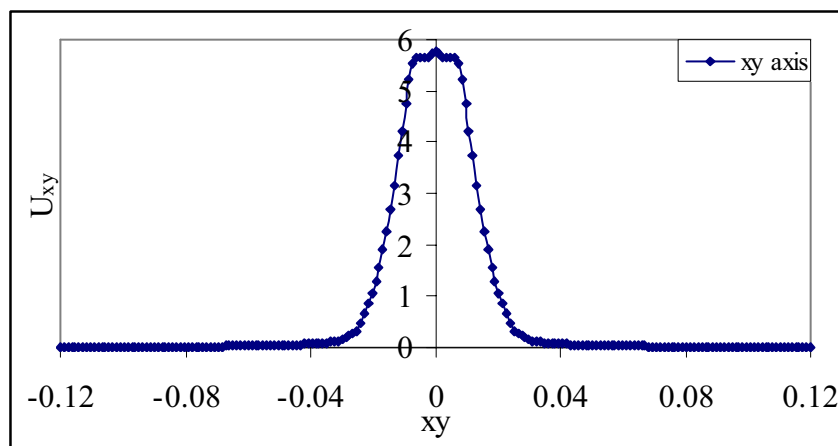


Fig 7.76 xy velocity profile at first merging point of 3d 4J 12 by 10+8 by 10 P6

The velocity profiles and velocity plot of the same jet at the final merging point are shown in figures 7.77 and 7.78.

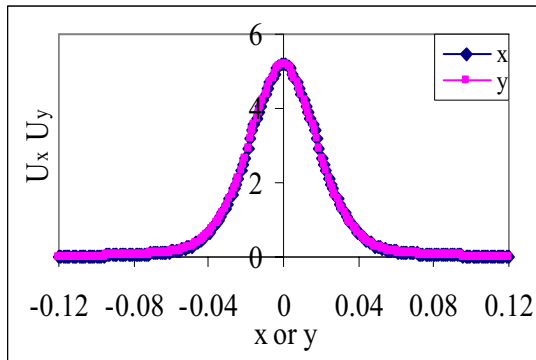


Fig 7.77 x and y velocity profiles at final merging point of 3d 4J 12 by 10+8 by 10 P6

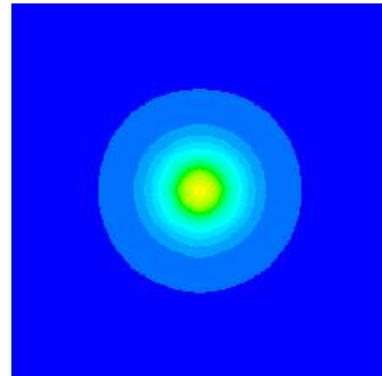


Fig 7.78 Velocity plot at final merging point of 3d 4J 12 by 10+8 by 10 P6

The velocity profiles and the velocity plot at this final merging point shows clear indications of complete merging of all the five jets. The velocity profile is similar to that of a single jet and the velocity plot is circular at centre showing that the jet has got only one core at this point. This merging condition is further confirmed by Fig 7.79 which shows the xy axis profile at this point. This plot also confirms that the merging is complete at this point.

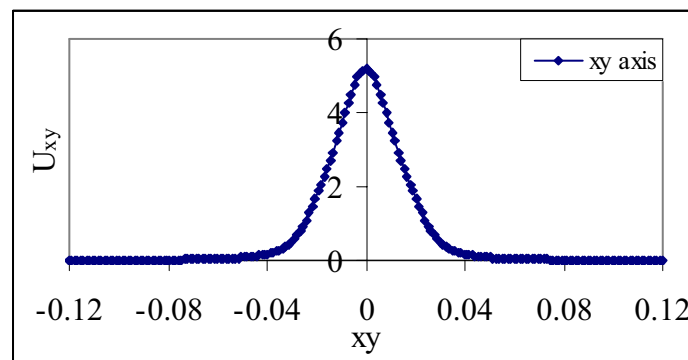


Fig 7.79 xy velocity profile at final merging point of 3d 4J 12 by 10+8 by 10 P6

All the three jet modules are analyzed for their merging characteristics in the similar method. All jet modules confirm to this merging conditions. The velocity

profiles and plots at final merging point of the other two jet modules are given in figures 7.80 to 7.85.

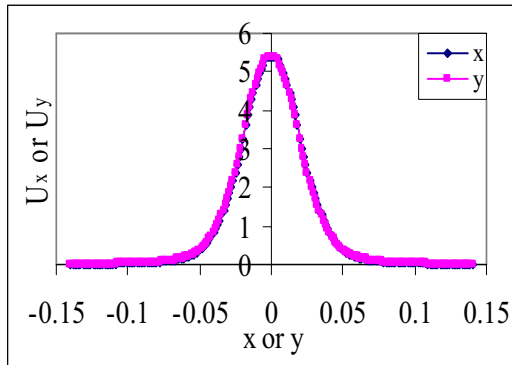


Fig 7.80 x and y velocity profiles at final merging 3d 4J 14 by 10+8 by 10 P6

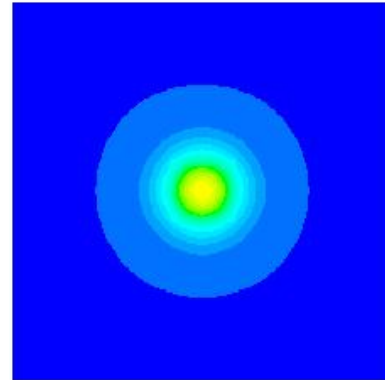


Fig 7.81 Velocity plot at final point of merging point of 3d 4J 14 by 10+8 by 10 P6

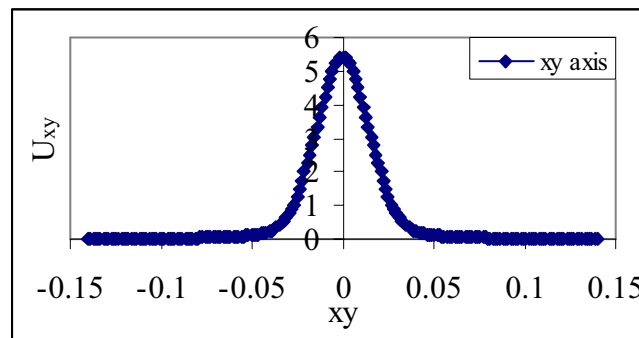


Fig 7.82 xy velocity profile at final merging point of 3d 4J 14 by 10+8 by 10 P6

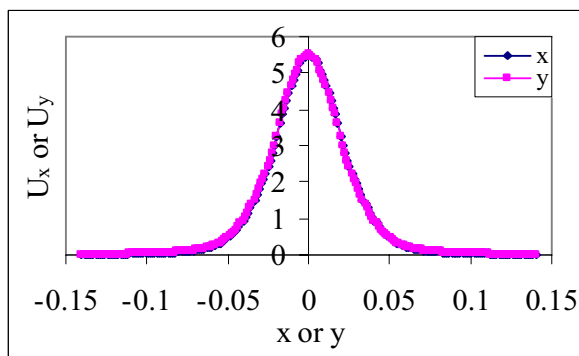


Fig 7.83 x and y velocity profiles at final merging point of 3d 4J 14 by 10+10 by 10 P6

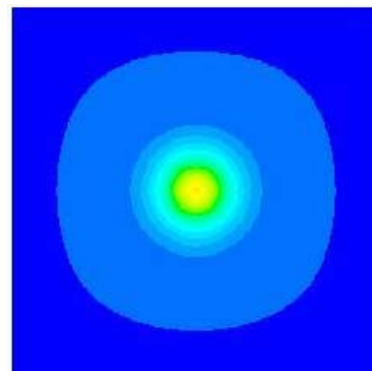


Fig 7.84 Velocity plot at final merging point of 3d 4J 14 by 10+10 by 10 P6

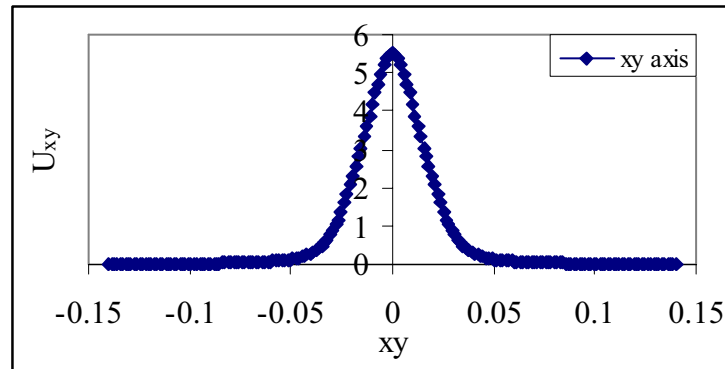


Fig 7.85 xy velocity profile at final merging point of 3d 4J 14 by 10+10 by 10 P6

The mass flow rates, merging locations and the velocity values are given in the Table 7.7.

Table 7.7 Comparison of mass flow rates and velocities of 3D five jet modules.

Model	$m_a * 10^3$	U_0	U_{0c}	x_m	U_m	U_{av}
3d4J12by10+8by10P6	4.8553	7.8743	7.8654	0.22338	5.1804	1.30315
3d4J14by10+8by10P6	6.4172	7.8834	7.8864	0.25092	5.3983	1.50102
3d4J14by10+10by10P6	6.6844	7.8788	7.8944	0.27549	5.5132	1.46179

U_{0c} - Central jet velocity m/sec

The mass flow rates obtained for individual jets of five jet modules are higher than that of a corresponding single jet. As the number of jet increases, the mutual entrainment increases. This will increase the jet velocities, which is evident from the table, and the increased velocity will increase the flow rates through the orifices. The merging point location and merging velocity is comparably lower for the first configuration with respect to the other two. Among the other two models with the same diameter four jet modules as base structure, as the central jet diameter increases the merging location and velocity increases but the average velocity beyond merging point reduces. The velocity distributions of the three five jet modules are compared with the corresponding base four jet module in figure 7.86.

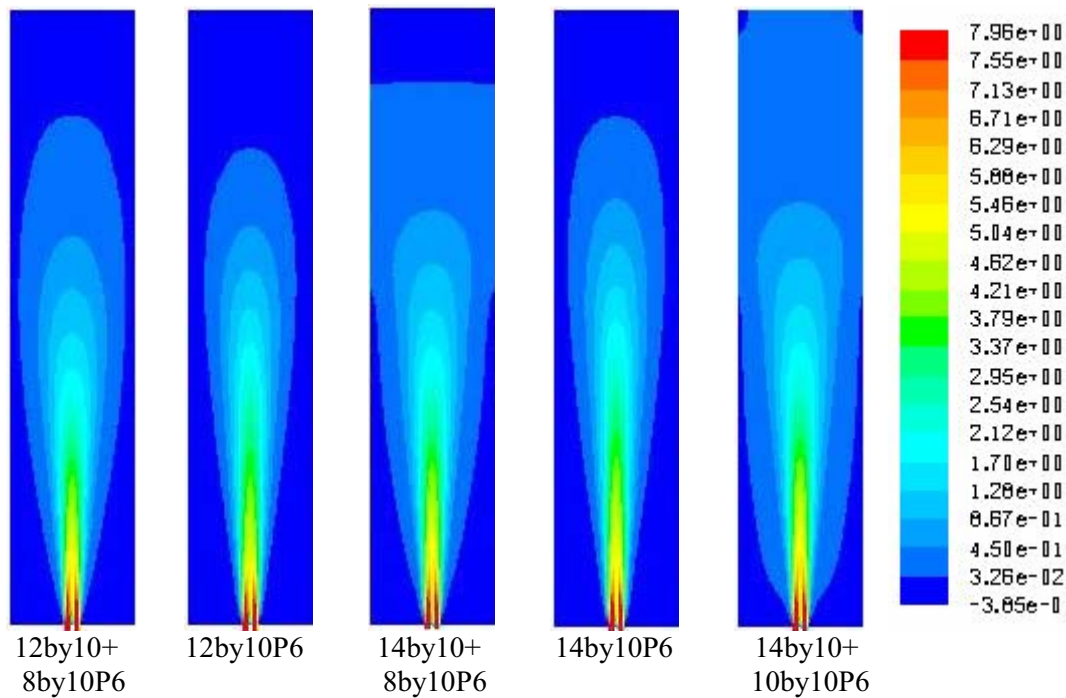


Fig 7.86 Comparison of velocity distribution of 5 jet modules with 4 jet modules.

The velocity distribution of 12 by 10 P6 and the corresponding five jet module with 8 by 10 jet is comparable but the five jet module shows more spread in the x and y direction and the spread is increasing from the jet exit itself. This is more predominant in the 14 by 10 five jets. When the 14 by 10 P6 four jet module is made a five jet module by introducing an 8 by 10 jet at the centre the velocity profile changes considerably. The spread increases more and it starts from the jet exit. The presence of a 10 by 10 jet at the centre causes the spread to extend and the spread near the jet exit increases. But even though the spread increases, the velocities decrease beyond the merging point. The average velocity calculated also shows a decrease in its value.

This shows that the diameter of jet at the centre of a five jet module has got significant effect on the jet velocity profile. But the central jet diameters cannot be increased beyond certain values. The minimum difference between the central and main jet diameter must be 4mm so that the minimum clear distance between the

orifices should be above 2mm. Even this 2mm clearance between orifices is not safe from practical point of view since it will affect the strength of the tile. So this minimum clearance can be considered only as a special case in tile design.

7.9 Conclusion

In this chapter, a detailed study of the three dimensional jets are presented. Studies made on single jet models revealed the significance of grid pattern that is to be used to trace the circular profile of the orifice. The mass flow correction factors that are to be used for other grid configurations are found out to get corrected mass flow rates. The velocity correction factors are also determined for other grid configurations but the correction factors are very close to unity since the velocity is more dependant on the pressure difference. The results of plane jet analysis were highly useful in the analysis of the multiple jets. The merging characteristics of multiple three dimensional jets are completely defined with the help of plane jet merging characteristics.

The basic jet modules for the standard tile and for combination tile are introduced as four jet module and five jet module respectively. The five jet module showed much different velocity patterns when compared with other configurations. When a central jet is introduced between a four jet module with pitch 4mm, the minimum clearance between the central jet and the main jet will be very much less than the pitch values. This minimum clearance is a function of the difference between the diameters of the main jet and the central jet. Clearance values below 2mm are practically not feasible as it will affect the strength of the tile. The safe minimum difference between the diameters must be 4mm in order to get a clearance higher than 2mm.

With the introduction of a central jet at the centre of a four jet module, the clear distance between the central jet and the main jet will be lower than the distance between the main jets (equal to pitch value). Hence the interaction of the

main jet with the central jet will be more intense than the interaction between two main jets themselves. This will alter the merging characteristics at the beginning and result in a different velocity distribution. The velocity distribution shows increased spread near the bottom of the jet as the central jet diameter increases which results in more mixing of the fluid within this jet module. Hence the use of combination tiles will help in getting more distributed velocity profiles within the cold aisle of a data centre. But it is not practically feasible to make combination with larger diameter jets at the centre as it will reduce the strength of the tile. So the combination tiles can be tried only for special applications.

The information obtained from the study of three dimensional jets are used for the design and analysis of full tiles of 2 feet by 2 feet (609.6 mm by 609.6mm) in dimension with number of orifices ranging from 650 to 1500.

.....END.....

DESIGN AND ANALYSIS OF PERFORATED VENT TILES

Contents	8.1 Introduction
	8.2 Tile Design and Solution Domain
	8.3 Tile Calculations
	8.4 Results and Discussion
	8.5 Conclusion

8.1 Introduction

In this chapter, design designation and analysis of perforated vent tiles are discussed. A tile designation code is introduced to identify the individual tiles based on their basic design parameters such as orifice diameter, tile thickness, clear unpunctured distance between adjacent orifices (pitch) and the open area ratio of the tile. For example a tile bearing a designation code of C10T10P4A30 refers to a standard perforated tile of orifice diameter 10mm, tile thickness 10mm, pitch 4mm and open area ratio of 30%. In this chapter the design and analysis of six standard tiles and one combination tile are discussed. The combination tile includes an additional matrix of orifices with smaller diameter than the base orifices placed in the intermediate spaces. The combination tile discussed is designated as C14C8T10P6A40. It refers to 14mm orifices with 6mm pitch on a 10mm thick tile, 8mm orifices are introduced into the intermediate spaces thereby increasing the open area ratio to 40%. The mass flow rate and the velocity distribution of all these tiles for different pressure difference across them are obtained by modelling each tiles and presented along with each tile.

8.2 Tile Design and Solution Domain

The conventional perforated vent tiles used in the data centre are having a standard dimension of 2 feet by 2 feet (609.6 mm by 609.6mm). Since the new tile

has to meet the industry standards, the tiles are designed for the same dimensions as that of the conventional tiles. The tile thickness can be varied in a narrow band and in this design the tile thickness is fixed as 10mm. The effects of tile thickness on operating parameters are explained in Chapter 6. Tile thickness is having another practical significance. As tile thickness increases, the weight of the tile increases which will introduce difficulty in lifting the tiles for inspection of under floor plenum which is a part of usual maintenance practice. High thickness of tiles will increase the cost also. Hence the thickness of the tiles is limited to 10-12mm which is satisfactory from the strength point of view of the tile. For a standard tile, a thickness of 10mm is sufficient from flow and strength point of view; but for a combination tile, larger thickness is preferred from the strength point of view.

The raised floor in a data centre is constructed by using mild steel fabrication which employs 1.5 inches (38.1mm) angle iron for making the floor and tile supports. Hence the design leaves a distance of 1.5 inches (38.1mm) from all four edges of the tile since any orifice punched in this region will be obstructed by the steel fabrication support. So the effective region available on a tile for perforation is only 21 inch by 21 inch (533.4mm by 533.4mm). Different tile geometries are developed by punching orifices of desired diameter at desired pitch values.

In the CFD analysis, if the full tile geometry is modelled, even for a coarse meshing pattern the number of grid cells will be very large and this will make the solution difficult and time consuming. Hence the modelling methodology followed in the present work considers only quarter portion of the tile since the tile is symmetrical about both the axes. In this way the number of grid cells can be reduced to 25% and better grid patterns can be selected for models for better accuracy. After solving the model the full tile can be developed from the quarter tile by using the symmetry boundary conditions assigned to respective boundaries. The modelling and solution methodology employed for tiles are similar to that followed in the previous chapters. The boundary condition 'pressure inlet' is used

to apply the pressure difference across the tiles and the 'symmetry' boundary condition will help in developing the full tile features. The analysis domain of the problem in the vertical (z) direction is selected as 2133.6 mm (7 feet) since the standard computer racks used in the data centres are having a height of 7 feet and the tiles are supposed to supply air up to this height. The basic boundary types and the basic tile dimensions are highlighted in figures 8.1(a) and (b).

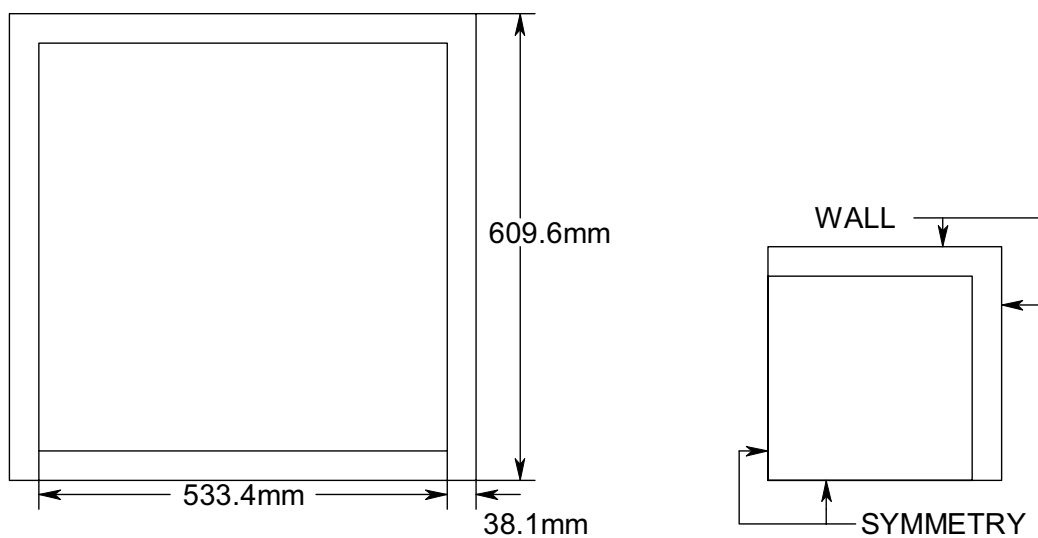


Fig 8.1 (a) Basic tile dimensions

(b) Quarter tile boundary conditions

For obtaining the flow rates and velocity distribution of the tiles, the boundary conditions are selected accordingly for the solution domain. The operation of a tile in a data centre is truly dynamic in nature. The flow rate through a tile in a real situation depends on the under floor plenum pressure, the rack suction pressure and the exit pressure of the tile at 7 feet height. It is not possible to standardize the flow and velocity profiles of a vent tile in a dynamic environment. Hence for standardizing the flow and for velocity calculations the tiles are assumed to be discharging into a confined volume with only one driving potential as the pressure difference across the tile which is the difference between the under floor plenum pressure and the exit pressure at 7 feet height. In this situation the racks are assumed to be non

functional. Since the rack suction pressure is not constant for all racks on the floor and within a rack, the suction pressure may be different depending on the hardware located on the racks at different heights. This situation is modelled by assigning the 'wall' boundary condition as shown in Fig 8.1(b). The exit face of the tile at 7 feet height is assigned the boundary condition of 'pressure outlet'. Here the tile is discharging into a confined volume due to a pressure difference existing between the under floor plenum and the tile exit at 7 feet height. The pressure outlet boundary condition will assume atmospheric pressure by default. The pressure inlet boundary condition assigned to the orifice inlet will be given excess pressures as ΔP ranging from 6.229Pa to 37.376Pa during the modelling.

While meshing the circular orifices the grid pattern selected is 2 grid points per face in order to reduce the number of grid cells. The flow rates are corrected with the help of mass flow correction factors obtained in Chapter 7. The velocity correction factors are not employed in the analysis since their values are very close to one. The models are solved with gravity consideration as it is done in the previous chapter.

8.3 Tile Calculations

Different tile geometries are developed by punching orifices of different diameters with the required pitch values in the available area of the full tile. The tile open area ratio is calculated from the total area of the full tile and the available orifice area on the tile. The tile area is calculated on the basis of full tile dimension of 2 feet by 2 feet. Hence

$$\text{Total tile area available} = (24 * 2.54)^2 \text{ cm}^2 = 3716.1216 \text{ cm}^2$$

The remaining calculation is explained for each tile in the following sections.

8.3.1 Tile C10T10P4A30

In this standard tile, 10mm orifices are punched on a 10mm thick plate in such a way that the minimum distance between successive orifices in both directions are 4mm.

Total number of orifices punched on the plate = 1444

Area of each orifice = 0.7854 cm^2

Total orifice flow area = 1134.1149 cm^2

Open area ratio = $(1134.1149/3716.1216) * 100 = 30.3 \%$

The open area ratio is assigned the value of 30 %. The designed tile is shown in Fig 8.2.

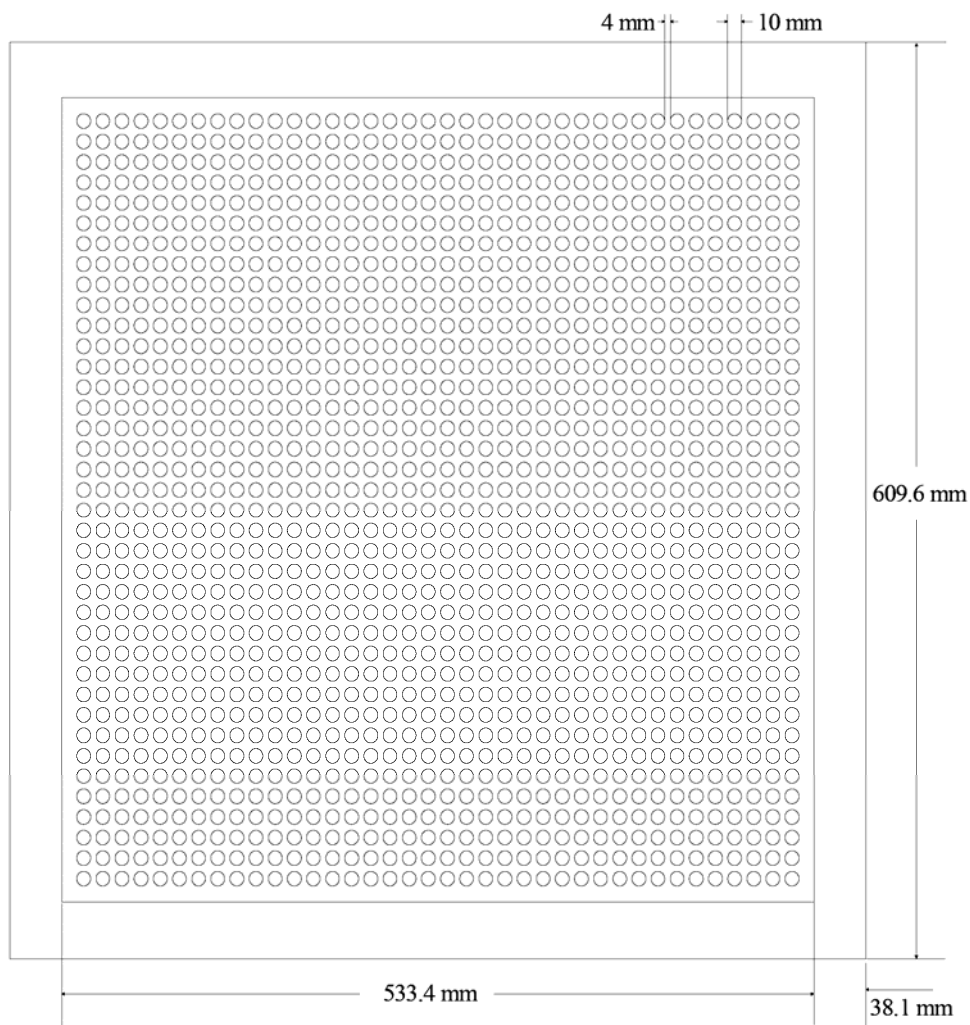


Fig 8.2 Details of standard tile C10T10P4A30

8.3.2 Tile C10T10P6A20

In this standard tile, 10mm orifices are punched on a 10mm thick plate in such a way that the minimum distance between successive orifices in both directions are 6mm.

Total number of orifices punched on the plate = 1024

Area of each orifice = 0.7854 cm^2

Total orifice flow area = 804.2477 cm^2

Open area ratio = $(804.2477/3716.1216) * 100 = 21.64 \%$

The open area ratio is assigned the value of 20 %. The designed tile is shown in Fig 8.3.

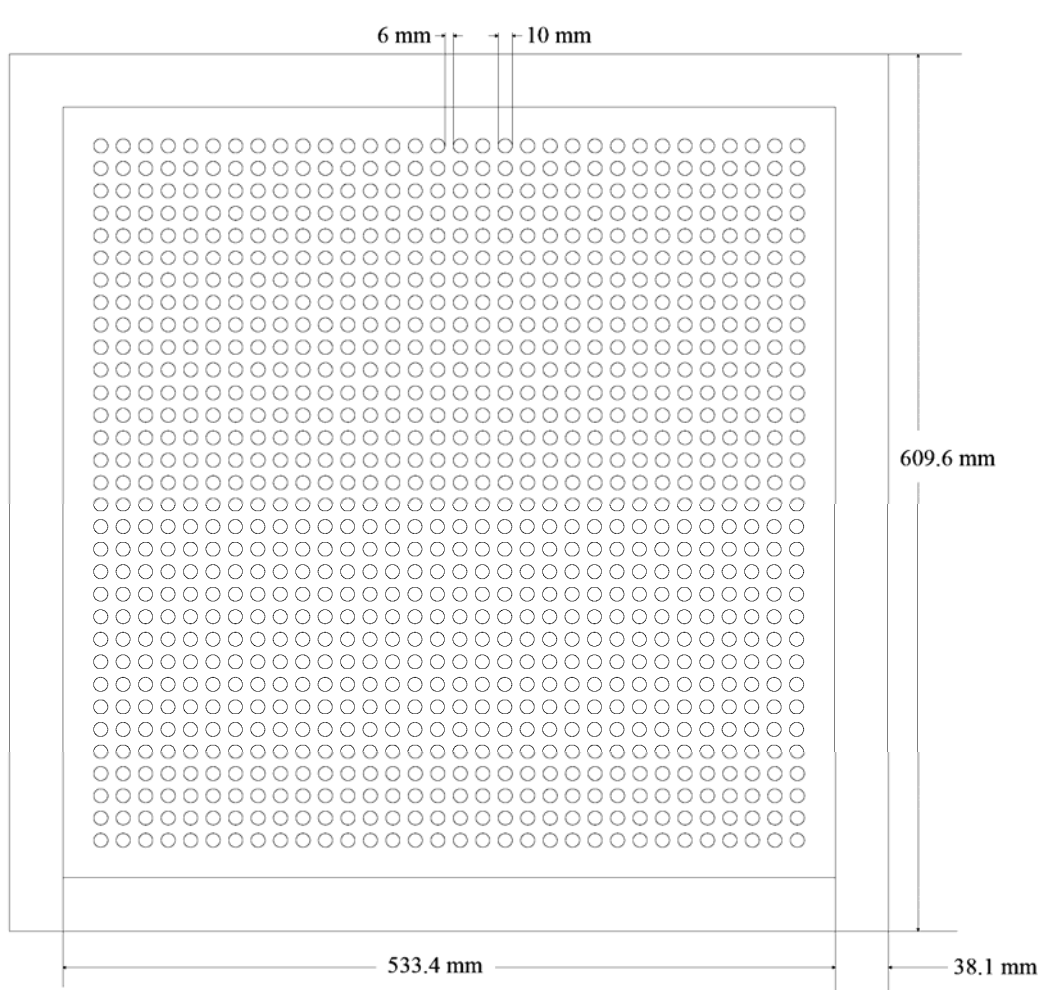


Fig 8.3 Details of standard tile C10T10P6A20

8.3.3 Tile C12T10P4A30

In this standard tile, 12mm orifices are punched on a 10mm thick plate in such a way that the minimum distance between successive orifices in both directions are 4mm.

Total number of orifices punched on the plate = 1024

Area of each orifice = 1.13097 cm^2

Total orifice flow area = 1158.1167 cm^2

Open area ratio = $(1158.1167/3716.1216) * 100 = 31.165 \%$

The open area ratio is assigned the value of 30%. The designed tile is shown in Fig 8.4.

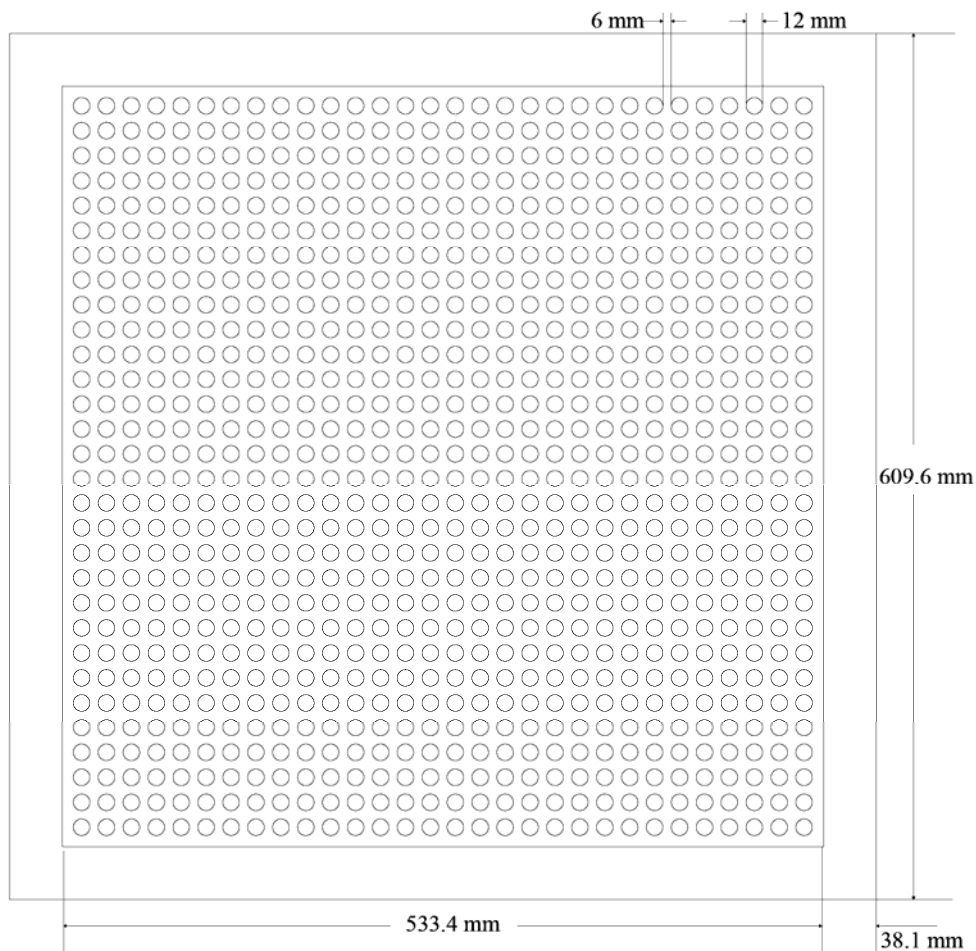


Fig 8.4 Details of standard tile C12T10P4A30

8.3.4 Tile C12T10P6A25

In this standard tile, 12mm orifices are punched on a 10mm thick plate in such a way that the minimum distance between successive orifices in both directions are 6mm.

Total number of orifices punched on the plate = 900

Area of each orifice = 1.13097 cm^2

Total orifice flow area = 1017.876 cm^2

Open area ratio = $(1017.876/3716.1216) * 100 = 27.391 \%$

The open area ratio is assigned the value of 25 %. The designed tile is shown in Fig 8.5.

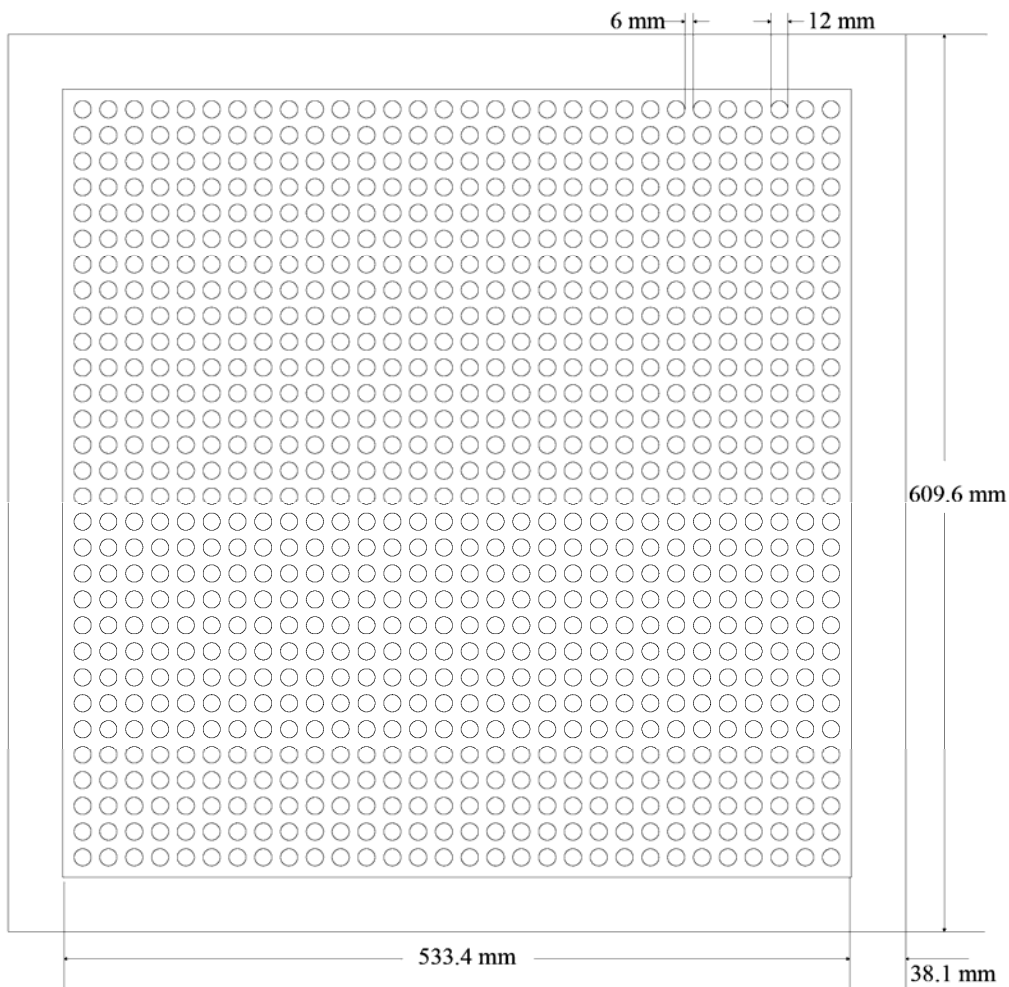


Fig 8.5 Details of standard tile C12T10P6A25

8.3.5 Tile C14T10P4A40

In this standard tile, 14mm orifices are punched on a 10mm thick plate in such a way that the minimum distance between successive orifices in both directions are 4mm.

Total number of orifices punched on the plate = 900

Area of each orifice = 1.5394 cm^2

Total orifice flow area = 1385.442 cm^2

Open area ratio = $(1385.442/3716.1216) * 100 = 37.282 \%$

The open area ratio is assigned the value of 40 %. The designed tile is shown in Fig 8.6

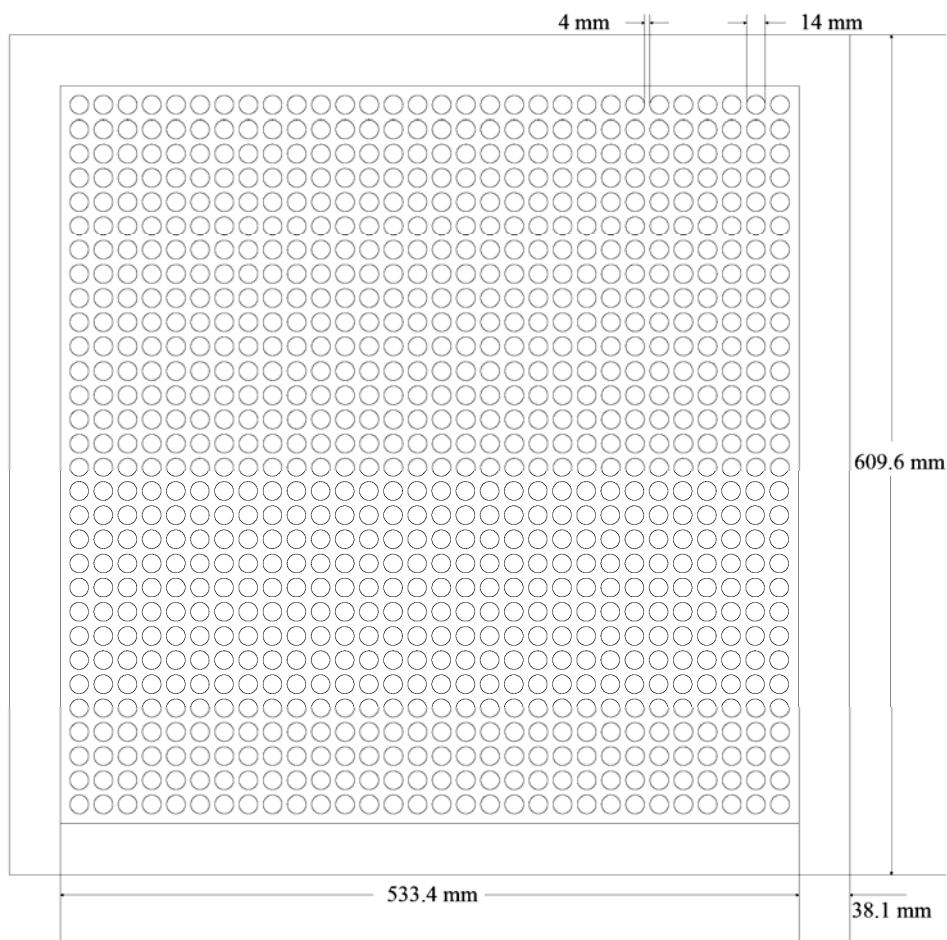


Fig 8.6 Details of standard tile C14T10P4A40

8.3.6 Tile C14T10P6A30

In this standard tile, 14mm orifices are punched on a 10mm thick plate in such a way that the minimum distance between successive orifices in both directions are 6mm.

Total number of orifices punched on the plate = 676

Area of each orifice = 1.5394 cm^2

Total orifice flow area = 1040.621 cm^2

Open area ratio = $(1040.621/3716.1216) * 100 = 28.002 \%$

The open area ratio is assigned the value of 30 %. The designed tile is shown in Fig 8.7

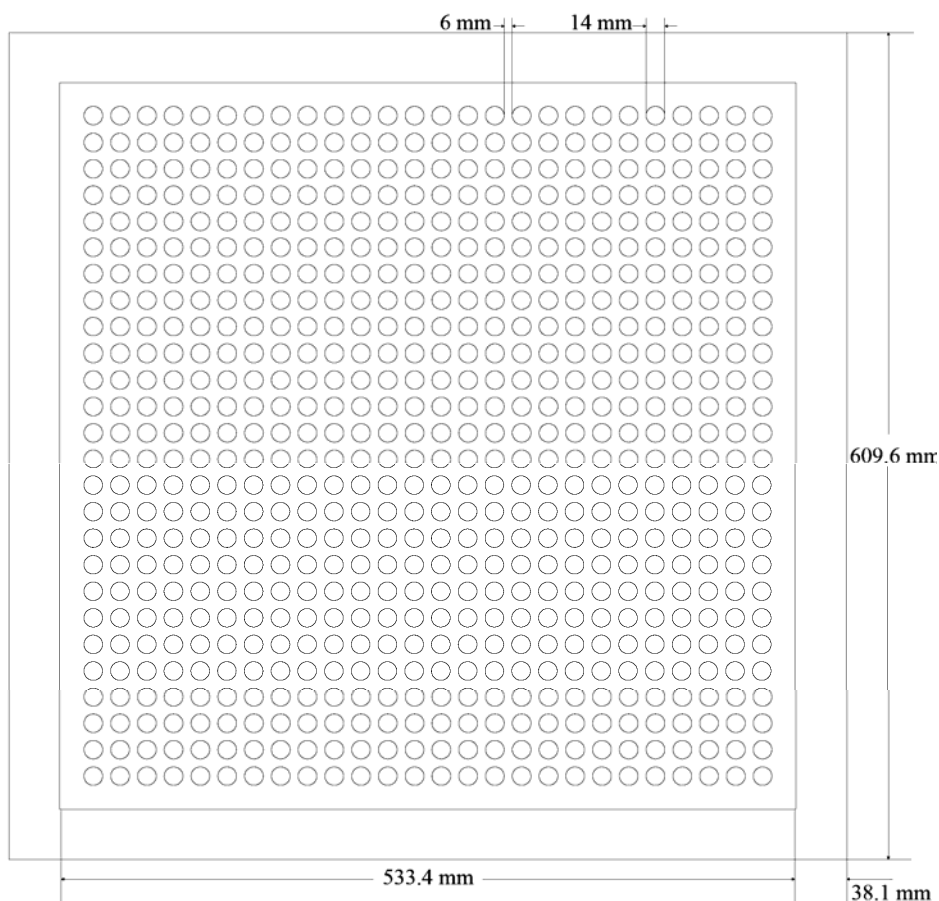


Fig 8.7 Details of standard tile C14T10P6A30

8.3.7 Tile C14C8T10P6A40

In this combination tile, 14mm orifices are punched on a 10mm thick plate in such a way that the minimum distance between successive orifices in both directions are 6mm. 8mm orifices are punched in the intermediate space to fill the matrix. Here the diagonal distance between the 14mm orifice and 8mm orifice is less than the pitch value.

Total number of 14mm orifices punched on the plate = 676

Total number of 8mm orifices punched on the plate = 729

Area of 14mm orifice = 1.5394 cm²

Area of 8mm orifice = 0.50265 cm²

Total orifice flow area = 1407.069 cm²

Open area ratio = (1407.069/3716.1216) *100 = 37.864 %

In the design of combination tile, the standard pitch values cannot be maintained between the larger and smaller orifices. The diagonal distance between the orifices will be less than the pitch values in a combination tile. Hence all combinations of orifices cannot be employed for designing combination tile. The introduction of 10mm orifice in between a matrix of 14mm orifices will lead to a minimum diagonal distance less than 2mm which is insufficient from the strength point of view and it is required to increase the tile thickness to a larger value for compensating the loss of material. Large tile thickness is not at all advisable simply due to increased weight and cost along with the flow problems as discussed in Chapter 6. Hence the design of combination tiles is suggested as custom made depending on the demand. Combination tiles can be designed according to the flow requirements. 10mm orifice matrix can be augmented only with orifices with diameters less than 6mm. 12 mm matrix can be augmented with orifices with diameter 6mm or below and 14mm matrix can be augmented with orifices with diameter 8mm or less.

The open area ratio is assigned the value of 40 %. The designed tile is shown in Fig 8.8.

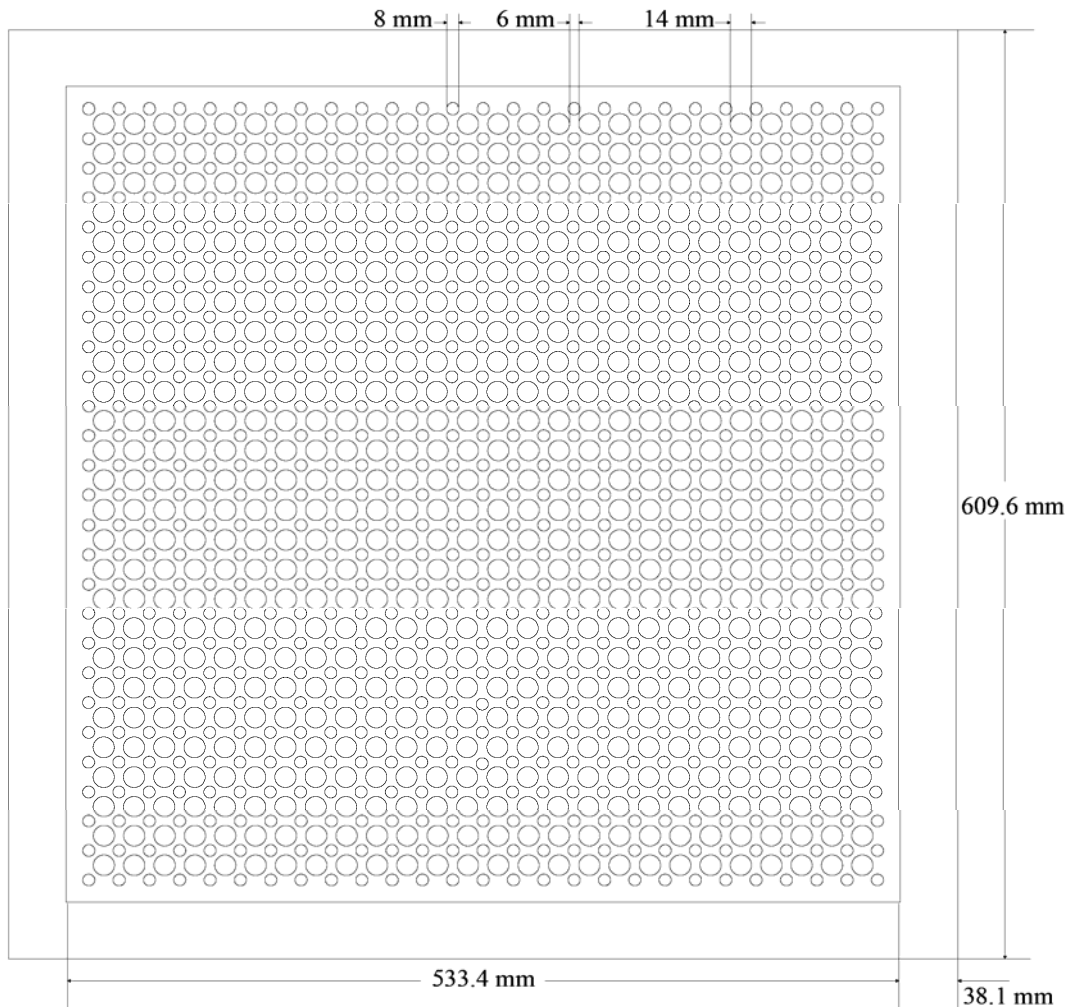


Fig 8.8 Details of combination tile C14C8T10P6A40

8.4 Results and Discussion

All the seven tiles are modelled and analyzed for different pressure differences across them. The converging criteria for all the cases were fixed at residual values less than 10^{-5} . The flow rates are obtained for each case and corrected to obtain the actual mass flow rate. The values of mass flow rates are plotted against the respective pressure drop across the tile for each tile. For all the tiles, the best curve fitted for the data follows power series. The equation of the

best fit curve is selected for each tile and is calibrated with standard values to get the characteristic flow rate curve for all tiles. The centre line velocity decay of all the tiles at different pressure difference across them is plotted. The velocity profiles along the x direction of the tiles at different height along the z direction are also compared. From these plots it is possible to get the velocity values at different x and z positions of the tile thereby defining the tile flow qualitatively. The velocity plots at different z positions are also made to obtain an understanding about the tile flow characteristics. All these results are discussed separately by considering each tile in the following sections.

8.4.1 Tile C10T10P4A30

The mass flow rates for the tile obtained are given in the Table 8.1. The corrected mass flow rates are obtained by multiplying the theoretical mass flow rate by the correction factor. The mass flow rate is expressed in both CFM and CMM and is given in the Table 8.1.

Table 8.1 Mass flow rate of tile C10T10P4A30

	ΔP Pa	37.376	31.147	24.917	18.688	12.459	6.229
C10T10P4A30	ΔP in of H ₂ O	0.15	0.125	0.1	0.075	0.05	0.025
mass flow correction	m_{th} Kg/sec	1.2833	1.1699	1.0446	0.9026	0.7329	0.5107
factor = 1.1296	m_{act} Kg/sec	1.4496	1.3215	1.18	1.0196	0.8279	0.5769
	CFM	2508	2286	2041	1764	1432	998
	CMM	71.0266	64.7395	57.8011	49.9565	40.5542	28.2634

m_{th} - theoretical mass flow rate obtained by the solution Kg/sec

m_{act} - corrected mass flow rate Kg/sec

CFM - Cubic Feet per Minute

CMM – Cubic Meter per Minute

Graphs are plotted for ΔP Pa vs CMM and ΔP inches of H₂O vs CFM. The best fit for both cases is found to be power series and the expressions for both the cases are obtained as follows.

For,

$$\Delta P \text{ Pa vs CMM} - 11.063 x^{0.514}$$

$$\Delta P \text{ inches of H}_2\text{O vs CFM} - 6663.3 x^{0.514}$$

The flow rates are calibrated for 0 -100 Pa and 0 – 0.4 inches of water column and are presented in Fig 8.9 and 8.10 as the characteristic calibration curve for the tile.

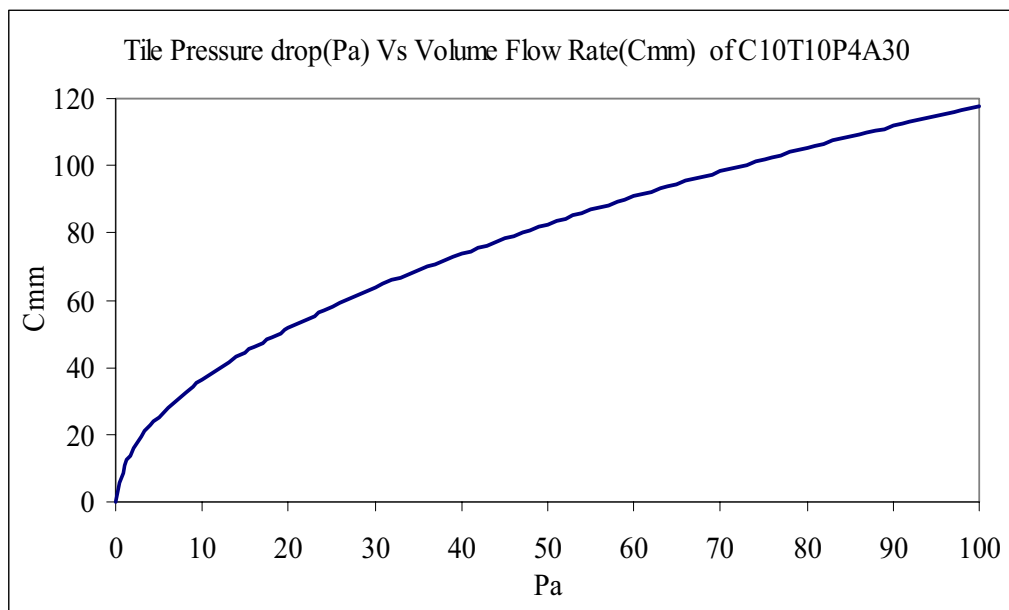


Fig 8.9 Mass flow rate calibration curve for tile C10T10P4A30 (a).

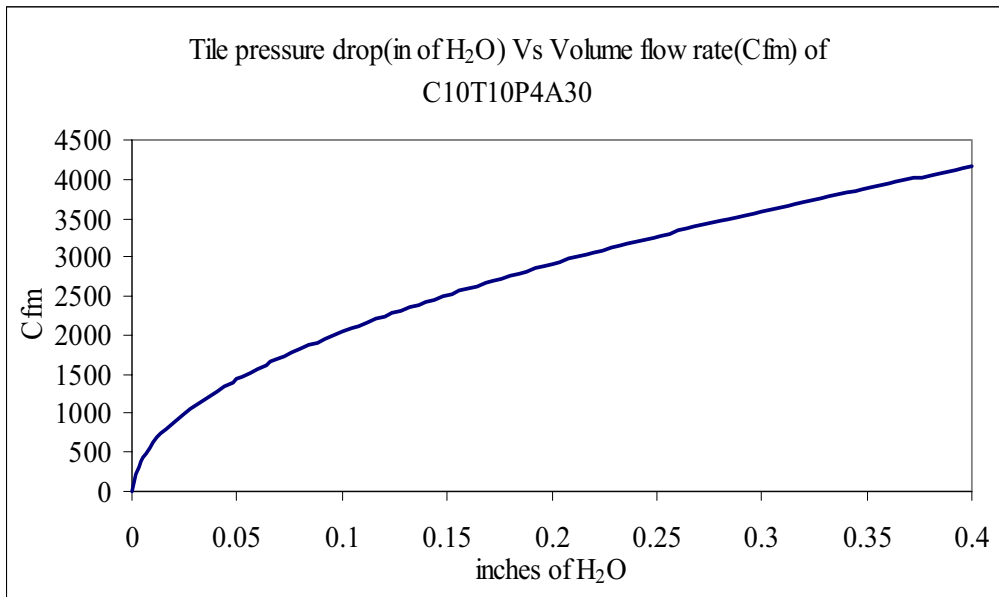


Fig 8.10 Mass flow rate calibration curve for tile C10T10P4A30 (b).

The variation of centre line velocity for various pressure differences across the tile is given in Fig 8.11.

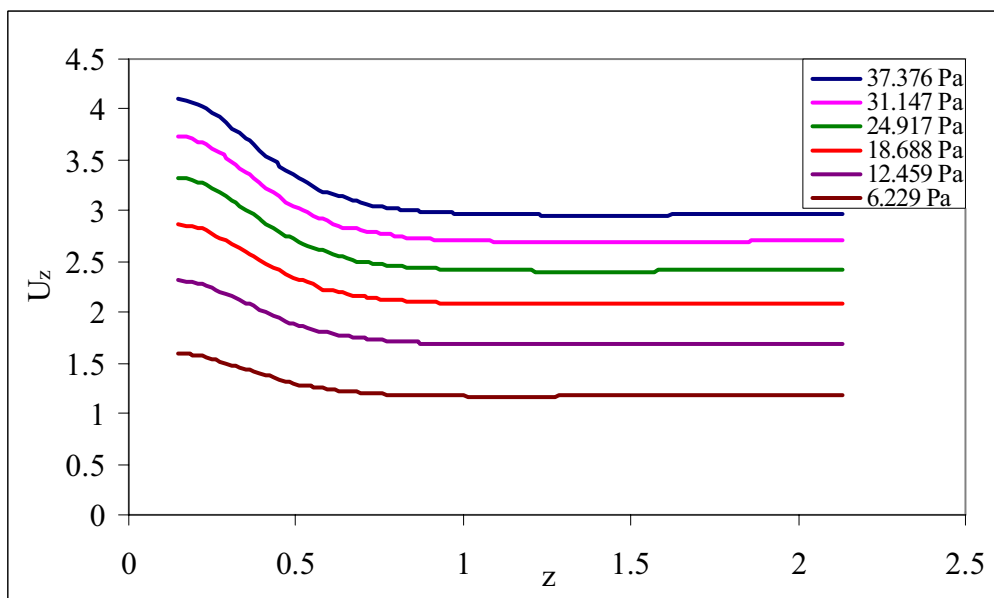


Fig 8.11 Variation of centre line velocity of tile C10T10P4A30 for various pressure differences

The variation of velocity along the x direction of the tile at different z positions for different pressure differences is given in Fig 8.12(a) to (f).

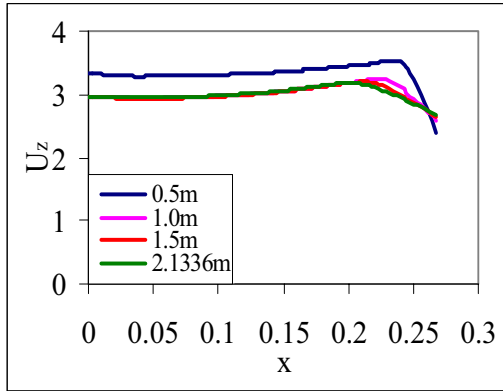
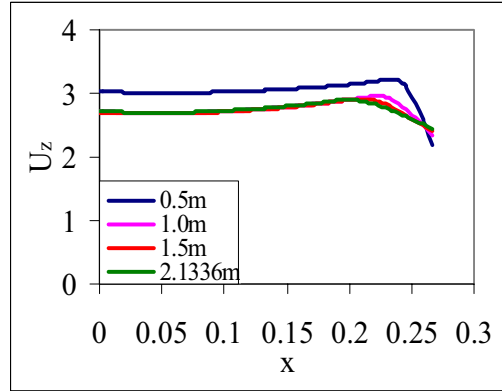


Fig 8.12 (a) Velocity in x direction for various z positions for $\Delta P = 37.376$ Pa



(b) Velocity in x direction for various z positions for $\Delta P = 31.147$ Pa

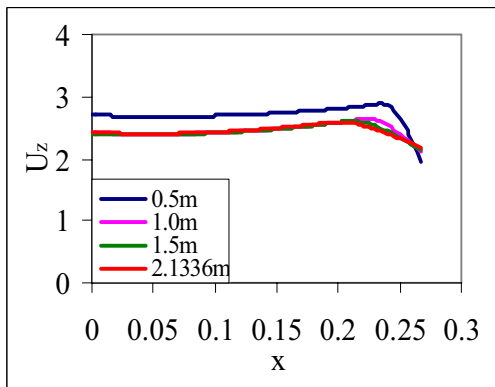
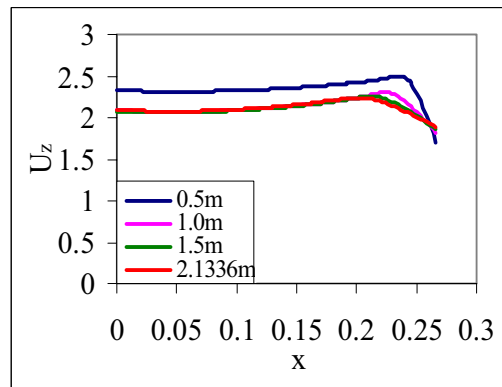


Fig 8.12 (c) Velocity in x direction for various z positions for $\Delta P = 24.917$ Pa



(d) Velocity in x direction for various z positions for $\Delta P = 18.668$ Pa

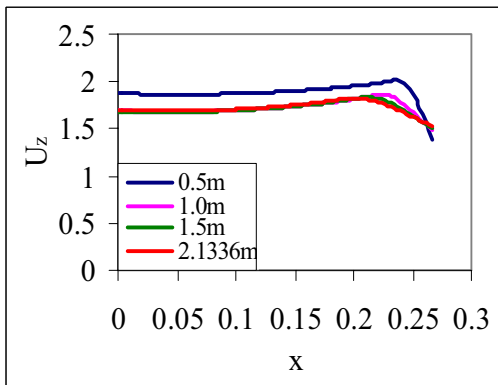
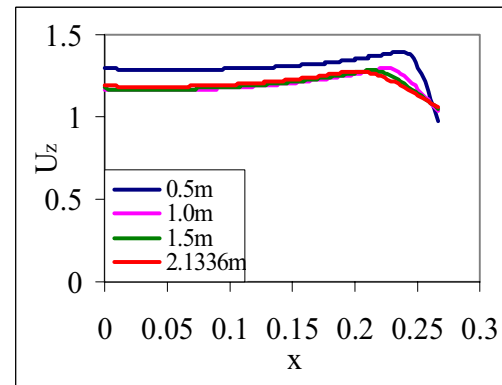


Fig 8.12 (e) Velocity in x direction for various z positions for $\Delta P = 12.459$ Pa



(f) Velocity in x direction for various z positions for $\Delta P = 6.229$ Pa

The velocity plots at different z locations for different pressure differences are given in figures 8.13 to 8.18.

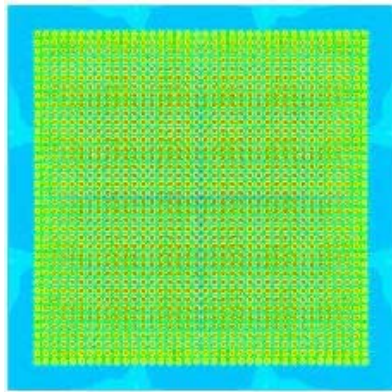
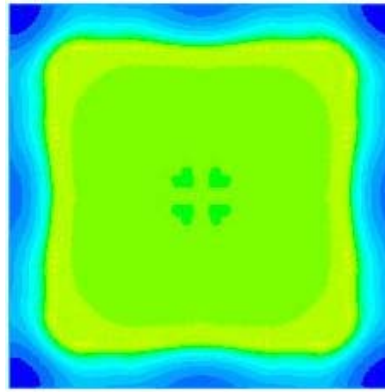
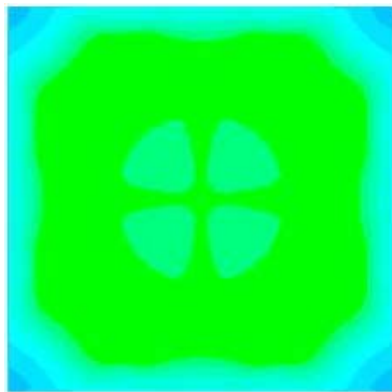


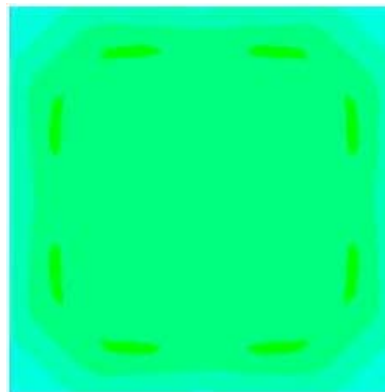
Fig 8.13 (a) Velocity plot at $z = 0.01$ m for $\Delta P = 37.376$ Pa



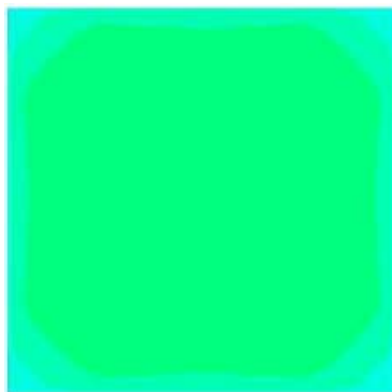
(b) Velocity plot at $z = 0.15$ m for $\Delta P = 37.376$ Pa



(c) Velocity plot at $z = 0.5$ m for $\Delta P = 37.376$ Pa



(d) Velocity plot at $z = 1.0$ m for $\Delta P = 37.376$ Pa

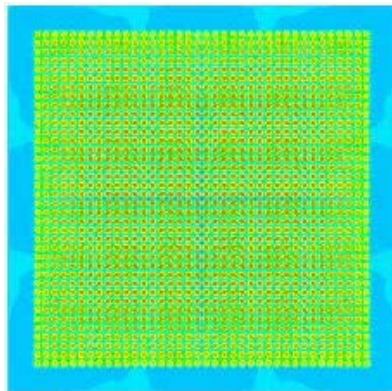


(e) Velocity plot at $z = 1.5$ m for $\Delta P = 37.376$ Pa

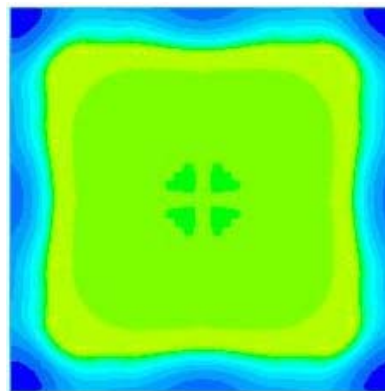


(f) Velocity plot at $z = 2.1336$ m for $\Delta P = 37.376$ Pa

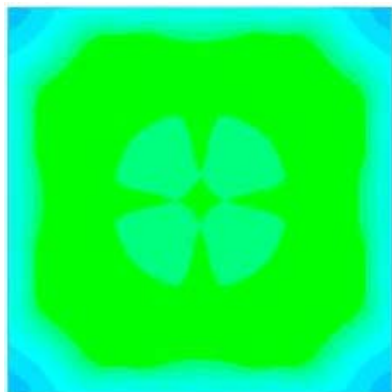




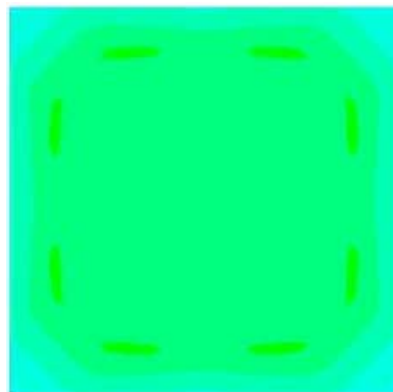
(a) Velocity plot at $z = 0.01$ m for $\Delta P = 31.147$ Pa



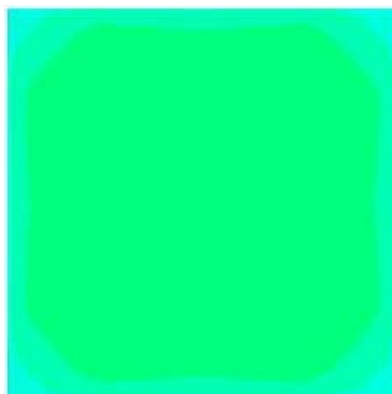
(b) Velocity plot at $z = 0.15$ m for $\Delta P = 31.147$ Pa



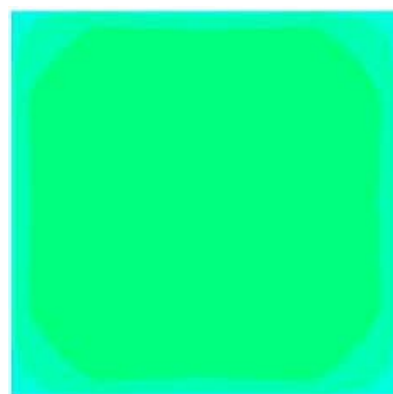
(c) Velocity plot at $z = 0.5$ m for $\Delta P = 31.147$ Pa



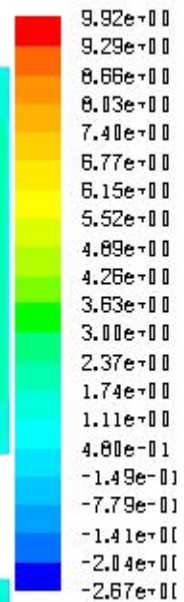
(d) Velocity plot at $z = 1.0$ m for $\Delta P = 31.147$ Pa

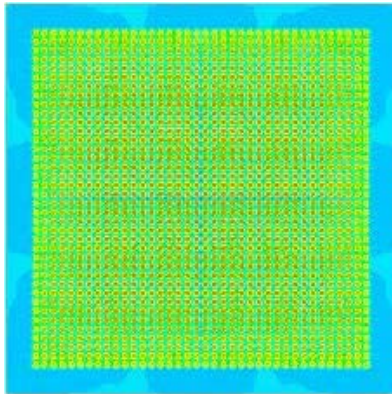


(e) Velocity plot at $z = 1.5$ m for $\Delta P = 31.147$ Pa

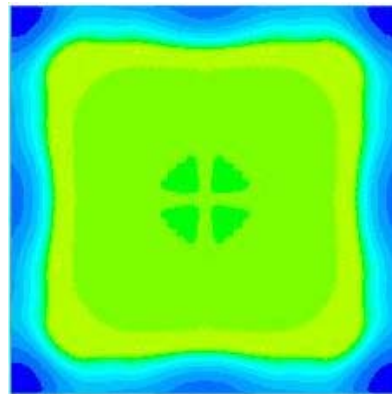


(f) Velocity plot at $z = 2.1336$ m for $\Delta P = 31.147$ Pa

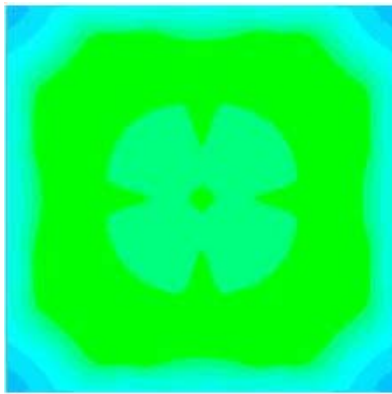




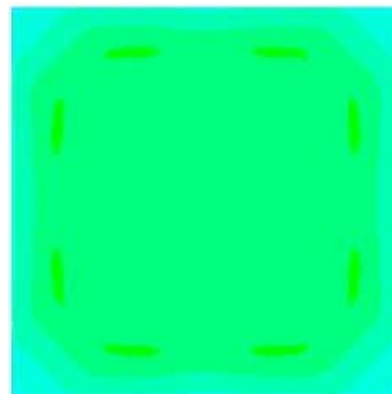
(a) Velocity plot at $z = 0.01$ m for $\Delta P = 24.917$ Pa



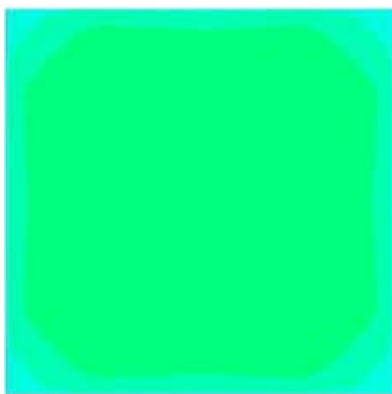
(b) Velocity plot at $z = 0.15$ m for $\Delta P = 24.917$ Pa



(c) Velocity plot at $z = 0.5$ m for $\Delta P = 24.917$ Pa



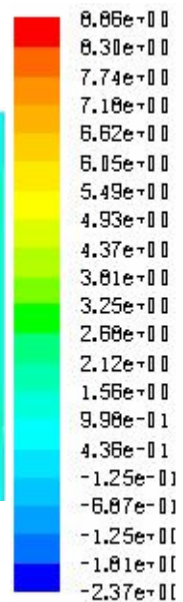
(d) Velocity plot at $z = 1.0$ m for $\Delta P = 24.917$ Pa



(e) Velocity plot at $z = 1.5$ m for $\Delta P = 24.917$ Pa



(f) Velocity plot at $z = 2.1336$ m for $\Delta P = 24.917$ Pa



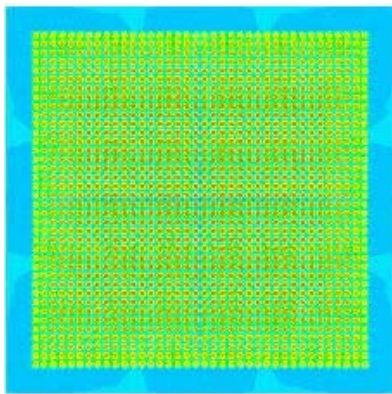
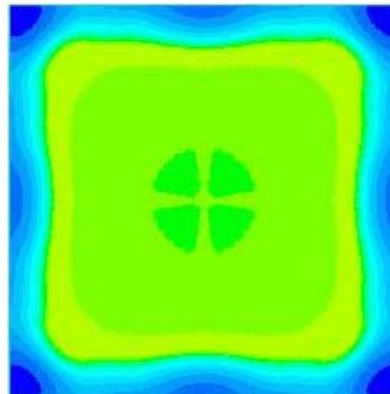
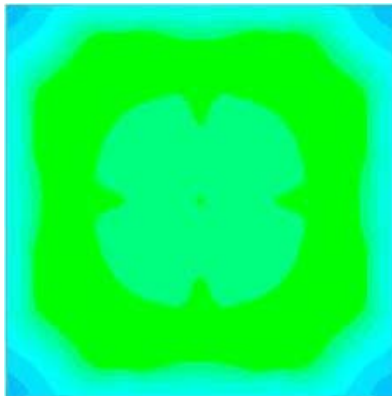


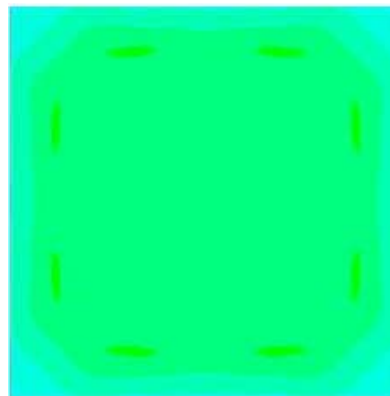
Fig 8.16: (a) Velocity plot at $z = 0.01$ m for $\Delta P = 18.688$ Pa



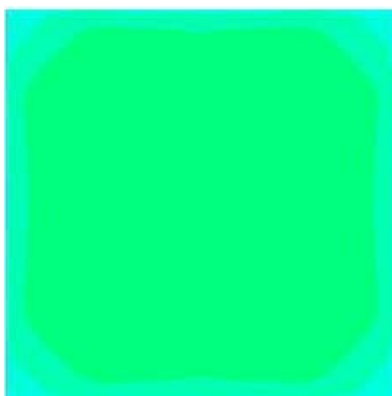
(b) Velocity plot at $z = 0.15$ m for $\Delta P = 18.688$ Pa



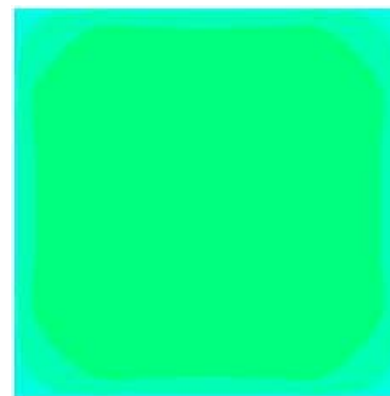
(c) Velocity plot at $z = 0.5$ m for $\Delta P = 18.688$ Pa



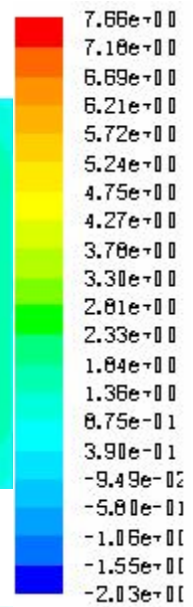
(d) Velocity plot at $z = 1.0$ m for $\Delta P = 18.688$ Pa



(e) Velocity plot at $z = 1.5$ m for $\Delta P = 18.688$ Pa



(f) Velocity plot at $z = 2.1336$ m for $\Delta P = 18.688$ Pa



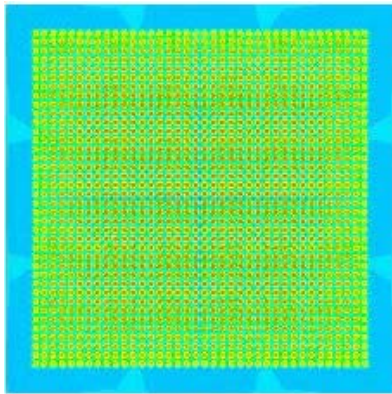
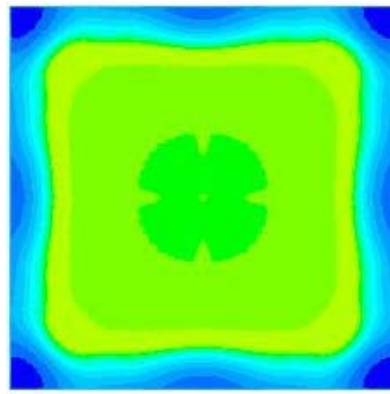
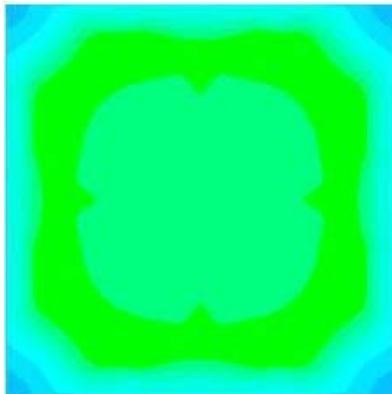


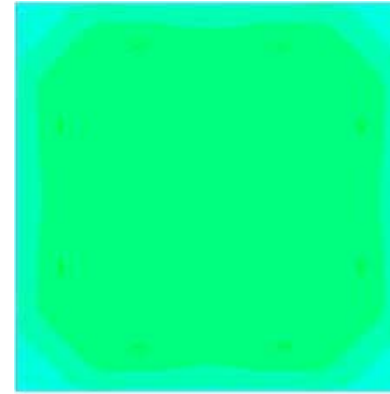
Fig 8.17: (a) Velocity plot at $z = 0.01$ m for $\Delta P = 12.459$ Pa



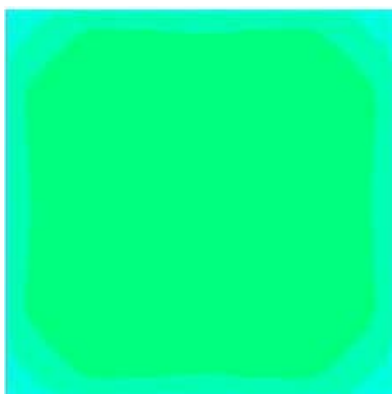
(b) Velocity plot at $z = 0.15$ m for $\Delta P = 12.459$ Pa



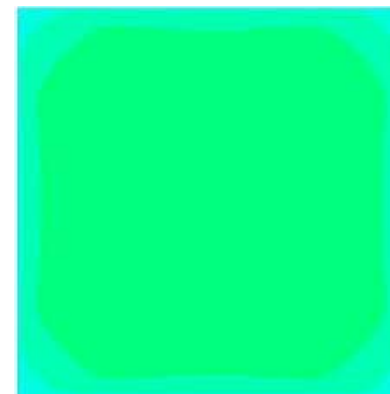
(c) Velocity plot at $z = 0.5$ m for $\Delta P = 12.459$ Pa



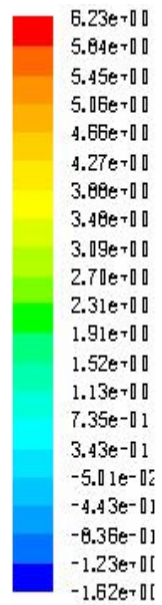
(d) Velocity plot at $z = 1.0$ m for $\Delta P = 12.459$ Pa



(e) Velocity plot at $z = 1.5$ m for $\Delta P = 12.459$ Pa



(f) Velocity plot at $z = 2.1336$ m for $\Delta P = 12.459$ Pa



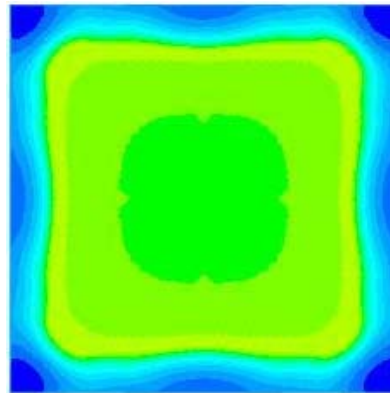
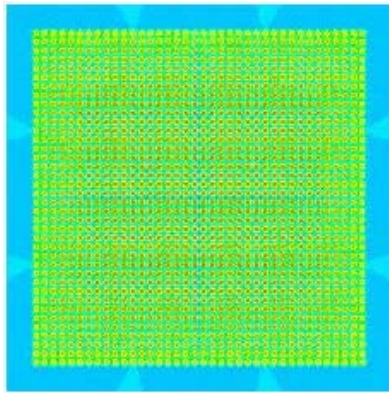
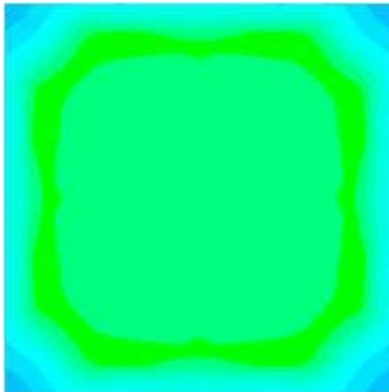


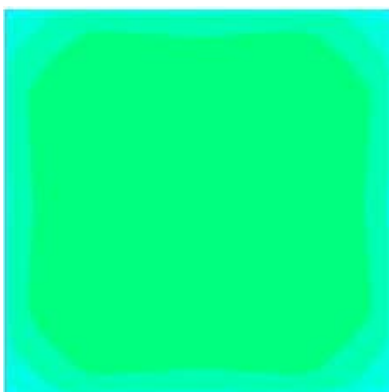
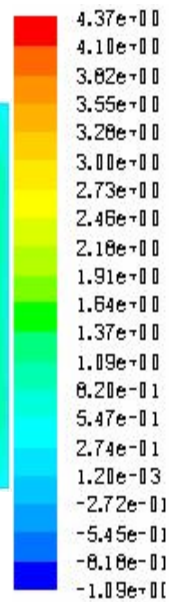
Fig 8.18: (a) Velocity plot at $z = 0.01$ m for $\Delta P = 6.229$ Pa

(b) Velocity plot at $z = 0.15$ m for $\Delta P = 6.229$ Pa



(c) Velocity plot at $z = 0.5$ m for $\Delta P = 6.229$ Pa

(d) Velocity plot at $z = 1.0$ m for $\Delta P = 6.229$ Pa



(e) Velocity plot at $z = 1.5$ m for $\Delta P = 6.229$ Pa

(f) Velocity plot at $z = 2.1336$ m for $\Delta P = 6.229$ Pa

8.4.2 Tile C10T10P6A20

The mass flow rates for the tile obtained are given in the Table 8.2. The corrected mass flow rates are obtained by multiplying the theoretical mass flow rate by the correction factor. The mass flow rate is expressed in both CFM and CMM and is given in the Table 8.2.

Table 8.2: Mass flow rate of tile C10T10P6A20

	ΔP Pa	37.376	31.147	24.917	18.688	12.459	6.229
C10T10P6A20	ΔP in of H ₂ O	0.15	0.125	0.1	0.075	0.05	0.025
mass flow correction	m_{th} Kg/sec	0.8523	0.7774	0.6945	0.6004	0.4879	0.3408
factor = 1.1296	m_{act} Kg/sec	0.9828	0.8781	0.7845	0.6782	0.5511	0.3849
	CFM	1666	1519	1357	1173	953	666
	CMM	47.1811	43.0181	38.4302	49.9565	26.9890	18.8611

m_{th} - theoretical mass flow rate obtained by the solution Kg/sec

m_{act} - corrected mass flow rate Kg/sec

CFM - Cubic Feet per Minute

CMM – Cubic Meter per Minute

Graphs are plotted for ΔP Pa vs CMM and ΔP inches of H₂O vs CFM. The best fit for both cases is found to be Power series and the expressions for both cases are obtained as follows.

For,

$$\Delta P \text{ Pa vs CMM} - 7.415 x^{0.5116}$$

$$\Delta P \text{ inches of H}_2\text{O vs CFM} - 4404.7 x^{0.5116}$$

The flow rates are calibrated for 0 -100 Pa and 0 – 0.4 inches of water column and are presented in Fig 8.19 and 8.20 as the characteristic calibration curve for the tile.

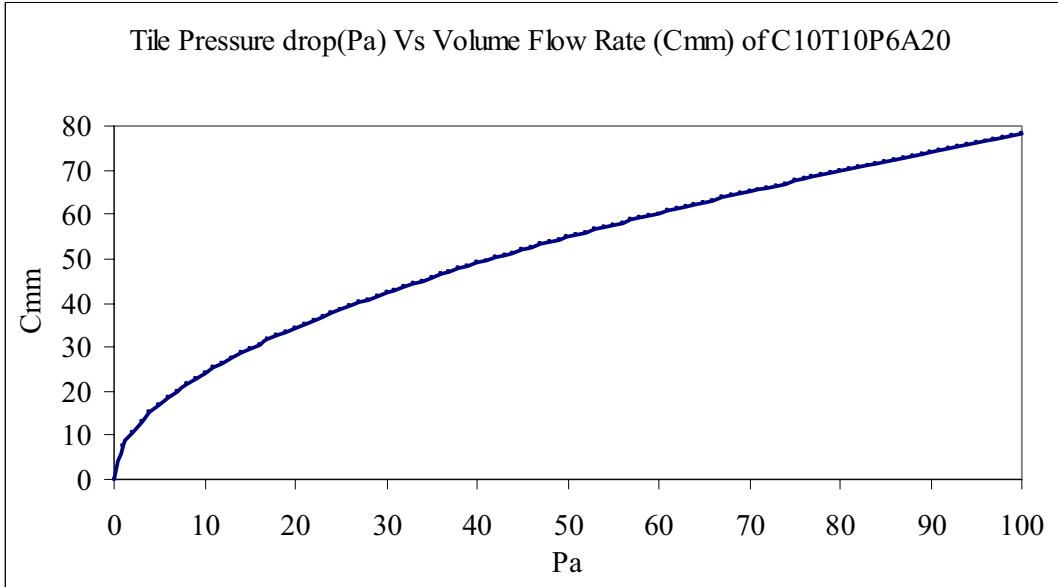


Fig 8.19: Mass flow rate calibration curve for tile C10T10P6A20 (a).

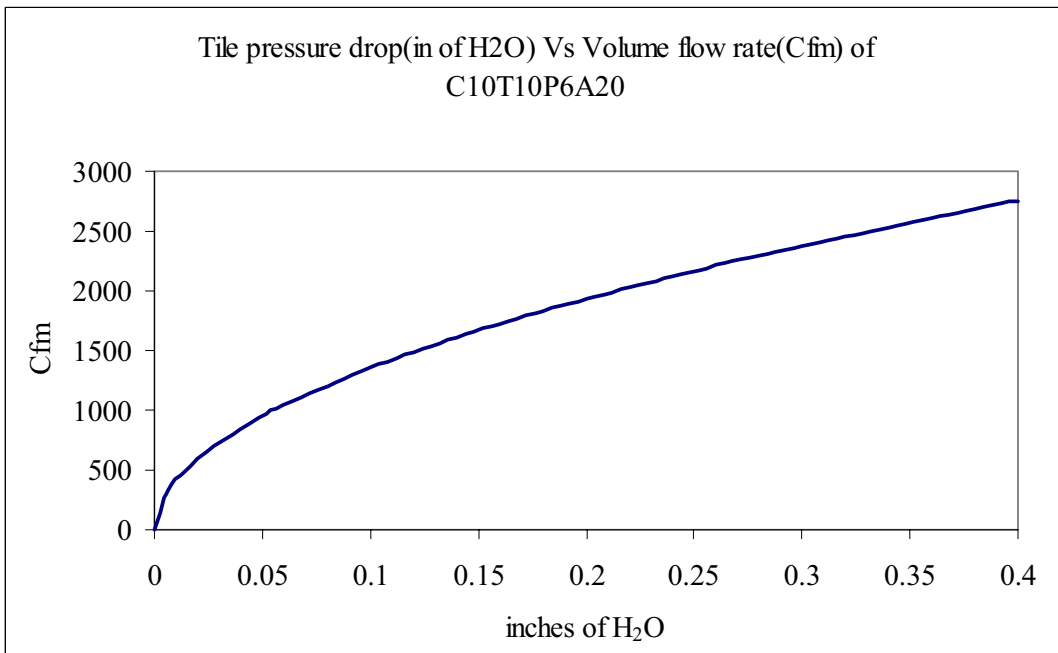


Fig 8.20: Mass flow rate calibration curve for tile C10T10P6A20 (b).

The variation of centre line velocity for various pressure differences across the tile is given in Fig 8.21.

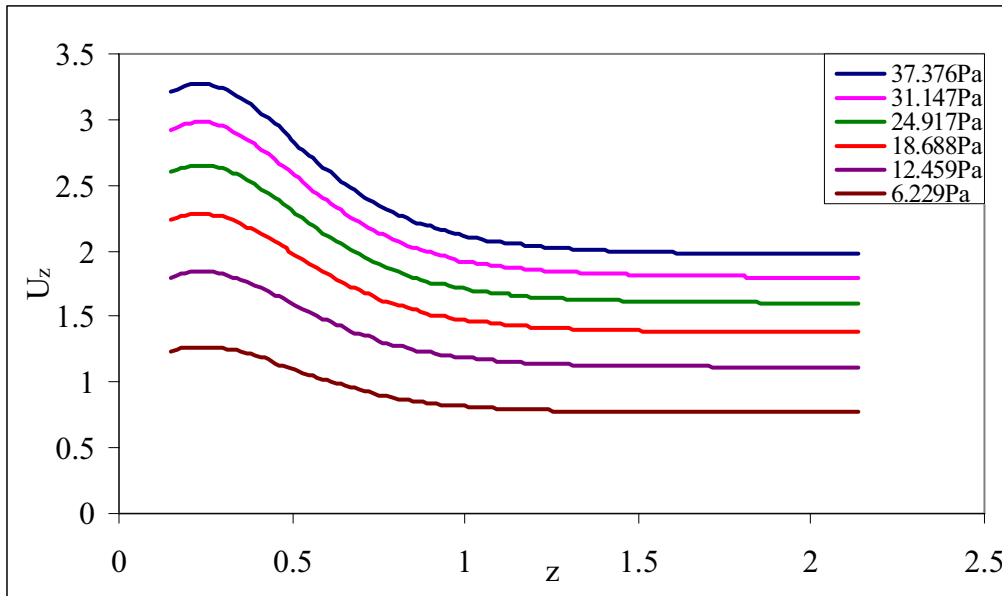


Fig 8.21: Variation of centre line velocity of tile C10T10P6A20 for various pressure differences

The variation of velocity along the x direction of the tile at different z positions for different pressure differences is given in Fig 8.22(a) to (f).

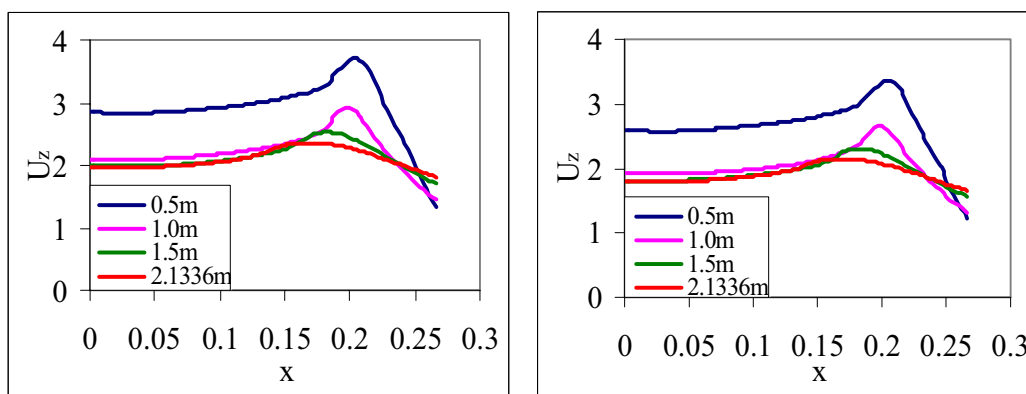
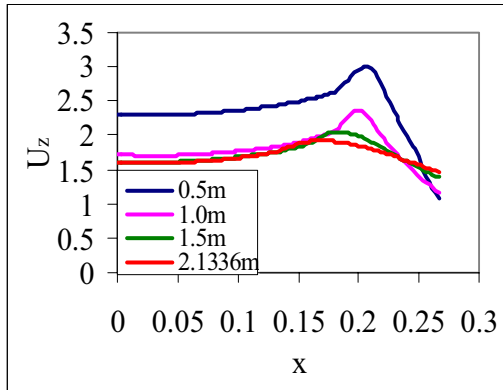
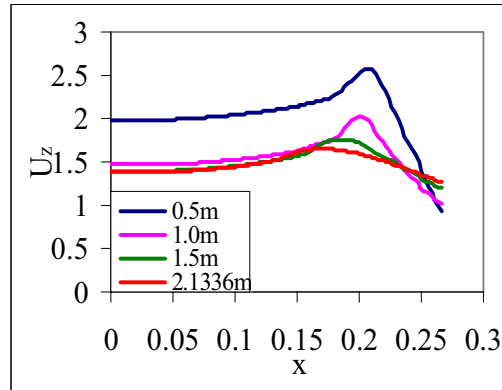


Fig 8.22: (a) Velocity in x direction for various z positions for $\Delta P = 37.376$ Pa

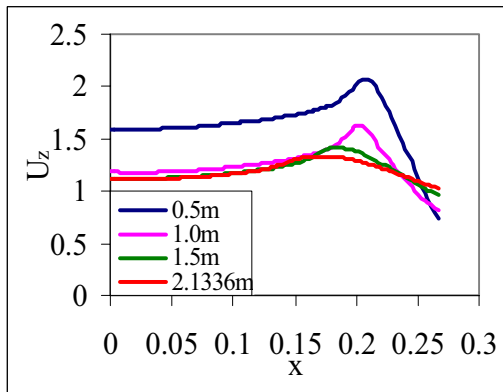
(b) Velocity in x direction for various z positions for $\Delta P = 31.147$ Pa



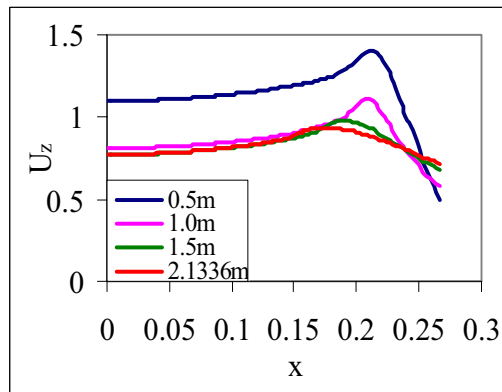
(c) Velocity in x direction for various z positions for $\Delta P = 24.917$ Pa



(d) Velocity in x direction for various z positions for $\Delta P = 18.688$ Pa



(e) Velocity in x direction for various z positions for $\Delta P = 12.459$ Pa



(f) Velocity in x direction for various z positions for $\Delta P = 6.229$ Pa

The velocity plots at different z locations for different pressure differences are not presented for the remaining standard tiles since they are similar for all standard tiles.

8.4.3 Tile C12T10P4A30

The mass flow rates for the tile obtained are given in the Table 8.3. The corrected mass flow rates are obtained by multiplying the theoretical mass flow rate by the correction factor. The mass flow rate is expressed in both CFM and CMM and is given in the Table 8.3.

Table 8.3: Mass flow rate of tile C12T10P4A30

	ΔP Pa	37.376	31.147	24.917	18.688	12.459	6.229
C10T10P6A20	ΔP in of H ₂ O	0.15	0.125	0.1	0.075	0.05	0.025
mass flow correction	m_{th} Kg/sec	1.3492	1.2304	1.0988	0.9499	0.7731	0.5411
factor = 1.1255	m_{act} Kg/sec	1.5186	1.3848	1.2367	1.0691	0.8701	0.6090
	CFM	2627	2395	2140	1850	1505	1053
	CMM	74.3966	67.8264	60.6048	52.392	42.6216	29.821

m_{th} - theoretical mass flow rate obtained by the solution Kg/sec

m_{act} - corrected mass flow rate Kg/sec

CFM - Cubic Feet per Minute

CMM – Cubic Meter per Minute

Graphs are plotted for ΔP Pa vs CMM and ΔP inches of H₂O vs CFM. The best fit for both cases is found to be Power series and the expressions for both cases are obtained as follows.

For,

$$\Delta P \text{ Pa vs CMM} - 11.754 x^{0.5099}$$

$$\Delta P \text{ inches of H}_2\text{O vs CFM} - 6921.3 x^{0.5099}$$

The flow rates are calibrated for 0 -100 Pa and 0 – 0.4 inches of water column and are presented in Fig 8.23 and 8.24 as the characteristic calibration curve for the tile.

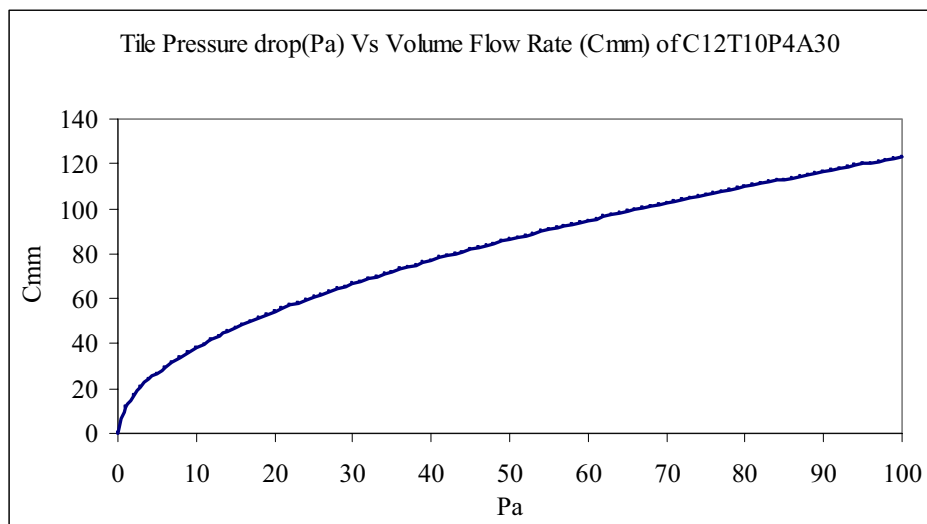


Fig 8.23: Mass flow rate calibration curve for tile C12T10P4A30 (a).

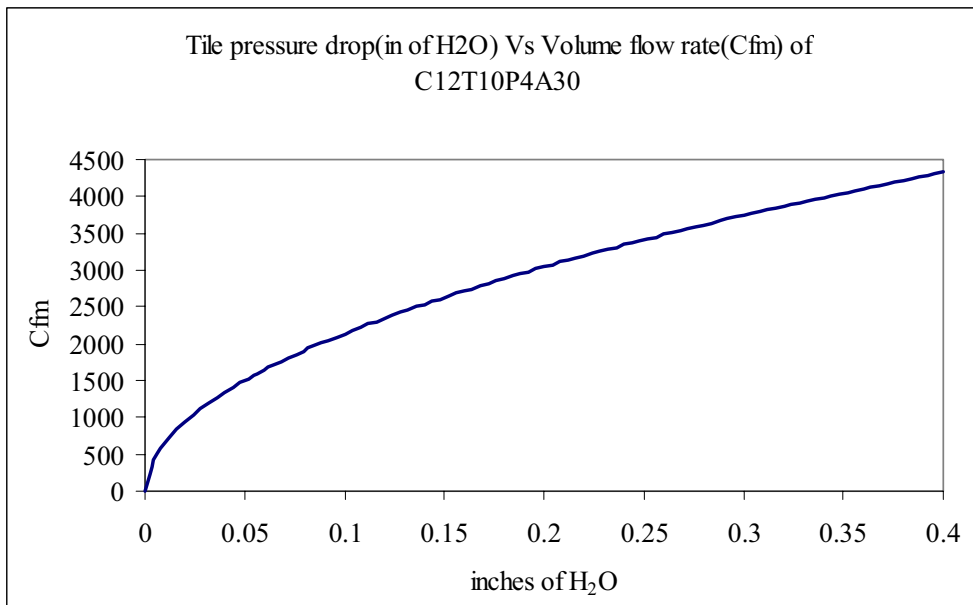


Fig 8.24: Mass flow rate calibration curve for tile C12T10P4A30 (b).

The variation of centre line velocity for various pressure differences across the tile is given in Fig 8.25.

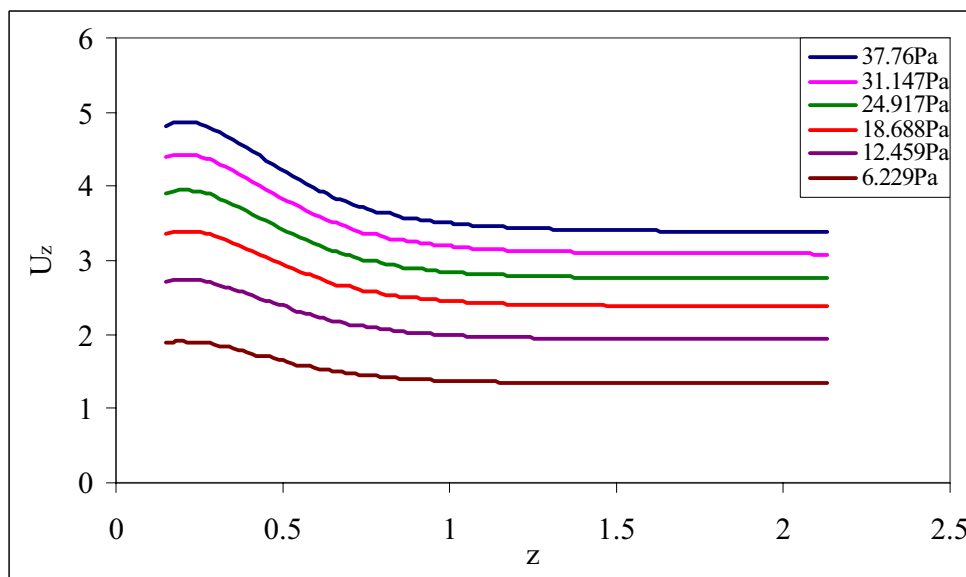


Fig 9.25: Variation of centre line velocity of tile C12T10P6A30 for various pressure differences

The variation of velocity along the x direction of the tile at different z positions for different pressure differences is given in the Fig 8.26(a) to (f).

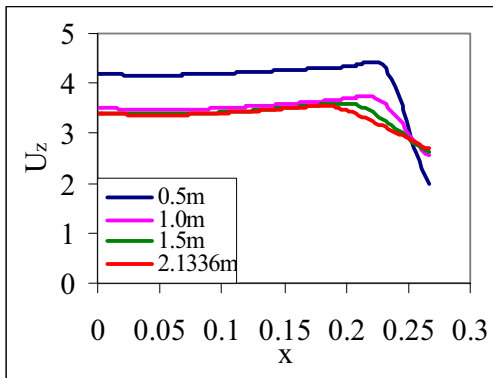
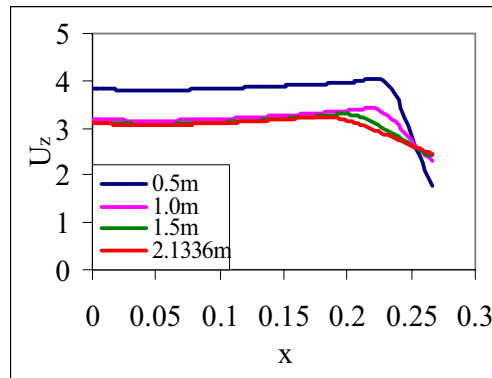
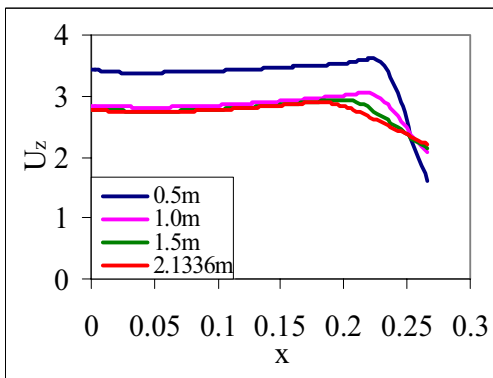


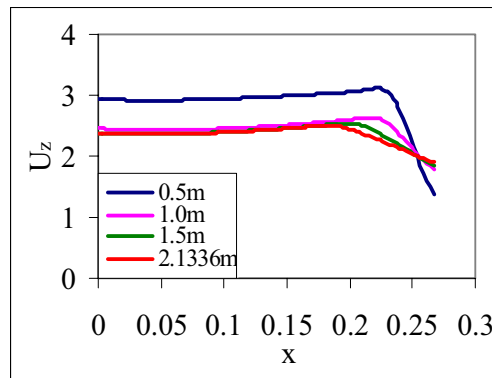
Fig 8.26: (a) Velocity in x direction for various z positions for $\Delta P = 37.376$ Pa



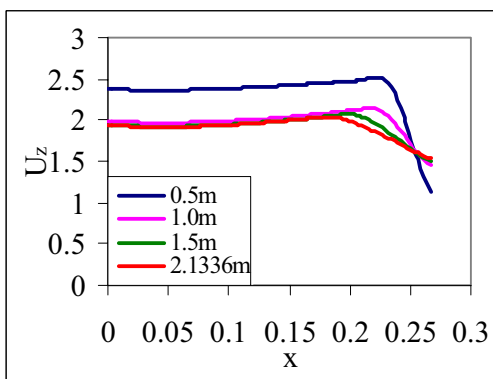
(b) Velocity in x direction for various z positions for $\Delta P = 31.147$ Pa



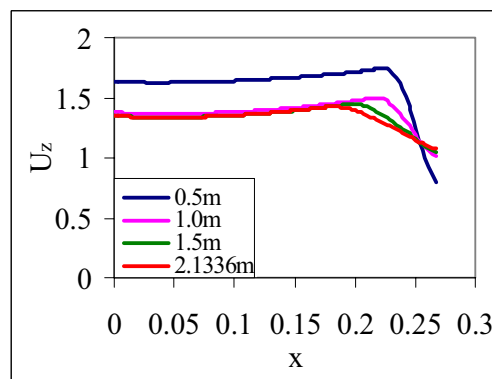
(c) Velocity in x direction for various z positions for $\Delta P = 24.917$ Pa



(d) Velocity in x direction for various z positions for $\Delta P = 18.688$ Pa



(e) Velocity in x direction for various z positions for $\Delta P = 12.459$ Pa



(f) Velocity in x direction for various z positions for $\Delta P = 6.229$ Pa

8.4.4 Tile C12T10P6A25

The mass flow rates for the tile obtained are given in the Table 8.4. The corrected mass flow rates are obtained by multiplying the theoretical mass flow rate by the correction factor. The mass flow rate is expressed in both CFM and CMM and is given in the Table 8.4.

Table 8.4: Mass flow rate of tile C12T10P6A25

	ΔP Pa	37.376	31.147	24.917	18.688	12.459	6.229
C10T10P6A20	ΔP in of H ₂ O	0.15	0.125	0.1	0.075	0.05	0.025
mass flow correction	m_{th} Kg/sec	1.1148	10169	0.9087	0.7860	0.6402	0.4489
factor = 1.1255	m_{act} Kg/sec	1.2547	1.1445	1.0227	0.8846	0.7206	0.5053
	CFM	2170	1980	1770	1530	1246	874
	CMM	61.4544	56.0736	50.1264	43.3296	35.2867	24.5168

m_{th} - theoretical mass flow rate obtained by the solution Kg/sec

m_{act} - corrected mass flow rate Kg/sec

CFM - Cubic Feet per Minute

CMM – Cubic Meter per Minute

Graphs are plotted for ΔP Pa vs CMM and ΔP inches of H₂O vs CFM. The best fit for both cases is found to be Power series and the expressions for both cases are obtained as follows.

For,

$$\Delta P \text{ Pa vs CMM} - 11.754 x^{0.5099}$$

$$\Delta P \text{ inches of H}_2\text{O vs CFM} - 6921.3 x^{0.5099}$$

The flow rates are calibrated for 0 -100 Pa and 0 – 0.4 inches of water column and are presented in Fig 8.27 and 8.28 as the characteristic calibration curve for the tile.

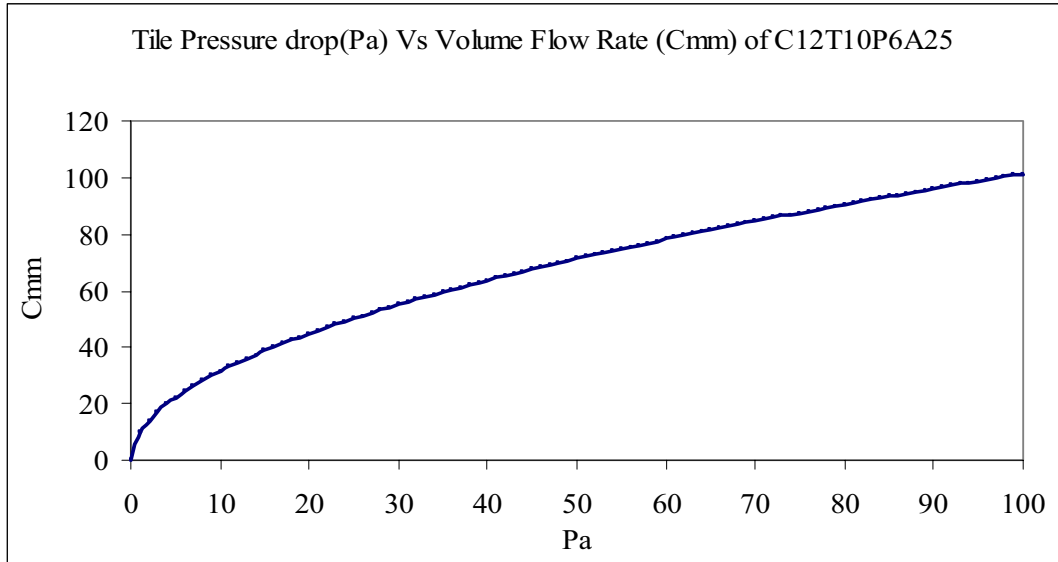


Fig 8.27 Mass flow rate calibration curve for tile C12T10P6A25 (a)

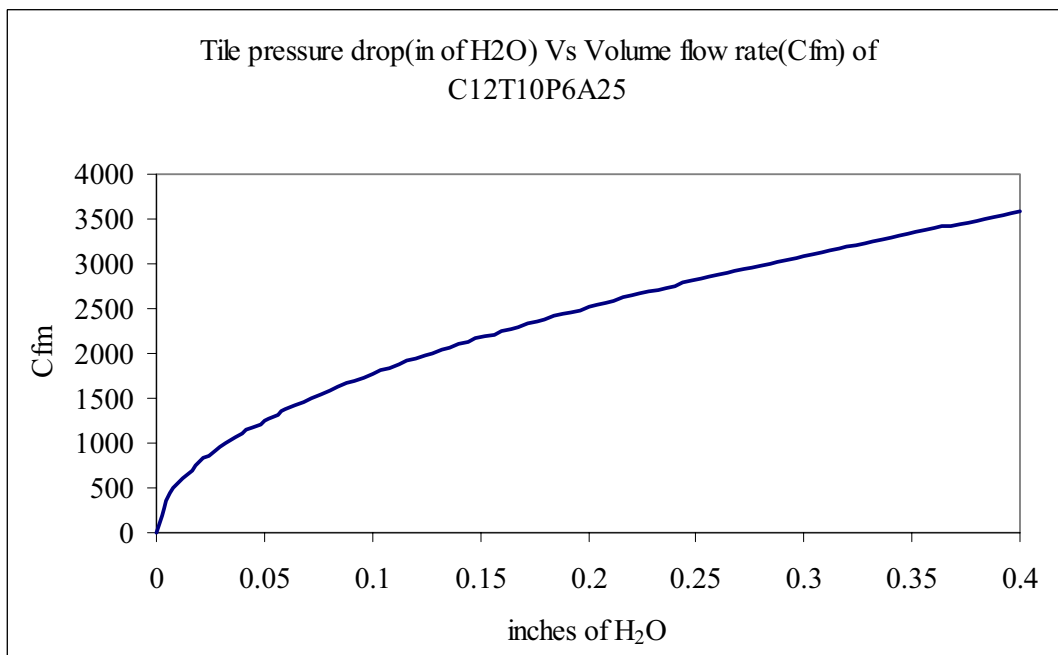


Fig 8.28 Mass flow rate calibration curve for tile C12T10P6A25 (b).

The variation of centre line velocity for various pressure differences across the tile is given in Fig 8.29

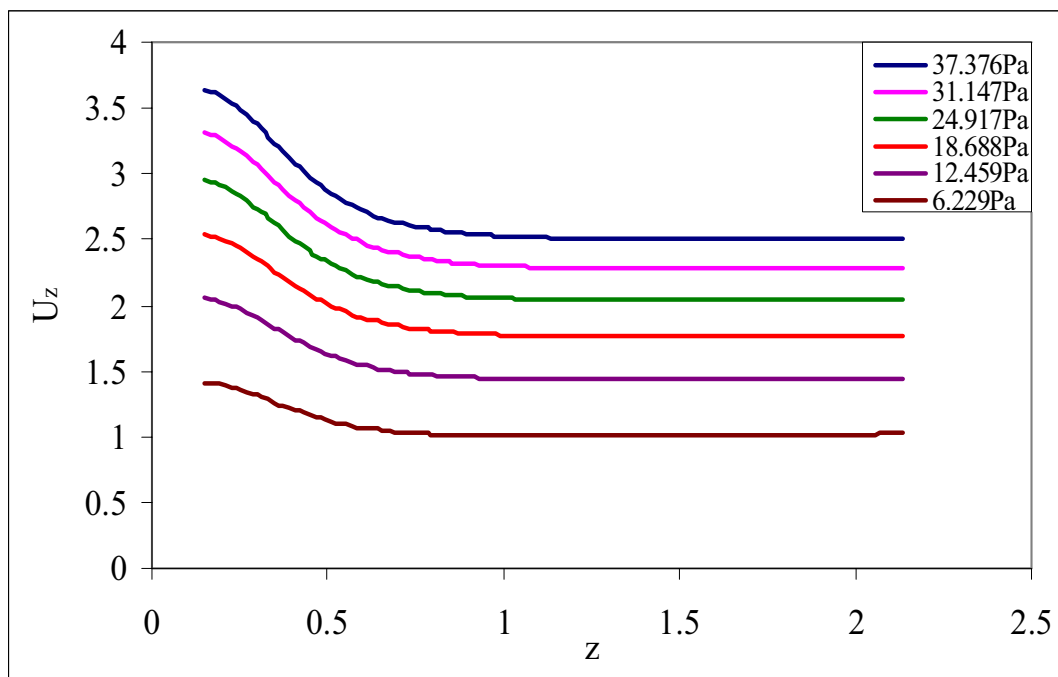


Fig 8.29: Variation of centre line velocity of tile C12T10P6A25 for various pressure differences

The variation of velocity along the X direction of the tile at different z positions for different pressure differences is given in Fig 8.30(a) to (f).

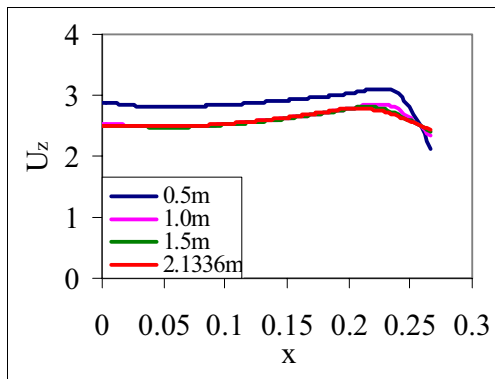
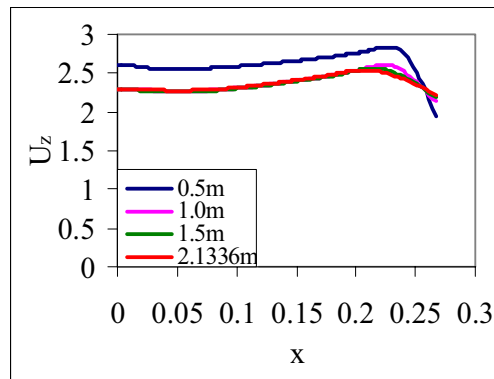
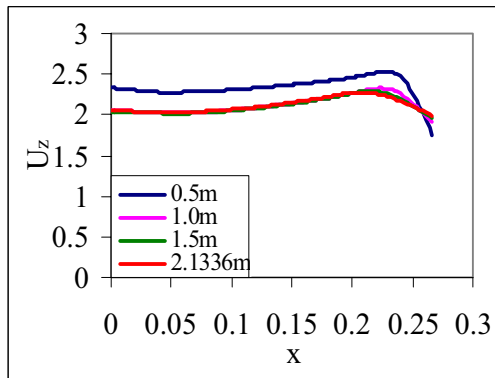


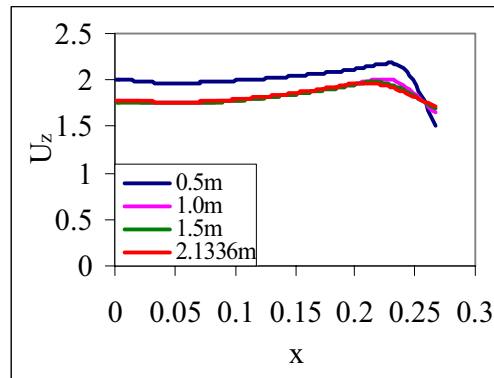
Fig 8.30 (a) Velocity in x direction for various z positions for $\Delta P = 37.376$ Pa



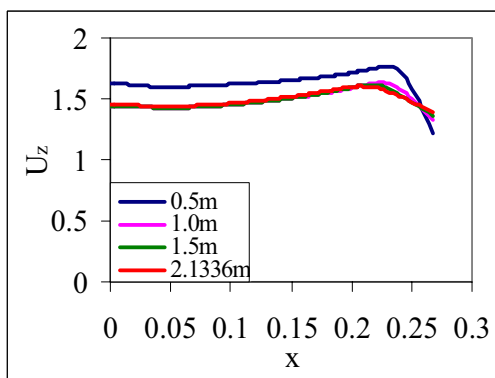
(b) Velocity in x direction for various z positions for $\Delta P = 31.147$ Pa



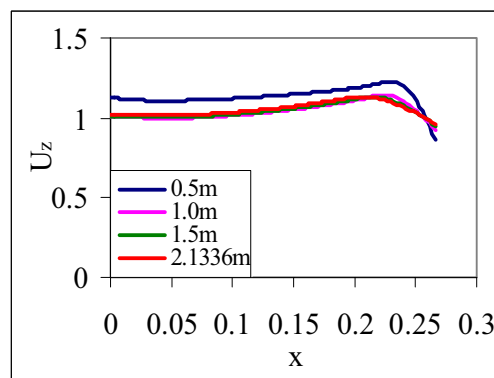
(c) Velocity in x direction for various z positions for $\Delta P = 24.917$ Pa



(d) Velocity in x direction for various z positions for $\Delta P = 18.688$ Pa



(e) Velocity in x direction for various z positions for $\Delta P = 12.459$ Pa



(f) Velocity in x direction for various z positions for $\Delta P = 6.229$ Pa

8.4.5 Tile C14T10P4A40

The mass flow rates for the tile obtained are given in the Table 8.5. The corrected mass flow rates are obtained by multiplying the theoretical mass flow rate by the correction factor. The mass flow rate is expressed in both CFM and CMM and is given in the Table 8.5.

Table 8.5: Mass flow rate of tile C14T10P4A40

	ΔP Pa	37.376	31.147	24.917	18.688	12.459	6.229
C10T10P6A20	ΔP in of H ₂ O	0.15	0.125	0.1	0.075	0.05	0.025
mass flow correction	m_{th} Kg/sec	1.6364	1.4926	1.3333	1.1526	0.9385	6574
factor = 1.1209	m_{act} Kg/sec	1.8342	1.6731	1.4945	1.2920	1.0520	0.7369
	CFM	3173	2894	2585	2235	1820	1275
	CMM	89.8594	81.9581	73.2072	63.2952	51.5424	34.108

m_{th} - theoretical mass flow rate obtained by the solution Kg/sec

m_{act} - corrected mass flow rate Kg/sec

CFM - Cubic Feet per Minute

CMM – Cubic Meter per Minute

Graphs are plotted for ΔP Pa vs CMM and ΔP inches of H₂O vs CFM. The best fit for both cases is found to be Power series and the expressions for both cases are obtained as follows.

For,

$$\Delta P \text{ Pa vs CMM} - 14.259 x^{0.5086}$$

$$\Delta P \text{ inches of H}_2\text{O vs CFM} - 8336.8 x^{0.5086}$$

The flow rates are calibrated for 0 -100 Pa and 0 – 0.4 inches of water column and are presented in Fig 8.31 and 8.32 as the characteristic calibration curve for the tile.

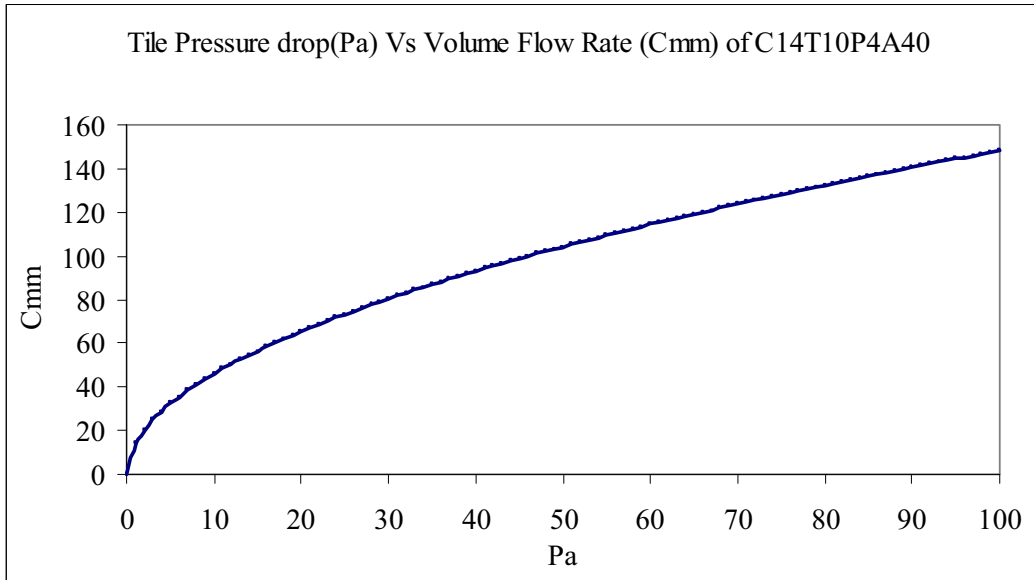


Fig 8.31: Mass flow rate calibration curve for tile C14T10P4A40 (a).

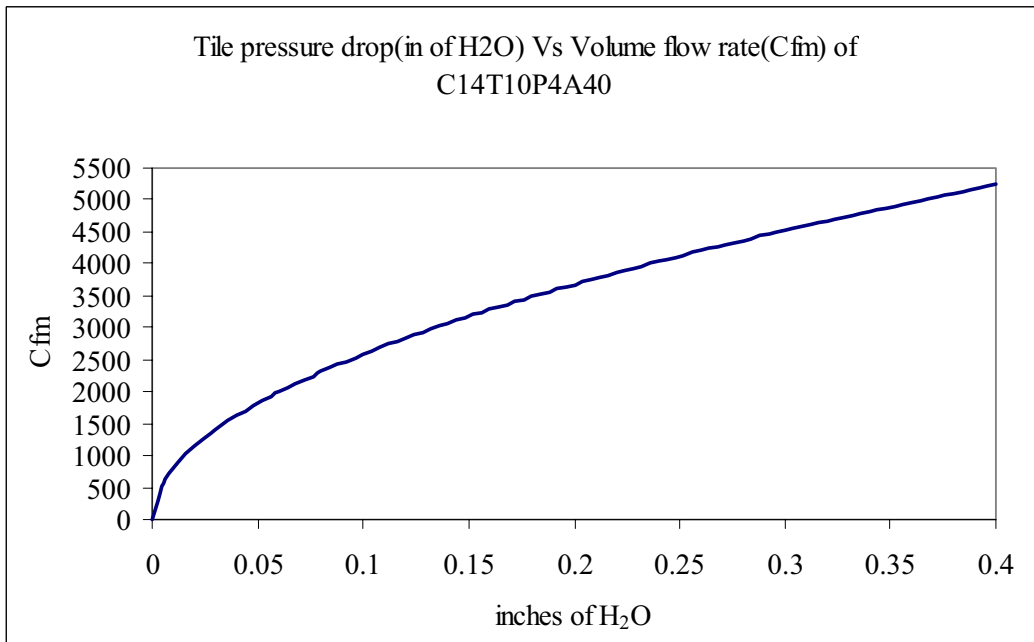


Fig 8.32: Mass flow rate calibration curve for tile C14T10P4A40 (b).

The variation of centre line velocity for various pressure differences across the tile is given in Fig 8.33

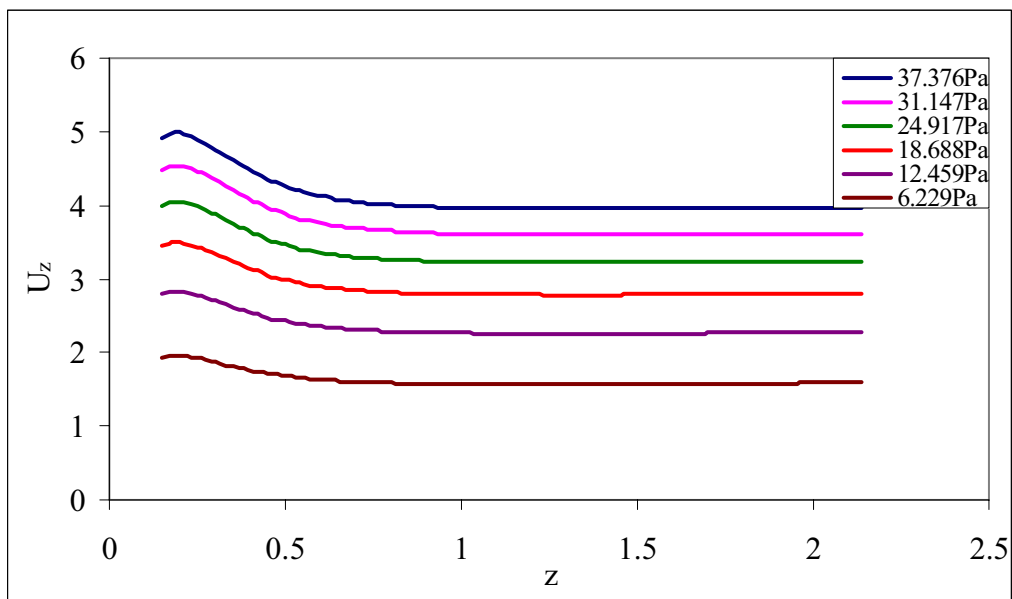


Fig. 8.33: Variation of centre line velocity of tile C14T10P4A40 for various pressure differences

The variation of velocity along the X direction of the tile at different z positions for different pressure differences is given in Fig 8.34(a) to (f).

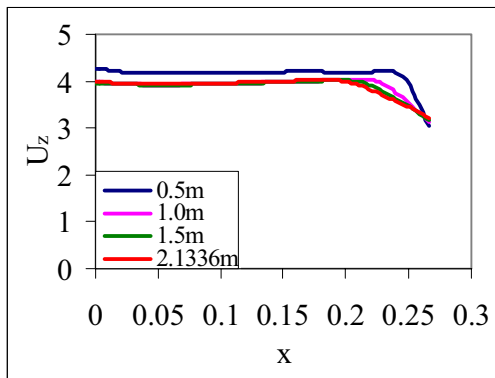
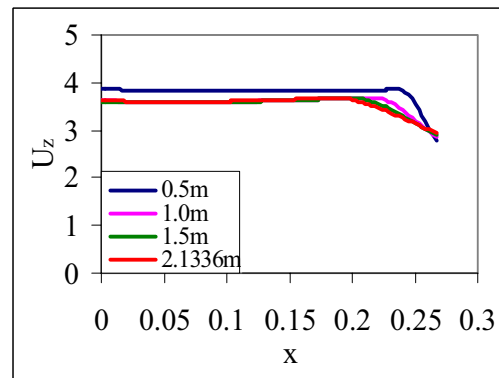
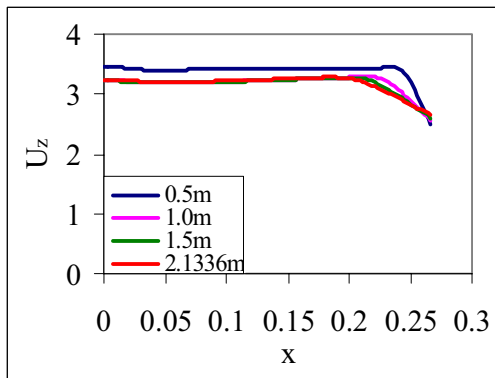


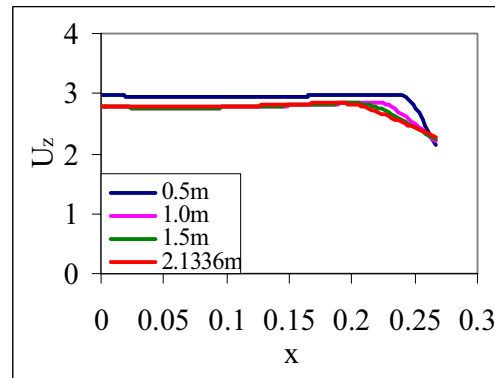
Fig 8.34: (a) Velocity in x direction for various z positions for $\Delta P = 37.376$ Pa



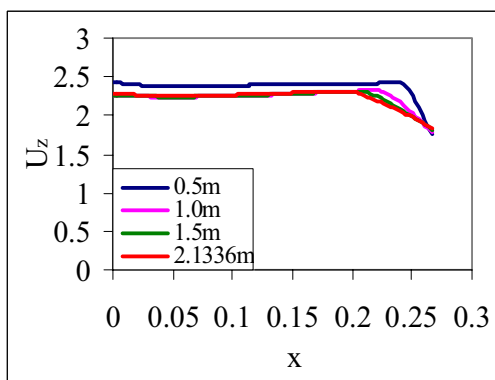
(b) Velocity in x direction for various z positions for $\Delta P = 31.147$ Pa



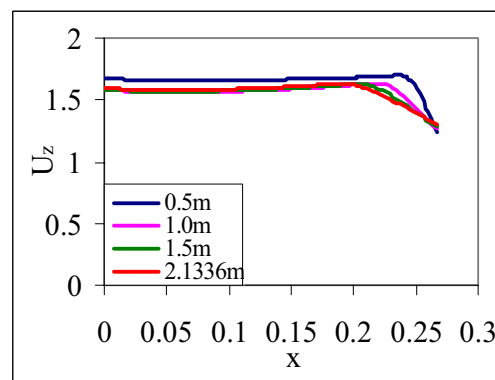
(c) Velocity in x direction for various z positions for $\Delta P = 24.917$ Pa



(d) Velocity in x direction for various z positions for $\Delta P = 18.688$ Pa



(e) Velocity in x direction for various z positions for $\Delta P = 12.459$ Pa



(f) Velocity in x direction for various z positions for $\Delta P = 6.229$ Pa

8.4.6 Tile C14T10P6A30

The mass flow rates for the tile obtained are given in the Table 8.6. The corrected mass flow rates are obtained by multiplying the theoretical mass flow rate by the correction factor. The mass flow rate is expressed in both CFM and CMM and is given in the Table 8.6.

Table 8.6: Mass flow rate of tile C14T10P6A30

	ΔP Pa	37.376	31.147	24.917	18.688	12.459	6.229
C10T10P6A20	ΔP in of H ₂ O	0.15	0.125	0.1	0.075	0.05	0.025
mass flow correction	m_{th} Kg/sec	1.1663	1.0641	0.9511	0.8227	0.6705	0.4707
factor = 1.1209	m_{act} Kg/sec	1.3073	1.1928	1.0661	0.9221	0.7515	0.5276
	CFM	2262	2063	1844	1595	1300	913
	CMM	64.0598	58.4242	52.2221	45.1704	36.816	25.8562

m_{th} - theoretical mass flow rate obtained by the solution Kg/sec

m_{act} - corrected mass flow rate Kg/sec

CFM - Cubic Feet per Minute

CMM – Cubic Meter per Minute

Graphs are plotted for ΔP Pa vs CMM and ΔP inches of H₂O vs CFM. The best fit for both cases is found to be Power series and the expressions for both cases are obtained as follows.

For,

$$\Delta P \text{ Pa vs CMM} - 10.253 x^{0.5061}$$

$$\Delta P \text{ inches of H}_2\text{O vs CFM} - 5912.6 x^{0.5061}$$

The flow rates are calibrated for 0 -100 Pa and 0 – 0.4 inches of water column and are presented in Fig 8.35 and 8.36 as the characteristic calibration curve for the tile.

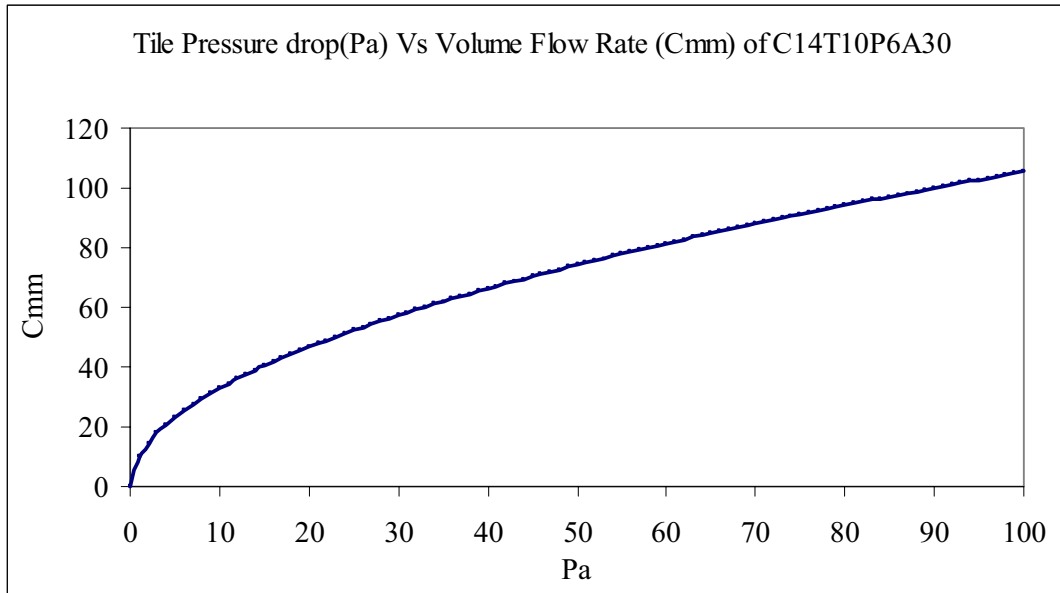


Fig 8.35: Mass flow rate calibration curve for Tile C14T10P6A30 (a)

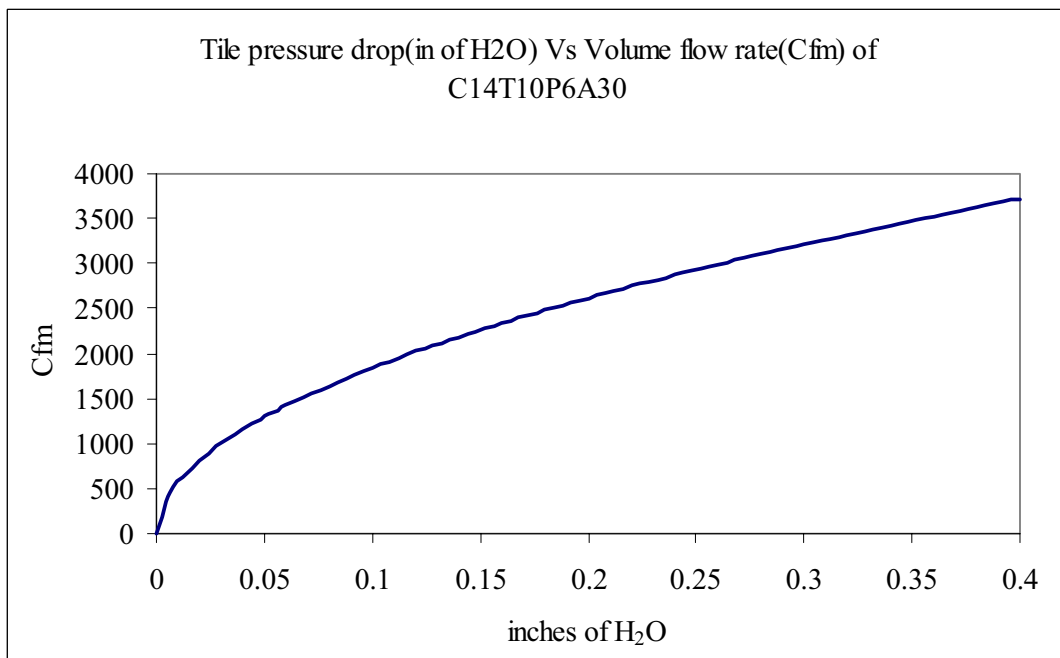


Fig 8.36: Mass flow rate calibration curve for Tile C14T10P6A30 (b)

The variation of centre line velocity for various pressure differences across the tile is given in Fig 8.37

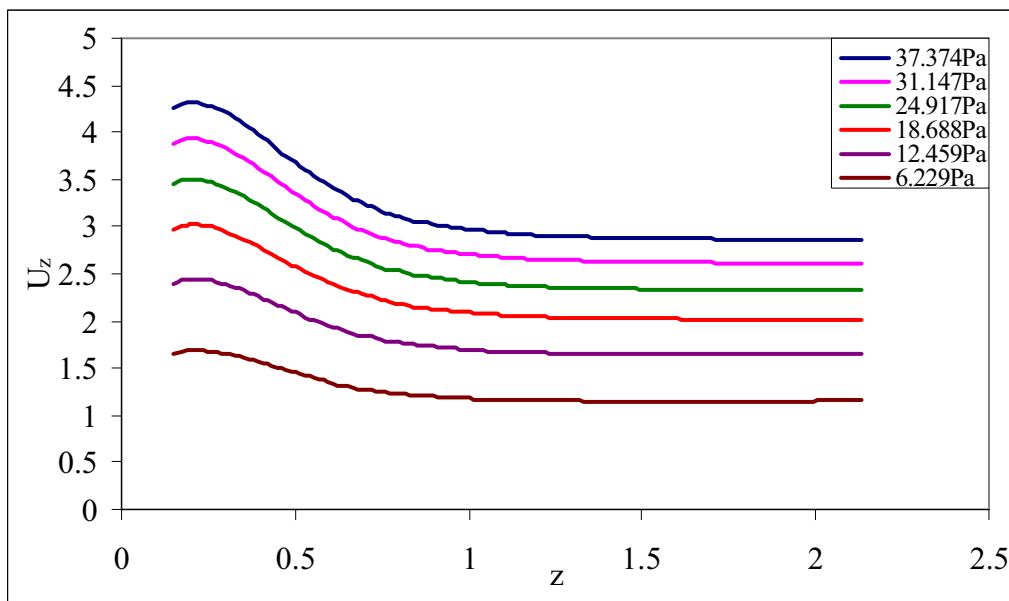


Fig 8.37: Variation of centre line velocity of tile C14T10P6A30 for various pressure differences

The variation of velocity along the X direction of the tile at different z positions for different pressure differences is given in Fig 8.38(a) to (f).

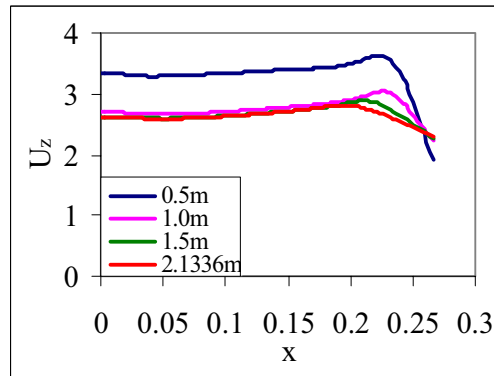
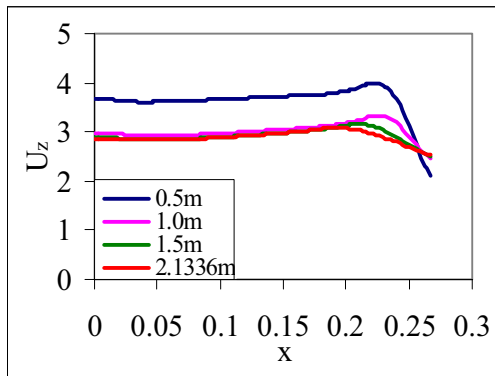
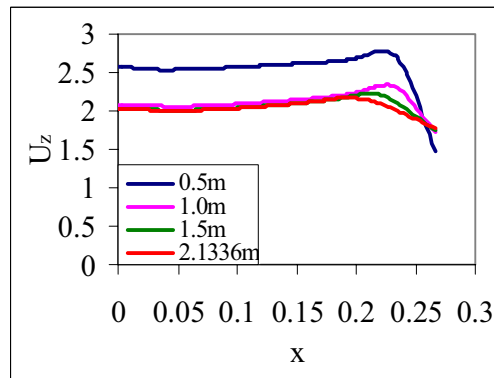
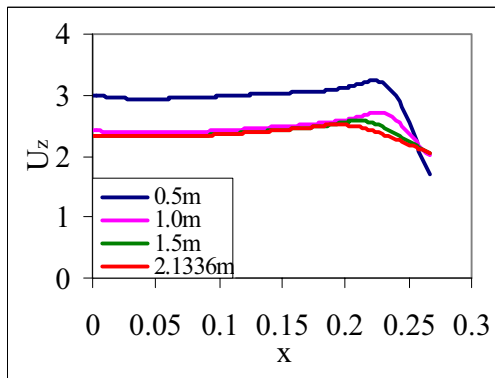


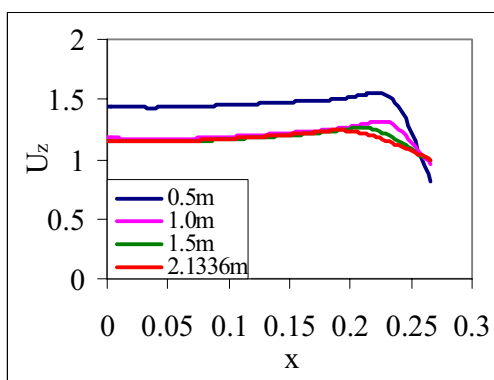
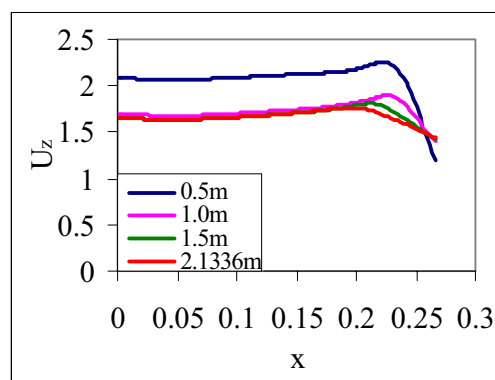
Fig 8.38: (a) Velocity in x direction for various z positions for $\Delta P = 37.376$ Pa

(b) Velocity in x direction for various z positions for $\Delta P = 31.147$ Pa



(c) Velocity in x direction for various z positions for $\Delta P = 24.917$ Pa

(d) Velocity in x direction for various z positions for $\Delta P = 18.688$ Pa



(e) Velocity in x direction for various z positions for $\Delta P = 12.459$ Pa

(f) Velocity in x direction for various z positions for $\Delta P = 6.229$ Pa

8.4.7 Tile C14C8T10P6A40

The mass flow rates for the tile obtained are given in the Table 8.7. The corrected mass flow rates are obtained by multiplying the theoretical mass flow rate by the correction factor. The mass flow rate is expressed in both CFM and CMM and is given in the Table 8.7.

Table 8.7: Mass flow rate of tile C14C8T10P6A40

	ΔP Pa	37.376	31.147	24.917	18.688	12.459	6.229
C10T10P6A20	ΔP in of H ₂ O	0.15	0.125	0.1	0.075	0.05	0.025
mass flow correction	m_{th} Kg/sec	1.6901	1.5404	1.3747	1.1872	0.9646	0.6730
factor C14 = 1.1209	m_{act} Kg/sec	1.9048	1.7361	1.5493	1.3380	1.0871	0.7585
C8 = 1.1446	CFM	3295	3003	2680	2315	1880	1312
	CMM	93.3144	85.4496	75.8976	65.5608	53.2416	37.1558

m_{th} - theoretical mass flow rate obtained by the solution Kg/sec

m_{act} - corrected mass flow rate Kg/sec

CFM - Cubic Feet per Minute

CMM – Cubic Meter per Minute

Graphs are plotted for ΔP Pa vs CMM and ΔP inches of H₂O vs CFM. The best fit for both cases is found to be Power series and the expressions for both cases are obtained as follows.

For,

$$\Delta P \text{ Pa vs CMM} - 14.541 x^{0.5137}$$

$$\Delta P \text{ inches of H}_2\text{O vs CFM} - 8745.1 x^{0.5137}$$

The flow rates are calibrated for 0 -100 Pa and 0 – 0.4 inches of water column and are presented in Fig 8.39 and 8.40 as the characteristic calibration curve for the tile.

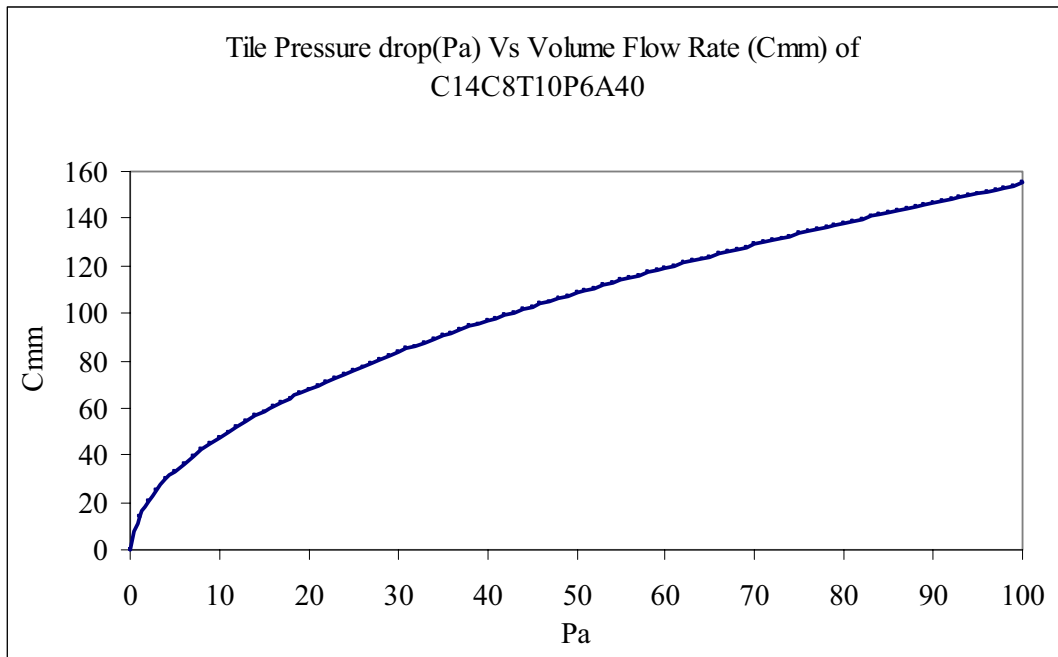


Fig 8.39: Mass flow rate calibration curve for tile C14C8T10P6A40 (a)

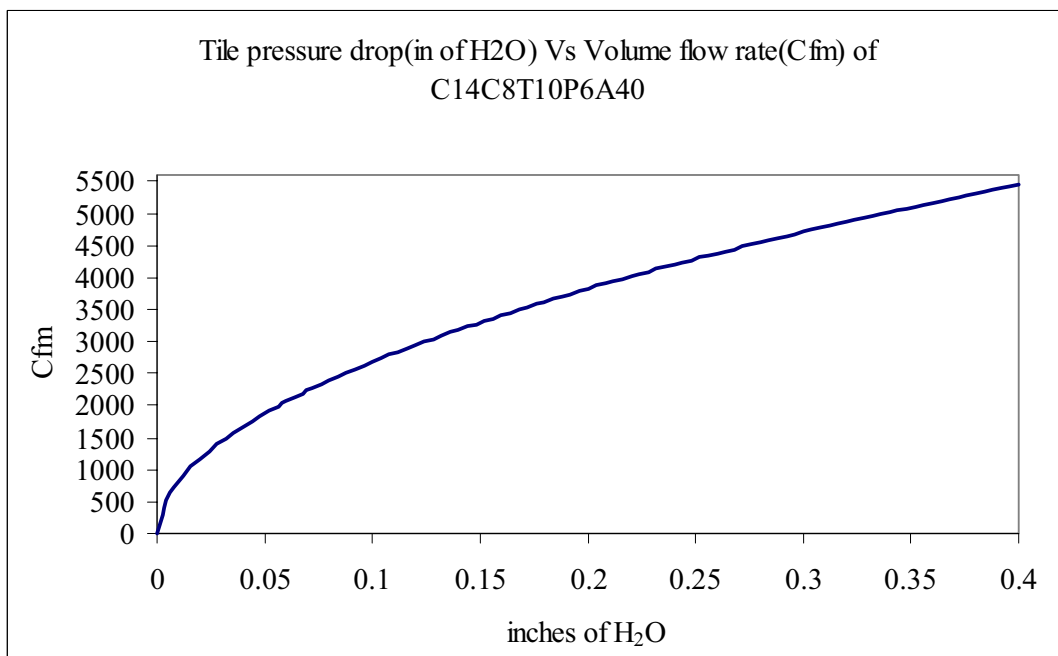


Fig 8.40: Mass flow rate calibration curve for tile C14C8T10P6A40 (b)

The variation of centre line velocity for various pressure differences across the tile is given in Fig 8.41

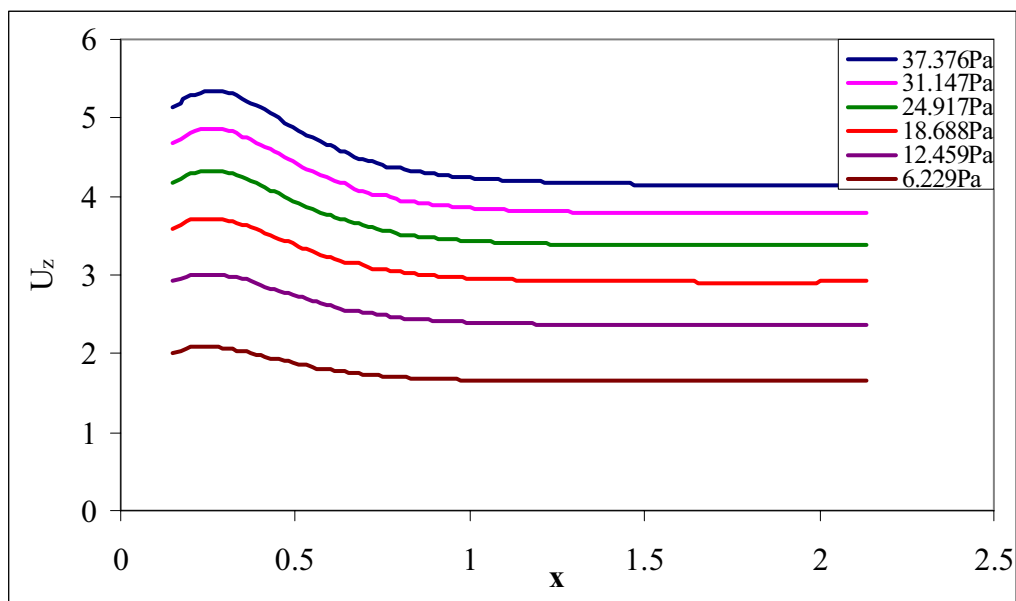


Fig 8.41: Variation of centre line velocity of tile C14C8T10P6A40 for various pressure differences

The variation of velocity along the X direction of the tile at different z positions for different pressure differences is given in the Fig 8.42(a) to (f).

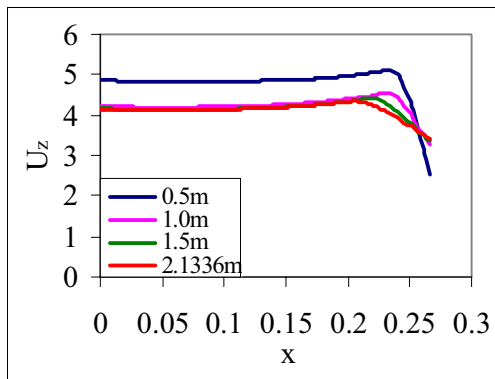
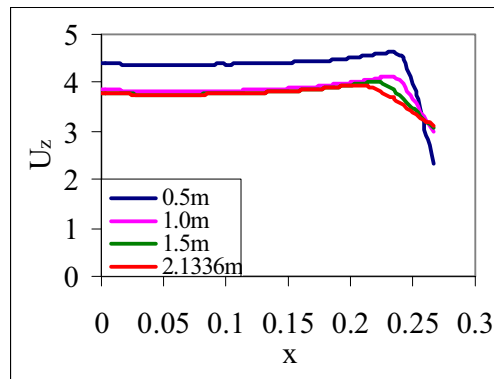
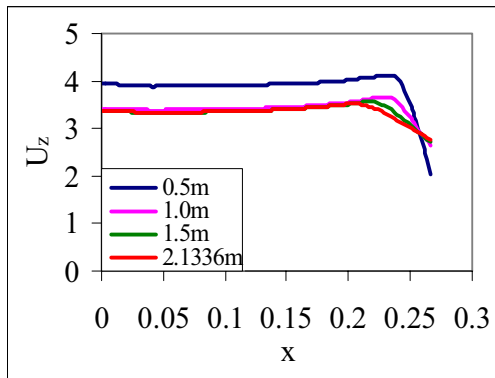


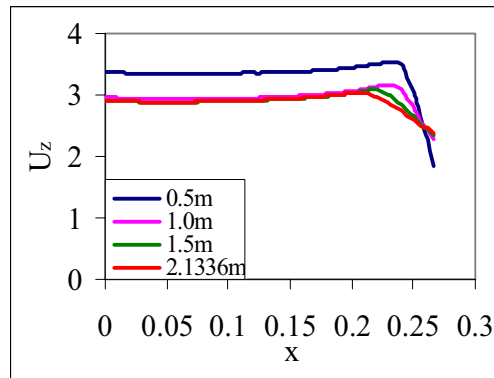
Fig 8.42 (a) Velocity in x direction for various z positions for $\Delta P = 37.376$ Pa



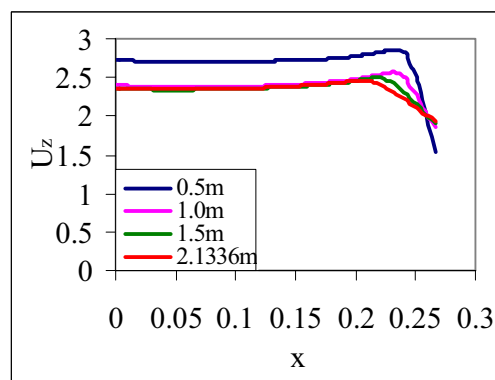
(b) Velocity in x direction for various z positions for $\Delta P = 31.147$ Pa



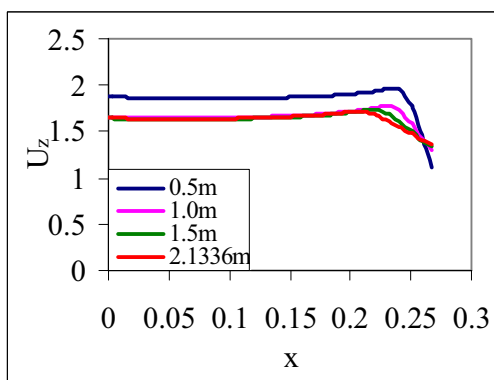
(c) Velocity in x direction for various z positions for $\Delta P = 24.917$ Pa



(d) Velocity in x direction for various z positions for $\Delta P = 18.688$ Pa



(e) Velocity in x direction for various z positions for $\Delta P = 12.459$ Pa



(f) Velocity in x direction for various z positions for $\Delta P = 6.229$ Pa

The velocity plots at different z locations for different pressure differences are given in figures 8.43 to 8.48

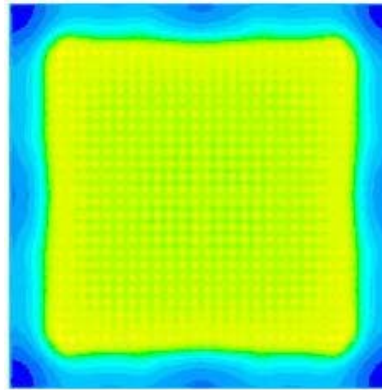
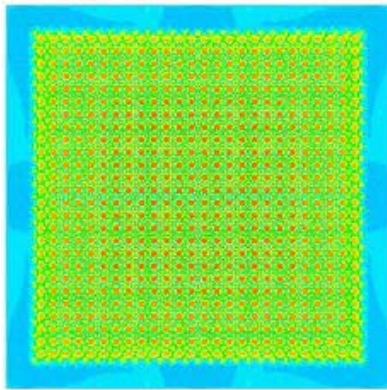
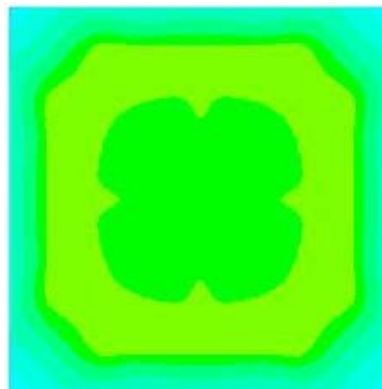
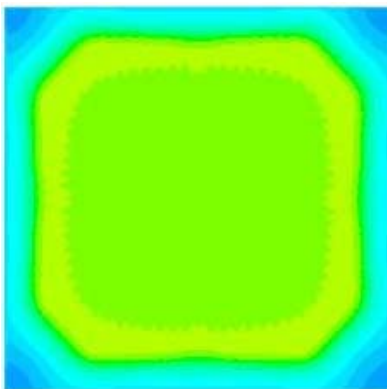


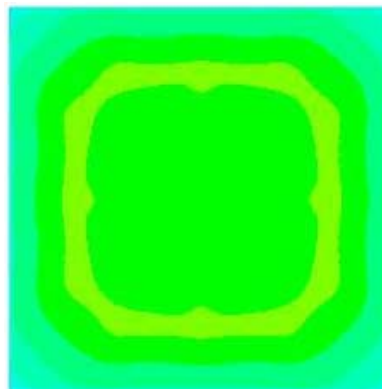
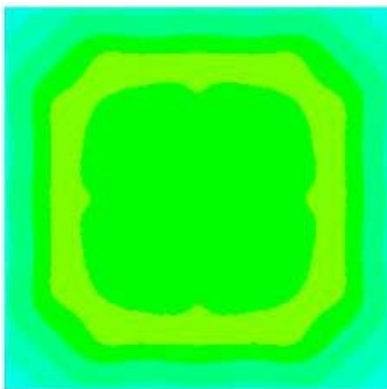
Fig 8.43: (a) Velocity plot at $z = 0.01$ m for $\Delta P = 37.376$ Pa

(b) Velocity plot at $z = 0.15$ m for $\Delta P = 37.376$ Pa



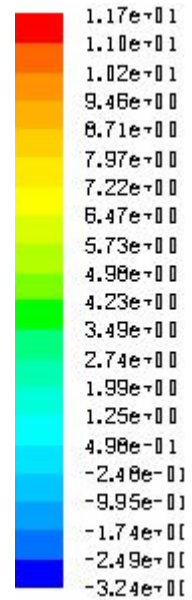
(c) Velocity plot at $z = 0.5$ m for $\Delta P = 37.376$ Pa

(d) Velocity plot at $z = 1.0$ m for $\Delta P = 37.376$ Pa



(e) Velocity plot at $z = 1.5$ m for $\Delta P = 37.376$ Pa

(f) Velocity plot at $z = 2.1336$ m for $\Delta P = 37.376$ Pa



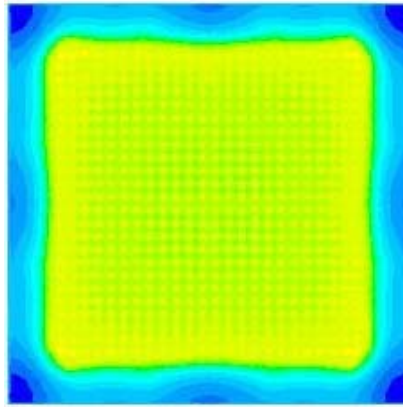
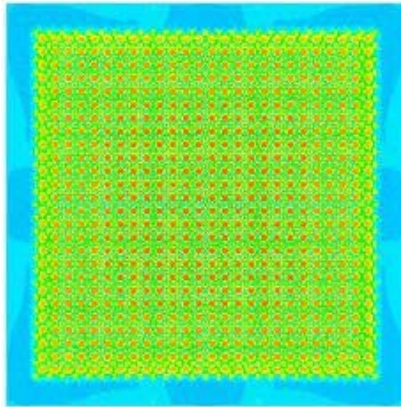
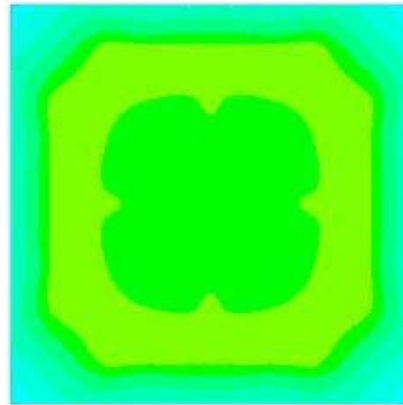
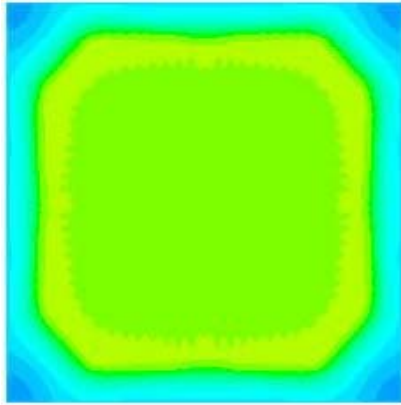


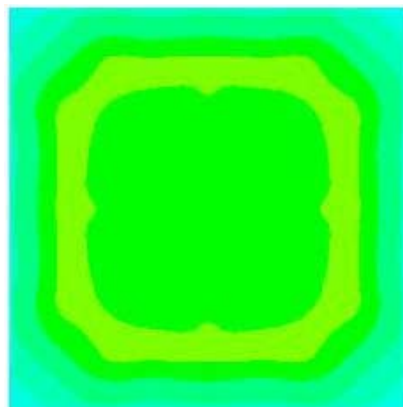
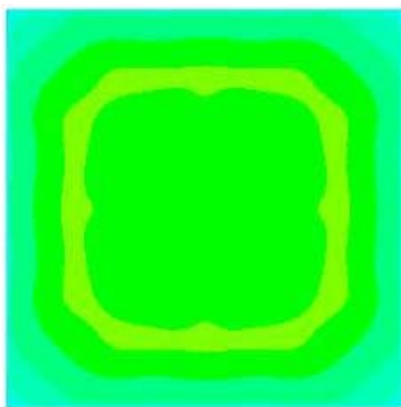
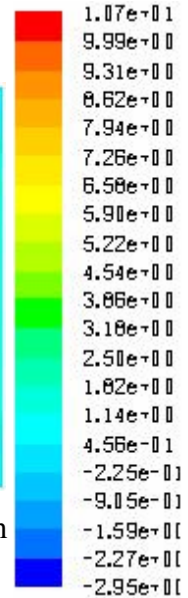
Fig 8.44: (a) Velocity plot at $z = 0.01$ m for $\Delta P = 31.147$ Pa

(b) Velocity plot at $z = 0.15$ m for $\Delta P = 31.147$ Pa



(c) Velocity plot at $z = 0.5$ m for $\Delta P = 31.147$ Pa

(d) Velocity plot at $z = 1.0$ m for $\Delta P = 31.147$ Pa



(e) Velocity plot at $z = 1.5$ m for $\Delta P = 31.147$ Pa

(f) Velocity plot at $z = 2.1336$ m for $\Delta P = 31.147$ Pa

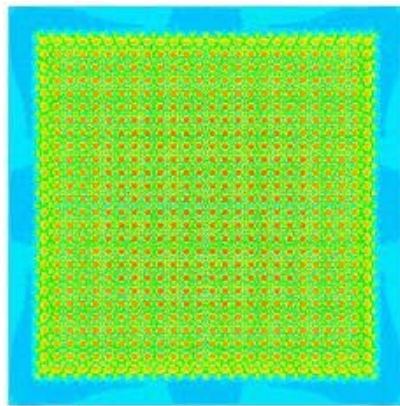
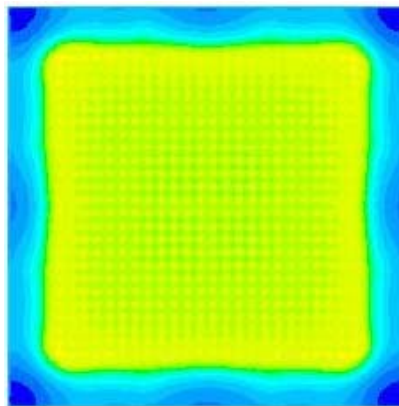
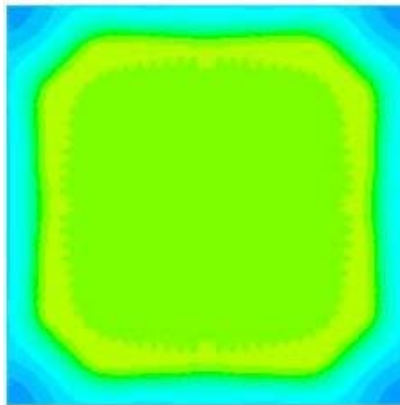


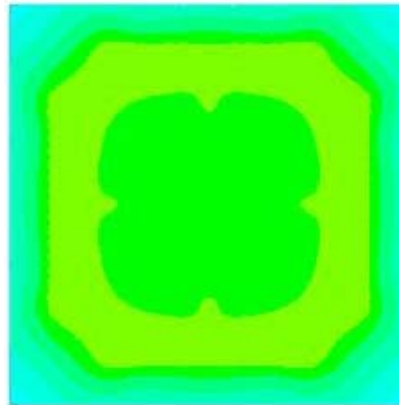
Fig 8.45: (a) Velocity plot at $z = 0.01$ m for $\Delta P = 24.917$ Pa



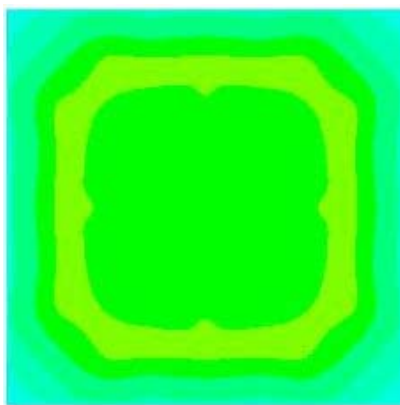
(b) Velocity plot at $z = 0.15$ m for $\Delta P = 24.917$ Pa



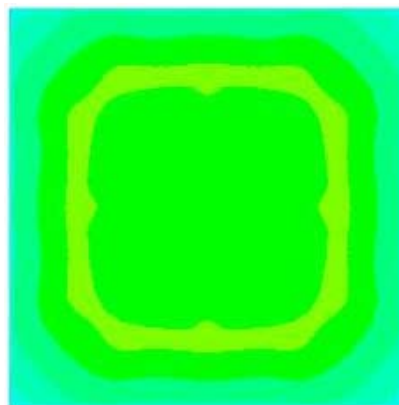
(c) Velocity plot at $z = 0.5$ m for $\Delta P = 24.917$ Pa



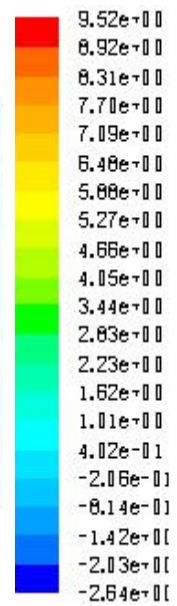
(d) Velocity plot at $z = 1.0$ m for $\Delta P = 24.917$ Pa

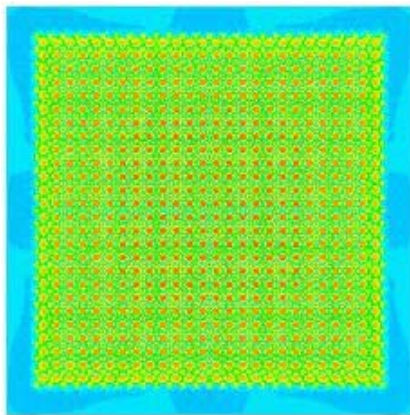


(e) Velocity plot at $z = 1.5$ m for $\Delta P = 24.917$ Pa

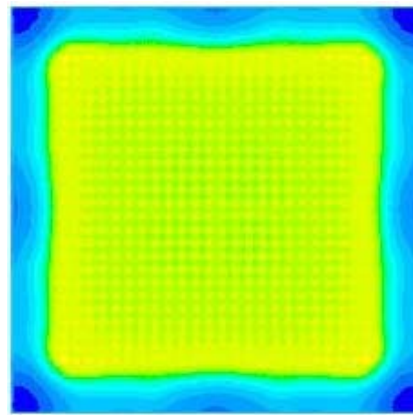


(f) Velocity plot at $z = 2.1336$ m for $\Delta P = 24.917$ Pa

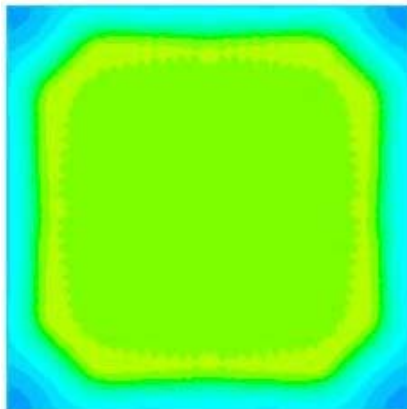




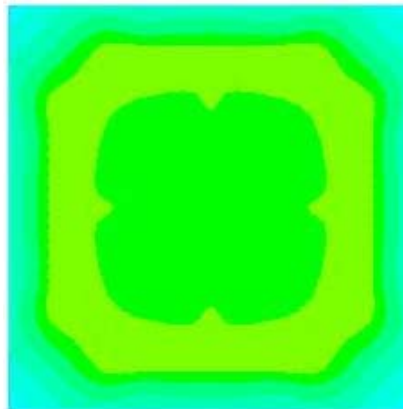
(a) Velocity plot at $z = 0.01$ m for $\Delta P = 18.688$ Pa



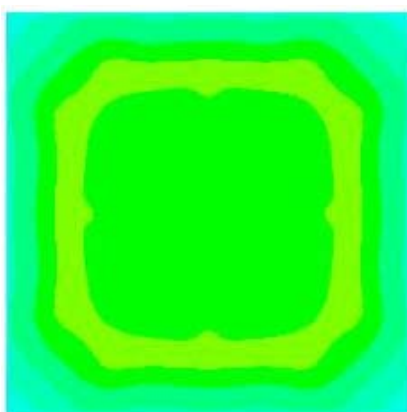
(b) Velocity plot at $z = 0.15$ m for $\Delta P = 18.688$ Pa



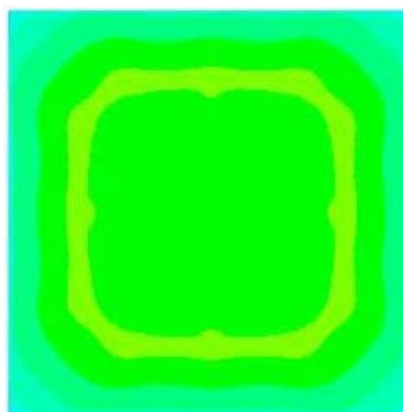
(c) Velocity plot at $z = 0.5$ m for $\Delta P = 18.688$ Pa



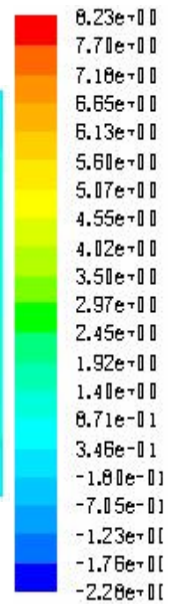
(d) Velocity plot at $z = 1.0$ m for $\Delta P = 18.688$ Pa



(e) Velocity plot at $z = 1.5$ m for $\Delta P = 18.688$ Pa



(f) Velocity plot at $z = 2.1336$ m for $\Delta P = 18.688$ Pa



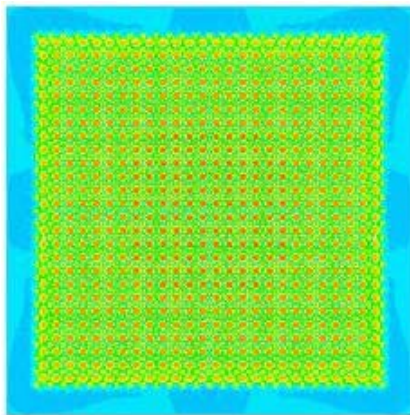
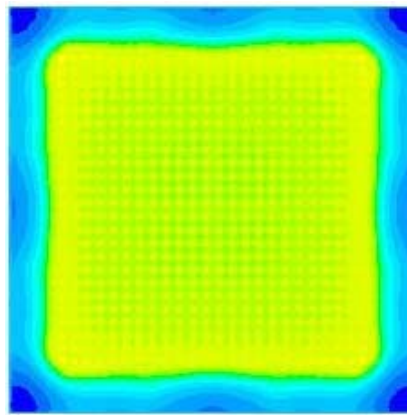
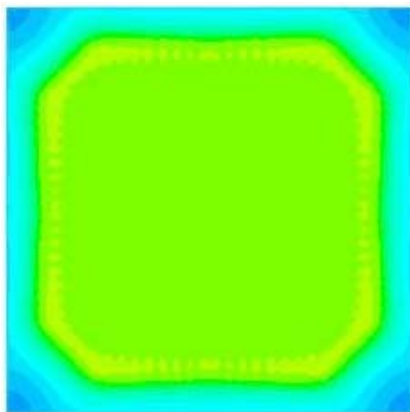


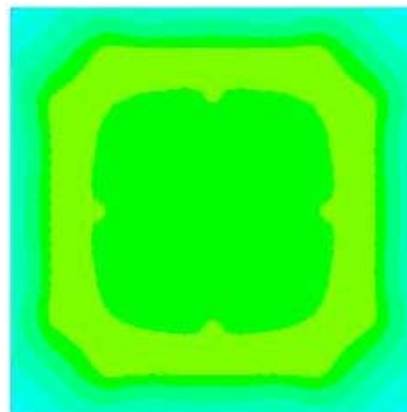
Fig 8.47: (a) Velocity plot at $z = 0.01$ m for $\Delta P = 12.459$ Pa



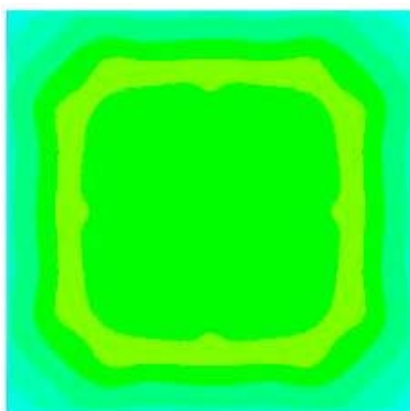
(b) Velocity plot at $z = 0.15$ m for $\Delta P = 12.459$ Pa



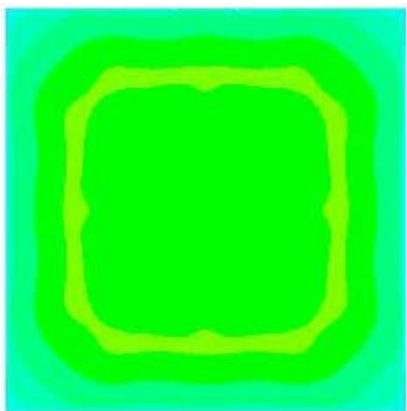
(c) Velocity plot at $z = 0.5$ m for $\Delta P = 12.459$ Pa



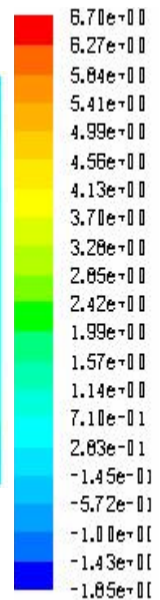
(d) Velocity plot at $z = 1.0$ m for $\Delta P = 12.459$ Pa



(e) Velocity plot at $z = 1.5$ m for $\Delta P = 12.459$ Pa



(f) Velocity plot at $z = 2.1336$ m for $\Delta P = 12.459$ Pa



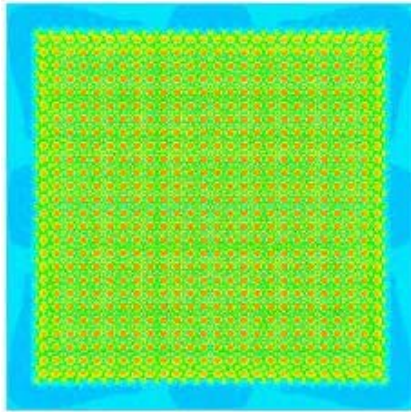
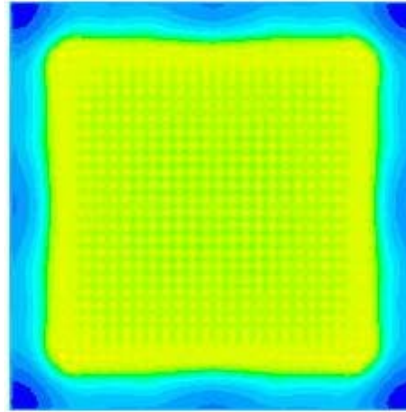
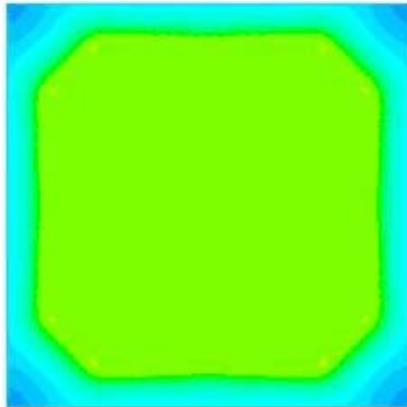


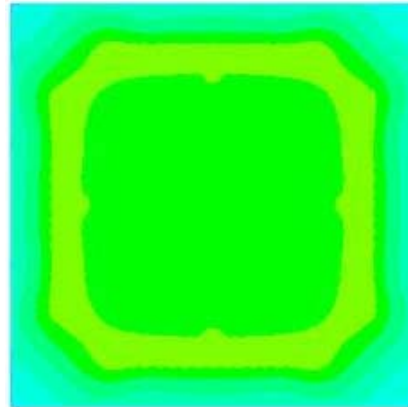
Fig 8.48: (a) Velocity plot at $z = 0.01$ m for $\Delta P = 6.229$ Pa



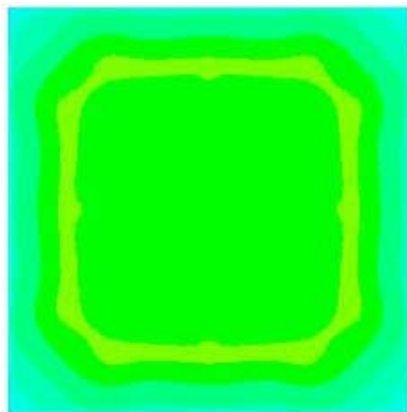
(b) Velocity plot at $z = 0.15$ m for $\Delta P = 6.229$ Pa



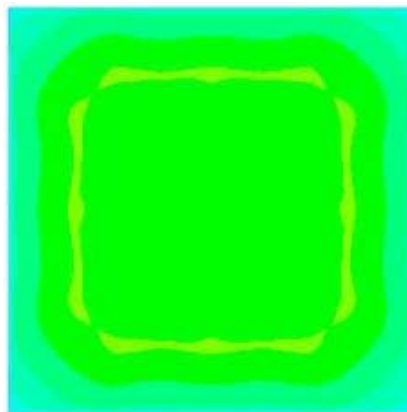
(c) Velocity plot at $z = 0.5$ m for $\Delta P = 6.229$ Pa



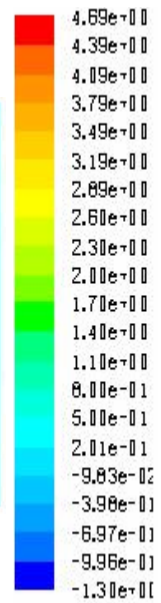
(d) Velocity plot at $z = 1.0$ m for $\Delta P = 6.229$ Pa



(e) Velocity plot at $z = 1.5$ m for $\Delta P = 6.229$ Pa



(f) Velocity plot at $z = 2.1336$ m for $\Delta P = 6.229$ Pa



The centre tile velocities of all the tiles are compared on the basis of average value of centre line velocity $U_{z_{avg}}$. For all tiles the average value decreases as the pressure difference across the tile decreases in a similar manner. The only difference is in the relative values. The variation of average centre line velocity for all the tiles are given in Fig 8.49.

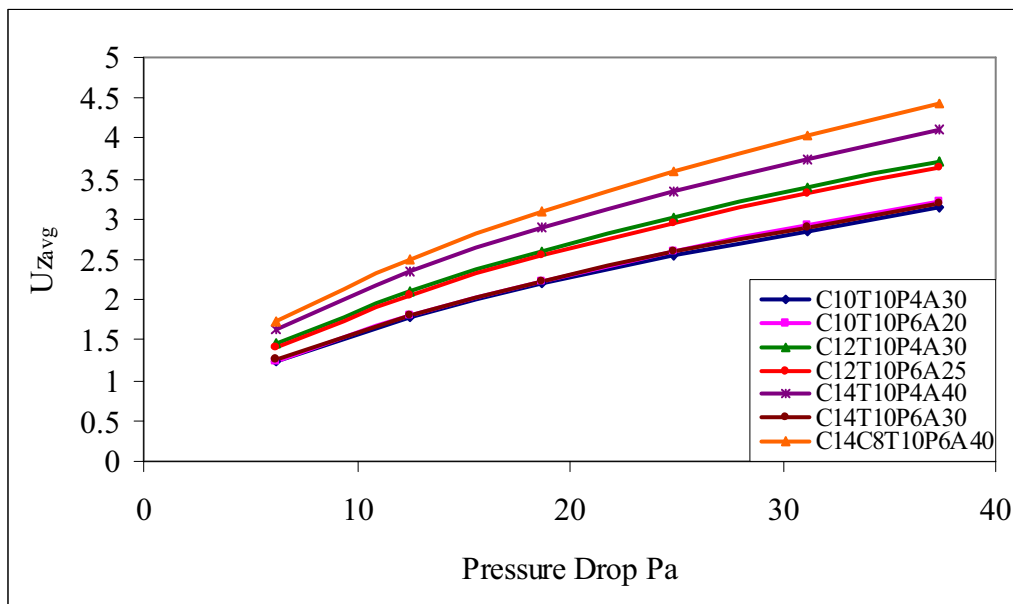


Fig 8.49: Comparison of average centre line velocity of various tile models

Variation of average centre line velocity with reduction in pressure difference is also analyzed and the percentage reduction for successive pressure difference is plotted and is shown in Fig 8.50. All the tiles showed the same reduction rate in the range of pressure ratios selected and all have an overall reduction of 60-61%. The percentage overall reduction of various tiles are given in the Table 8.8

Table 8.8: Percentage overall velocity reduction of various tile models

Tile	% Overall Reduction
C10T10P4A30	60.66
C10T10P6A20	61.38
C12T10P4A30	60.74
C12T10P6A25	61.17
C14T10P4A40	60.26
C14T10P6A30	60.31
C14C8T10P6A40	60.77

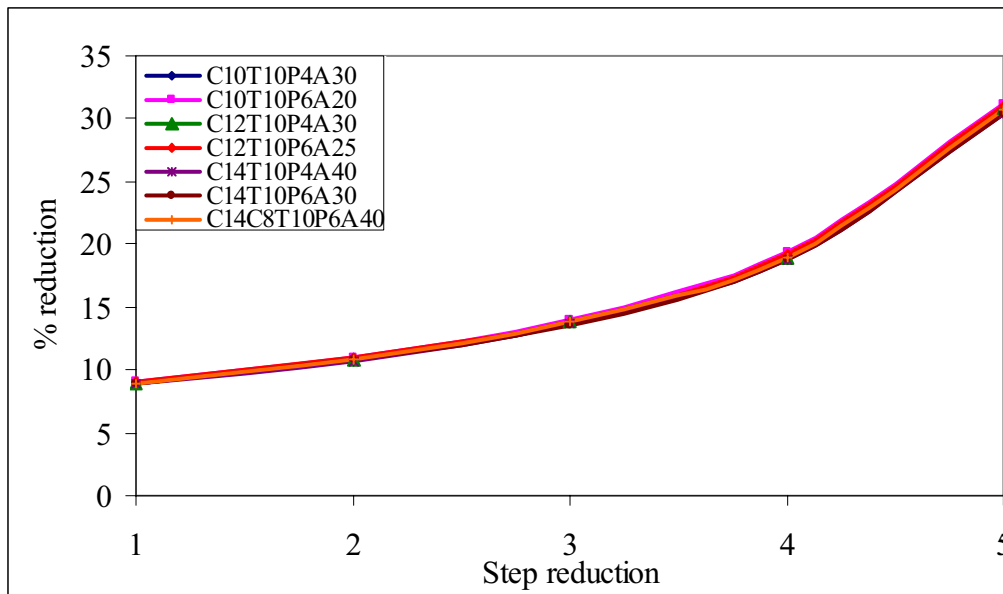


Fig 8.50: Percentage velocity reduction of various tile models

The above discussion suggests that no tile configuration is superior to the other. Different types of tiles find their own application in the range of their flow rate and velocities. From the centre line velocity decay curves of the tiles, it is observed that after a distance of 0.75m in z direction from the floor the velocity is steady and this steady velocity decreases as the pressure difference across the tile decreases. For the region from 0-0.75m the velocities are higher, and from the velocity plots at z locations 0.01m,

0.15m and 0.5m, it can be seen that there is considerable recirculation in this region (region of negative pressure where the effect of jet is not felt). Since the z velocities are higher in this zone, it is difficult for hardware placed at this location to suck air from the tiles and may become hot spots. So this region of racks should be used to deploy very low power density devices such as storage devices. The region of steady velocity is having only moderate but sufficient velocities and the racks can suck air from this region without much difficulty, hence medium or high power density hardware can be located at this region of the racks. Deploying high density hardware at the top region of the racks may cause hot air recirculation due to the scarcity of air that may occur depending on the hardware at the bottom region.

From the z velocity plots along the x direction of all tiles explained in the respective sections, it can be seen that the z velocity along x direction are the same for a tile above a distance of 0.5m above the floor. This suggests that the velocity distribution in the confined volume enclosed by the racks will have a constant velocity distribution irrespective of the z position beyond a distance of 0.5m. This is an important observation with respect to data centre design. This observation suggests that the hardware located at any position above 0.5m from the floor will get air at constant velocity at their inlet. This information will give a lot of flexibility in deploying the hardware in the racks. Further to this, the z velocity along x direction increases slightly and it reaches a maximum value at a particular point depending on the tile and the pressure difference across the tile and reduces thereafter. The maximum velocity point depends on the distance from the floor for all tiles and for all pressure differences across the tile. As the distance from the floor increases, the maximum velocity occurs earlier. The increase in velocity along the x direction is due to the fact that as the distance in the x direction increases, the orifice matrix grows which will increase the number of jets interacting. The outer jets will suppress the development of the inner jets while the outer jets will entrain the neighbouring jets and will grow. This effect will terminate as the distance increases and reaches the wall boundary condition. The

presence of the wall boundary condition will restrict the growth of the jets at that region and the velocity reduces to a lower value near the wall. It can be concluded that a few rows in the jet matrix near the racks do not contribute to the velocity distribution, but they are helping in maintaining the required flow rates. However these jets will be effective when the rack suction pressure is introduced.

As the distance from the floor increases, the maximum velocity point occurs earlier and also this maximum velocity decreases. After a particular distance from the floor the influence of outer jet on inner jet will be less and the inner jet will develop more but with a reduced velocity. As the distance increases the jets will loose its momentum and will start to diffuse. As the jet matrix develops, the profile tends towards that of a single circular jet as explained in Chapter 7 which is evident from the velocity plots at different locations shown along with the tile results.

The velocities of all the tiles in z direction along the x direction are summarized in Fig 8.51 to Fig 8.54 for a pressure difference of 37.376 Pa.

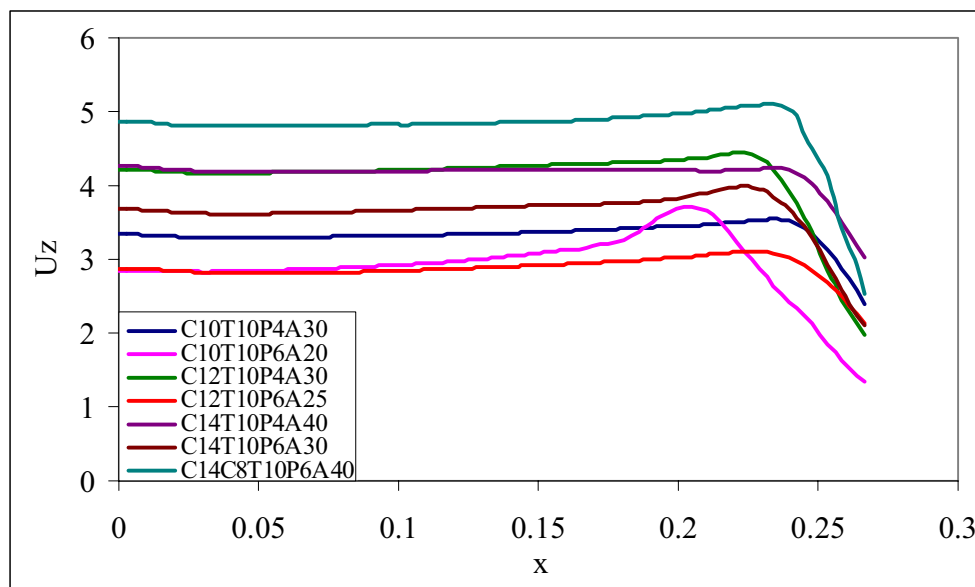


Fig 8.51: Comparison of z velocity along x direction for $\Delta P = 37.376$ Pa at $x = 0.5$ m for various tile models.

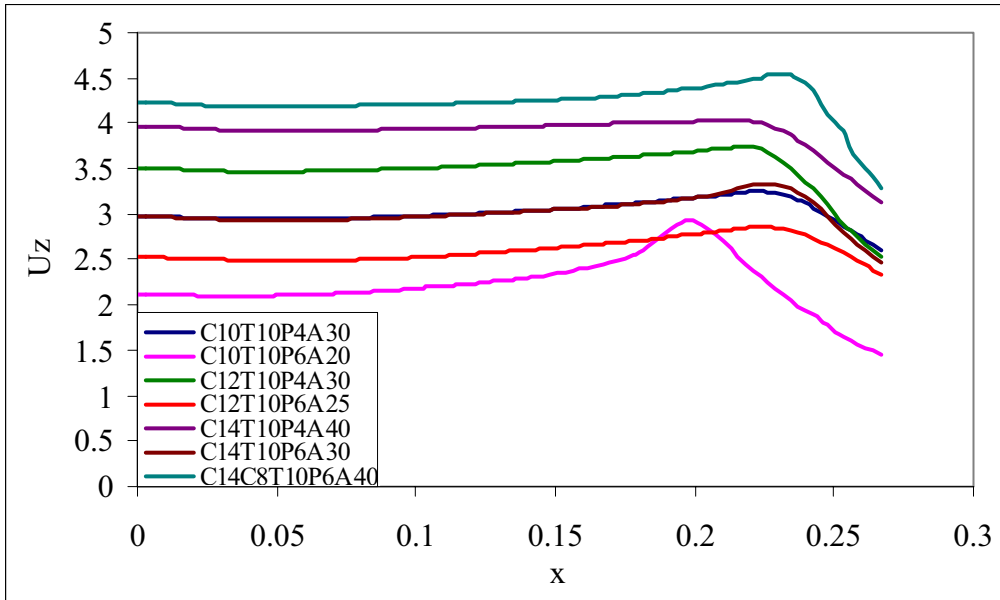


Fig 8.52: Comparison of z velocity along x direction for $\Delta P = 37.376$ Pa at $x = 1.0$ m for various tile models.

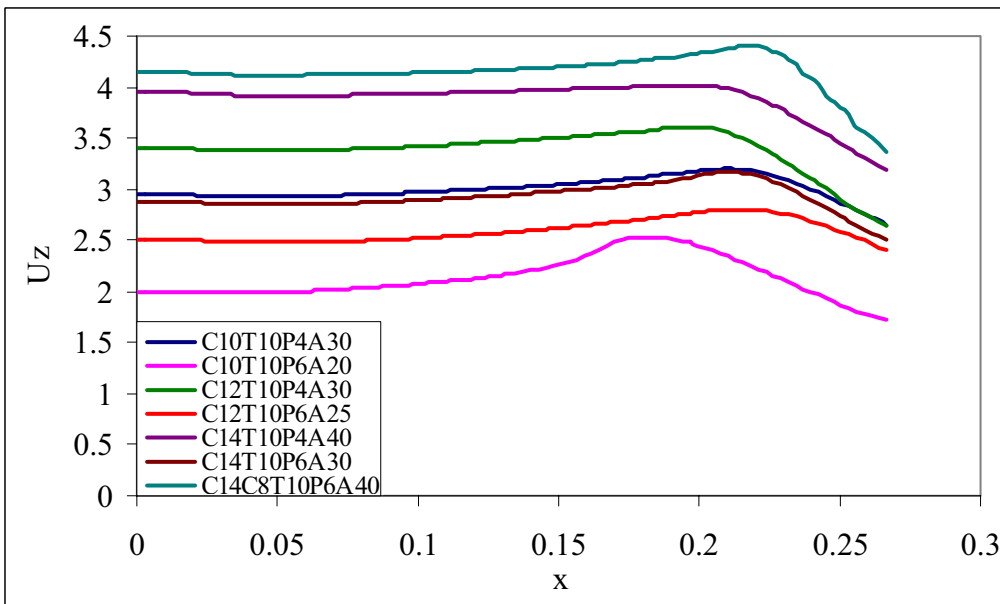


Fig 8.53: Comparison of z velocity along x direction for $\Delta P = 37.376$ Pa at $x = 1.5$ m for various tile models.

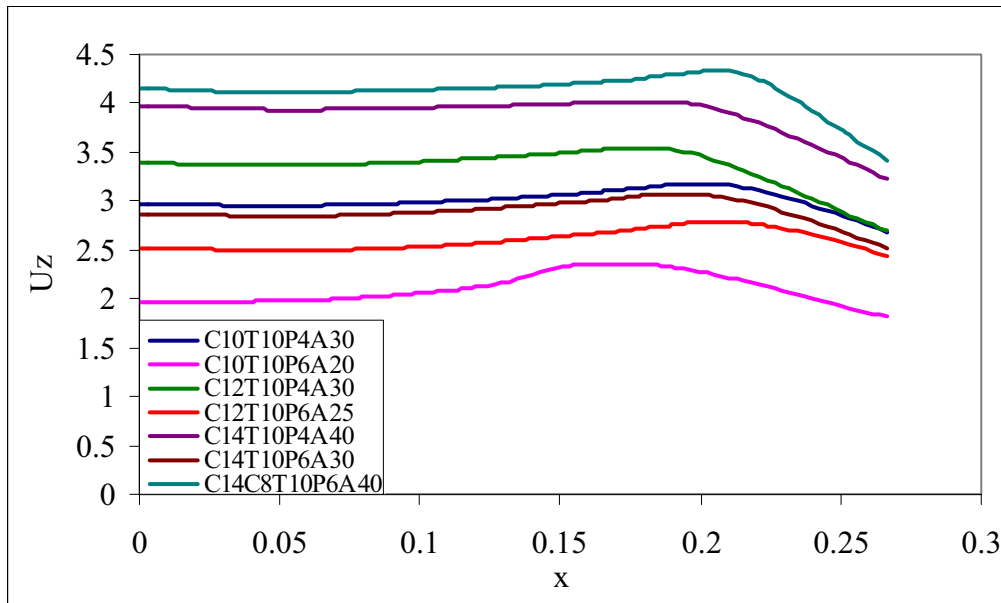


Fig 8.54: Comparison of z velocity along x direction for $\Delta P = 37.376$ Pa at $x = 2.1336$ m for various tile models.

From the above plots it can be inferred that at the same pressure difference across the tiles, the performance of the tiles are different. The combination tile performs better than standard tiles for all pressure differences. Among the standard tiles, the tiles with pitch value 4mm performs better than those with pitch value of 6mm. And among tiles of same pitch value, the tiles with larger diameters perform better. Hence it can be concluded that for better performance of tiles, selection of diameter and pitch plays a significant role. Larger the diameter and smaller the pitch, better the performance.

8.5 Conclusion

In this chapter, the detailed design and designation of perforated vent tiles is carried out. The design of six standard tiles and one combination tile are presented with necessary flow area calculations for the complete designation of the tile. Thus in the present work, for the first time, a new tile code is established for designating perforated vent tiles. The solution domain and necessary boundary conditions employed for the solution are explained in detail and the specific advantages of

these boundary conditions are illustrated. Detailed sketch of each tile is given in the respective sections along with the important dimensions.

The design can be extended with orifice diameters ranging from 6mm onwards to get a number of standard tiles and different geometries of combination tiles by selecting appropriate major and minor matrix of orifices. The standard tile can give only one characteristic flow rate and velocity distribution with respect to a specific pressure difference. The combination tile can give three different characteristic curves for mass flow and velocity distribution. With all the orifices on the tile open, it will give the full tile characteristics. With the minor matrix orifices closed with a blocking pad, it will give the major tile characteristics. And with the major matrix orifices closed with a suitable blocking pad, it will give the minor tile characteristics. Hence it can be seen that combination tile is more versatile and flexible in operation and can be used for dynamic loading situations.

A detailed analysis of the performance of the tiles are made and the flow rate calibration charts are presented in the respective sections which will help in finding out the flow rate through that tile for any pressure difference across it. A qualitative analysis of the tiles is made to bring out the velocity distribution pattern within the confined volume. With the help of these velocity plots it is possible to predict the velocities at any x, y or z location within the confined volume, which gives high degree of flexibility for data centre designers. Even though the present work is restricted to the design of seven tiles, it is possible to design any configuration to get the desired flow rates and velocities by changing the design parameters of the tile. Proper combinations of circular orifices, pitch values and tile thickness can be selected to get different tile configurations. The shape of orifices can be changed from circular to square, rectangle, hexagon or combination of these to get different open area ratios which will change the flow rates. These different combinations will result in different open area ratios and hence different flow rates, but they will not differ much from the basic design with respect to the velocity

distribution, since all configurations finally have the universal characteristics of a single circular jet. Hence the present work establishes a systematic and scientific design and coding of perforated vent tiles for the optimization of data centre air flow for the first time.

During the analysis of the tiles it is observed that the single parameter on which the entire tile flow depends is the pressure difference across the tiles. As this pressure difference changes, the tile performance will change both in qualitative and quantitative aspects. The existing computational design and analysis of data centre do not account for this factor. Currently in the design and analysis of data centre the pressure difference across the tiles is considered as a dependant variable which is controlled by other system variables. Since the air flow dynamics solely depends on the pressure difference, which being a dependant variable in this analysis, naturally, the results obtained from such analysis will be unrealistic with respect to the actual air flow mechanism. The present study emphasizes that the pressure difference across the tile should not be taken as a dependant variable rather it must be considered as an independent variable for the design and analysis of data centres as it directly controls the air flow pattern. A modern methodology of design and analysis of data centres must be evolved on the basis of the above facts, which is beyond the scope of the present work.

.....✍.....

EFFECT OF DAMPER AND RECIRCULATION

Contents	9.1 Introduction
	9.2 Effect of Damper
	9.3 Effect of Recirculation
	9.4 Results and Discussion
	9.5 Conclusion

9.1 Introduction

In this chapter, the effect of damper on the air flow pattern within the cold aisle is discussed in detail. The damper has got two effects on the tile air flow pattern. They introduce an additional pressure drop across the tile and they make a total change in the orifice configuration matrix. In this chapter, the effect of additional pressure drop on flow pattern alone is discussed since the configuration changes are asymmetrical and hence cannot be modelled. The effect of hot air recirculation is an important phenomenon in data centre operation which is not discussed much theoretically. An attempt is made here to explain the serious effects of recirculation. This is done by introducing rack suction effect and the velocity pattern is studied while the racks are sucking air from the cold aisle. In this analysis rack suction pressure is assumed as a constant through out the rack height for a particular case. In real case the rack suction pressure will vary along the rack height depending on the hardware deployment. Different values of rack suction pressures are considered to obtain the effect of rack suction on hot air recirculation. For the analysis, the standard tile C14T10P6A30 is considered and it is found that all other tiles follow the same trend.

9.2 Effect of Damper

The major purpose of employing dampers in data centre floor tiles is to have capacity control of the air flow. All types of dampers used in the tiles serve this purpose quantitatively by changing the open area ratio of the tile. But nothing is known about the influence of dampers on the qualitative air flow dynamics through the tiles. While controlling the air flow quantitatively by using the damper, they introduce an additional pressure drop across the tile, which is a hidden undesirable effect of the damper. The damper used in all the tiles is a solid structure having considerable thickness which will introduce an additional obstruction to the air flow. When the air flows through the dampers the energy of the air imparted by the CRAC blower will be lost and the effective pressure at the bottom of the tile will be reduced. Effectively the damper will create a situation similar to that of a flow occurring at a reduced under floor plenum pressure. In order to study the effect of dampers, no separate modelling and analysis are carried out; they are deduced from the flow calibration models of the standard tile C14T10P6A30.

9.3 Effect of Recirculation

The normal direction of air flow in a data centre occurs from the tiles as the cold air flows into the cold aisle from where it is sucked by the system fans of the hardware located in the racks at different heights. After cooling the hardware the hot air is discharged through the rear of the racks into the hot aisle from where the hot air moves up due to thermal stratification and it reaches the hot plenum through the hot tiles placed in the hot aisle. If this flow pattern is strictly maintained within the data centre there will not be any issue of hot air drip and recirculation. But under certain conditions of tile flow, especially flow with reduced pressure difference across the tiles, the cold air may not be capable of reaching the top region of the racks. At reduced pressure differences the flow rate as well as the velocities will be low and the air may be completely sucked by the systems situated at the lower and middle region of racks depending on the suction fan capacities.

This situation will create a deficiency of cold air in the near vicinity of the hardware located at the top region of the racks. The system fans at this region will suck air from anywhere and the possibility of sucking air from the space above the racks where hot air is present is more. This introduces the effect of hot air drip and recirculation. The temperature of air that enters into the racks at this region depends on the degree of mixing of hot and cold air in the cold aisle. If the temperature of the recirculated air is high the hardware located at the top region will become hot and the severe issue of hot air recirculation occurs.

The occurrence of recirculation is strongly dependant on the flow pattern within the cold aisle. If sufficient cold air is available at the top region of the racks, recirculation effect will be less. Hence the effect of recirculation can be effectively explained by the air flow dynamics of the cold aisle. Separate modelling is required for this purpose. For this, the basic flow calibration model of the standard tile C14T10P6A30 is selected and the boundary conditions are modified as shown in Fig 9.1

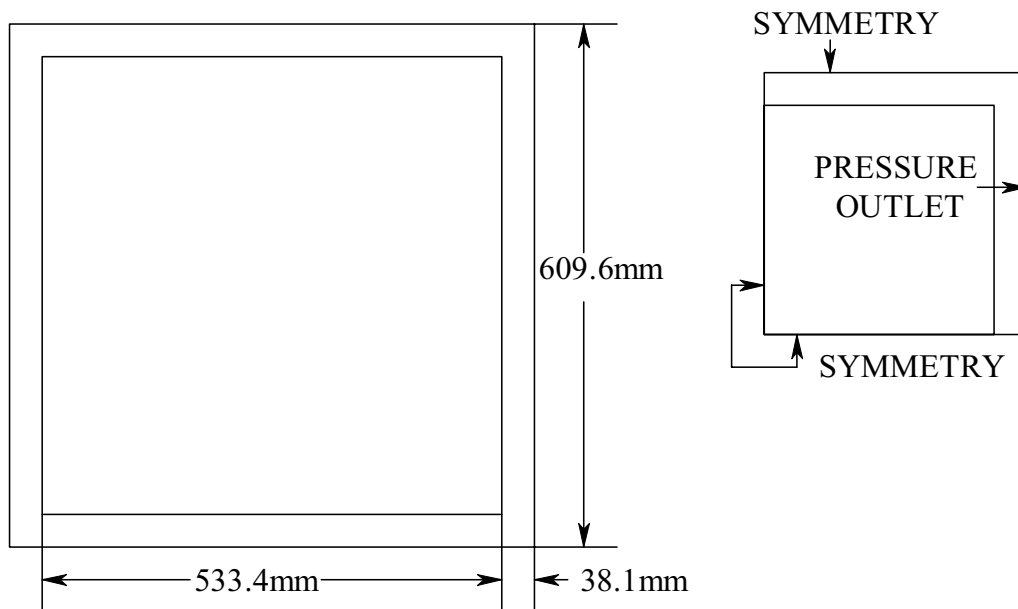


Fig 9.1 (a) Basic tile dimensions

(b) Quarter tile boundary conditions

Both the wall boundary conditions given for the flow calibration model is changed. The wall boundary condition assigned at the rack side is changed to pressure outlet boundary condition and the wall boundary condition assigned at the aisle side is changed to symmetry boundary condition. The pressure outlet boundary condition can be suitably given any pressure values to simulate the rack suction effect. In the present analysis, three different rack suction pressures 4 Pa, 6 Pa and 8 Pa are used. These values will designate the pressure difference across the system fans situated in the racks. The symmetry boundary condition assigned at the aisle side will help in simulating multiple tiles in the y direction along the aisle. This will enhance the result by introducing the effect of adjacent tiles onto the tile under consideration.

9.4 Results and Discussion

The results for both the above cases are discussed separately in the following sections. The information required for analyzing the effect of dampers are obtained from the models of C14T10P6A30 solved for the purpose of obtaining the flow rate and velocity determination. The rack suction models are developed separately and solved with the usual convergence criteria.

9.4.1 Effect of Damper

The curves showing the effect of dampers on the flow rates are the same as that of the flow rate calibration curves for the tile which is given in Figures 8.35. This is because the effect of damper is to reduce the effective pressure difference across the tile. Hence it can be seen that as the damper closes, the effective pressure difference across the tile reduces and the flow rate is also reduced. This is the desired effect of the damper which has gained importance in data centre for controlling the flow.

But it is seldom discussed about what happens to the flow velocities when the dampers are closed or opened. The variation of upstream velocities in the cold aisle with respect to varying pressure difference is given in Fig 8.37. It can be seen from the

figure that the velocity profile is seriously affected by the pressure difference across the tile. As the pressure difference decreases due to the closing of the damper the velocity in the cold aisle decreases considerably. At a pressure difference of 6.229 Pa the velocities are only in the range of 1-1.5 m/sec. These velocities are not sufficient to ensure sufficient air at the top region of the racks due to lack of momentum. The variation of z velocities along the x direction with reducing pressure differences across the tile at different locations from the floor are given in the Fig 9.2 (a) to (d).

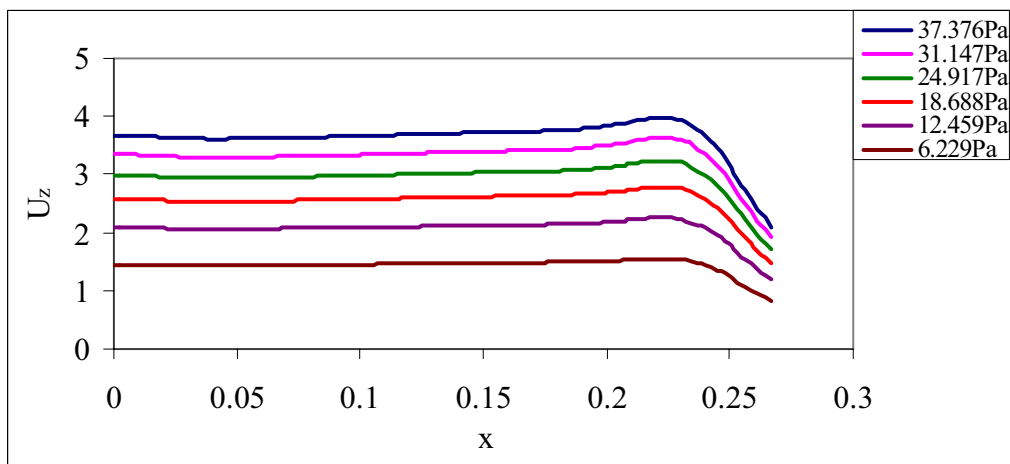


Fig 9.2(a) z velocity along x direction at 0.5m from the floor for various pressure differences

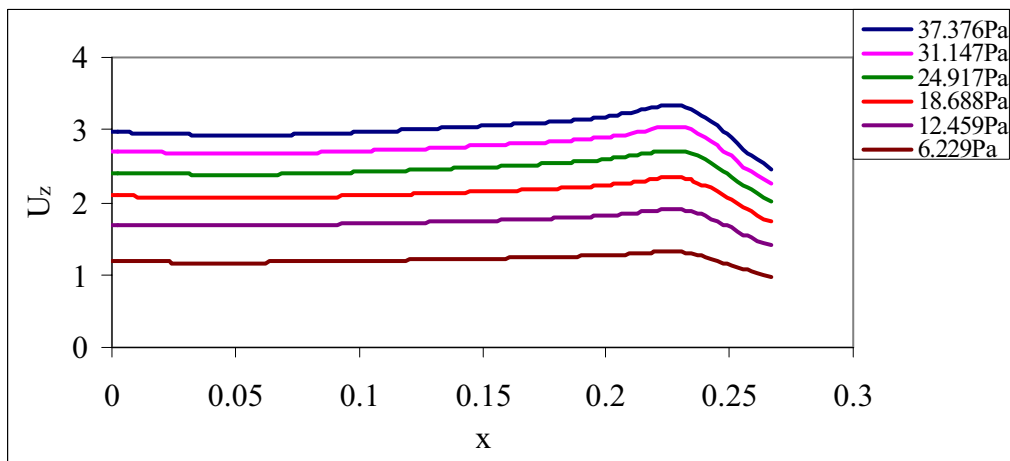


Fig 9.2(b) z velocity along x direction at 1.0m from the floor for various pressure differences

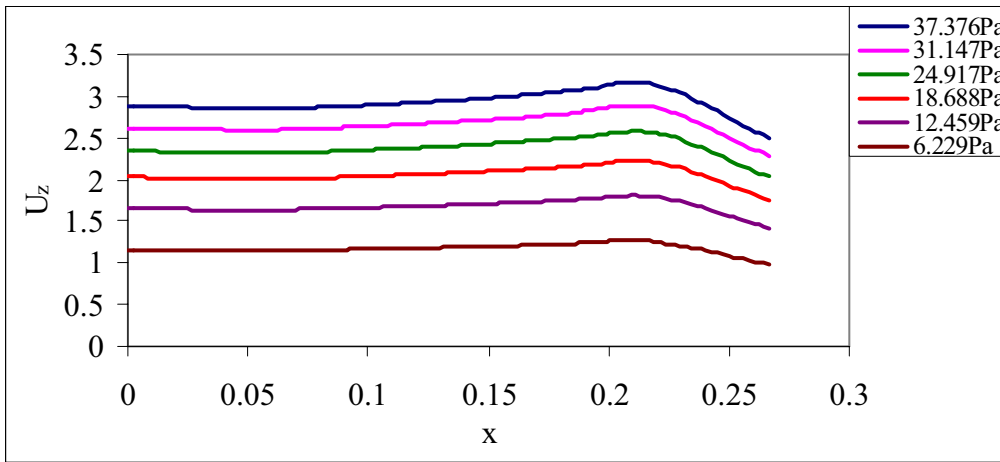


Fig 9.2(c) z velocity along x direction at 1.5m from the floor for various pressure differences

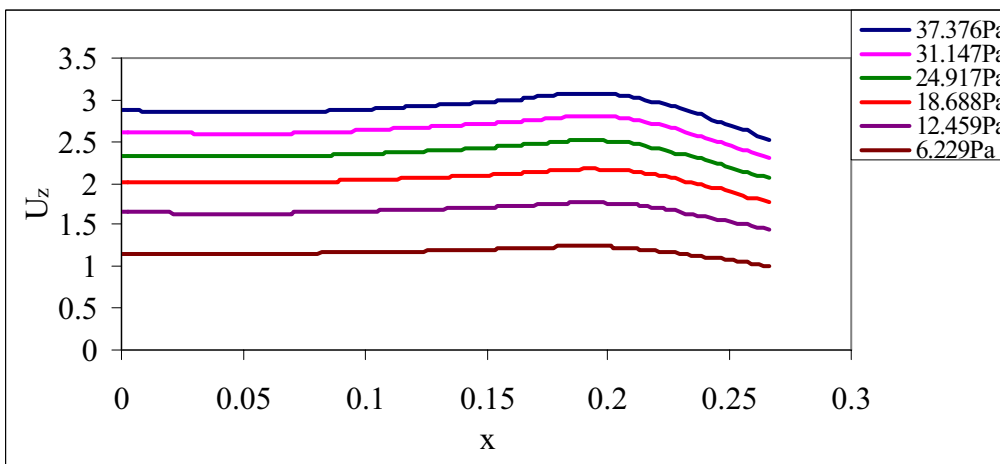


Fig 9.2(d) z velocity along x direction at 2.1336m from the floor for various pressure differences

It can be seen that at higher pressure difference across the tile the velocities are higher and as pressure difference decreases, the velocity values decrease to lower values. Hence it can be stated that as the pressure difference across the tile falls, the velocity values at all points in the cold aisle in all directions decrease and this will affect the effective usage of cold air in the data centre. Thus, it can be concluded that the use of dampers for capacity control will seriously affect the velocity distribution within the cold aisle and should be avoided for effective air flow utilization.

The above study reveals that the capacity control of the tiles by using dampers must be avoided for the sake of maintaining sufficient velocity distribution within the cold aisle. This study emphasizes the use of constant plenum pressure to have a steady velocity distribution pattern within the cold aisle. Whenever capacity control is required, the corresponding tiles must be replaced by another tile having different flow rates at the same pressure difference. In this way it is possible to maintain constant plenum pressure thereby constant velocity distribution within the cold aisle.

9.4.2 Effect of Recirculation

The physical mechanism of recirculation of air at the top region of the data centre can be explained by considering the mass flow rates and velocity profiles created within the cold aisle due to rack suction. Both cases are discussed separately. While considering the recirculation with the boundary conditions specified, there are three different mass flows involved within the cold aisle. Since the aisle side is assigned with the boundary condition of symmetry it will give infinite number of similar tiles placed in that direction. This condition is similar to the practical situation where number of tiles is aligned in a row in the cold aisle, with the only difference that they need not be similar tiles. In this situation the flow from three adjacent tiles will interact and mix each other thereby preventing the movement of air in that direction. Now there are three flows that are to be considered, flow from the tile, flow through the racks and the recirculation flow. Flow through the tile and recirculation flows are the flows into the cold aisle hence they are considered as positive flows while the flow through the rack is considered negative since it flows out from the cold aisle. Since the directions of these flows are obvious from their names itself the sign convention is not followed in the analysis. The different flow rates for different pressure difference across the tile at different rack suction pressures are summarized in the Table 9.1

Table 9.1 Flow rates in the cold aisle with varying rack suction pressure

Pressure	Rack	Tile flow	Tile flow	Rack Suction	Recirculation
difference Pa	Suction Pa	CFM	CMM	CFM	CFM
37.376	0	2262	64.06	0	0
	4	2159	61.15	3384	1225
	6	2210	62.6	3831	1621
	8	2260	64	4308	2048
31.147	0	2063	58.42	0	0
	4	1989	56.34	3250	1261
	6	2043	57.87	3789	1746
	8	2091	59.22	4135	2044
24.917	0	1844	52.22	0	0
	4	1803	51.08	3095	1292
	6	1860	52.67	3591	1731
	8	1912	54.15	4016	2104
18.688	0	1595	45.16	0	0
	4	1595	45.16	2899	1304
	6	1655	46.88	3410	1755
	8	1718	48.67	3884	2166
12.459	0	1300	36.82	0	0
	4	1351	38.27	2736	1385
	6	1430	40.47	3228	1798
	8	1510	42.74	3010	1500
6.229	0	913	25.86	0	0
	4	1062	30.07	2366	1304
	6	1155	32.72	2715	1560
	8	1241	35.15	2612	1371

The three flows are compared separately with respect to different pressure differences across the tile to study the variation of these flows as a function of pressure difference across the tile and are shown in Fig 9.3(a) to (c).

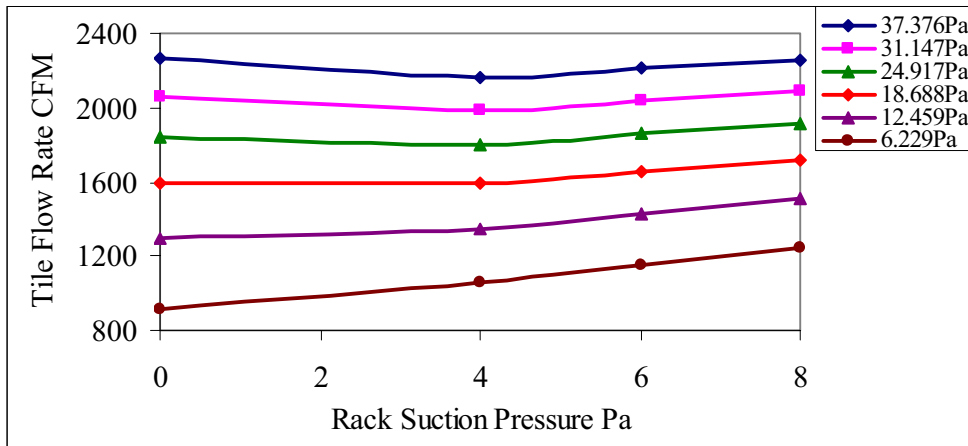


Fig 9.3(a) Variation of tile flow with rack suction pressure for various pressure differences across the tile.

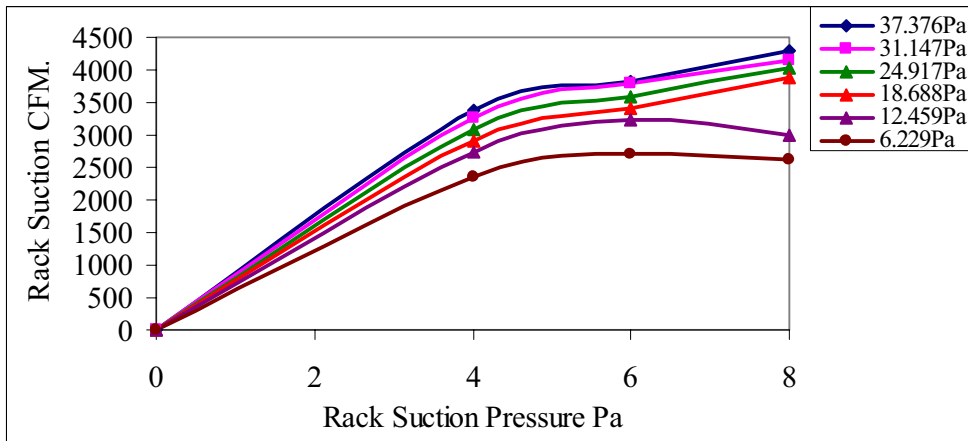


Fig 9.3(b) Variation of rack flow with rack suction pressure for various pressure differences across the tile.

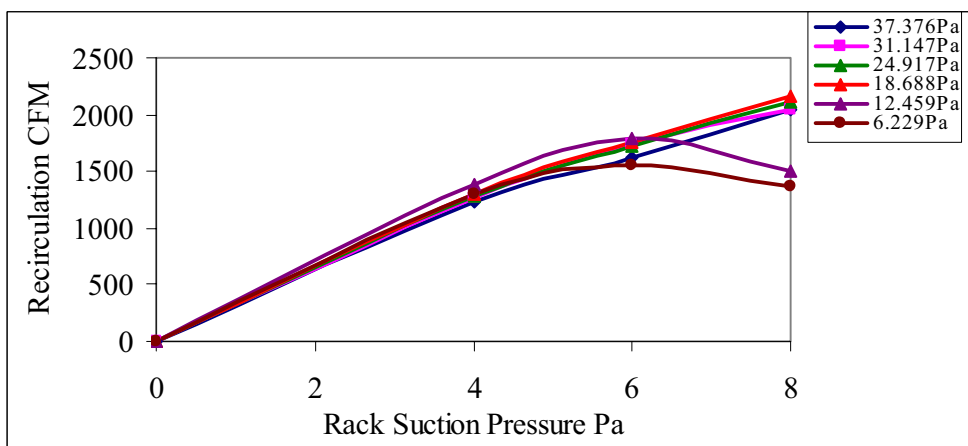


Fig 9.3(c) Variation of recirculation flow with rack suction pressure for various pressure differences across the tile.

Fig 9.3(a) shows the variation of tile flow with respect to the rack suction pressure. The curves show that, for higher pressure differences across the tile, the tile flow reduces as the rack suction pressure is introduced. This is against the usual expectation that, the tile flow should increase as the rack suction pressure is introduced. This is due to the additional pressure difference created by the introduction of rack suction. But for a rack suction pressure of 4 Pa, the tile flow reduces for the first three cases of pressure difference across the tile. Hence it is concluded that, there are two factors controlling the tile flow as the rack suction is introduced. The first one is the additional pressure difference created due to the rack suction, which will tend to increase the tile flow and the second one is the recirculation flow from the top which will obstruct the development of the upward flow from the tile thereby reduces the tile flow. The net flow from the tile will be a resultant of these two factors depending on the relative influence of these two factors. For higher pressure difference across the tile, when the rack suction is introduced, the effect of recirculation is more predominant than the additional pressure difference created by the introduction of rack suction and the tile flow reduces. When the rack suction pressure is increased, the influence of additional pressure drop dominates the recirculation and the tile flow increases. At reduced pressure differences across the tile, the rack suction pressures will have a dominant effect on the increased pressure difference and the tile flow will increase.

It is important to note the relative values of the flow rates at different pressure differences across the tile. For a pressure difference of 37.376 Pa across the tile, the flow rate without rack suction is approximately equal to the flow rate that corresponds to a rack suction pressure of 8 Pa. As the pressure difference across the tile reduces, the flow rate exceeds the flow rates without rack suction when rack suction pressure is introduced. At a pressure difference of 6.229 Pa the flow rate with rack suction of 8 Pa is about 50% higher than that of without rack

suction. Hence it can be concluded that the tile flow is significantly affected by the rack suction especially at reduced pressure difference across the tile.

Fig 9.3(b) show the variation of rack flow with respect to rack suction pressure. It is expected that, as the rack suction pressure increases the rack flow must increase. This is found to be true for cases with higher pressure difference across the tile. For all of the first four cases of pressure drop across the tile, the rack flow increases as expected. But when the pressure difference across the tile reduces, especially for the last two cases, the rack flow reduces as the rack suction pressure increases. This is a reversed phenomenon of flow which must be considered in detail. In order to explain this phenomenon it is necessary to consider Fig 9.3(c) also. This shows the variation of recirculation flow with respect to various rack suction pressure. For the first four cases of higher pressure difference across the tile, the recirculation flow increases as the rack suction pressure increases. The net flow through the racks will be the sum of the tile flow and the recirculation flow. At higher pressure difference across the tile, the tile flow and recirculation flow show an increasing trend and hence the rack flow is also increasing. But at reduced pressure difference across the tile and at higher rack suction pressures, the recirculation flow reduces even though the tile flow increases. The increase in tile flow is less when compared with the decrease in recirculation flow and hence the rack flow reduces. This phenomenon happening at reduced pressure difference across the tile and at higher rack suction pressure is due to the complex velocity distribution within the cold aisle. This results from the recirculation creep from the top into the cold aisle which could be obtained only by the velocity profile analysis of the cold aisle.

The centre line velocity decay of the tile for different pressure difference across the tile with varying rack suction pressures are given in Fig 9.4(a) to (f).

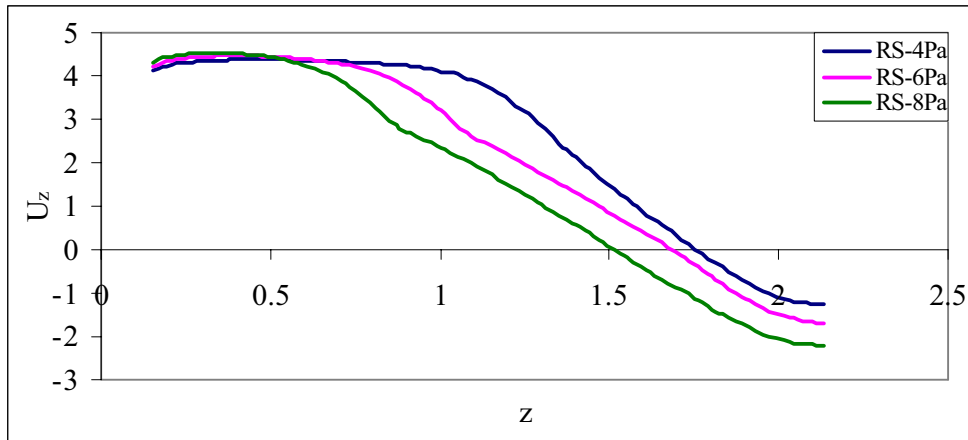


Fig 9.4(a) Centre line velocity of the tile at 37.376 Pa pressure difference across the tile for various rack suction pressure.

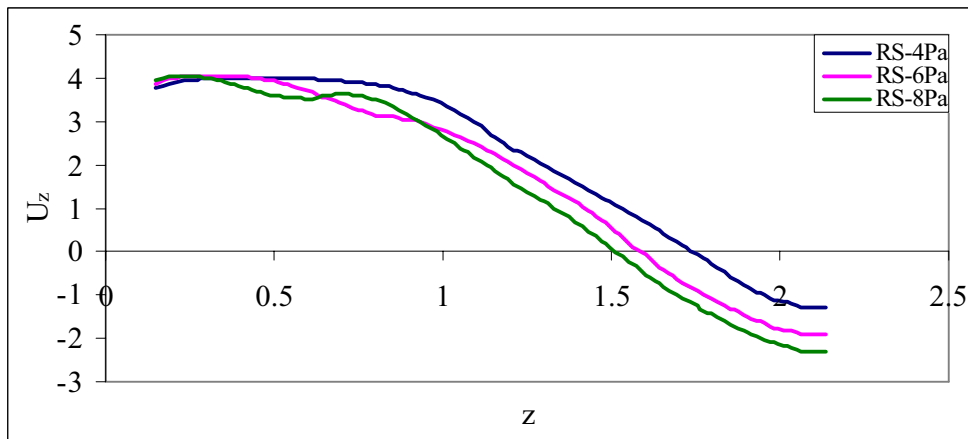


Fig 9.4(b) Centre line velocity of the tile at 31.147 Pa pressure difference across the tile for various rack suction pressure.

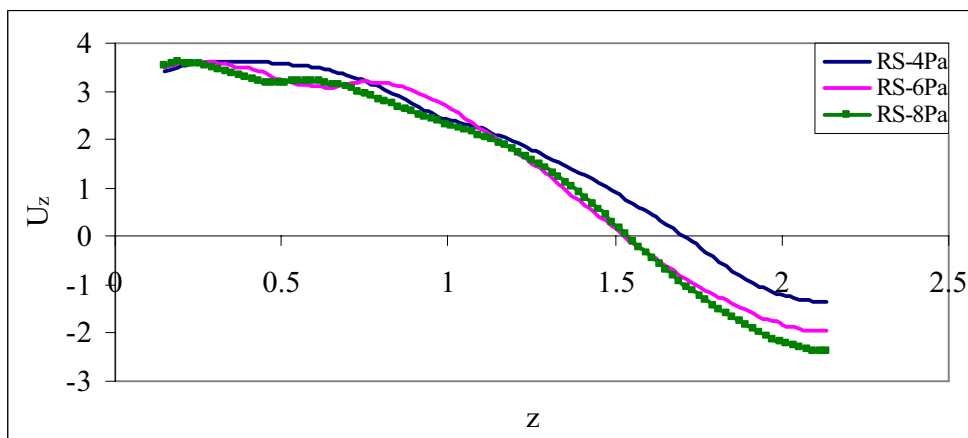


Fig 9.4(c) Centre line velocity of the tile at 24.917 Pa pressure difference across the tile for various rack suction pressure.

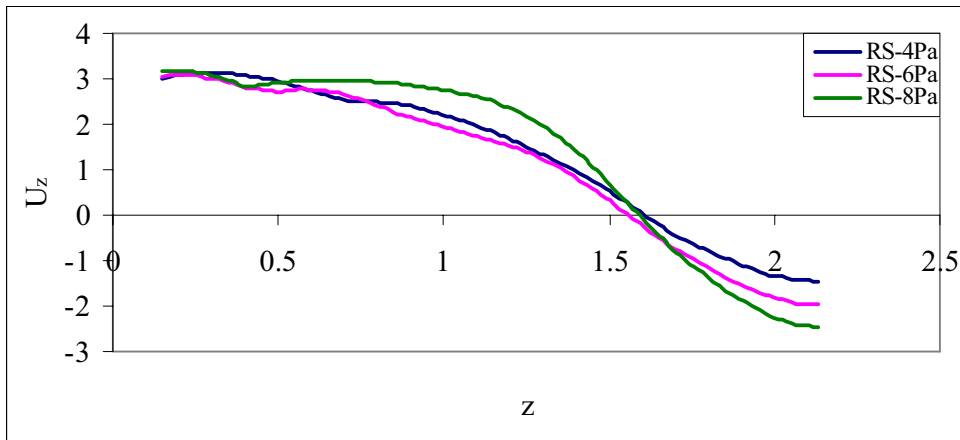


Fig 9.4(d) Centre line velocity of the tile at 18.688 Pa pressure difference across the tile for various rack suction pressure.

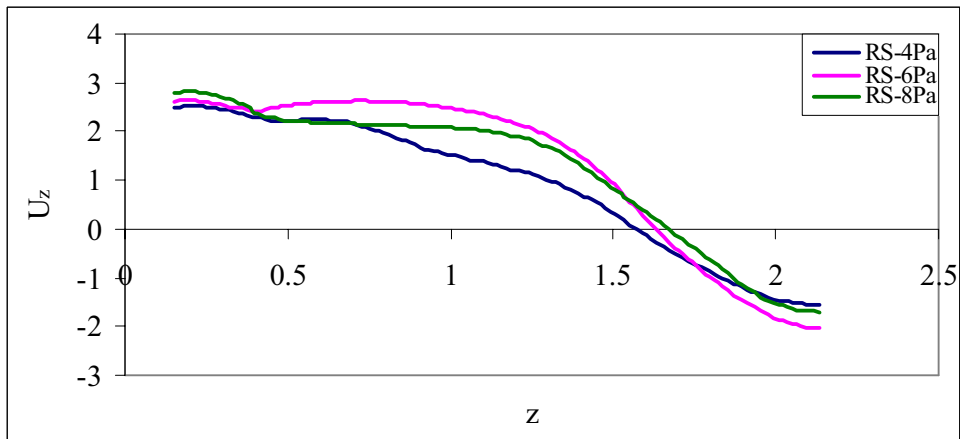


Fig 9.4(e) Centre line velocity of the tile at 12.459 Pa pressure difference across the tile for various rack suction pressure.

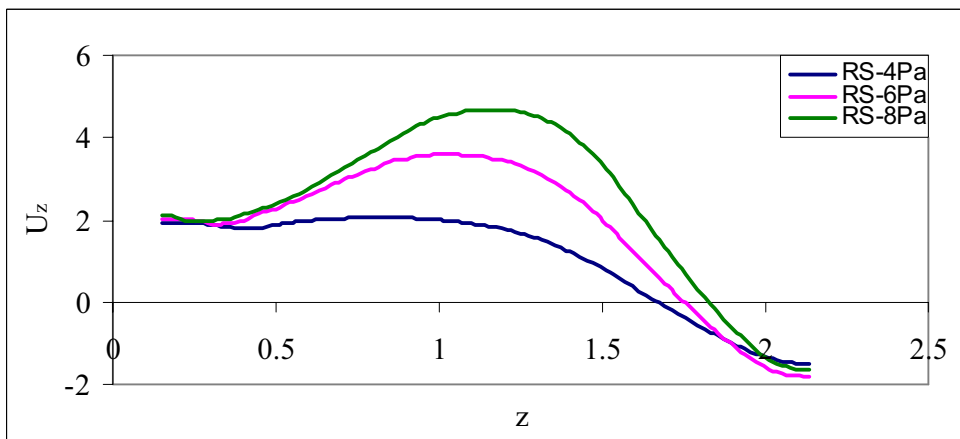


Fig 9.4(f) Centre line velocity of the tile at 6.229 Pa pressure difference across the tile for various rack suction pressure.

From the above figures, it can be seen that, the centre line velocity decay curve of the tile at different pressure differences across the tile crosses the x axis at different points and thereafter the velocities are negative. The negative velocity region shows the recirculation zone. Since in this region the velocities are negative, indicating that the flow is taking place from the top into the cold aisle. The point where the centre line velocity decay curve meets the x axis is called the recirculation point. This is the point from the tile surface measured in the z direction where the recirculation effect begins. The distance between this point to the top of the rack is called the recirculation creep.

From Fig 9.4(a), as the rack suction pressure increases the recirculation point shifts inward thereby the creep increases. Increased creep means more volume at top region of the cold aisle is susceptible for recirculation and the recirculation flow is also high. From Fig 9.4(b), it can be seen that the creep corresponding to rack suction pressure of 4 Pa and 8 Pa remains almost constant but the creep at 6 Pa increases and approaches towards that for 8 Pa. In Fig 9.4(c) the creep values for rack suction pressure of 6 Pa and 8 Pa are almost equal. From the Fig 9.4(d), the creep at rack suction pressure of 8 Pa is lesser than that at 6 Pa and almost equal to that at 4 Pa. From Fig 9.4 (e), the creep at rack suction pressure of 8 Pa is less than the other two and more importantly the creep of 6Pa is less than that of 4 Pa. This is the reverse phenomenon observed while discussing with the flow rates in the previous paragraphs. In Fig 9.4 (f) the same trend continues and the creep at higher rack suction is much lesser than that at lower rack suction. Thus we can conclude that as the pressure difference across the tile decreases while the rack suction pressure increases, the recirculation point shifts to the top thereby reducing the creep. Reducing the creep means lower volumes at the top region of the cold aisle is experiencing recirculation. This effect was already discussed while discussing the three mass flow rates, but the exact mechanism behind this behaviour can only be obtained by the introduction of the concepts of recirculation point and creep. Discussion

on these velocity profiles complete the discussion of the reversed phenomenon of decreased rack flow at increased rack suction pressures for lower pressure difference across the tile.

The centre line velocity decay is compared for same rack suction pressure with varying pressure difference across the tile in figures 9.5(a) to (c). These figures show how the recirculation point shifts as the rack suction pressure increases for a particular pressure difference across the tile. It is clear from Fig 9.5 (a), that the recirculation point of pressure difference 6.229 Pa is already lower than that for 12.459 Pa and 18.688 Pa. Fig 9.5 (b) clearly shows that the recirculation point for 6.229 Pa is lower than all other and the next lower pressure difference of 12.459 Pa advances to the front. In Fig 9.5 (c) it is clear that the entire pattern is totally reversed in the order. This indicates that, the pressure difference across the tile and rack suction pressures is influencing each other and this must be considered while designing the data centre air flow.

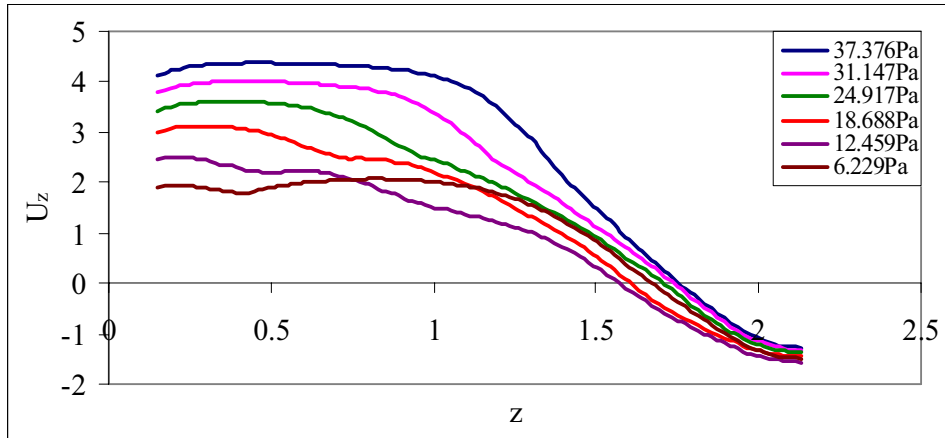


Fig 9.5 (a) Comparison of centre line velocity at Rack suction pressure of 4 Pa for various pressure difference across the tile

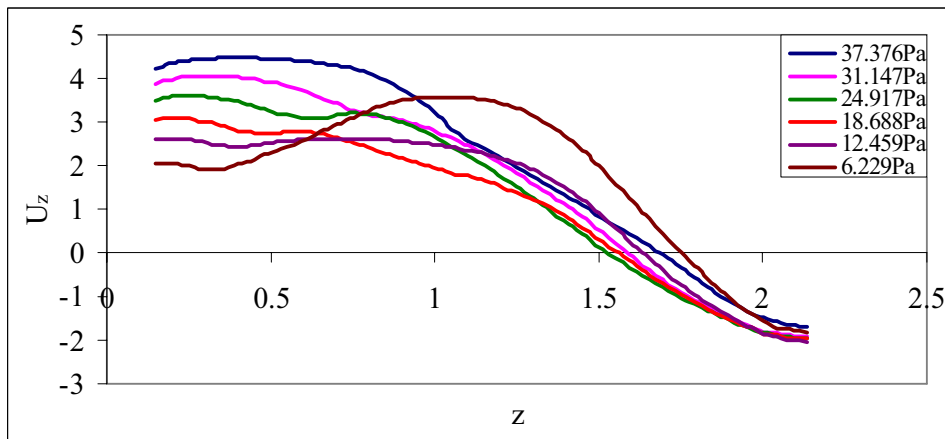


Fig 9.5 (b) Comparison of centre line velocity at Rack suction pressure of 6 Pa for various pressure difference across the tile

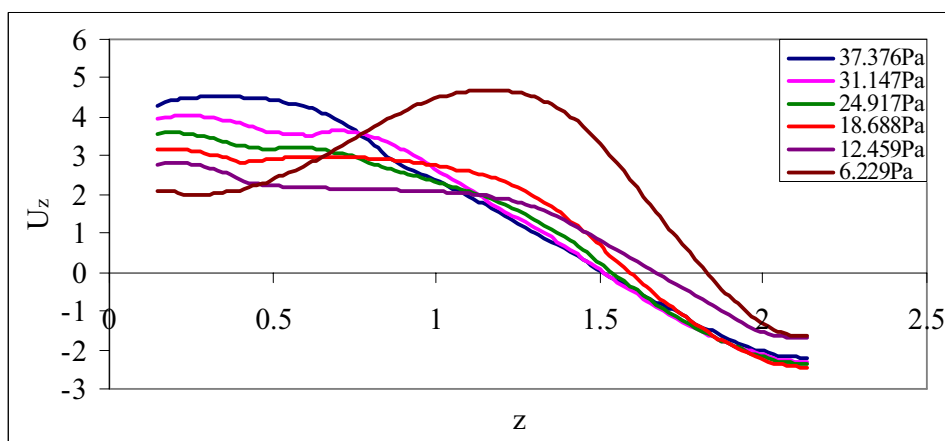


Fig 9.5 (c) Comparison of centre line velocity at Rack suction pressure of 8 Pa for various pressure difference across the tile

The z velocity profiles in the x direction for different rack suction pressures for various pressure differences across the tile and are given in figures 9.6 to 9.11.

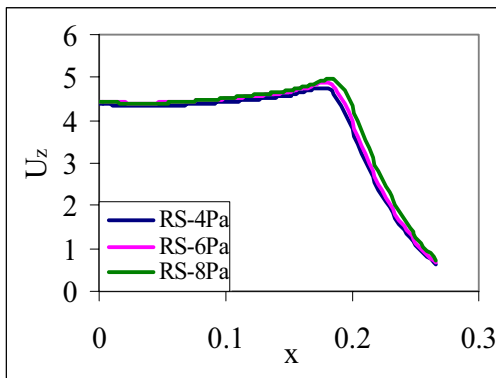
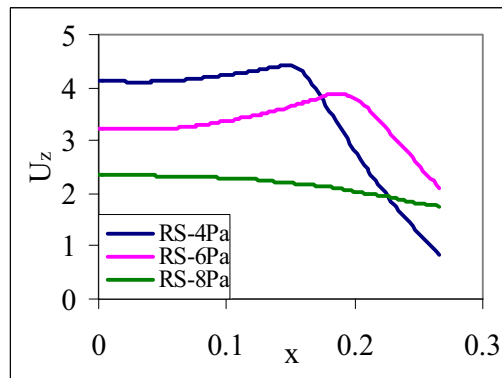
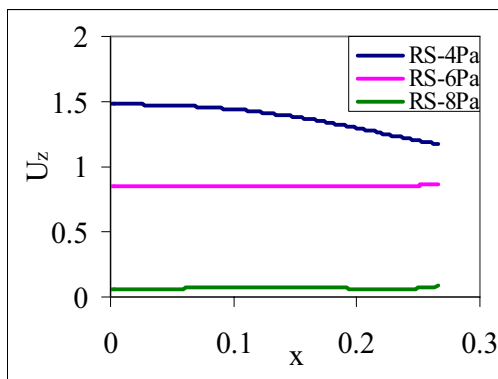


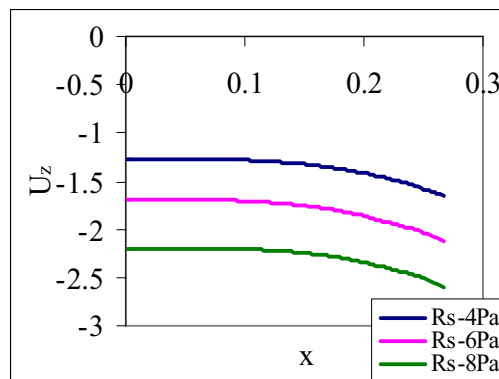
Fig 9.6 (a) z velocity in x direction for $\Delta P = 37.376$ Pa at $z = 0.5$ m



(b) z velocity in x direction for $\Delta P = 37.376$ Pa at $z = 1.0$ m



(c) Velocity in x direction for $\Delta P = 37.376$ Pa at $z = 1.5$ m



(d) Velocity in x direction for $\Delta P = 37.376$ Pa at $z = 2.1336$ m

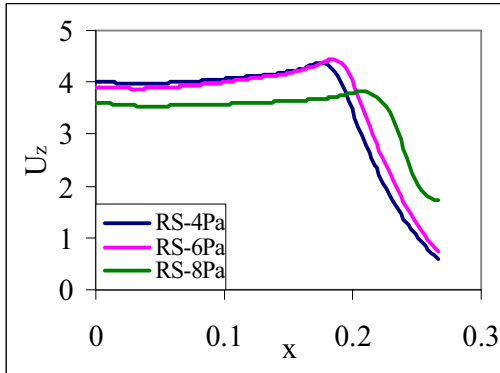
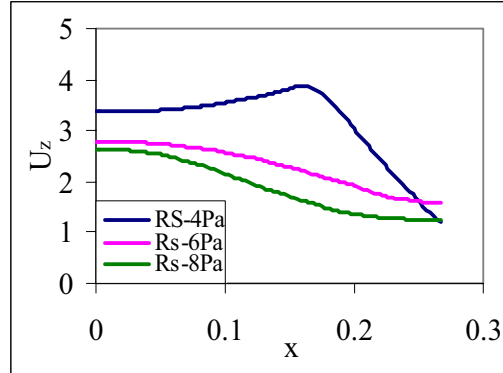
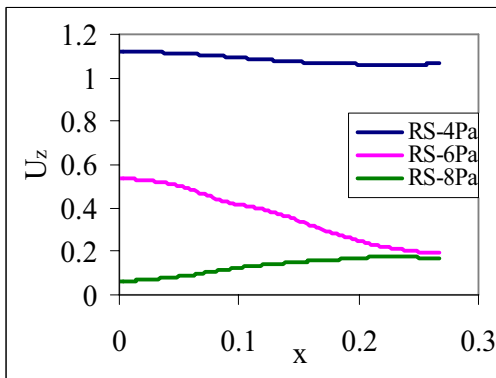


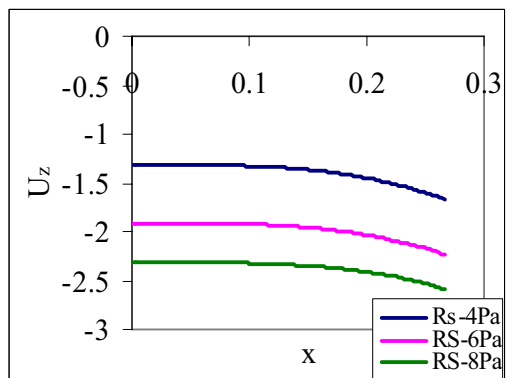
Fig 9.7 (a) Velocity in x direction for $\Delta P = 31.147$ Pa at $z = 0.5$ m



(b) Velocity in x direction for $\Delta P = 31.147$ Pa at $z = 1.0$ m



(c) Velocity in x direction for $\Delta P = 31.147$ Pa at $z = 1.5$ m



(d) Velocity in x direction for $\Delta P = 31.147$ Pa at $z = 2.1336$ m

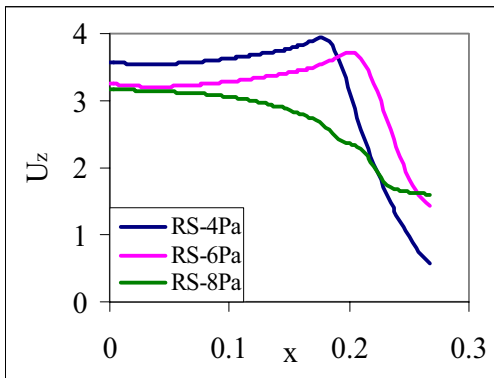
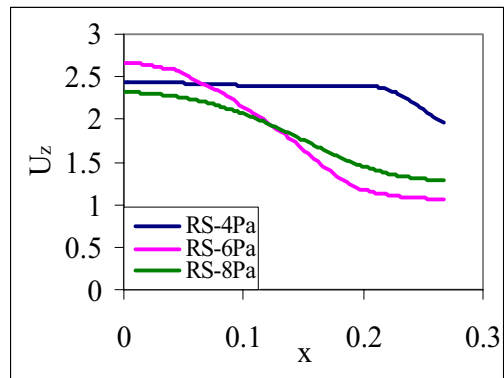
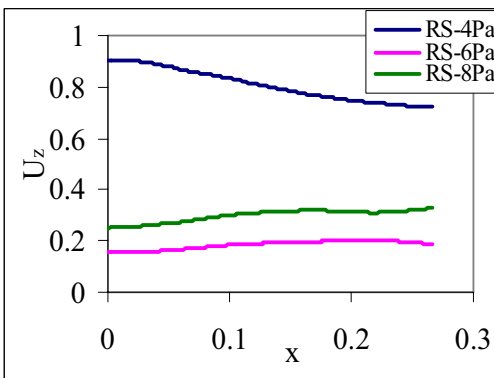


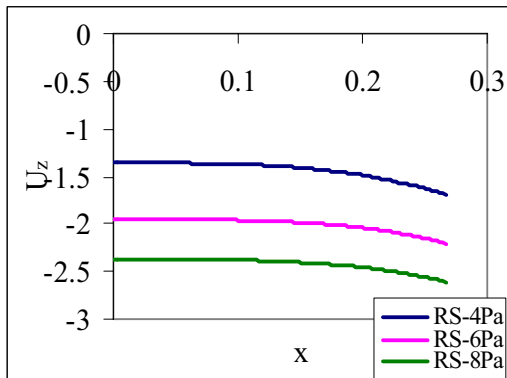
Fig 9.8 (a) Velocity in x direction for $\Delta P = 24.917$ Pa at $z = 0.5$ m



(b) Velocity in x direction for $\Delta P = 24.917$ Pa at $z = 1.0$ m



(c) Velocity in x direction for $\Delta P = 24.917$ Pa at $z = 1.5$ m



(d) Velocity in x direction for $\Delta P = 24.917$ Pa at $z = 2.1336$ m

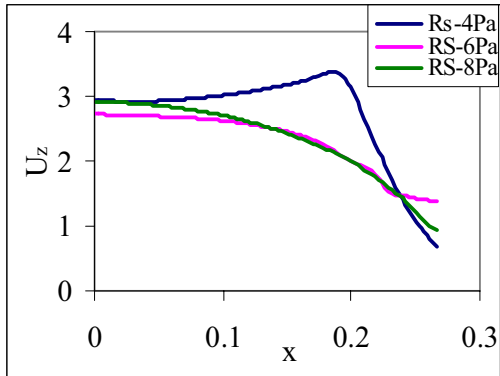
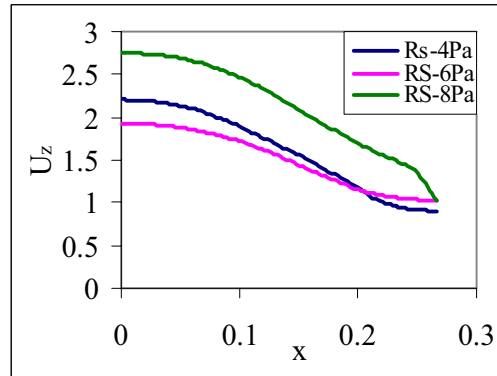
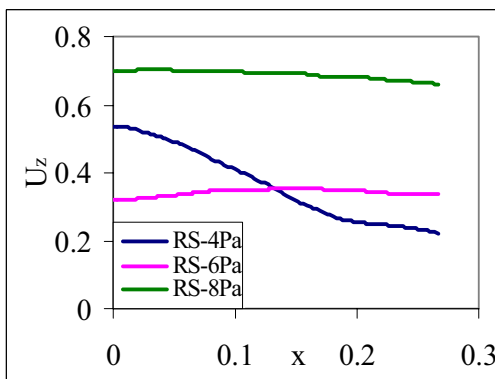


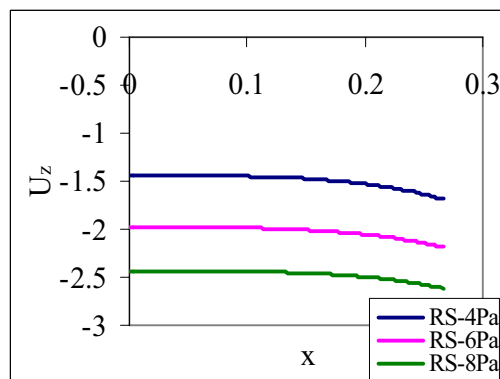
Fig 9.9 (a) Velocity in x direction for $\Delta P = 18.688$ Pa at $z = 0.5$ m



(b) Velocity in x direction for $\Delta P = 18.688$ Pa at $z = 1.0$ m



(c) Velocity in x direction for $\Delta P = 18.688$ Pa at $z = 1.5$ m



(d) Velocity in x direction for $\Delta P = 18.688$ Pa at $z = 2.1336$ m

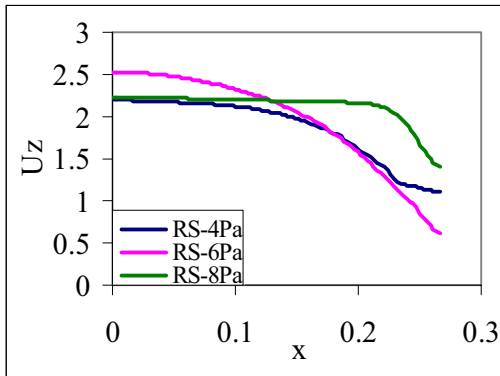
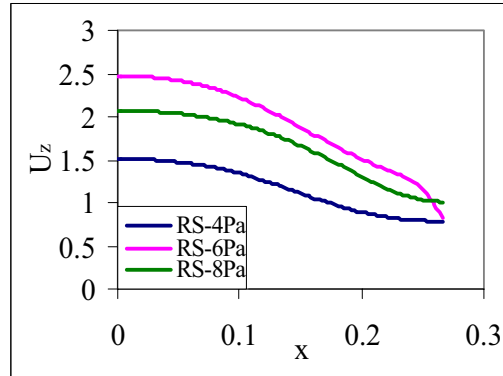
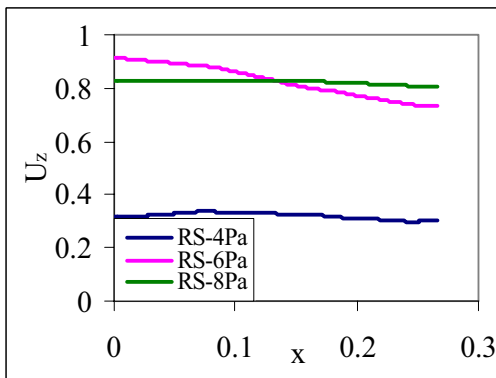


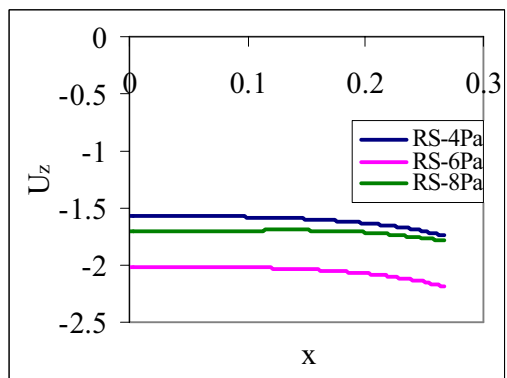
Fig 9.10 (a) Velocity in x direction for $\Delta P = 12.459$ Pa at $z = 0.5$ m



(b) Velocity in x direction for $\Delta P = 12.459$ Pa at $z = 1.0$ m



(c) Velocity in x direction for $\Delta P = 12.459$ Pa at $z = 1.5$ m



(d) Velocity in x direction for $\Delta P = 12.459$ Pa at $z = 2.1336$ m

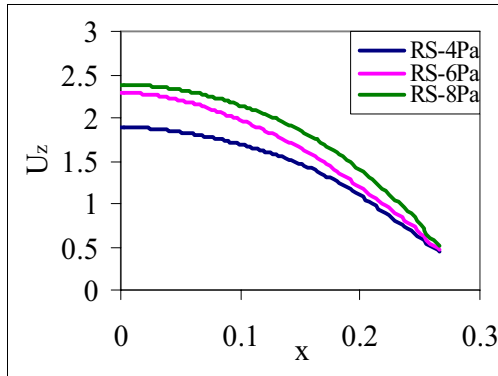
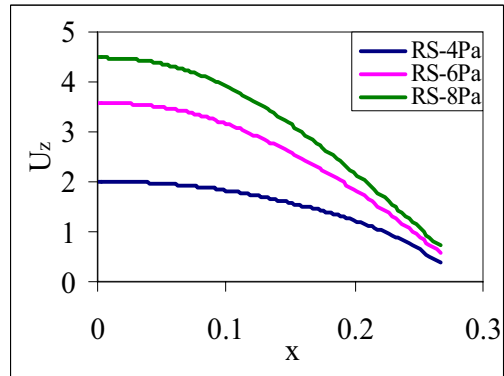
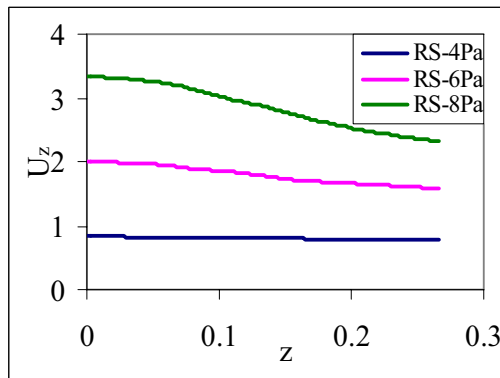


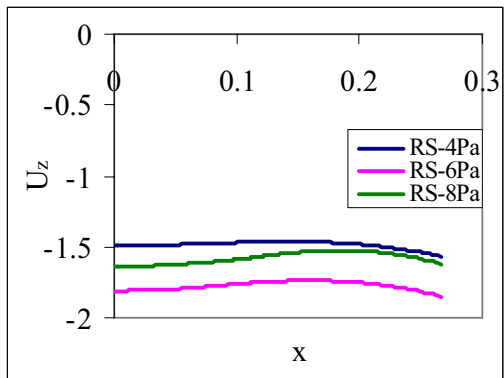
Fig 9.11 (a) Velocity in x direction for $\Delta P = 6.229$ Pa at $z = 0.5$ m



(b) Velocity in x direction for $\Delta P = 6.229$ Pa at $z = 1.0$ m



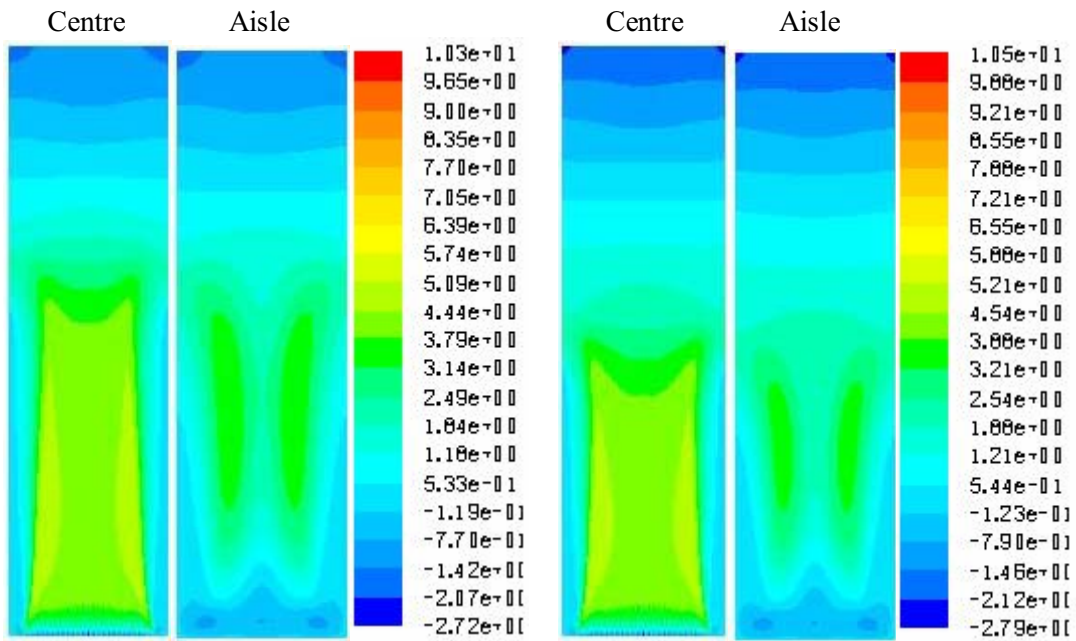
(c) Velocity in x direction for $\Delta P = 6.229$ Pa at $z = 1.5$ m



(d) Velocity in x direction for $\Delta P = 6.229$ Pa at $z = 2.1336$ m

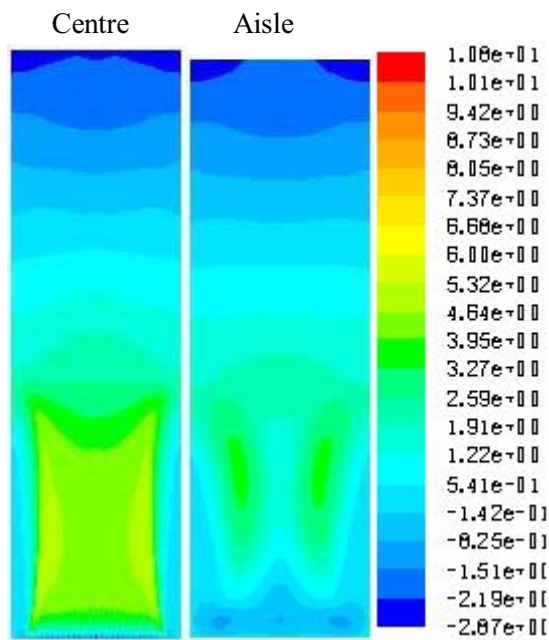
From the above figures it can be concluded that, the reverse effect of velocity takes place in the x direction also. As the pressure difference across the tile reduces, for higher rack suction pressures the velocity profiles in the x direction are improving. For a pressure difference of 6.229 Pa higher rack suction pressures develop far more velocities than the other cases. This is due to the fact that the pressure difference across the tile is lower than the rack suction pressure.

The velocity plots shown in figures 9.12 to 9.17 illustrate the velocity distribution and recirculation flow within the cold aisle in the direction at different locations for varying rack suction pressures for varying pressure difference across the tile.



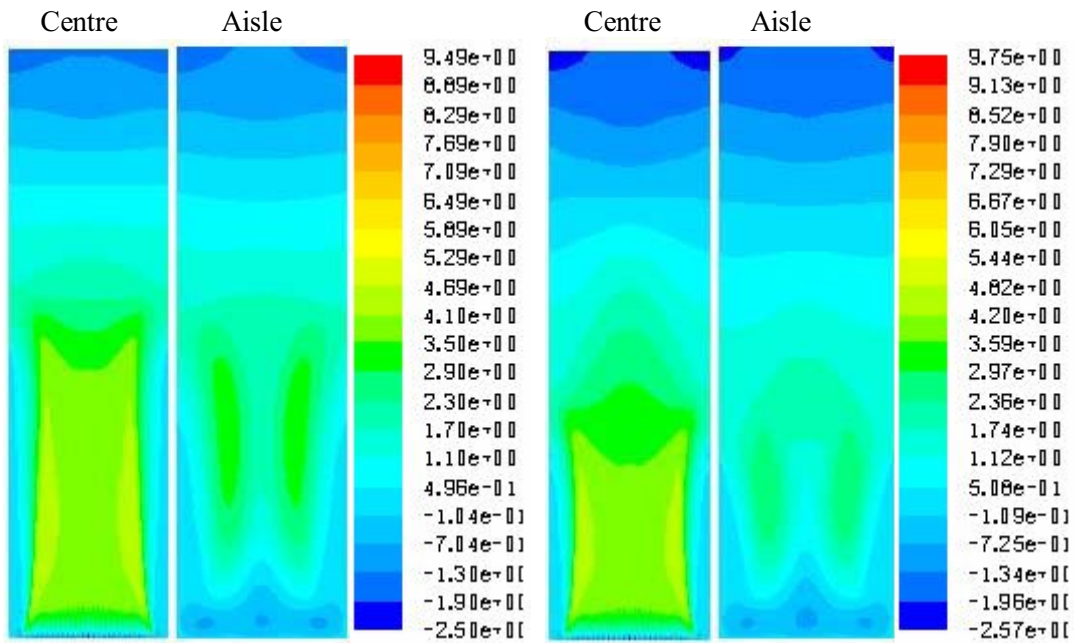
(a) For rack suction pressure 4 Pa

(b) For rack suction pressure 6 Pa



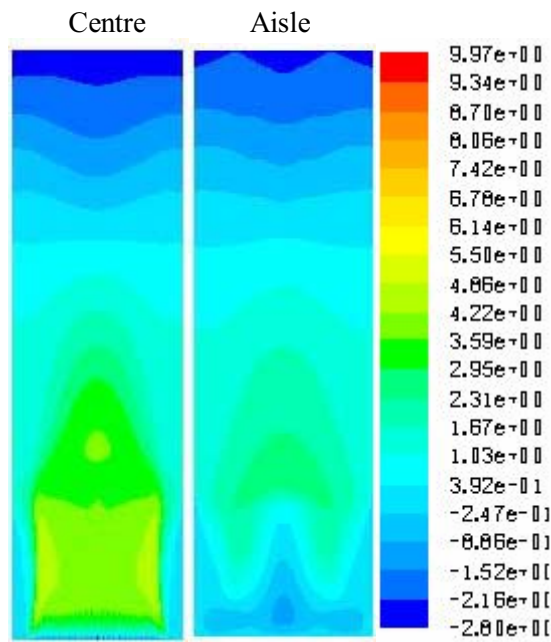
(c) For rack suction pressure 8 Pa

Fig 9.12 Velocity plots at the centre of the tile and the aisle side at a pressure difference of 37.376 Pa across the tile for various rack suction pressure.



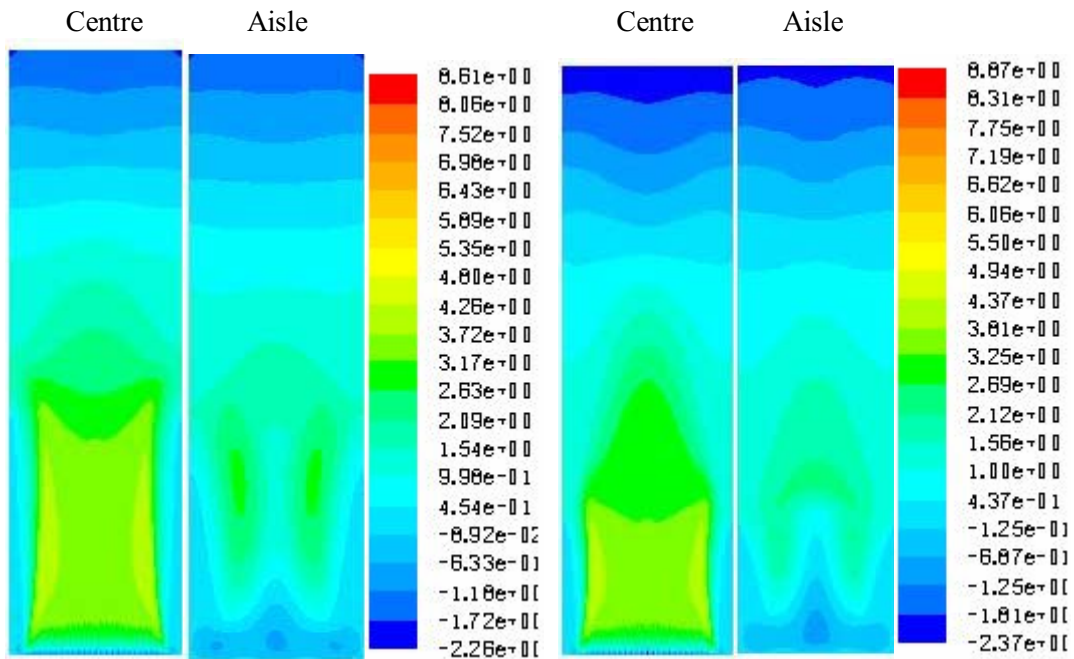
(a) For rack suction pressure 4 Pa

(b) For rack suction pressure 6 Pa



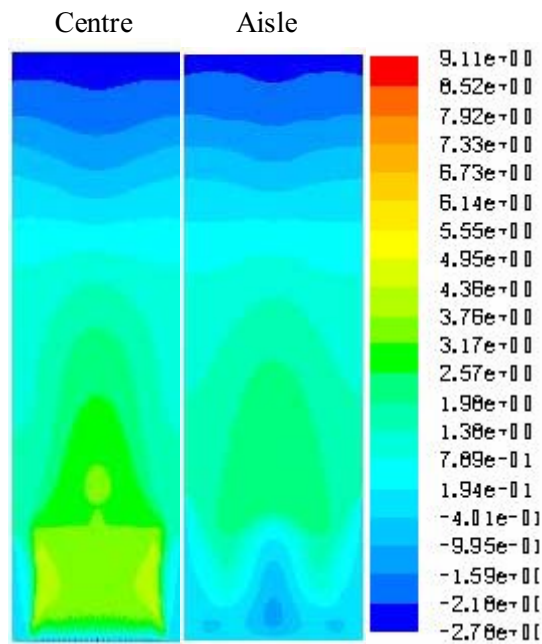
(c) For rack suction pressure 8 Pa

Fig 9.13 Velocity plots at the centre of the tile and the aisle side at a pressure difference of 31.147 Pa across the tile for various rack suction pressure.



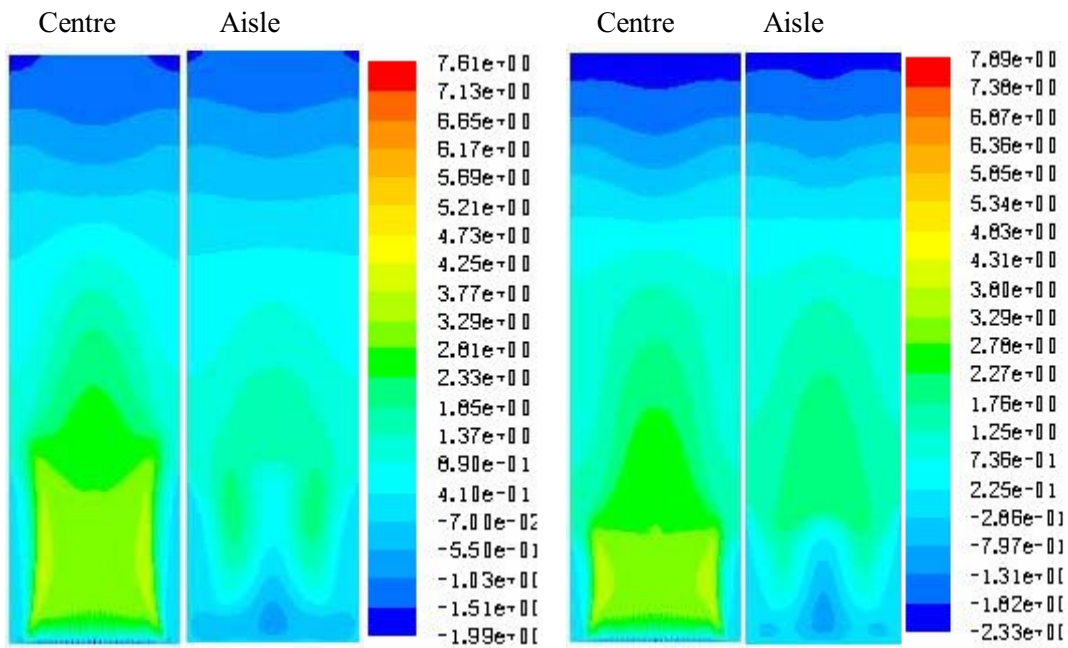
(a) For rack suction pressure 4 Pa

(b) For rack suction pressure 6 Pa



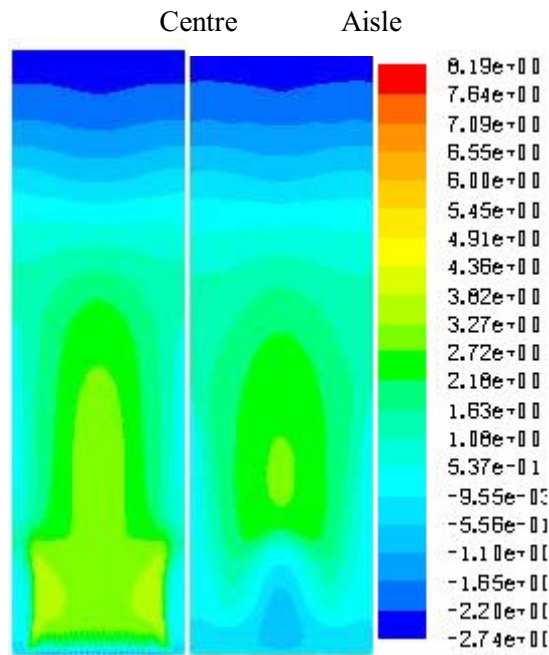
(c) For rack suction pressure 8 Pa

Fig 9.14 Velocity plots at the centre of the tile and the aisle side at a pressure difference of 24.917 Pa across the tile for various rack suction pressure.



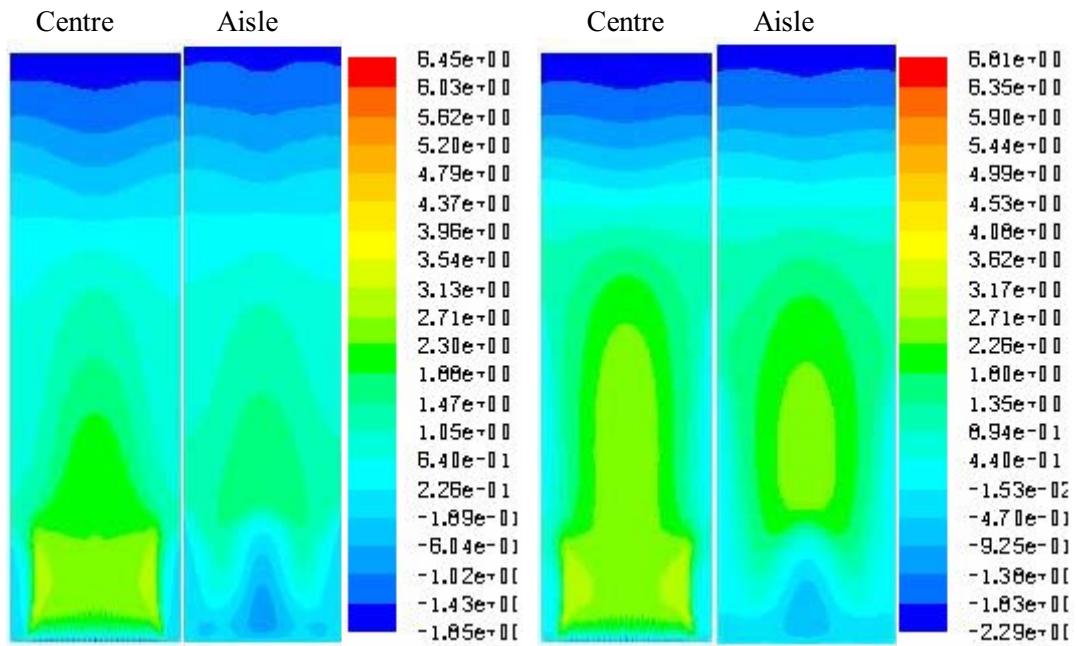
(a) For rack suction pressure 4 Pa

(b) For rack suction pressure 6 Pa



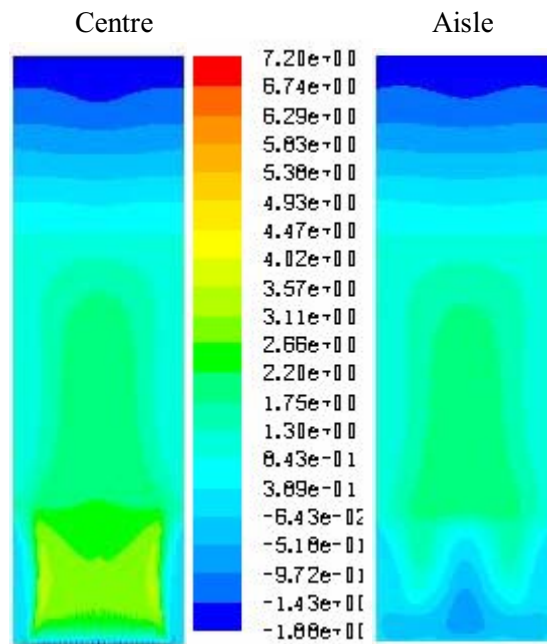
(c) For rack suction pressure 8 Pa

Fig 9.15 Velocity plots at the centre of the tile and the aisle side at a pressure difference of 18.688 Pa across the tile for various rack suction pressure.



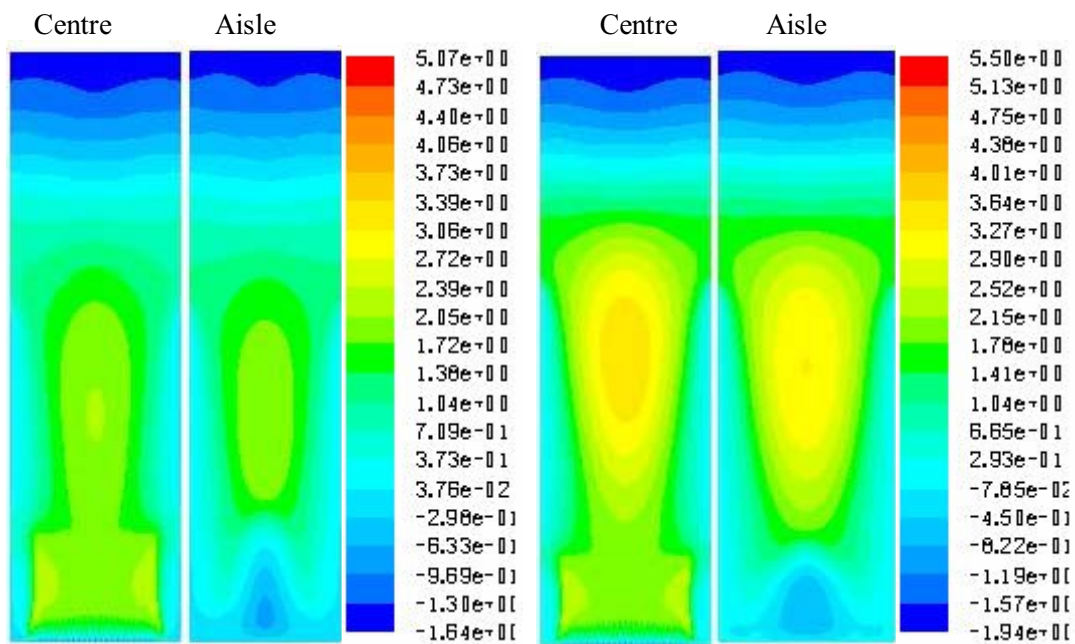
(a) For rack suction pressure 4 Pa

(b) For rack suction pressure 6 Pa



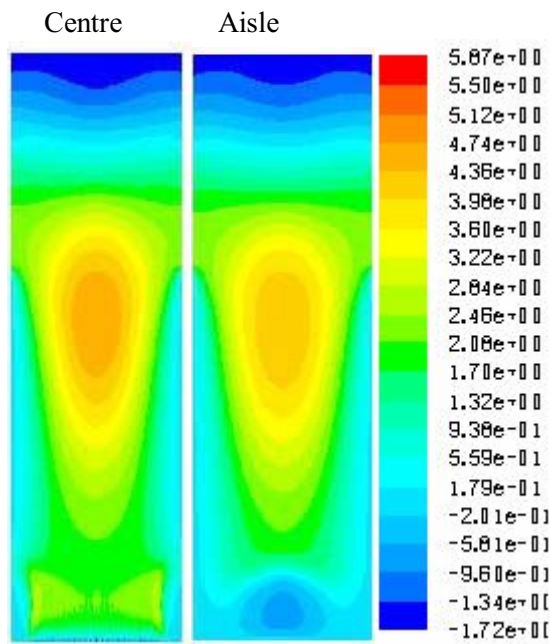
(c) For rack suction pressure 8 Pa

Fig 9.16 Velocity plots at the centre of the tile and the aisle side at a pressure difference of 12.459 Pa across the tile for various rack suction pressure.



(a) For rack suction pressure 4 Pa

(b) For rack suction pressure 6 Pa



(c) For rack suction pressure 8 Pa

Fig 9.17 Velocity plots at the centre of the tile and the aisle side at a pressure difference of 6.229 Pa across the tile for various rack suction pressure.

The figures 9.18 to 9.23 show the velocity distribution with in the cold aisle in x and y directions at different z locations. The velocity plot shows two tiles hence the interactions of the flow from two tiles are more visible in these plots.

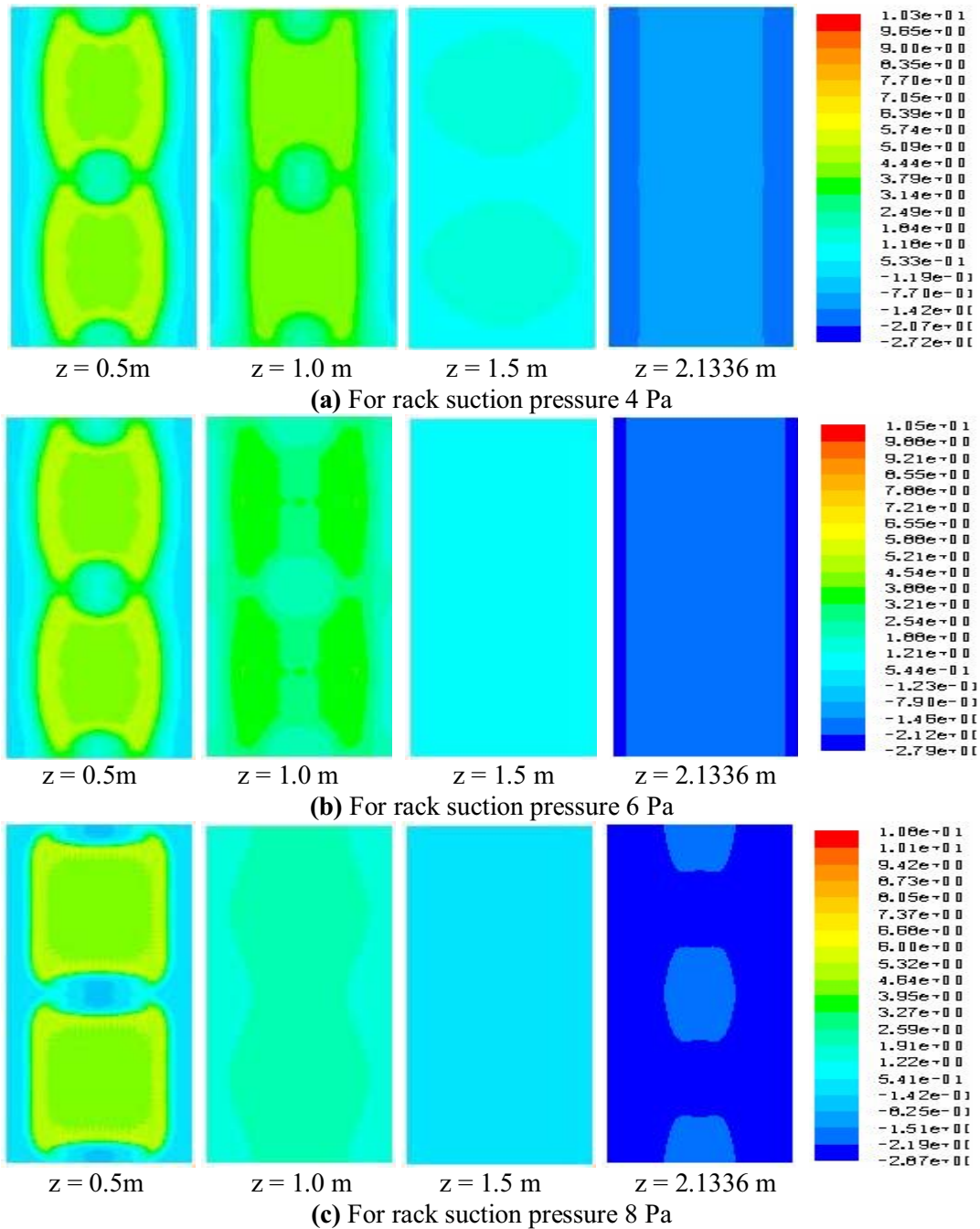
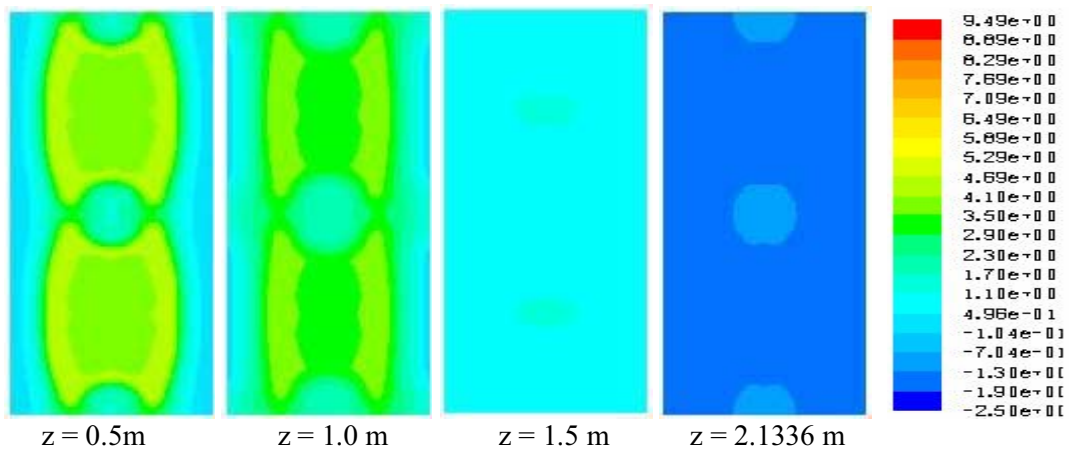
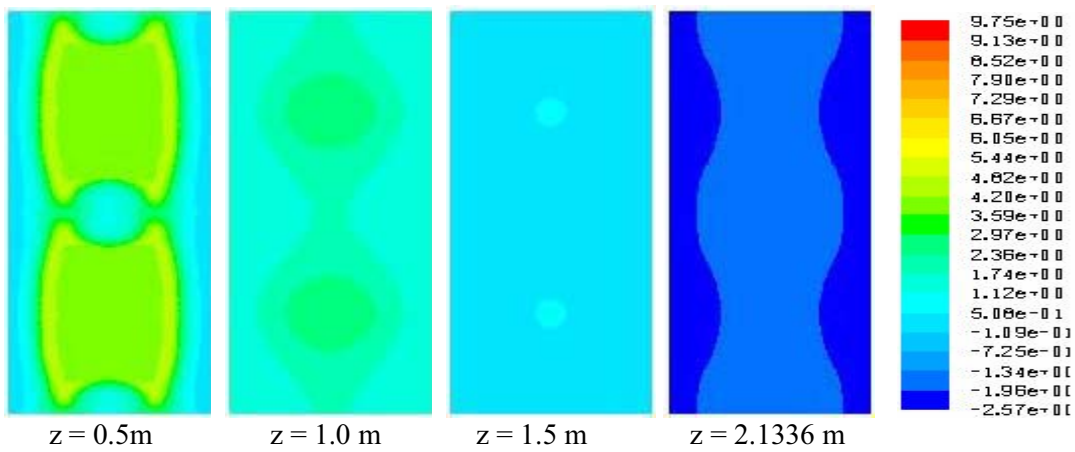


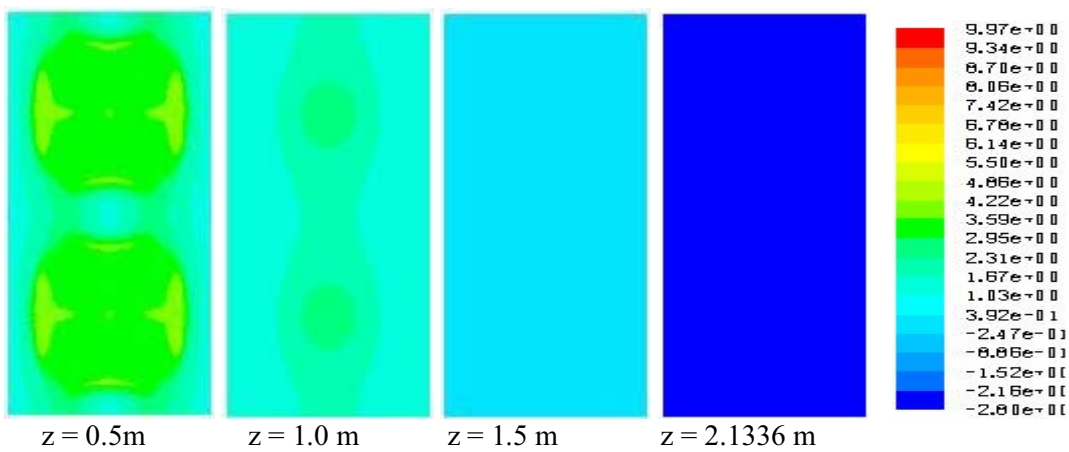
Fig 9.18 Velocity plots in x and y directions for 37.376 Pa at different z locations for various rack suction pressure.



(a) For rack suction pressure 4 Pa



(b) For rack suction pressure 6 Pa



(c) For rack suction pressure 8 Pa

Fig 9.19 Velocity plots in x and y directions for 31.147 Pa at different z locations for various rack suction pressure.

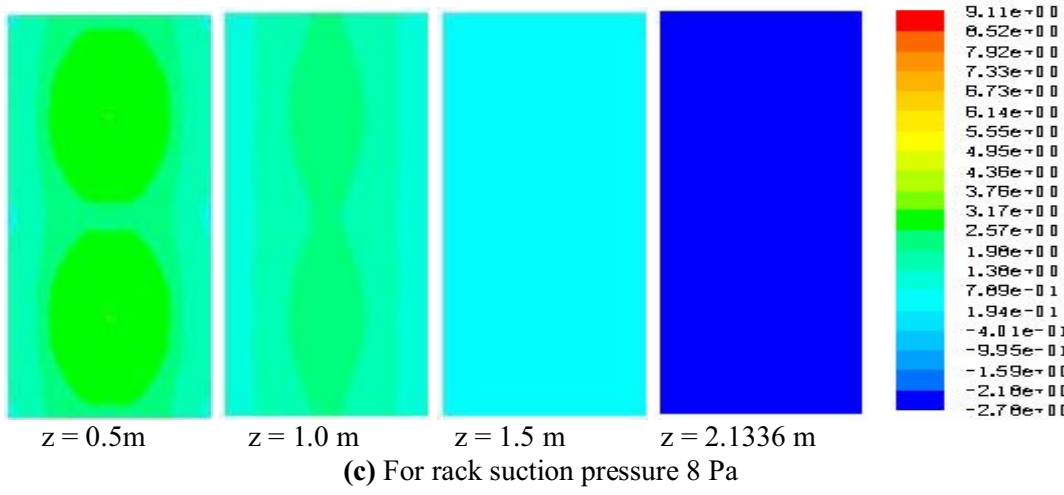
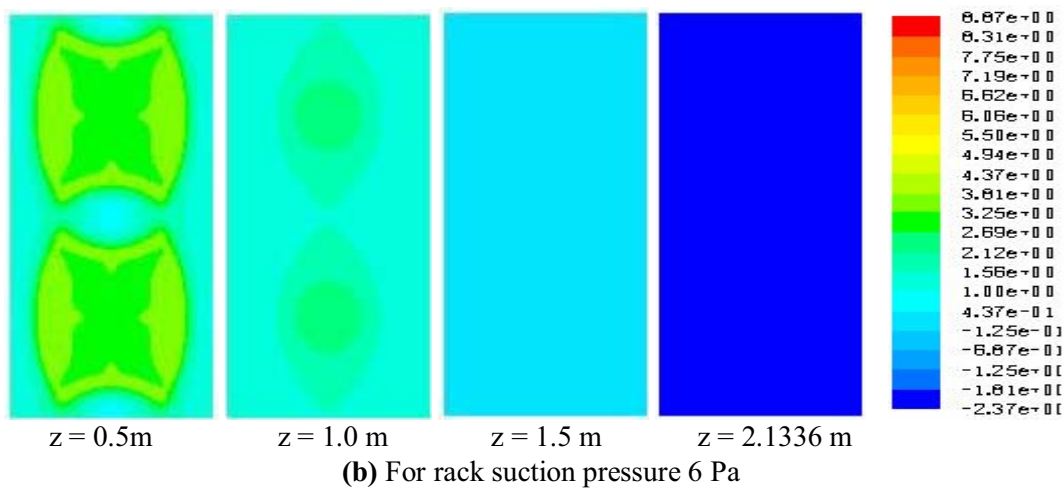
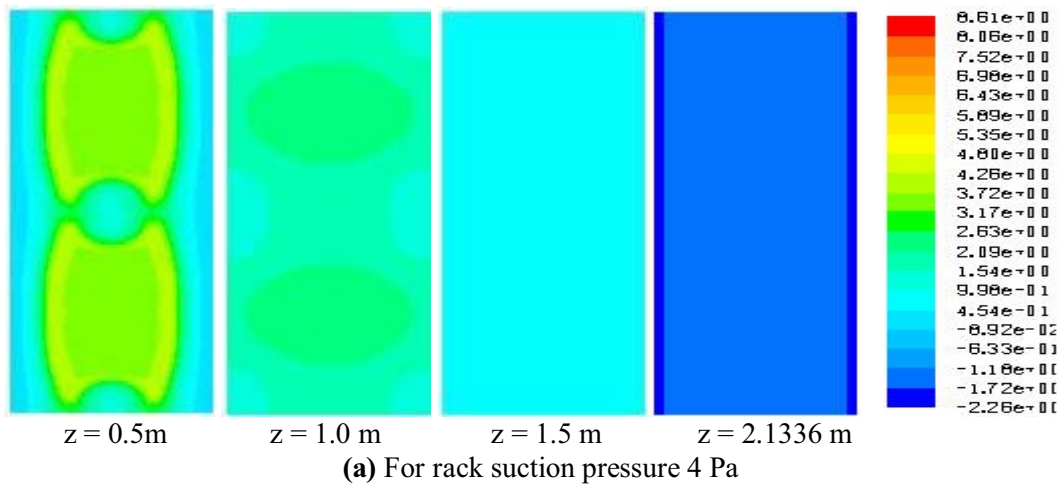


Fig 9.20 Velocity plots in x and y directions for 24.917 Pa at different z locations for various rack suction pressure.

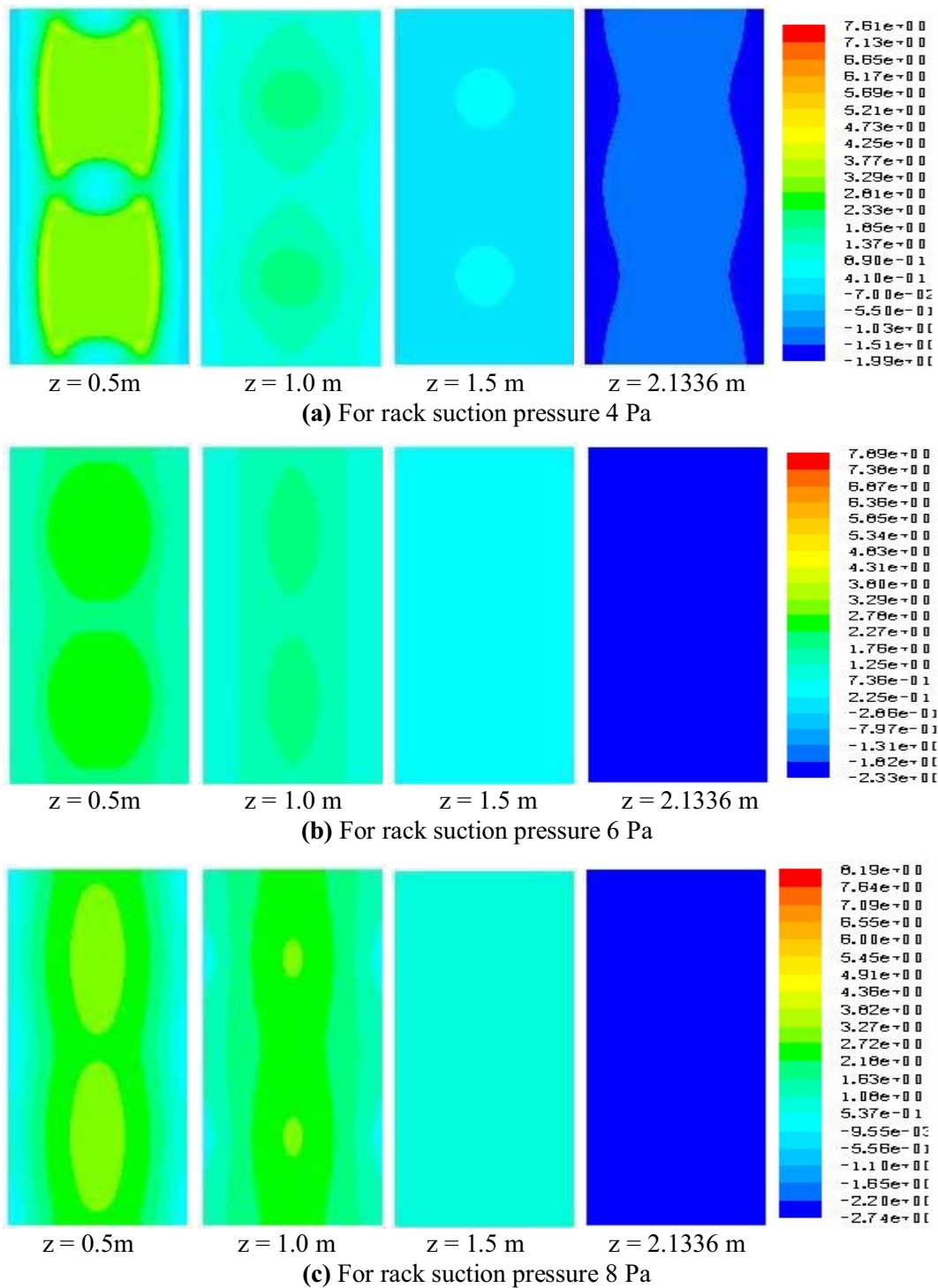
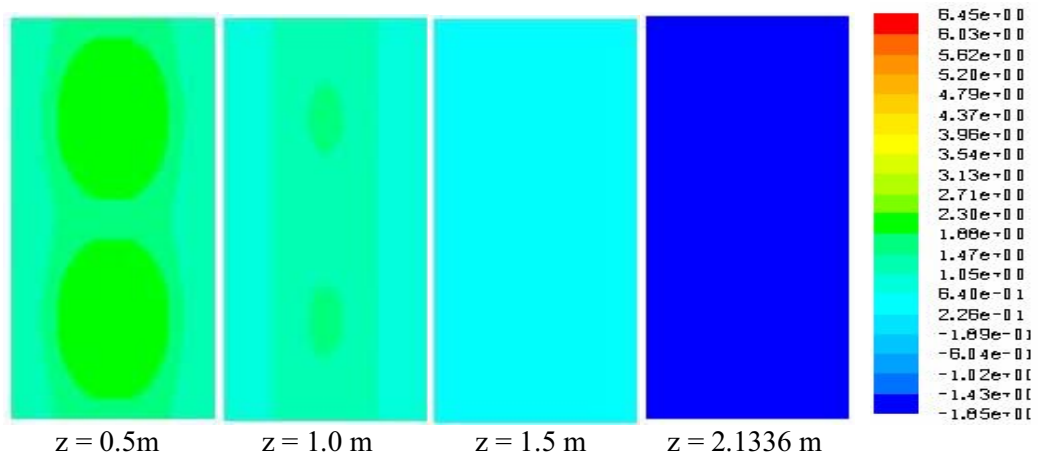
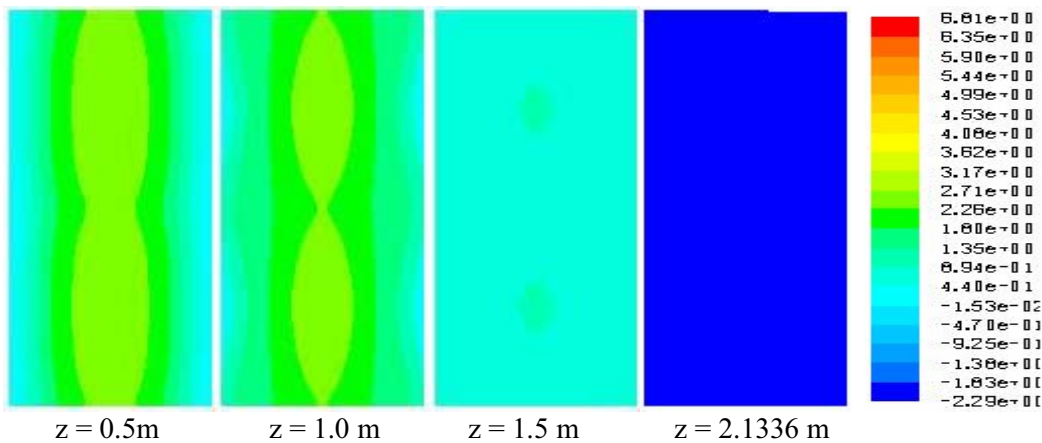


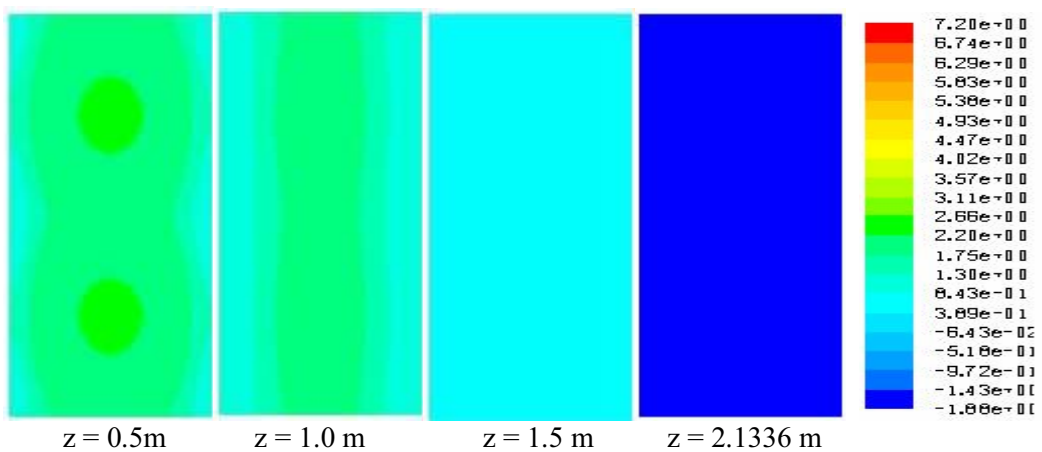
Fig 9.21 Velocity plots in x and y directions for 18.688 Pa at different z locations for various rack suction pressure.



(a) For rack suction pressure 4 Pa



(b) For rack suction pressure 6 Pa



(c) For rack suction pressure 8 Pa

Fig 9.22 Velocity plots in x and y directions for 12.459 Pa at different z locations for various rack suction pressure.

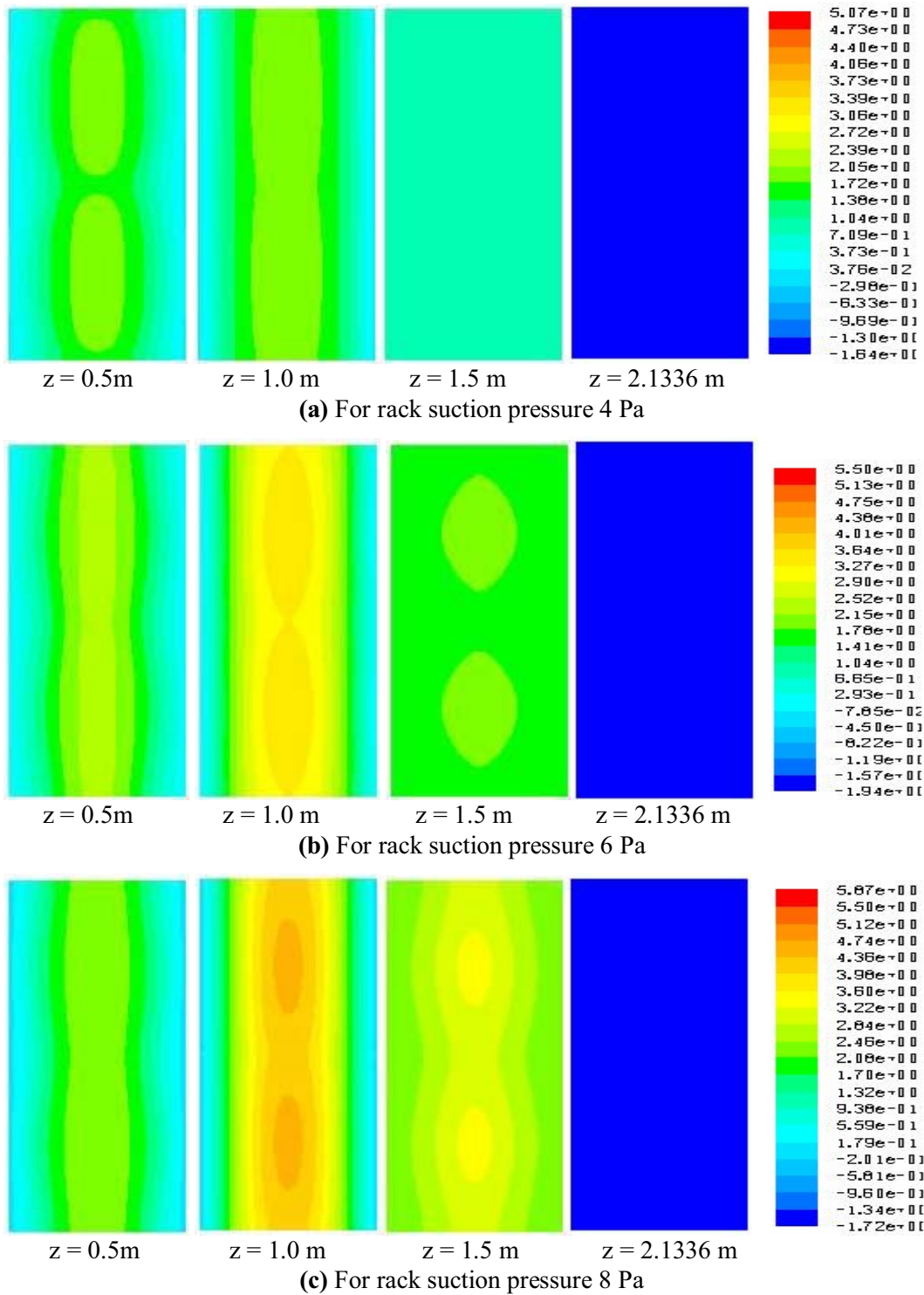


Fig 9.23 Velocity plots in x and y directions for 6.229 Pa at different z locations for various rack suction pressure.

From the figures, it can be observed that for all pressure differences across the tile, the velocity distribution above a height of 1.5m for all rack suction pressures are similar and the velocity values are very low and insufficient for maintaining the required flow. Hence it is essential to study these velocity distributions before arriving at the design of rack power deployment. Other wise the hardware kept at the top region of the rack will suffer from heavy recirculation and will be referred as hot spots during analysis.

9.5 Conclusion

The aim of this chapter was to introduce the effect of damper on the qualitative flow of air through the tiles and to explain the phenomenon of recirculation. The adverse effect of damper on the tile flow is successfully explained with the help of the present analysis. The damper has got two important factors that influence the tile flow. The additional pressure drop created across the damper reduces the effective pressure difference across the tile and the asymmetric configuration change occurring due to the opening and closing of the damper. In the present analysis, only the first factor is considered for analysis. If the effect of configuration change is also considered, the impact on the qualitative air flow will be more adverse. Hence the present studies conclude that the use of dampers for capacity control in tiles while using in data centre must be avoided.

The recirculation effect is explained in detail in the present study. The present study has got the drawback of assuming same rack suction pressure through out the front face of the rack, which is a rare possibility in real situation of data centre. Hence the present study results will have numerical deviation from the real situation. The study helped in establishing a relation between the pressure difference across the tile and the rack suction pressure. The present study finds its importance in explaining the mechanism of recirculation qualitatively and quantitatively for the first time.

.....END.....

CONCLUSIONS AND SUGGESTIONS FOR FUTURE WORK

10.1 Major Conclusions from the Present Study

The aim of the present study was to explain the air flow pattern in a data centre scientifically and systematically. The air flow pattern within the data centre is found to depend on the operating characteristics of the perforated vent tiles. In order to explain the data centre air flow, it was essential to find a suitable methodology by which the vent tiles can be analysed scientifically. In the present study, jet theory is proposed to explain the tile flow. Data centre tiles can be modelled as multiple jet arrays and hence its characteristics can be established. This concept is successfully implemented in the present work.

In order to arrive at the multiple jet arrays, a thorough study of the basic jet theory and modelling of different jet configurations was necessary. Simple axisymmetric jets were first taken up for study. The results of this study helped to understand the behaviour of the jets with respect to the orifice diameter and the orifice thickness. Based on the results, it is concluded that orifice diameters below 10mm are not suitable for use as major orifice matrix in tiles. Orifice diameters below 10mm will result in lower area ratios of the tile. The velocity distribution of such orifices will not be suitable for application in a data centre. Orifice diameters ranging from 10mm to 14mm are found to be suitable for using as major matrix array in the standard tiles. Orifice diameters below 10mm are recommended for use as minor matrix array in combination tiles. From the study, it is observed that the orifice thickness plays an important role in the velocity distribution of the jet as well as the load bearing capacity of the tile. As the tile thickness increases, the jet quality decreases due to increased friction, whereas, the load bearing capacity of

the tile increases. Hence the decision on the tile thickness is a compromise between the above two aspects. An orifice thickness in the range of 10mm to 12mm is found to satisfy both the aspects.

Detailed studies on plane jets are made in the present study with different jet configurations. This includes, single jet, twin jet, triple jet and differential triple jet. The studies on different jet configurations showed that the jet exit velocity and the maximum velocity are the same for any pressure difference across the orifice. The location of maximum velocity was found to get extended as the diameter of the orifice increases. As the jet diameter increases, the jet strength increases and the decay is less. From this study it is concluded that, orifice diameters 10mm, 12mm and 14mm are equally suitable to be used as major matrix array in the tile. The selection of a particular orifice depends only on the total area ratio required by the tile.

The studies on twin jets revealed that all the twin jet combinations show an increase in the jet exit velocity when compared to the respective exit velocity for single jets. This is found to be due to the creation of an additional pressure drop between the jets resulting from the mutual entrainment of the twin jets. The merging point of twin jet combinations are identified as the maximum velocity point on the central merging axis.

In triple jet geometries, it is found that the jet exit velocity decreases as the jet diameter increases. The jet exit velocity shows an increasing trend as the pitch increases. The central jet shows higher velocities when compared with the outer jets. The central jet is entrained by the two neighbouring jets from both sides, thereby enabling the central jet to accelerate more. The complete merging conditions of the triple jet geometry are established in this study. The physical mechanism of merging of triple jets consists of two stages. In the first stage, the neighbouring jets will merge with the central jet. This merging location can be identified as the maximum velocity point on the merging axis. In the second stage,

the potential core of the central jet merges with the partially merged side jets. This merging location is fixed by transferring the primary merging point velocity onto the central jet velocity axis. This is further verified by obtaining the centreline velocity decay of the central jet. This plot shows a specific point where the slope of the curve changes. This point corresponds to the final merging point obtained. Hence the complete merging of the triple jet is established in this study.

The complete merging of differential triple jets is also found to follow the same trend as that for triple jets. The studies on differential triple jets established the effects of a dissimilar jet introduced between two similar jets. The introduction of a larger diameter jet between two smaller diameter jets will effectively reduce the velocities of the three jets from their corresponding triple jet velocities. However, the introduction of a smaller diameter jet between two larger diameter jets will increase all the velocities including the merging velocity. The results obtained from the study of differential triple jets have great significance in the design of combination tiles. The combination tile can be considered as a cluster of differential triple jet modules.

The studies on three dimensional jets revealed that the meshing pattern adopted for tracing the circular orifice influences the mass flow and velocity calculations through the orifice. The study resulted in the development of correction factors for mass flow and velocity. The correction factors for different mesh patterns are presented in this work. With the help of these correction factors, suitable modelling methodologies can be selected for different three dimensional jet configurations.

The studies on three dimensional single jets showed that jets of diameters 12mm and 14mm have better velocity characteristics than 10mm and 8mm jets. Merging of three dimensional twin jets is found to be different from the merging mechanism of plane twin jets. The study shows that the basic methodology adopted for plane jets cannot be applied to three dimensional twin jets. Three dimensional

twin jets will spread more in x direction and converge in y direction during merging. Hence the position of maximum velocity on the merging axis will not confirm to the actual merging point. But the merging of plane twin jets and three dimensional twin jets exhibit a unique similarity. When the merging location of a plane twin jet is transferred to a similar three dimensional twin jet, this point is found to represent the actual merging point of the three dimensional twin jet. Hence the complete merging of the three dimensional twin jet is obtained.

In the case of three dimensional triple jets, it is observed that the complete merging point can be arrived from the information obtained from similar plane triple jets. The study revealed a strong interdependence between the plane and three dimensional triple jets with respect to their merging characteristics. Whether it is a plane triple jet or three dimensional triple jet, the final merging position follows a similar pattern. This is found to be true for differential triple jets also. The merging mechanism of three dimensional 4 jet and 5 jet modules can also be explained by the procedure followed for other three dimensional jet configuration.

A scientific and systematic tile design and designation coding system is presented in this work. Presently there is no specific coding system available for data centre tiles. The coding system introduced includes all the salient features that are to be considered with respect to a tile. This coding system includes the orifice diameter, the tile thickness, the pitch and the open area ratio of the tile. Different tiles are modelled and analysed. The mass flow calibration charts and velocity distribution charts of the tiles selected for analysis have been developed. From the mass flow charts, it is possible to find the flow rate through the tile corresponding to a specific pressure difference across it. The velocity distribution chart can be used to find out the velocity at any location within the cold aisle. This will give enormous flexibility in data centre design and implementation. The tiles described in this work are defined both qualitatively and quantitatively.

Dampers are used along with the tiles for capacity control in data centre. The effect of damper in data centre tiles for capacity control is studied in the present work. The damper will change the open area ratio of the tile while closing or opening. This will change the mass flow rates through the tiles. This serves the purpose of quantitative control of the air flow. The present study identifies that the operation of a damper will introduce an additional resistance across the tile. This will create a pressure drop across the damper. The effective pressure drop across the tile will come down due to this reason. This will affect the velocity distribution from the tiles. Operation of the damper will lead to a change in the configuration of the flow geometry of the tile, which in turn will affect the development and merging of jets discharged through the orifices of the tile. Hence the study strongly proposes that dampers are not suitable for the capacity control of air flow in data centre. Custom made designer tiles must be used for capacity control in data centre.

The studies on recirculation effects showed that the recirculation of air can be controlled by proper design of vent tiles. The data centre air flow is a balance between the flow from the tile, the flow through the racks and the recirculation flow. The present study shows that the recirculation point is dependant on the rack flow and the tile flow. If the tile flow and the rack flow are balanced, there will not be any recirculation. But it is seldom possible to achieve this, as the data centre environment is dynamic in nature. It is observed that the use of dampers will increase the recirculation effect. It is concluded that well designed tiles can control the recirculation effects in a data centre. Hence the present study emphasises the need for systematic and scientific design of perforated vent tiles in data centre.

10.2 Scope for Future Work

In the present work, the feasibility of the concept of airflow management in a data centre through systematic design of the perforated vent tiles is explored. The study established the need for qualitative air flow management in data centre. The theories developed here need to be experimentally verified before being applied to

a real life data centre. But the experimental procedure is difficult and highly expensive as data centre are mission critical facilities with very limited access. Experimental investigations in a live data centre is time consuming and expensive. Major IT organizations need to be convinced about the importance of setting up research data centre to promote investigations on qualitative air flow management.

Future research in this area should also concentrate on the development of specialised software which can be used for the design and analysis of the data centre. The presently available software considers the quantitative aspects of air flow within the data centre while modelling. They do not account the air flow distribution pattern within the data centre. Most of the software consider the tiles as simple resistances placed in the airflow and calculates mass flow rates according to the resistance values assigned to the tile. This approach has its own limitations and the results obtained from the modelling will not reflect the reality. If the tile design is modified based on the findings of the present research work, there can be a qualitative change in the data centre operation. The software must be restructured to include the design aspects of the tiles and the qualitative aspects of airflow.

Present work opens up an area which needs continuous research. Any valid conclusions in this field will gain acceptance with industry and academic. Present work is only a pilot work in this field which introduces an entirely new concept.

Another area for future research may be the potential for energy conservation measures in data centre. There is a need to quantify the energy savings obtained by qualitative air flow management in data centre air conditioning.

10.3 SWOT Analysis

The present work introduces a new concept of data centre air flow management through scientific and systematic design of the vent tiles. It will be beneficial to have a

brief SWOT analysis of the entire scenario. The STRENGTH, WEAKNESS, OPPORTUNITY and THREATS related to the work are summarized below.

10.3.1 Strength

Data centre is a hot topic of discussion in IT industry for the last few decades and any work which improves the quality of performance of the data centre will be well appreciated by the industry. The present work emphasises the importance of air flow management in data centre air conditioning system and introduces a new concept of design and designation of vent tile for better performance of the data centre. A qualitative air flow management system in data centre is a new concept in energy conservation and hence must attract attention in the near future. This is the STRENGTH of the present work.

10.3.2 Weakness

The core concept of the present work does not suffer from any WEAKNESS. However, the qualitative treatment of the air flow made in the present work entirely depends on the computational results, the hence the reliability and accuracy of the results may differ from the actual situation. The experimental validation of the results presented in this work is very difficult as it has to be done in a live data centre environment. Setting up of a research data centre facility is highly expensive and not available with any of the companies who are engaged in researches in this field. The future research may focus on the experimental investigations in data centre set up for research purpose.

10.3.3 Opportunity

Any work in the data centre field opens up lot of OPPORTUNITIES since a data centre is the heart of the present IT revolution. This field demands a lot of research activities from both industry and academia. A combined effort from industry and academic experts in this field will strengthen the advancements in this direction and will result in remarkable achievements towards efficient operation of data centre.

10.4.4 Threats

“Technology delayed is technology obsolete”. Even though the core concept of this work was developed a few years back, it has not been adopted by the IT industry so far. The concept of air flow management does not suffer any THREATS as it is always beneficial to the industry.

.....❧.....

- [1]. **Albini, F. A** (1965) Approximate computation of under expanded jet structure, *AIAA Journal*, **3**, 1535-1537.
- [2]. **Bachelor, G.K., H.K. Moffatt, and M.G. Worster** (2000) *Perspectives in fluid dynamic research-A collective introduction to current research*. Cambridge University Press, New York.
- [3]. **Becker.H.A, Massaro.T.A** (1968), Vortex evolution in a round jet, *Journal of Fluid Mechanics*, **31**, 435-448.
- [4]. **Blazek.J** (2001) *Computational fluid dynamics: Principles and application*, Elsevier Publishing Co., Amsterdam and New York.
- [5]. **Bradbury, L.J.S** (1965) The Structure of a self preserving turbulent plane jet. *Journal of Fluid Mechanics*, **23 (1)**, 31-64.
- [6]. **Bradshaw, P** (1966) The effect of initial conditions on the development of a free shear layer. *Journal of Fluid Mechanics*, **26 (2)**, 225-236.
- [7]. **Bradshaw.P** (1971) *An introduction to turbulence and its measurement*, Pergoman Press.
- [8]. **Brent Goren, P.Eng** (2008) Scalable design – creating data centre efficiencies using closed coupled design, *Wright Line LCC*, 160 Gold Star Boulevard, Worcester, MA 01606, www.wrightline.com.
- [9]. **Chandrakant D. Patel, Cullen E. Bash, Ratnesh Sharma, Monem Beitelmal** (2001) Smart Cooling: An Energy Management Proposition for High Compute Density Data Centres of Tomorrow, *Internet Systems and Storage Laboratory*, HP Laboratories Palo Alto.
- [10]. **Chervay.R, Tutu.N.K** (1978), Intermittency and preferential transport of heat in a round jet, *Journal of Fluid Mechanics*, **88**, 133-160.

- [11]. **Christopher Kurkjian** (2006) Air conditioning design for data centres – Accommodating current loads and planning for the future, *EYP mission critical facilities White paper*, 54 State Street, Albany, NY 12207, www.eypmcf.com.
- [12]. **Comings.E.W, Miller.D.R** (1957), Static pressure distribution in the free turbulent jet, *Journal of Fluid Mechanics*, **3**, 1-16.
- [13]. **Cullen E Bash, Chandrakanth D Patel, Ratnesh K Sharma** (2006) Dynamic Thermal Management of Air Cooled Data centres, Hewlett-Packard Laboratories, Palo Alto -2006-11, January 13, 2006.
- [14]. **Data Centre Resource Guide** (2007) Anixter Inc. 1.800.ANIXTER, World Headquarters: 2301 Patriot Boulevard, Glenview, IL, 60026-8020, www.anixter.com.
- [15]. **Deo.R.C, Mi.J and Nathan.G.J** (August 2007) The influence of nozzle aspect ratio on plane jets, *Experimental thermal and fluid sciences*, Volume **31**, issue 8, 825-838.
- [16]. **Deo.R.C, Mi.J and Nathan.G.J** (November 2007) Comparison of turbulent jets issuing from rectangular nozzles with and without side walls, *Experimental thermal and fluid sciences*, Volume **32**, issue 2, 596-606.
- [17]. **Eastman, D. W, Radtke. L. P** (1963) Location of the normal shock wave in the exhaust plume of a jet, *AIAA Journal*, **1**, 918-919.
- [18]. **Elbanna. H, Sabbagh. J. A** (1989) Flow visualization and measurements in a two-dimensional two-impinging-jet flow, *AIAA Journal*, **27**, 420-426.
- [19]. **Elbanna. H, Gahin. S, Rashed. M. I. I** (1983) Investigation of two plane parallel jets, *AIAA Journal*, **21**, 986-991.
- [20]. **Fluent 6 users guide volume** (2005) Fluent Inc.
- [21]. **Guillaume Carazzo, Edouard Kaminski, Stephen Tail** (2006) The rout to self similarity in turbulent jets and plumes, *Journal of Fluid Mechanics*, Volume **547**, 137-148.

-
- [22]. **Hussain. A.K.M.F** (1983) Coherent structures –reality and myth. *Physics of Fluids*. **26(10)**, 2816-2850.
- [23]. **Ian Seaton** (2008) Hot Air Isolation Cools High-Density Data Centres, *Business Management Magazine* Winter 2008.
- [24]. **Ian Seaton** (2008) How to decrease data centre cooling cost up to 40%, *Communication News*, Power Play column.
- [25]. **Kailash C Karki, Amir Radmehr, Suhas V. Patankar** (2003) Use of computational fluid dynamics for calculating flow rates through perforated tiles in raised floor data centres, *International Journal of Heating, Ventilation, Air Conditioning and Refrigeration Research*. Volume **9**, Number **2**, April 2003, 153-166.
- [26]. **Klaus.A.H, Steve.T.C** (1993) Computational fluid dynamics for engineers – Volume I, Engineering Education System, P.O.Box 20078, Wichita, KS 67208-1078, USA.
- [27]. **Kostovinos.N.E, List.J** (1977) Plane turbulent buoyant jets, Part 1, Integral properties, *Journal of Fluid Mechanics*, Volume **81**, Part 1, 35-44.
- [28]. **Kotsovinos.N.E** (1978) A note on the conservation of the volume flux in free turbulence, *Journal of Fluid Mechanics*, **87**, 210-203.
- [29]. **Kotsovinos.N.E**, (1978) A note on the conservation of the axial momentum of a turbulent jet, *Journal of Fluid mechanics*, **86**, 55-63.
- [30]. **Krothapalli A, Baganoff D, Karamcheti. K** (1981) Partially confined multiple jet mixing, *AIAA Journal*, **19**, 324-328.
- [31]. **Krothapalli. A, Baganoff. D, Karamcheti. K**, (1981) On the mixing of a rectangular jet, *Journal of Fluid Mechanics*, **107**, 201-220.
- [32]. **Krothapalli. A, Baganoff. D, Karamcheti. K**, (1980) Development and structure of a rectangular jet in a multiple jet configuration, *AIAA Journal*, **18**, 949-950.
- [33]. **Launder.B.E, Reece.G.J, Rodi.W** (1975) Progress in the development of a Reynolds stress turbulent closure, *Journal of Fluid Mechanics*, **68**, 537-566.

- [34]. **Launder.B.E, Spalding.D.B** (1974) The numerical computation of turbulent flows, *Computer Methods in Applied Mechanics & Engineering*, **3**, 269-289.
- [35]. **Launder.B.E, Hanjalic.K** (1972) A Reynolds stress model of turbulence and its applications to thin shear flows, *Journal of fluid Mechanics*, **52**, 609-638.
- [36]. **Lin. Y. F, Sheu. M. J** (1991) Interaction of parallel turbulent plane jets, *AIAA Journal*, **29**, 1372-1373.
- [37]. **List.E.J** (1982) Turbulent jets and plumes, Annual revision of Fluid Mechanics, **14**, 189.
- [38]. **Liu. Y, Bellhouse. B** (2005) Prediction of jet flows in supersonic nozzle and diffuser, *International Journal for Numerical Methods in Fluids*, **47**, 1147-1155.
- [39]. **Looney.M.K, Walsh.J.J** (1984) Mean-flow and turbulent characteristics of free and impinging jet flows, *Journal of Fluid mechanics*, **147**, 397-429.
- [40]. **Love, E. S.** (1958) An approximation of a boundary of a supersonic axisymmetric jet exhausting into supersonic stream, *Journal of the Aeronautical Sciences*, February, 130-131.
- [41]. **Martynenko.O.G, Korovkin.V.N** (1993) Concerning the calculation of plane turbulent jets on the basis of the k- ϵ model of turbulence, *International Journal of Heat and Mass Transfer*, **35**, 3389-3395.
- [42]. **McGuirk. J. J, Rodi W** (1979) Mathematical modeling of three-dimensional heated surface jets, *Journal of Fluid Mechanics*, **95**, 609-633.
- [43]. **Moustafa. G. H** (1995) Interaction of axisymmetric supersonic twin jets, *AIAA Journal*, **33**, 871-875.
- [44]. **Moustafa. G. H** (1994) Experimental investigation of high-speed twin jets, *AIAA Journal*, **32**, 2320-2322.
- [45]. **Murai. K, Taga M, Akagawa. K** (1976) An experimental study confluence of two two-dimensional jets, *Bulletin of the JSME*, **19**, 958-964.
- [46]. **Namer. I, Otugen. M.V** (1988) Velocity measurements in a plane turbulent jet at moderate Reynolds number, *Experiments in Fluids*, **6**, 387-389.

- [47]. **Niimi T, Fujimoto. T, Taoi N** (1996) Flow fields of interacting supersonic free jets, *JSME International Journal (series B)*, **39**, 95-100.
- [48]. **Okamoto.T, Yagita. M, A.Watanabe, Kawamura K** (1985) Interaction of twin turbulent circular jets, *Bulletin of JSME*, **28**, 618-622.
- [49]. **Panchapakesan, N. R, Lumley. J. L** (1993) Turbulence measurements in axisymmetric jets of air and helium. Part 1. Air jet, *Journal of Fluid Mechanics*, **246**, 225-247.
- [50]. **Paully.A.J, Melnik.R.E, Rubel.A, Rudman.S, Siclari.M.J** (1985) Similarity solutions for plane and radial jets using a k- ϵ turbulence model, *ASME Journal of Fluids Engineering*, **107**, 79-85.
- [51]. **Peterson.J.E, Hotton.D.K** (1995) Numerical analysis of turbulent cross stresses and pressure in the developing region of an axisymmetric jet, *International Communications in Heat and Mass transfer*, **22**, 871-883.
- [52]. **Pope** (2000) Turbulent flows, Cambridge University Press.
- [53]. **Pope.S.B** (1978) An explanation of the turbulent round jet/plane jet anomaly, *AIAA Journal*, **16**, 279-281.
- [54]. **Pulliam.T.H** (1994) Notes on solution methods in computational fluid dynamics, NASA, Ames research center, Moffett Field, California.
- [55]. **Raghunathan. S, Reid. I. M** (1981) A study of multiple jets, *AIAA Journal*, **19**, 124- 127.
- [56]. **Rajaratnam. N** (1976) Turbulent jets, Elsevier Publishing Co., Amsterdam, and New York.
- [57]. **Robert.F.Sullivan** (2002) Alternating cold and hot aisles provides more reliable cooling for server farms, *THE UPTIME INSTITUTE*, 1347 Tano Ridge Rd, Santa Fe, NM, 87505.
- [58]. **Rodi.W, Scheuerer.G** (1986) Scrutinizing the k- ϵ model of turbulence model under adverse pressure gradient conditions, *ASME Journal of Fluids Engineering*, **108**, 174-179.

- [59]. **Rodi.W** (1975), A new method of analyzing hot-wire signals in highly turbulent flow, and its evaluation in a round jet, *DISA Inf*, **17**, 9-18.
- [60]. **Sata. H, Sakao.F** (1964) An experimental investigation of the stability of a two dimensional jet low Reynolds numbers, *Journal of Fluid Mechanics*, **20**,337.
- [61]. **Seffal.R, Michaelides.E.E** (1996) Similarity solution for a turbulent round jet, *ASME Journal of Fluids Engineering*, **118**, 618-621.
- [62]. **Seiner, J. M, Manning. J. C, Ponton. M. K** (1988) Dynamic pressure loads associated with twin supersonic plume resonance, *AIAA Journal*, **26**, 954-960.
- [63]. **Sforza. P. M, Steiger. M. H, Trentacoste. N** (1966) Studies on three-dimensional viscous jets, *AIAA Journal*, **4**, 800-806.
- [64]. **Spalart.S.R, Allmaras.S.A** (1992) A one-equation turbulence model for Aerodynamic flows, AIAA paper **92-0439**, also, *La Recherche Aérospatiale*, 1 (1994) 5-21.
- [65]. **Tanaka. E** (1974) The interface of two-dimensional parallel jets (2nd report, experiments on combined flow of dual jets), *Bulletin of the JSME*, **17**, 920-927.
- [66]. **Tanaka. E** (1970) The interface of two-dimensional parallel jets (1st report, experiments on dual jets), *Bulletin of the JSME*, **13**, 272-280.
- [67]. **The Green Grid** (2007) Green Grid Metrics: Describing Data Centre Power Efficiency, *The Green Grid, Technical Committee*, www.thegreengrid.org.
- [68]. **Thomas.F.O and Brehob.E.J** (1986) An investigation of large-scale structure-I, the similarity region of a two-dimensional jets, *Physics of Fluids*, **29**, 6, 1788-1795.
- [69]. **Wlezien. R. W** (1989) Nozzle geometry effects on supersonic jet interaction, *AIAA Journal*, **27**, 1361-1367.
- [70]. **Wyganaski. I, Fiedler.H** (1969) Some measurements in the self-preserving jet, *Journal of Fluid Mechanics*, **39**, 577-612.
- [71]. **Yue. Z** (1999) Air jet velocity decay in ventilation applications. *Bulletin No.48*, Building services division, Royal Institute of Technology, Sweden.

.....✂.....



List of Publications Based on Research Work

- [1]. **Premnath.R, Madhu. G,** (2010) Data centre airflow dynamics – Need for a qualitative airflow management system for data centres, *International Journal of Fluids Engineering (IJFE)*, ISSN 0974-3138, Volume **2**, Number **2** (2010), pp.75-85.
- [2]. **Premnath.R, Suresh.P.R, Madhu. G,** (2011) Studies on Effect of Pitch on the Merging Characteristics of Isothermal Two Dimensional Twin Jets Using CFD, *International Journal of Dynamics of Fluids (IJDF)*, ISSN 0973-1784 Volume **7**, Number **1** (2011), pp. 17–23.
- [3]. **Premnath.R, Madhu. G,** (2011) Studies on Merging Characteristics of Isothermal Two Dimensional Identical Triple Jets Using CFD, *International Journal of Dynamics of Fluids (IJDF)*, ISSN 0973-1784 Volume **7**, Number **1** (2011), pp. 101–107.

Curriculum Vitae

PREMNATH.R

S/O K.Ramankutty Menon,
Chelat, Mythri Nagar, Kallepully,
Palakkad – 678018, Kerala.
premnathusha@rediffmail.com
0491-2533242, +91 9447365245.

Premnath.R, born on 31-05-1964 in Changanacherry, Kottayam (Dist) Kerala. He obtained B.Tech degree in Mechanical Engineering from Government Engineering College, Trichur in 1986 with First class. He obtained M.Tech degree in Industrial Refrigeration and Cryogenic Engineering from T K M College of Engineering, Kollam in 1991 with First Class, Distinction and Second Rank. He joined as Lecturer in Mechanical Engineering in N S S College of Engineering, Palakkad in 1991. Presently he is working as Associate Professor in Mechanical Engineering since 2006. He is a life member of Indian Society for Technical Education (ISTE) and Combustion Institute India chapter. His area of interest includes, Refrigeration, Heat transfer, Fluid mechanics, Data centre air conditioning design and thermal assessment.